

Experimental and Theoretical Investigation of Heat and Mass Transfer Processes in Porous Media

BY

WENSHUO ZHANG

B.S., Southwest Petroleum University, Chengdu, China, 2013

M.S., Illinois Institute of Technology, Chicago, USA, 2015

THESIS

Submitted as partial fulfillment of the requirements
for the degree of Doctor of Philosophy in Mechanical Engineering
in the Graduate College of the
University of Illinois at Chicago, 2019

Chicago, Illinois

Defense Committee:

Alexander L. Yarin,	Chair and Advisor
W.J. Minkowycz,	Mechanical and Industrial Engineering
Kenneth Brezinsky,	Mechanical and Industrial Engineering
Eduard Karpov,	Civil and Materials Engineering
Suman Sinha-Ray,	Mechanical and Industrial Engineering

I dedicate this thesis to my mother Congfang Zhang and my father Cheng Zhang,
without whose love and support it would never have been accomplished

ACKNOWLEDGEMENTS

First and foremost, I want to thank my advisor, Professor Alexander Yarin for being the best and tremendous mentor. Words cannot express my gratitude and appreciation to Professor Yarin for giving me the opportunity and letting me be his Ph.D. student. Since the day I joined his lab on May 21st, 2015, Professor Yarin gives me tremendous help and advises about my work. I am really grateful for the significant contributes of his time and ideas to my Ph.D. work. Professor Yarin teaches me a serious and hard-working attitude to the researches and shapes me into a researcher. His help expands my knowledge of different research fields and his enthusiasm for the work will always be my motivation. Without Professor Yarin`s trust, encouragement and support, I would never ever finish my Ph.D. work and this dissertation would never have been possible.

My thesis committee members also provided me with a significant support in my Ph.D. work and thesis preparation. Professor Minkowycz extended my knowledge in the field of heat transfer; Professor Brezinsky, Professor Karpov and Dr. Sinha-Ray give me many valuable suggestions about my thesis work. I really appreciate their help.

I want to thank my parents for the endless support. Without their encouragement, this oversea education journey would never come true. Their trust always motivates me when I have a tough time in my Ph. D. work. I will always remember their sacrifices. Words cannot express how grateful I am to my parents.

I feel great appreciation to Professor Changjun Zou from Southwest Petroleum University in China, who led me when I was an undergraduate student. I am also grateful for help and support provided by the other senior members of that University. Many thanks to Dr. Suman Sinha-Ray and Dr. Sumit Sinha-Ray for helping me at the initial phase of my Ph. D career. Thanks to Dr.

ACKNOWLEDGEMENTS (Continued)

Rakesh Prasad Sahu and Dr. Soumyadip Sett, who always be my older brothers and help me with the experimental issues. I am grateful to Dr. Minwook Lee and Dr. Seongpil An, whose precious help means a lot to me. My appreciations to Dr. Christopher Staszal and Dr. Patrick Comiskey, who always give me support and help with the experiments and simulations no matter when I needed them. Many thanks to my friends Abhilash Sankaran, Dr. Alex Kolbasov, and Dr. Arkaprov Ghosal: I would never enjoy the lab life and finish my work without your support and help. Special appreciations to my friends Gen Li, Kailin Chen, Xiaoyu Wang, and my roommate Yanjing Li.

I wish to express my sincere thanks to Professor Eyal Zussman from The Technion-Israel Institute of Technology and Professor Behnam Pourdeyhimi from the Nonwovens Institute. Professor Zussman helped me with my adsorption experiments and Professor Pourdeyhimi strongly supported me with my nonwovens research.

W. Z

Some of this thesis have been published in peer-reviewed journals. Subsection 2.1.1, section 3.1, and chapter 4 were published in International Journal of Heat and Mass Transfer of Elsevier [Zhang, W., Vilensky, R., Zussman, E., & Yarin, A. L. (2018). Adsorption and mass transfer in granular porous membranes/media due to inserted volatile materials. International Journal of Heat and Mass Transfer, 116, 248-258]. Subsection 2.1.2, section 3.2, and chapter 5 were published in International Journal of Heat and Mass Transfer of Elsevier [Zhang, W., Zussman, E., & Yarin, A. L. (2018). Detection of vapor released from sublimating materials encased in porous medium. International Journal of Heat and Mass Transfer, 118, 1357-1372]. Subsection 2.2.1, section 3.3, and chapter 7 were published in Polymer of Elsevier [Zhang, W., Staszal, C., Yarin, A. L., Shim, E., & Pourdeyhimi, B. (2018). Point-bonded polymer nonwovens and their rupture in stretching. Polymer, 146, 209-221]. Subsection 2.2.2, section 3.4, and chapter 8 were published in Polymer Testing of Elsevier [Zhang, W., Yarin, A. L., & Pourdeyhimi, B. (2019). Cohesion energy of thermally-bonded polyethylene terephthalate nonwovens: Experiments and theory. Polymer Testing, 78, 105984]. Permission letters given by the publisher are in Appendix D.

CONTRIBUTION OF AUTHORS

Dr. Yarin supervised all the experiments and theoretical work and contributed to writing the manuscripts. The adsorption work in subsection 2.1.1, section 3.1, and chapter 4 represents a published manuscript [Zhang et al. (2018)] for which I am the primary author. I designed and conducted experiments with one of the setups. Dr. Vilensky contributed to the design and conducted experiments with the other two setups. The work on the vapor detection at the free surface of porous media in the subsection 2.1.2, section 3.2, and chapter 5 represents a published manuscript [Zhang et al. (2018)] for which I am the primary author: I conducted all the experiments and analyzed the experimental results. The work on the heat transfer in point-bonded polymer nonwovens and their rupture in stretching in subsection 2.2.1, section 3.3, and chapter 7 represents a published manuscript [Zhang et al. (2018)] for which I am the primary author, conducted all experiments and analyzed experimental results. Dr. Staszal contributed to analyzing the results and writing the manuscript. The work in subsection 2.2.2, section 3.4, and chapter 8 represents a published manuscript for which I am the primary author and conducted all the experiments [Zhang et al. (2019)]. Chapter 6 is an unpublished work related to sensing of gas release from underground. Chapter 9 is an unpublished work related to the thermal bonding patterns effect on the mechanical properties of nonwovens conducted for the Nonwovens Institute. Chapter 10 is an unpublished work related to the method of characterization of the Clapeyron effect in polymers during heating-up under pressure conducted for the Nonwovens Institute. Chapter 11 is an unpublished work related to explosive-like ejections from plant stems in fire and the estimate of vapor mass ejection at distillation stage of a forest fire. Chapter 12 is an unpublished work related to the velocity of flame propagation of canopy fire in a model system. In chapters 9-12 I conducted all the experiments and analyzed the results.

TABLE OF CONTENTS

<u>CHAPTER</u>	<u>PAGE</u>
1. INTRODUCTION.....	1
1.1 Porous media	1
1.2 Heat and mass transfer in porous media.....	2
1.3 Thesis objectives.....	4
2. BACKGROUND AND LITERATURE SURVEY	5
2.1 Mass transfer in sands	5
2.1.1 Vapor adsorption/ desorption process in porous media	5
2.1.2 Vapor detection at the free surface of a porous medium	8
2.2 Heat transfer in nonwovens	9
2.2.1 Mechanical properties of the nonwovens	9
2.2.2 Cohesion/ adhesion of nonwovens	13
2.2.3 Thermal bonding effects on nonwovens.....	14
2.2.4 The Clapeyron effect	15
2.3 Heat and mass transfer during bio-mass burning in forest fires.....	16
3. RESEARCH OUTLINE.....	20
3.1 Adsorption and mass transfer in granular porous media	20
3.2 Detection of vapor released from sublimating materials encased in porous media	21
3.3 Rupture mechanism of nonwoven being stretched.....	22
3.4 Cohesion energy of thermally-bonded nonwovens	23
3.5 Thermal bonding patterns effect on mechanical properties of nonwovens	23
3.6 Characterization of the Clapeyron effect.....	24
3.7 Explosive- like ejections formed from plant stem in fire	24
3.8 Flame propagation of canopy fire in a model system.....	25
4. ADSORPTION AND MASS TRANSFER IN GRANULAR POROUS MEMBRANES/MEDIA DUE TO INSERTED VOLATILE MATERIALS	26
4.1 Introduction	26
4.2 Experimental: Materials and methods	26

TABLE OF CONTENTS (Continued)

<u>CHAPTER</u>	<u>PAGE</u>
4.2.1 Materials	26
4.2.2 Experimental setups.....	27
4.2.3 Methods	30
4.3 Theoretical background	31
4.4 Results	37
4.4.1 Experimental setup I.....	37
4.4.2 Experimental setups II and III	40
4.4.3 Experimental setup III: Morphological observations	44
4.5 Conclusions	47
5. DETECTION OF VAPOR RELEASED FROM SUBLIMATING MATERIALS ENCASED IN POROUS MEDIA.....	49
5.1. Introduction	49
5.2 Experiments with original sand	49
5.2.1 Materials and experimental setup.....	49
5.2.2 Experiments results	51
5.2.3 Quantification of the amount of collected crystals.....	54
5.2.4 Correlation of the image intensity with the deposited vapor mass.....	58
5.3 Experiments with kaolinite.....	59
5.4 Theoretical	63
5.5 Comparison of the theory with experimental data	67
5.6 Experiments with sand with coated grains	73
5.7 Conclusions	80
6. SENSING UNDERGROUND GAS RELEASE	82
6.1 Introduction	82
6.2 Theoretical	82
6.3 Experimental.....	84
6.3.1 Materials	84
6.3.2. Experimental setup	85
6.3.3 Data processing and saturated pressure of naphthalene vapor	86
6.3.4 Experimental results	87

TABLE OF CONTENTS (Continued)

<u>CHAPTER</u>	<u>PAGE</u>
6.4 Discussion: Comparison of the theoretical predictions with the experimental data	88
6.5 Conclusions	91
7. HEAT-TRANSFER IN POINT-BONDED POLYMER NONWOVENS AND THEIR RUPTURE IN STRETCHING	92
7.1 Introduction	92
7.2 Experimental.....	92
7.2.1 Materials	92
7.2.2 Thermal bonding.....	93
7.2.3 Tensile tests of bonded nonwovens	95
7.2.4 Imaging.....	96
7.3 Results and discussion.....	97
7.3.1 Results of the tensile tests of the as-received nonwovens as well as the bonded nonwovens	97
7.3.2 Results of the tensile tests of the thermally bonded nonwovens	100
7.3.3 Rupture patterns.....	107
7.3.4 Theoretical prediction of the stress concentration and rupture location.....	109
7.4 Conclusions	114
8. HEAT-TRANSFER AND COHESION ENERGY OF THERMALLY-BONDED NONWOVENS: EXPERIMENTS AND THEORY	115
8.1 Introduction	115
8.2 Experimental.....	115
8.2.1 Tensile tests of the as-received and thermally-bonded PET nonwovens.....	115
8.2.2 Blister tests of thermally-bonded PET nonwovens	122
8.3 Theoretical	132
8.3.1 Calendar bonding in the nip	132
8.3.2 Forces acting on nonwoven beyond calendar nip.....	135
8.3.3 Sintering area in thermal bonding	138
8.3.4 The effect of cooling on sintering area in thermal bonding.....	143
8.3.5 Cohesion energy due to thermal bonding	144
8.4 Conclusions	146

TABLE OF CONTENTS (Continued)

<u>CHAPTER</u>	<u>PAGE</u>
9. THERMAL BONDING PATTERNS EFFECT ON MECHANICAL PROPERTIES OF NONWOVENS.....	148
9.1 Introduction	148
9.2 Experimental: Tensile test	148
9.2.1 Materials and thermal bonding setup	148
9.2.2 The rupture patterns of the as-received and thermally-bonded PP nonwovens.....	151
9.2.3 Results of the tensile tests of the as-received and thermally-bonded PP nonwovens.....	152
9.3 Experimental: The effects of the thermal bond area.....	156
9.4 Theoretical: The numbers of fiber-fiber intersections sintered under a single thermal bond.....	166
9.5 Conclusions	169
10. METHOD OF CHARACTERIZATION OF THE CLAPEYRON EFFECT IN POLYMERS DURING HEATING-UP UNDER PRESSURE.....	171
10.1 Introduction	171
10.2 Experimental.....	171
10.3 Experimental results and discussions	174
10.3.1 Melting of PBT, PET and PP nonwovens under the upper cylinder weight without additional applied weight	174
10.3.2 Melting of PBT nonwovens under different applied weights (pressures)	177
10.3.3 Melting of PET nonwovens under different applied weights (pressures)	181
10.3.4 Melting of PP nonwovens under different applied weights (pressures) vs. PBT and PET nonwovens.....	184
10.4 Conclusion.....	188
11. EXPLOSIVE-LIKE EJECTIONS FORMED FROM PLANT STEM IN FIRE AND THE ESTIMATE OF VAPOR MASS EJECTION AT DISTILLATION STAGE OF FOREST FIRE	189
11.1 Introduction	189
11.2 Materials and experimental setup	189
11.3 Experiments conducted with stems	191
11.3.1 Experiments conducted with freshly-cut stems	191

TABLE OF CONTENTS (Continued)

<u>CHAPTER</u>	<u>PAGE</u>
11.3.2 Experiments conducted with ethanol-immersed stems.....	195
11.4 Model experiments conducted with needles filled up with liquids	198
11.4.1 Model experiments conducted with the 25G needles filled up with D.I. water	198
11.4.2 Model experiments conducted with the 18G needles filled up with D.I. water	203
11.4.3 Model experiments conducted with needles filled up with pure ethanol	206
11.5 Theoretical of explosive-like ejections from plant stems in fire and discussion	211
11.5.1 Theoretical	211
11.5.2 Discussion.....	215
11.6 Conclusions	216
12. VELOCITY OF FLAME PROPAGATION OF CANOPY FIRE IN A MODEL SYSTEM	217
12.1 Introduction	217
12.2 Experimental.....	217
12.2.1 Experimental materials and setup.....	217
12.2.2 The fire propagation in upslope/downslope direction with cotton dipped in ethanol as flame source with no wind effect.	218
12.2.3 The fire propagation in upslope / downslope direction with pure cotton as flame source with no wind effect.	224
12.2.4 The fire propagation in upslope / downslope direction with pure cotton as flame source with wind effect.	228
12.3 Conclusions	232
13. CONCLUSIONS	233
14. CITED LITERATURE.....	238
15. APPENDICES.....	250
Appendix A: Characterization of sand particles	250
Appendix B. Permeability measurements	254
Appendix C: The origin of the rupture pattern surrounding bonds	259

TABLE OF CONTENTS (Continued)

<u>CHAPTER</u>	<u>PAGE</u>
Appendix D: Publisher permissions	267
16. CURRICULUM VITAE.....	272

LIST OF TABLES

<u>TABLE</u>	<u>PAGE</u>
Table 4.1 The adsorption/desorption kinetics constants and the equilibrium constant for the three volatile substances studied. The saturated pressure P_{sat} was used to find the values of C_w	40
Table 7. 1 Average mechanical properties of as-received PBT and PBT/PE 80/20 nonwovens.	99
Table 7. 2 Average mechanical properties of bonded PBT and PBT/PE 80/20 nonwovens.	103
Table 8. 1 Mechanical properties of the as-received and thermally-bonded PET nonwovens. Measurements were repeated at least 10 times in each case and used to obtain these results.	119
Table 9. 1 The numbers of the ratios of the cumulative area of the original bonds overlaid by the additional single circular thermal bond to the area of the latter in a specific ratio range.	162
Table 9. 2 The numbers of the ratios of the cumulative area of the original bonds overlaid by the additional single rhombic thermal bond to the area of the latter in a specific ratio range.	164
Table B1. Three values of the hydraulic head, the measured filtrate volumes and the corresponding values of sand permeability.....	258

LIST OF FIGURES

<u>FIGURES</u>	<u>PAGE</u>
Figure 4.1 Chemical structure of the adsorbates: (a) Camphor, (b) Naphthalene, and (c) 2,4-Dinitrotoluene (DNT).	27
Figure 4.2 Schematics of the experimental setups. (a) Setup I is a closed system which consists of 2 compartments separated by a membrane. A thin layer of sand is placed on top of the membrane, with a sublimating substance located at the bottom of the lower compartment. The adsorbed vapor in sand can be measured taking samples and analyzing them using UV–VIS spectrophotometer or 1H-NMR. (b) In setup II the sublimating substance is located at the bottom of a sand column. A membrane is located ~3 mm below the sand/air interface. Sand located above the membrane is open to atmosphere. Samples can be taken from this upper sand layer and the amount of the adsorbed vapor on sand can be measured at different time moments using UV–VIS spectrophotometer or 1H-NMR. (c) In setup III, the volatile substance is located at the bottom of a sand column, which is opened to the atmosphere. A glass is mounted vertically, at the center of the column. Vapor deposit morphologies on the slide were optically observed at heights A, B and C, after the slide had been withdrawn from sand column. Also, samples of sand were taken for analysis and rinsed, while the removed deposit weighed for comparison with the data from setup II.	29
Figure 4.3 HR-SEM image of a sand particle. The inset shows the surface at a larger magnification.	32
Figure 4.4 Adsorbed amount of naphthalene, camphor and 2,4-DNT vs. time, at ~24 °C. The inset shows the adsorption of naphthalene and camphor during the first 20 h.	38
Figure 4.5 Normalized experimental adsorption data for the three substances: naphthalene, camphor and 2,4-DNT (shown by symbols) reduced to a single master curve according to Eq. (4.22).	39
Figure 4.6 Absorbed mass of naphthalene at 24 °C versus time for two pore diameters, $d=0.001$ and 0.0002 cm. Black symbols correspond to the experimental data, red and blue symbols – to the numerical simulations.	41
Figure 4.7 Absorbed mass of naphthalene at 24 °C versus time at $d= 0.0002$ cm and two values of porosity, $\phi=0.3$ and 0.8 . Black symbols correspond to the experimental data, pink and blue symbols – to the numerical simulations.	42

LIST OF FIGURES (Continued)

<u>FIGURES</u>	<u>PAGE</u>
Figure 4.8 Absorbed mass of naphthalene at 50 °C measured experimentally using setups II and III (the results are shown by symbols the corresponding colors listed in the panel).....	43
Figure 4.9 Morphology of camphor deposits on a vertical glass slide. Optical images (at magnifications $\times 50$ and $\times 20$) were taken after the slide had been withdrawn from the sand column, at three positions A=20 mm, B=10 mm and C=3 mm measured from the lower end of the glass slide (cf. Figure 2). (a) Position A ($\times 20$), (b) Position A ($\times 50$), (c) Position B ($\times 20$), (d) Position B ($\times 50$), (e) Position C ($\times 20$), and (f) Position C ($\times 50$).....	45
Figure 4.10 Morphology of naphthalene deposits on a vertical glass slide. Optical images (at magnifications $\times 50$ and $\times 20$) were taken after the slide had been withdrawn from the sand column, at two positions, A=15 mm, and B=5 mm, measured from the lower end of the glass slide (cf. Figure 2). (a) Position A ($\times 20$), (b) Position A ($\times 50$), (c) Position B ($\times 20$), and (d) Position B ($\times 50$).....	46
Figure 4.11 Morphology of camphor deposits adsorbed on glass slides. (a) The $\times 10$ magnification, and (b) The $\times 20$ magnification.	46
Figure 4.12 Morphology of naphthalene deposits adsorbed on glass slides. (a) The $\times 10$ magnification, and (b) The $\times 20$ magnification.	47
Figure 5.1 Morphology of naphthalene crystal deposits on transparent film at the free surface in the case of a 1.9 cm naphthalene ball buried in the middle under h=3 cm of the original sand: (a) at t=0, (b) at t=2 h, (c) at t=4 h, (d) at t=6 h, (e) at t=8 h, (f) at t=10 h. The time is reckoned from the delay time $t_{\text{delay}}=12$ h.	52
Figure 5.2 Measurement of the deposit surface area using the green outlines. The case of a 1.9 cm naphthalene ball buried in the middle under h=3 cm of the original sand: (a) at t=0, (b) at t=2 h, (c) at t=4 h, (d) at t=6 h, (e) at t=8 h, (f) at t=10 h. The time is reckoned from the delay time $t_{\text{delay}}=12$ h.	53
Figure 5.3 The measured deposit area for naphthalene crystal deposition. The case of the original sand, and a 1.9 cm naphthalene ball buried in the middle. (a) The area versus time, with time being reckoned from the delay times. (b) The area versus sand layer thickness. The experimental data is shown by symbols and spanned by lines.	54

LIST OF FIGURES (Continued)

<u>FIGURES</u>	<u>PAGE</u>
Figure 5.4 Measurement process of pixel values. a) The image corresponds to Figure 5.2b. b) Histogram of pixel intensity versus number of pixels at position 1. c) Histogram of pixel intensity versus number of pixels at position 2.	55
Figure 5.5 Total pixel intensity per unit area covered with naphthalene crystals. A 1.9 cm naphthalene ball was buried in the middle. The experiments with the original sand. (a) Total pixel intensity per unit area versus time, with time being reckoned from the delay times. (b) Total pixel intensity per unit area versus sand layer thicknesses. The experimental data is shown by symbols and spanned by lines.	56
Figure 5.6 Comparison of the albedo method and the image intensity method. Squares indicate locations A and B used in the measurements.	57
Figure 5.7 Deposited vapor mass versus the total intensity. The red line is the linear fit.	59
Figure 5.8 SEM images of plate-like structure of kaolinite.	60
Figure 5.9 Morphology of naphthalene crystal deposits on transparent film at the free surface in the case of a 1.9 cm naphthalene ball buried in the middle under $h=3.0$ cm of kaolinite: (a) at $t=1$ h, (b) at $t=2$ h, (c) at $t=3$ h, (d) at $t=4$ h, (e) at $t=5$ h, (f) at $t=6$ h. The time is reckoned from the delay time $t_{\text{delay}}=19$ h.	61
Figure 5.10 The measured area of the naphthalene crystal deposition. The case of the kaolinite porous medium, and a 1.9 cm naphthalene ball buried in the middle of the tank bottom. (a) The area versus time, with time being reckoned from the delay times. (b) The area versus the kaolinite layer thickness. The experimental data is shown by symbols and spanned by lines.	62
Figure 5.11 Total pixel intensity per unit area covered with naphthalene crystals. A 1.9 cm naphthalene ball was buried in the middle of the tank bottom. The experiments with the kaolinite layers. (a) Total pixel intensity per unit area versus time, with time being reckoned from the delay times. (b) Total pixel intensity per unit area versus the kaolinite layer thickness. The experimental data is shown by symbols and spanned by lines.	63

LIST OF FIGURES (Continued)

<u>FIGURES</u>	<u>PAGE</u>
<p>Figure 5.12 Naphthalene vapor mass per unit area versus the original sand layer thickness at different time moments after the adsorption/desorption process has been saturated, and vapor transport is fully determined by diffusion. (a) Theoretical results at different time moments listed in the panel. The deposited mass distribution versus the sand layer thickness. In the following five panels the theoretical results are shown separately by lines, while the corresponding experimental data - by symbols. (b) $t= 2$ h. (c) $t= 4$ h. (d) $t= 6$ h. (e) $t= 8$ h. (f) $t= 10$ h.</p>	<p>68</p>
<p>Figure 5.13 Naphthalene vapor mass per unit area versus time after the adsorption/desorption process has been saturated, and vapor transport is fully determined by diffusion at different thicknesses of the original sand layers. (a) Theoretical results at different sand layer thicknesses listed in the panel. In the following four panels the theoretical results are shown separately by lines, while the corresponding experimental data - by symbols. (b) Sand layer thickness of 3.0 cm. (c) Sand layer thickness of 4.5 cm. (d) Sand layer thickness of 5.5 cm. (e) Sand layer thickness of 7.0 cm.</p>	<p>70</p>
<p>Figure 5.14 Naphthalene vapor mass per unit area versus the kaolinite layer thickness at different time moments after the adsorption/desorption process has been saturated, and vapor transport is fully determined by diffusion. (a) Theoretical results at different time moments listed in the panel. The distribution of the deposited mass per unit area versus kaolinite layer thickness. In the following six panels the theoretical results are shown separately by lines, while the corresponding experimental data - by symbols. (b) $t= 1$ h. (c) $t= 2$ h. (d) $t= 3$ h. (e) $t= 4$ h. (f) $t= 5$ h. (g) $t= 6$ h.</p>	<p>71</p>
<p>Figure 5.15 Naphthalene vapor mass per unit area versus time after the adsorption/desorption process has been saturated, and vapor transport is fully determined by diffusion at different thicknesses of the kaolinite layers. (a) Theoretical results at different kaolinite layer thicknesses listed in the panel. In the following four panels the theoretical results are shown separately by lines, while the corresponding experimental data - by symbols. (b) Kaolinite layer thickness of 3.0 cm. (c) Kaolinite layer thickness of 4.5 cm. (d) Kaolinite layer thickness of 5.5 cm. (e) Kaolinite layer thickness of 7.0 cm.</p>	<p>72</p>
<p>Figure 5.16 Transparent film formed after evaporating 0.1 g droplet of 5 wt% PAN solution in DMF.</p>	<p>74</p>

LIST OF FIGURES (Continued)

<u>FIGURES</u>	<u>PAGE</u>
Figure 5.17 (a) and (b) SEM images of sand grains after they were dipped into 5 wt% PAN solution and dried. The grains are covered by a thin PAN layer and are smoother than the original sand grains in panels (c) and (d).	75
Figure 5.18 Morphology of naphthalene crystal deposits on transparent film at the free surface in the case of a 1.9 cm naphthalene ball buried in the middle of the tank bottom under $h=3.0$ cm of the PAN-coated sand: (a) at $t=0$, (b) at $t=2$ h, (c) at $t=4$ h, (d) at $t=6$ h, (e) at $t=8$ h, (f) at $t=10$ h. The time is reckoned from the delay time $t_{\text{delay}}=1.5$ h.	77
Figure 5.19 The measured deposit area of the naphthalene crystals deposition. The case of the PAN-coated sand, and the naphthalene ball buried in the middle of the tank bottom. (a) The area versus time, with time being reckoned from the delay times. (b) The area versus the thickness of the PAN-coated sand layers. The experimental data is shown by symbols and spanned by lines.	77
Figure 5. 20 Total pixel intensity per unit area covered with naphthalene crystals. The naphthalene ball was buried in the middle of the tank bottom. The experiments with the PAN-coated sand. (a) Total pixel intensity per unit area versus time, with time being reckoned from the delay times. (b) Total pixel intensity per unit area versus sand layer thickness. The experimental data is shown by symbols and spanned by lines.	78
Figure 5. 21 Total pixel intensity per unit area covered with naphthalene crystals. A 1.9 cm naphthalene ball was buried in the middle of the tank bottom. The experiments with the original sand, the hydrophobic sand and the PAN-coated sand. The experimental data is shown by symbols and spanned by lines.	80
Figure 6. 1 Naphthalene concentration in the sensor space at different sand height ratio versus time. (a) The height ratio of 0.238. (b) The height ratio of 0.368. (c) The height ratio of 0.529. (d) The height ratio of 0.833.	88
Figure 6. 2 Naphthalene vapor concentration versus time at different sand height ratios: the comparison between the theory and the experimental data. (a) Theoretical results at four different sand layer height ratios listed in the panel. In the following four panels the theoretical results are shown separately by lines while the corresponding experimental data - by symbols. (b) The height ratio of 0.238. (c) The height ratio of 0.368. (d) The height ratio of 0.529. (e) The height ratio of 0.833.	90

LIST OF FIGURES (Continued)

<u>FIGURES</u>	<u>PAGE</u>
<p>Figure 7. 1 (a) Thermal bonding setup for the additional bond patterning with the aluminum case attached and used for point bonding. (b) Schematic of the aluminum case with an interchangeable thermal punch inserted. (c) Schematic of two types of thermal punches, rhombic and circular. (d) The temperature controller (Watlow EZ-ZONE). (e) Example of PBT nonwoven sample with a single circular bond pattern as well as a single rhombic bond pattern formed by the setup of panel (a).....</p>	94
<p>Figure 7. 2 An example of the stress-strain curve of the as-received PBT nonwovens measured in tensile tests. The data is shown by the black curve, the phenomenological Green equation (7.1) fit- by the red curve.....</p>	97
<p>Figure 7. 3 (a) An example stress-strain curve of the as-received PBT/ PE 80/20 nonwovens measured in tensile tests. The data is shown by the black curve, the phenomenological Green equation (7.1) fit- by the red curve. (b) A zoomed-in view of the elastic section followed by the perfectly plastic section.</p>	98
<p>Figure 7. 4 Mechanical properties in tension of the as-received PBT and PBT/PE 80/20 nonwovens. (a) Average values of Young’s modulus E. (b) Average values of the yield stress Y. (c) Average values of the maximum stress ($\sigma_{xx, \max}$). (d) Average values of the toughness (T).</p>	99
<p>Figure 7. 5 Examples of the stress-strain curves of the nonwoven samples bonded with an additional single circular bond. (a) The PBT nonwoven bonded by a circular bond at 190 °C. (b1) The PBT/ PE 80/20 nonwoven bonded by a circular bond at 120 °C and (b2) a zoomed-in view of the elastic region. (c1) The PBT/ PE 80/20 nonwoven bonded by a circular bond at 110 °C and (c2) a zoomed-in view of the elastic region. The data is shown by the black curves, the Green equation fit- by the red curves.</p>	101
<p>Figure 7. 6 Examples of the stress-strain curves of the nonwoven samples bonded with an additional single rhombic bond. (a) The PBT nonwoven bonded by a rhombic bond at 190 °C. (b1) The PBT-PE nonwoven bonded by a rhombic bond at 120 °C and (b2) a zoomed-in view of the elastic region. (c1) The PBT/ PE 80/20 nonwoven bonded by a rhombic bond at 110 °C and (c2) a zoomed-in view of the elastic region. The data is shown by the black curves, the Green equation fit- by the red curves.</p>	102

LIST OF FIGURES (Continued)

<u>FIGURES</u>	<u>PAGE</u>
<p>Figure 7. 7 Mechanical properties of the as-received PBT nonwovens, PBT nonwovens with an additional single circular bond imposed at 190 °C, and PBT nonwovens with an additional single rhombic bond imposed at 190 °C. (a) Average values of Young`s modulus. (b) Average values of the yield stress. (c) Average values of the maximum stress at failure. (d) Average values of toughness.</p>	<p>104</p>
<p>Figure 7. 8 Mechanical properties of the as-received PBT/PE 80/20 nonwovens in comparison with those bonded at 110 °C and 120 °C with a single circular or rhombic bond. (a) Average values of Young`s modulus. (b) Average values of the yield stress. c) Average values of the maximum stress. (d) Average values of toughness.</p>	<p>105</p>
<p>Figure 7. 9 Examples of the effect of stretching in tensile tests on rupture patterns. (a) The as-received PBT nonwoven before and after tensile test, (b) the PBT nonwoven with a circular bond before and after tensile test, and (c) the PBT nonwoven with a rhombic bond before and after tensile test. The red and blue dashed lines encompass the bond pattern implemented on the circular bonded as well as rhombic bonded samples.</p>	<p>107</p>
<p>Figure 7. 10 Examples of the effect of tensile test on rupture patterns. (a) The as-received PBT/PE 80/20 nonwoven before and after tensile test, (b) the PBT/PE 80/20 nonwoven with a 110 °C circular bond before and after tensile test, (c) the PBT/PE 80/20 nonwoven with a 120 °C circular bond before and after tensile test, (d) the PBT/PE 80/20 nonwoven with a 110 °C rhombic bond before and after tensile test, and (e) the PBT/PE 80/20 nonwoven with a 120 °C rhombic bond before and after tensile test. The red and blue dashed lines encompass the bond pattern implemented on the circular bonded as well as rhombic bonded samples. Black dots and horizontal lines on the samples were drawn to facilitate the experiments and do not represent holes.</p>	<p>108</p>
<p>Figure 7. 11 The field of displacement v.</p>	<p>110</p>
<p>Figure 7. 12 The field of displacement u.</p>	<p>110</p>
<p>Figure 7. 13 Displacement v in material 1 along the stretching axis.</p>	<p>111</p>
<p>Figure 7. 14 The stress field σ_{xx}.</p>	<p>112</p>
<p>Figure 7. 15 The stress field σ_{xy}.</p>	<p>112</p>

LIST OF FIGURES (Continued)

<u>FIGURES</u>	<u>PAGE</u>
Figure 7. 16 The stress field σ_{yy}	113
Figure 8. 1 Schematic of the thermal bonding setup.....	117
Figure 8. 2 (a) A single layer of the as- received nonwovens. (b) Schematic of the rectangular thermal punch.....	117
Figure 8. 3 Examples of the stress-strain curves of the as-received and thermally-bonded nonwoven samples. (a) The as- received PET nonwovens. (b) The PET nonwovens thermally-bonded at 160 °C. (c) The PET nonwovens thermally- bonded at 170 °C. (d) The PET nonwovens thermally- bonded at 180 °C. (e) The PET nonwovens thermally-bonded at 190 °C. (f) The PET nonwovens bonded at 200 °C.	121
Figure 8. 4 Thermal bonding process used for PET nonwovens. Mat B was placed on the top of mat A, which had a 3.1 mm through hole at the center. Then, both mats were thermally bonded together by the rectangular thermal punch. The red dashed lines encompass the bonding area. The non-bonded part (outside the red dashed line) was trimmed after the thermal bonding process.	123
Figure 8. 5 SEM images of the as-received and thermally-bonded PET nonwovens. (a) and (b) The as-received PET nonwovens. (c) and (d) PET nonwovens thermally bonded at 160 °C. (e) and (f) PET nonwovens thermally bonded at 170 °C.....	124
Figure 8. 6 SEM images of PET nonwovens thermally bonded at different temperatures. (a) and (b) PET nonwovens thermally bonded at 180 °C. (c) and (d) PET nonwovens thermally bonded at 190 °C. (e) and (f) PET nonwovens thermally bonded at 200 °C.....	125
Figure 8. 7 The schematic of the prepared sample for the upcoming blister test. Thermally-bonded PET nonwoven mats were fixed by double-sided tape on the stainless-steel substrate. The steel substrates, the double-sided tape and mat A had concentric 3.1 mm holes at the center.....	126
Figure 8. 8 Schematic of the blister test. The maximum force (P) before the failure of the nonwoven sample and the maximum blister diameter (2a) were measured.	127

LIST OF FIGURES (Continued)

<u>FIGURES</u>	<u>PAGE</u>
Figure 8. 9 Blister profiles of PET nonwovens obtained at the maximum force before the failure. The nonwovens were thermally-bonded at different temperatures. The blister tests were conducted at the rate of 2 mm/min. (a) Bonding temperature of 160 °C. (b) Bonding temperature of 170 °C. (c) Bonding temperature of 180 °C. (d) Bonding temperature of 190 °C. (e) Bonding temperature of 200 °C.	128
Figure 8. 10 (a) The load-extension curve. The thermal bonding temperature is 200 °C. (b) The maximum blister diameter versus bonding temperature. The blister tests conducted at 2 mm/ min.	129
Figure 8. 11 Blister profiles of PET nonwovens obtained at the maximum force before the failure. The nonwovens were thermally-bonded at different temperatures. The blister tests were conducted at the rate of 10 mm/min. (a) Bonding temperature of 160 °C. (b) Bonding temperature of 170 °C. (c) Bonding temperature of 180 °C. (d) Bonding temperature of 190 °C. (e) Bonding temperature of 200 °C.	130
Figure 8. 12 (a) The load-extension curve. The thermal bonding temperature is 200 °C. (b) The maximum blister diameter versus bonding temperature. The blister tests conducted at 10 mm/ min.	131
Figure 8. 13 Cohesion energy of thermally-bonded PET nonwovens versus the bonding temperature. (a) Blister test conducted at the shaft rate of 2 mm/ min. (b) Blister test conducted at the shaft rate of 10 mm/ min.	132
Figure 8. 14 Nonwoven passing through the calendar nip between two rollers.	135
Figure 8. 15 Schematic of a nonwoven beyond the calendar nip. The angle $\Delta\alpha$ in this figure can be arbitrary (depending on the equipment used), and not necessarily 90°	136
Figure 8. 16 Schematic of sintering (thermal bonding) under the action of compressive force acting on nonwoven.	139
Figure 8. 17 Sintering of two fibers.	140
Figure 9. 1 Optical images of the PP fibers in the as-received nonwovens. (a) The $\times 4$ magnification. (b) The $\times 10$ magnification.	149

LIST OF FIGURES (Continued)

<u>FIGURES</u>	<u>PAGE</u>
<p>Figure 9. 2 The schematics of the as-received nonwoven and the nonwoven specimens with three types of thermal bonding patterns. Green dashed lines and red dashed lines indicated the positions of the pneumatic grips and the centerline of the PP nonwoven specimens, respectively. The shaded circles or rectangle show the shapes and the locations of thermal bonds.</p>	150
<p>Figure 9. 3 The failure patterns of the as-received and thermally-bonded PP nonwovens. (a) The as-received PP nonwovens. (b) The PP nonwovens with type B thermal bond. (c) The PP nonwovens with type C thermal bond. (d) The PP nonwovens with type D thermal bond. Green dashed lines indicate the positions of the Instron grips. Black dashed lines encompass the thermal bonds.</p>	152
<p>Figure 9. 4 Stress-strain curves of the as-received and thermally-bonded nonwovens measured in tensile tests. The experimental data is shown by black lines and fitted by the phenomenological Green`s equation, as shown by red lines. (a) The as-received PP nonwoven. (b) The PP nonwoven with type B thermal bond. (c) The PP nonwoven with type C thermal bond. (d) The PP nonwoven with type D thermal bond.</p>	153
<p>Figure 9. 5 Mechanical properties of the as-received PP nonwovens and those with type B and type C thermal bonds. (a) Average values of Young`s moduli. (b) Average values of the yield stress. (c) Average values of the maximum stress at failure. (d) Average values of the toughness.</p>	155
<p>Figure 9. 6 Mechanical properties of the as-received PP nonwovens and those with type B and type D thermal bonds. (a) Average values of Young`s moduli. (b) Average values of the yield stress. (c) Average values of the maximum stress at failure. (d) Average values of the toughness.</p>	156
<p>Figure 9. 7 Specimens of as-received light-weight RHT bonding pattern nonwoven, and of those with single circular bond pattern, as well as single rhombic bond. (a) The as-received light- weight RHT bonding pattern nonwoven specimen. (b) The light-weight nonwoven with single circular thermal bond. (c) The light-weight nonwoven with single rhombic thermal bond. The periphery of the circular or rhombic thermal bond was highlighted by black lines.</p>	157

LIST OF FIGURES (Continued)

<u>FIGURES</u>	<u>PAGE</u>
<p>Figure 9. 8 Mechanical properties of the as-received light-weight SMS RHT pattern nonwovens in comparison with those bonded at 150 °C with a single circular or rhombic bond. (a) Average values of Young`s modulus. (b) Average values of the yield stress. (c) Average values of the maximum stress. (d) Average values of toughness.</p>	158
<p>Figure 9. 9 (a) A specimen of the light-weight RHT pattern SMS nonwoven with blackened original bonds. (b) The corresponding processed specimen image. The specimen size is 15 mm × 90 mm.</p>	160
<p>Figure 9. 10 Measurement procedure used to find the area ratio in the case of an additional circular thermal bond. (a) – (e) Various possible bonding positons within the black and white zone. The blue circles in panels (a) to (e) encompass the additional circular bond and the overlaid original bonds are shown in red.</p>	161
<p>Figure 9. 11 The probability density function of the area ratios of the cumulative original bonds overlaid by the additional single circular thermal bond to the area of the latter.</p>	163
<p>Figure 9. 12 Measurement of the area ratio in the case of an additional rhombic thermal bond configuration and the corresponding probability density function of the area ratio. (a) The beginning measuring position. (b) The ending measuring position. (c) The probability density function of the area ratio. The blue lines in panels (a) and (b) encompass the additional rhombic bond and the overlaid original bonds are shown in red.</p>	165
<p>Figure 10. 1 As-received single layers of PBT, PET and PP nonwovens. (a) PBT; (b) PET; (c) PP.</p>	173
<p>Figure 10. 2 Schematic of the experimental setup. (a) The entire setup. The red dashed oval in this panel encompasses the domain zoomed-in in panel (b). (b) The magnified view of the gap between the upper and lower cylinder, where the nonwoven samples were located.</p>	173
<p>Figure 10. 3 Melting process of a PBT nonwoven sample without an applied weight at different time moments: (a) t = 0, the inter-cylinder gap is 0.56 mm. (b) t = 25 s, the inter-cylinder gap is 0.39 mm, (c) t = 50 s, the inter-cylinder gap is 0.28 mm, (d) t = 75 s, the inter-cylinder gap is 0.21 mm, (e) t = 95 s, the inter-cylinder gap is 0.18 mm.</p>	175

LIST OF FIGURES (Continued)

<u>FIGURES</u>	<u>PAGE</u>
Figure 10. 4 Melting process of PET nonwoven sample without an applied weight at different time moments: (a) $t=0$, the inter-cylinder gap is 0.48 mm; (b) $t = 5$ s, the inter-cylinder gap is 0.38 mm; (c) $t = 10$ s, the inter-cylinder gap is 0.31 mm; (d) $t = 15$ s, the inter-cylinder gap is 0.28 mm; (e) $t = 20$ s, the inter-cylinder gap is 0.25 mm.	176
Figure 10. 5 Melting process of a PP nonwoven sample without an applied weight at different time moments; (a) $t=0$, the inter-cylinder gap is 0.38 mm. (b) $t = 5$ s, the inter-cylinder gap is 0.28 mm. (c) $t = 10$ s, the inter-cylinder gap is 0.24 mm. (d) $t = 15$ s, the inter-cylinder gap is 0.22 mm. (e) $t = 20$ s, the inter-cylinder gap is 0.21 mm.....	177
Figure 10. 6 Dependence of melting temperature on the applied pressure for the PBT nonwovens.	179
Figure 10. 7 Change in the sample height for the PBT nonwovens due to melting. Panels (a1) and (a2) show the 9 mm ² sample with no applied weight at the beginning and ending moments of melting. Panels (b1) and (b2) show the 9 mm ² sample with 1071.50 g of the applied weight, namely, under the pressure of 11.65 atm, at the beginning and ending moments of melting. Panels (c1) and (c2) show the 4 mm ² sample with 1071.50 g of the applied weight, namely, under the pressure of 26.22 atm, at the beginning and ending moments of melting. Panels (d1) and (d2) show the 1 mm ² sample with 1071.50 g of the applied weight, namely, under the pressure of 104.86 atm, at the beginning and ending moments of melting. Panels (e1) and (e2) show the 1 mm ² sample with 2859.50 of the applied weight, namely, under the pressure of 277.79 atm, at the beginning and ending moments.	180
Figure 10. 8 Melting temperature dependence on pressure for the PET nonwovens.	182
Figure 10. 9 Change in the sample height for the PET nonwovens due to melting. Panels (a1) and (a2) show the 9 mm ² sample with no applied weight at the beginning and ending moments of melting. Panels (b1) and (b2) show the 9 mm ² sample with 1071.50 g of the applied weight, namely, under the pressure of 11.65 atm, at the beginning and ending moments of melting. Panels (c1) and (c2) show the 4 mm ² sample with 1071.50 g of the applied weight, namely, under the pressure of 26.22 atm, at the beginning and ending moments of melting. Panels (d1) and (d2) show the 1 mm ² sample with 1071.50 g of the applied weight, namely, under the pressure of 104.86 atm, at the beginning and ending moments of melting.	183

LIST OF FIGURES (Continued)

<u>FIGURES</u>	<u>PAGE</u>
Figure 10. 10 Melting temperature dependence on pressure for the PP nonwovens.	185
Figure 10. 11 Comparison of the melting temperature dependence on pressure for the PBT, PET and PP nonwovens.	185
Figure 10. 12 Change in the sample height of the PP nonwovens due to melting. Panels (a1) and (a2) show the 4 mm ² sample with only upper cylinder weight (the 0.31 atm pressure), at the beginning and ending moments of melting process, respectively. Panels (b1) and (b2) show the 9 mm ² sample with 1071.50 g applied weight (the 11.65 atm pressure), at the beginning and ending moments of melting process, respectively. Panels (c1) and (c2) show the 4 mm ² sample with 1071.50 g applied weight (the 26.22 atm pressure), at the beginning and ending moments of melting process. Panels (d1) and (d2) show the 1 mm ² sample with 1071.50 g applied weight (the 104.86 atm pressure), at the beginning and ending moments of melting process.....	187
Figure 11. 1 Experimental materials. (a) The entire <i>Epipremnum aureum</i> plant. (b) A fresh-cut stem from the plant. (c) Both ends of a fresh-cut stem became brown after 20 h immersion in ethanol.....	190
Figure 11. 2 Cross-sectional morphology of an <i>Epipremnum aureum</i> stem with liquid-filled channels visible. (a) ×4 magnification. (b) ×20 magnification.	190
Figure 11. 3 Experimental setup.	191
Figure 11. 4 Burning of a freshly-cut plant stem, recorded by high-speed camera. (a) t=0.7 s. (b) t=1.7 s. (c) t=2.7 s. (d) t= 3.7 s. (e) t= 4.7 s. (f) t= 5.7 s. (g) t= 6.7 s. (h) t=7.7 s. (i) t=8.7 s. (j) t= 9.7 s. (k) t= 10.7 s. (l) t= 11.7 s. (m) t= 12.7 s. (n) t=13.7 s. (o) t=14.7 s. The green arrows point at the jet blown from the stem.	193
Figure 11. 5 Burning of the freshly-cut plant stem, recorded by the IR camera. (a) t=0.7 s. (b) t=1.7 s. (c) t=2.7 s. (d) t= 3.7 s. (e) t= 4.7 s. (f) t= 5.7 s. (g) t= 6.7 s. (h) t=7.7 s. (i) t=8.7 s. (j) t= 9.7 s. (k) t= 10.7 s. (l) t= 11.7 s. (m) t= 12.7 s. (n) t=13.7 s. (o) t=14.7 s.	194
Figure 11. 6 Burning of the ethanol-immersed stem recorded by high-speed camera. (a) t=0.5 s. (b) t=1.5 s. (c) t=2.5 s. (d) t= 3.5 s. (e) t= 4.5 s. (f) t= 5.5 s. (g) t= 6.5 s. (h) t=7.5 s. (i) t=8.5 s. (j) t= 9.5 s. (k) t= 10.5 s.(l) t= 11.5 s. (m) t= 12.5s. (n) t=13.5 s. (o) t=14.5 s. The green arrows point at the torch developing from the stem.	196

LIST OF FIGURES (Continued)

<u>FIGURES</u>	<u>PAGE</u>
Figure 11. 7 Burning condition of an ethanol-immersed stem recorded by the IR camera. (a) $t=0.5$ s. (b) $t=1.5$ s. (c) $t=2.5$ s. (d) $t= 3.5$ s. (e) $t= 4.5$ s. (f) $t= 5.5$ s. (g) $t= 6.5$ s. (h) $t=7.5$ s. (i) $t=8.5$ s. (j) $t= 9.5$ s. (k) $t= 10.5$ s. (l) $t= 11.5$ s. (m) $t= 12.5$ s. (n) $t=13.5$ s. (o) $t=14.5$ s. The red arrows point at the torch developing from the stem.	197
Figure 11. 8 A 25G stainless steel dispensing needle with luer lock connection, purchased from McMaster- Carr.	198
Figure 11. 9 Water droplet shaped as a spherical segment protruding from the edge of the 25G needle engulfed in flame. (a) $t= 0.0603$ s. (b) $t=0.0606$ s. (c) $t=0.0609$ s. (d) $t= 0.0612$ s. (e) $t= 0.0615$ s. (f) $t= 0.0618$ s. The red arrows point at the protruding droplet.	199
Figure 11. 10 The evolution of a liquid water jet issued from the 25G needle horizontally with the speed of about 10 m/s. (a) $t= 1.3470$ s. (b) $t=1.3473$ s. (c) $t=1.3476$ s. (d) $t= 1.3479$ s. The red arrows in each image indicate the head of the water jet.	200
Figure 11. 11 The ejected water vapor issued from the 25G needle entraining the surrounding flame. (a) $t= 1.3630$ s. (b) $t=1.3633$ s. (c) $t=1.3636$ s. (d) $t= 1.3639$ s.	201
Figure 11. 12 The 2.50 s period of spreading of the reddish section of the 25G stainless steel needle. (a) $t= 0.89$ s. (b) $t=1.39$ s. (c) $t=1.89$ s. (d) $t= 2.39$ s. (e) $t= 2.89$ s. (f) $t= 3.39$ s.	202
Figure 11. 13 A 18G stainless steel dispensing needle with luer lock connection, purchased from McMaster- Carr.	203
Figure 11. 14 Two initial water droplets issued from the 18G needle. (a) $t=0.530$ s. (b) $t=0.560$ s. (c) $t=0.573$ s. (d) $t= 0.577$ s.	204
Figure 11. 15 The water jet issued from the 18G needle with the velocity of ~ 5 m/s. (a) $t=0.6227$ s. (b) $t=0.6234$ s. (c) $t=0.6240$ s. (d) $t=0.6247$ s. (f) $t= 0.6234$ s. The red arrows point at the head of the ejected water jet.	205
Figure 11. 16 Intermittent water vapor and droplets issued from the 18G needle. (a) $t=0.08167$ s. (b) $t=0.8207$ s. (c) $t=0.8247$ s. (d) $t=0.8287$ s. The red arrows point at the intermittent jet.	206

LIST OF FIGURES (Continued)

<u>FIGURES</u>	<u>PAGE</u>
Figure 11. 17 The burning ethanol jets issued from the 25G needle initially filled up with pure ethanol. (a) $t=0.250$ s. (b) $t=0.473$ s. (c) $t=0.476$ s. (d) $t=0.479$ s. (e) $t=0.482$ s. (f) $t=0.485$ s. (g) $t=0.488$ s. (h) $t=0.491$ s. (i) $t=0.494$ s.	207
Figure 11. 18 A single burning ethanol droplet ejected from the 18G needle. The droplet was ignited by the flame surrounding the needle and kept diminishing. (a) $t=0.7213$ s. (b) $t=0.7246$ s. (c) $t=0.7249$ s. (d) $t=0.7252$ s. (e) $t=0.7255$ s. (f) $t=0.7258$ s. The red arrows point at the ejected ethanol droplet.	209
Figure 11. 19 Liquid ethanol jet, and the flame propagating backward over it. (a) $t=0.7433$ s. (b) $t=0.7473$ s. (c) $t=0.7513$ s. (d) $t=0.7553$ s. (e) $t=0.7593$ s. (f) $t=0.7633$ s. The red arrows point at the jet.	210
Figure 11. 20 The flame formed by the burning ethanol vapor issued from the 18G needle. (a) $t=0.8246$ s. (b) $t=0.8286$ s. (c) $t=0.8326$ s. (d) $t=0.8376$ s.	211
Figure 11. 21 The left- and right-hand sides of Eq. (11.6) are shown by the red and green lines, respectively. Their intersection determines the solution of Eq. (11.6), i.e. the value of the temperature T inside the channel.	214
Figure 12. 1 The flame propagation setup. (a) Photograph. (b) Schematic.	218
Figure 12. 2 The progress of flame propagating in cotton dipped in ethanol serving as flame source, recorded by DSLR camera. The flame was not affected by wind. The spatial step of this trial was 9 mm and the inclination angle was 0° . (a) $t=0$ s. (b) $t=0.066$ s. (c) $t=0.132$ s. (d) $t=0.198$ s. (e) $t=0.264$ s. (f) $t=0.330$ s. (g) $t=0.396$ s. (h) $t=0.462$ s. (i) $t=0.528$ s. (j) $t=0.594$ s. (k) $t=0.660$ s. (l) $t=0.726$ s. (m) $t=0.792$ s. (n) $t=0.858$ s.	220
Figure 12. 3 The progress of fire transported in cotton dipped in ethanol serving as flame source, recorded by IR camera. The flame was not affected by wind. The spatial step was 9 mm and the inclination angle was 0° . (a) $t=0$ s. (b) $t=0.066$ s. (c) $t=0.132$ s. (d) $t=0.198$ s. (e) $t=0.264$ s. (f) $t=0.330$ s. (g) $t=0.396$ s. (h) $t=0.462$ s. (i) $t=0.528$ s. (j) $t=0.594$ s. (k) $t=0.660$ s. (l) $t=0.726$ s.	221
Figure 12. 4 Total propagation time versus propagation distance in the trial of 9 mm spatial step with 0° of inclination. Cotton dipped in ethanol served as flame source. The red line indicated the fitting curve with the fitting equation $L = 148.76t - 2.86$	222

LIST OF FIGURES (Continued)

<u>FIGURES</u>	<u>PAGE</u>
<p>Figure 12. 5 The measured overall velocity with various spatial step and inclination angles. The cotton dipped in ethanol was used as flame source. The fire transported in upslope direction. a) The overall velocity versus the inclination angles. b) The overall velocity versus the spatial step.....</p>	223
<p>Figure 12. 6 The measured overall velocity with various spatial step and inclination angles. The cotton dipped in ethanol was used as flame source. The fire transported in downslope direction. a) The overall velocity versus the inclination angles. b) The overall velocity versus the spatial step.....</p>	224
<p>Figure 12. 7 The progress of flame propagating in pure cotton as flame source, recorded by DSLR camera. The flame was not effected wind. The spatial step of this trial was 11 mm and the inclination angle was 40.0°. (a) t=0 s. (b) t=5 s. (c) t=25 s. (d) t= 35 s. (e) t= 45 s. (f) t= 55 s.</p>	226
<p>Figure 12. 8 The progress of flame propagating in pure cotton as flame source, recorded by IR camera. The flame was not effected wind. The spatial step of this trial was 11 mm and the inclination angle was 40.0° (a) t=0 s. (b) t=5 s. (c) t=25 s. (d) t= 35 s. (e) t= 45 s. (f) t= 55 s.....</p>	226
<p>Figure 12. 9 The measured overall velocity with various spatial step and inclination angles. The pure cotton was used as flame source. The fire transported in upslope direction. a) The overall velocity versus the inclination angles. b) The overall velocity versus the spatial step.....</p>	227
<p>Figure 12. 10 The measured overall velocity with various spatial step and inclination angles. The pure cotton was used as flame source. The fire transported in downslope direction. a) The overall velocity versus the inclination angles. b) The overall velocity versus the spatial step.....</p>	228
<p>Figure 12. 11 The progress of flame propagating in pure cotton as flame source, recorded by DSLR camera. The flame was affected by 2.0 m/s horizontal blowing wind. The spatial step of this trial was 9 mm and the inclination angle was 0°. (a) t=0 s. (b) t=2 s. (c) t=4 s. (d) t= 6 s. (e) t= 8 s. (f) t= 10 s. (g) t=12 s. (h) t=14 s.</p>	229

LIST OF FIGURES (Continued)

<u>FIGURES</u>	<u>PAGE</u>
Figure 12. 12 The progress of flame propagating in pure cotton as flame source, recorded by IR camera. The flame was affected by 2.0 m/s horizontal blowing wind. The spatial step of this trial was 9 mm and the inclination angle was 0°. (a) t=0 s. (b) t=2 s. (c) t=4 s. (d) t= 6 s. (e) t= 8 s. (f) t= 10 s. (g) t=12 s. (h) t=14 s.	230
Figure 12. 13 The measured overall velocity with various spatial step, inclination angles and 2m/s wind. The pure cotton was used as flame source. The fire transported in upslope direction. a) The overall velocity versus the inclination angles. b) The overall velocity versus the spatial step.....	232
Figure A1. Sand particles observed with ×4 magnification.	250
Figure A2. The image processed of a sand particle processed by Image-Pro Plus 6.0 software. (a) The original image. (b) The corresponding processed image.....	251
Figure A3. Sand-size distribution.....	252
Figure A4. Measurement of sphericity. (a) The original images of two sand particles. (b) The corresponding processed images of these particles, with the green circles being the smallest circles circumscribing them.	253
Figure A5. Sphericity distribution of 100 sand particles.....	253
Figure B1. Experiment setup used for permeability measurements. (a) Measurement of the glass-fiber filter permeability. (b) Measurement of sand layer permeability.....	255
Figure C1. (a) Sketch of the Kirsch problem. (b) The polar coordinates and the complex z-plane.	259
Figure C2. Split of the problem on stretching of elastic material (1) with a circular elastic inclusion (2) into a linear superposition of three problems (I), (II) and (III).	263

LIST OF ABBREVIATIONS

BET method	Brunauer-Emmett-Teller method
2,4-DNT	2,4-Dinitrotoluene
SEM	Scanning electron microscope
PAN	Polyacrylonitrile
DMF	N, N-dimethylformamide
PBT	Polybutylene Terephthalate
PE	Polyethylene
GSM	Gram per square meter
PET	Polyethylene Terephthalate
PP	Polypropylene
SMS	Spunbond- Meltblown- Spunbond

SUMMARY

The goal of this work is to investigate peculiarities of heat and mass transfer processes in porous media relevant in several applications. Namely, various porous substances, either natural or man-made, were explored experimentally, and a number of novel phenomena and properties were studied under different scenarios, each one in a separate chapter. The corresponding numerical/theoretical models were also developed.

The first stage of the work is comprised of three chapters has mass transfer through a granular porous medium with a buried sublimating source in focus. This research is relevant in forensic applications. The volatile material inevitably sublimates, its vapor diffuses through the porous media and is adsorbed/desorbed on the granular surfaces. The description of the mechanisms of mass transfer would inevitably involve kinetics constants. The question arises, how to obtain these kinetics constants for multiple forensic situations associated with different volatile substances? The molecules from the inserted sublimating sources are not only adsorbed by the porous materials but also diffuse through the porous body and thus, can be detected at the free surface. The diffusion process poses the question of how to detect those diffused molecules and recognize different sources embedded in porous media. It is also important to evaluate the required sensor sensitivity. The questions raised are studied both experimentally and theoretically in this part of the thesis.

For the exploration of the adsorption/desorption processes, the present work contributes to the detection methods based on the removal of minuscule amounts of the adsorbed material delivered by diffusing vapor from a sublimating volatile source. The theory which employs the kinetics constants is proposed and demonstrated to be a useful tool for the description of multiple forensic situations associated with different volatile substances. The detection of the vapor

SUMMARY (Continued)

sublimation from a buried source was conducted at several porous layer thicknesses above the buried source. Here I developed a method based on the measurement the deposited sublimated and diffused vapor at the surface of porous media to determine the source size, location and vapor sublimation distribution. The theory predicting mass deposition on a detector located at the free surface is also proposed and can be used as a predictive tool for any other vapor diffusing from underground objects to evaluate the required sensor sensitivity for any buried material, sensor size, the observation time, and for any other type of soil.

The second part of the thesis is comprised of four chapters which have heat transfer through porous media in nonwovens manufacturing in focus. Different types of nonwovens were used as target materials. The bonding parameters that effect the mechanical properties of nonwovens are of interest here. Tensile testing and blister testing were employed in this part of the thesis to measure the mechanical properties and cohesion energies arising due to the thermal bonding process. The theory is proposed and used to predict the corresponding stress distribution in stretched bonded nonwoven specimens. Also, I determined the characteristics of calendar bonding process to estimate the resulting cohesion energies and the number of fiber-fiber intersections under a single thermal bond. These results can help to determine optimal bonding patterns. The Clapeyron effect, i.e., the dependence of polymer melting temperature on the applied load is also relevant in this context. A method, which can visualize the melting moment of nonwovens under different applied loads was proposed and used to determine the corresponding melting temperature, and its dependence on the load.

The third part of the thesis is comprised of two chapters. The first of these chapters describes the discovery of a novel phenomenon: volatiles and water ejection from pores during biomass

SUMMARY (Continued)

burning in forest fires. The experiments were conducted using freshly-cut stems collected from *Epipremnum aureum* (Golden Pothos). A theory of these the explosive-like ejections from plant stems in the fire was developed. The theory proposed here can be used for the estimation of the fuel supply rate at the distillation stage of forest fire. Velocity of flame propagation in forest fires and its dependence on the slope and wind velocity are also of utmost importance. In model experiments I measured the velocity of flame propagation of canopy fire. The experimental results obtained in this part of the work are also useful for the evaluation of the flame zones.

CHAPTER 1

INTRODUCTION

1.1 Porous media

Porous materials are abundant. Water filtration through soil and being enhanced oil recovery are typical of natural and technical phenomena characteristic of porous media, which contain multiple inter-connected pores in their bulk. Soils, rocks, plants, biological tissues and woods, all can be characterized as natural porous media, while the substances like cement and nonwovens are examples of man-made porous materials.

Porous structure of natural porous media is usually complicated and random because the solid matrix has irregular dimensions and shapes, whereas the man-made materials can possess non-random made on demand porous structures. Such properties as porosity, permeability, and the internal surface area are often used to characterize porous media. Several methods have been demonstrated as highly effective for quantification of these properties. Scanning electron microscopy (SEM) and helium porosimetry are the common ways to determine the porosity, the Brunauer–Emmett–Teller (BET) method can be used to measure the internal surface area of porous media, and permeability of porous materials relevant for the oil industry is often measured with the dry air.

In many relevant cases pores in porous media are filled partially or fully with liquid, gas or both of them. The inter-connected pores allow a single-phase or multi-phase fluid flow through the porous medial either in the filtration, or diffusion modes, or both of them. The transport phenomena in porous media attracted significant attention due to abundance of porous media and

their importance in nature and engineering. Essentially, the researches on heat and mass transfer in porous media date back to the 18-th century.

1.2 Heat and mass transfer in porous media

The significant developments of theoretical studies related to porous media in the 18th century are associated with Euler, who introduced the concept of volume fraction and the theory of ideal fluids. The first systematic descriptions of the porous media started with applying of these important theories and concepts during that era [De Boer (2000)].

The subject of mass transport in porous media experienced significant advances in the 19th century. For example, Fick`s law was inspired by hydro-diffusion through membranes and described in 1855 as a phenomenological theory, which governs the diffusive mass transport. In addition, in 1856, Darcy`s law was established experimentally and described the proportionality of total discharge of water through porous media to the applied pressure drop.

The studies of mass transport in porous media encompass additional subjects. One important topic is related to the adsorption/ desorption processes in porous materials. For example, when gas or liquid flow through such porous media, as soil or activated carbon, their molecules inevitably have direct contacts with the porous structure and are partially absorbed by it. Desorption happens in parallel with adsorption and competes with it. Single or multiple layers of the adsorbate are formed on the pore surfaces acting as the adsorbent. The adsorption/desorption properties of porous materials have been widely employed in many areas, such as filtration or pollution purification. Although the adsorption/desorption processes in porous media were already explored in many preceding works, a further understanding and in-depth studies are still required in relation to novel applications.

The general studies of the heat transfer through porous media have already date back to the 18th century, and dealt with the overall thermal conductivity and thermal dispersion. Most of these theories considered non-deformable porous media [Nield and Bejan (2017)]. On the other hand heat transfer in deformable porous materials are in demand in relation to the modern technology, especially in the nonwoven fabric industries. The nonwoven products currently are widely used for protective clothing, medical and surgical applications, building and roofing, etc. The performance enhancement of nonwoven fabrics under different conditions is tremendously important. The thermal bonding method has been demonstrated to be an effective way to improve the mechanical properties of nonwovens. Its idea is to heat a web of fibers to the melting or softening temperature under significant pressure at bonding sites and cool it down in the bonded state. This method was first introduced in 1942. The properties of the products resulting from the thermal bonding process highly rely on the thermal energy supplying method. The thermal bonding parameters, such as bonding temperature [Bhat et al. (2003)], can significantly affect the mechanical properties of some specific polymer nonwovens. Although these effects were demonstrated on the fully empirical grounds, a deeper understanding of the heat transfer mechanisms through flexible porous materials is still needed for the further optimization of such processes.

Another important phenomenon in porous substance involves simultaneous heat and mass transport in biomass burning in forest fires, which determines and affects flame propagation. Plants being natural porous materials contain tiny pores in stems, leaves, roots, etc., which facilitate gas exchange or moisture absorption. When such vegetation materials are on fire, water and volatiles can be ejected through the porous structure due to the high surrounding temperature and supply fuel which sustains the surrounding flame and water vapor that can ballast and quench it.

Understanding of these phenomena is currently incomplete and a further research is in high demand.

1.3 Thesis objectives

The present work aims at the further understanding of peculiarities of heat and mass transfer in porous media by the experimental and theoretical approaches. Chapters 4, 5 and 6 are devoted to the mass transfer processes in non-deformable porous materials. In these three chapters, the adsorption/desorption processes during the diffusion mass transport and the detection methods of the released vapor are studied for such porous materials as sand and clay. Highly sublimating materials, such as camphor and naphthalene, are buried in these porous media and used as a model sublimating vapor source. In relation to the experiments, theoretical/numerical models are also developed in these three chapters. Chapters 7- 10 have the heat transfer process in porous deformable nonwovens in focus, which is relevant for the enhancement of mechanical properties using thermal bonding. Tensile testing and blister testing are applied to measure the mechanical properties and the cohesion energy, respectively, of different thermally-bonded nonwovens. Several models related to the descriptions of nonwoven properties and the industrial calender thermal bonding process are developed. Heat and mass transfer mechanisms in vegetation in forest fire are explored experimentally and theoretically in chapters 11 and 12. Chapter 11 explores volatiles and water vapor ejection from pores during biomass burning in forest fires, and chapter 12 studies the velocity of flame propagation of the canopy fire in a model system. Conclusions are drawn in chapter 13.

CHAPTER 2

BACKGROUND AND LITERATURE SURVEY

2.1 Mass transfer in sands

Vapor and gas transfer in porous media is an important subject which is relevant in such applications as petroleum and natural gas exploration, mining, water vapor transport through soil layers, leakage, and smoke detection, etc. Forensic applications require a clear understanding of the presence of a volatile material (which might be drugs or explosives) inserted under a layer of granular porous material or buried elsewhere. Any volatile material inevitably sublimates, its vapor diffuses through the porous media and is adsorbed/desorbed on the granular surfaces.

2.1.1 Vapor adsorption/ desorption process in porous media

(This section has been partially published in Zhang, W., Vilensky, R., Zussman, E., Yarin, A. L. (2018). Adsorption and mass transfer in granular porous membranes/media due to inserted volatile materials. *International Journal of Heat and Mass Transfer*, 116, 248-258)

The presence of the adsorption, in principle, can be detected by the presence of a deposited layer of the volatile material on the granular matrix or the other surfaces [Griffy (1992); Brunauer et al. (1938)]. The detection methods can be based on the removal of the adsorbed layer from granules or the other surfaces, in particular by raising the surrounding temperature, which changes the adsorption/desorption equilibrium, and using the released vapor for sensing purposes. Rinsing and weighing of the adsorbed material are also possible. Such plan of action requires a clear understanding of the amount of the adsorbed volatile material in equilibrium, as well as of the

amount of the desorbed (released) vapor when the temperature has been raised.

The classical theory of heat and mass transfer and the adsorption/desorption processes, as well as chromatography and spectroscopy, provide useful tools to these aims [Brunauer et al. (1938); Zambra et al. (2011); Ma and Chen (2014); Bouddour et al. (1998); Dobre et al. (2016); Ding et al. (2004); Dantas et al. (2003); Zhang et al. (2015); Zhu et al. (2011); Sajjadi and Azaiez (2015); Zhang et al. (2014); Brunauer (1944); Lennard-Jones (1932); Ignatowicz (2011); Langmuir (1918); Jones (1951); Jones (1952); Gregg and Sing (1982); Gehrke et al. (2011)]. The adsorption processes are generally subdivided into chemisorption and physisorption [Brunauer (1944); Lennard-Jones (1932);]. Chemisorption implies surface chemical reactions between the adsorbent and adsorbate, i.e. a strong covalent interaction between them. On the other hand, in the case of physisorption, no chemical reactions between the adsorbent and adsorbate take place, which means that the electronic structure of molecules stays practically unchanged [Oura et al. (2003)]. The adsorption equilibria are typically described using the adsorption isotherms, such as the monolayer Langmuir isotherm, the multilayer Brunauer-Emmett-Teller (BET) isotherm, the Freundlich isotherm, etc. In brief, the Freundlich adsorption isotherm [Freundlich (1906)] dating back to 1906 is an empirical model, which involves two fitting parameters describing the isothermal adsorption equilibria of the adsorbed gas at different pressures. The Langmuir isotherm implies monolayer adsorption and theoretically treats the equilibrium adsorption on a homogeneous adsorbent surface [Langmuir (1916)] with the adsorbed molecules considered to be immobile [Masel (1996)]. Brunauer, Emmett, and Teller generalized the Langmuir-type equilibrium adsorption for the multilayer adsorption cases [Brunauer et al. (1938)]. Multiple subsequent works were devoted to further verification and modification of the adsorption isotherms to improve their capability to fit the experimental data. The Freundlich isotherm

revealed the best performance in describing the experimental results related to the adsorption of uranium trioxide U(VI) on polypyrrole for wastewater remediation [Abdi et al. (2017)]. The Freundlich isotherm was also used to explain the process of metal ions adsorption in soil [Mishra et al. (2017)]. Also, it was shown that the semi-empirical Thomas and Yoon- Nelson models can be used to describe the arsenate As(V) adsorption process on iron-zirconium binary oxide-coated sand from water [Chaudhry et al. (2017)]. Temporary evolution of adsorption has been fitted by the empirical pseudo-first-order and pseudo-second-order models in the study of benzene adsorption on clay and sandy soil [Temkin and Pyzhay (1940); Lagergren (1898); Ho and McKay (1999); Osagie and Owabor (2015)].

Several semi-empirical models were proposed for specific adsorption processed in porous media, for example, the kinetic model of Zhu et al. (2017), which fitted well the experimental data for CO₂ adsorption on a modified layered double hydroxide at high pressure and elevated temperature [[Zhu et al. (2017)]. Similarly, the adsorption of benzaldehyde and benzyl alcohol from supercritical CO₂ on the polymeric resin was described in the framework of the kinetic model developed in Yang et al. (2017). A novel diffusion adsorption nonlinear model based on the Hill model and the kinetic Boltzmann equation was developed in Bouzid et al. (2017). It was used to describe the adsorption of ethanol molecules on three types of activated carbon. The parameters of this model can be also accurately fitted to the data on the adsorption in refrigeration systems. The semi-empirical model of Wang et al. (2003) was fitted to the data on metal ion removal by several adsorbents. The present group recently proposed a physical model of mass transfer in porous medium accompanied by a Langmuir-like adsorption kinetics, which was successfully applied to the heavy metal ion adsorption from polluted water on nano-textured biopolymer-containing membranes [Kolbasov et al. (2017)].

2.1.2 Vapor detection at the free surface of a porous medium

(This section has been partially published in Zhang, W., Zussman, E., Yarin, A. L. (2018). Detection of vapor released from sublimating materials encased in porous medium. *International Journal of Heat and Mass Transfer*, 118, 1357-1372.)

Vapor or gas diffusing through the encasing porous media and being partially adsorbed in the pores, can also partially achieve the free surface and be, in principle, detected there. It should be emphasized that a detectable vapor or gas release to the free surface could be delayed due to the adsorption in the pores at the beginning of the process. Such detection methods as polymer-coated acoustic wave sensors [Grate et al. (1999)], chromatography [Swinnerton et al. (1962)], hyperspectral imaging [Theiler and Wohlberg (2013)], etc. were demonstrated to be effective for unknown vapor detection and determination. Besides that, detection and concentration of known vapor accompanied by mass quantification are also important. The methods for detection of specific known vapor are quite mature now. Many kinds of vapor sensors and methods have been developed, such as polymer sensors [Toal and Trogler (2006)], resonating micro-cantilevers [Thundat et al. (1995)], and methods employing carbon nanotubes [Snow et al. (2006); Li et al. (2003)]. However, these sensors still have limitations when the spatial distribution of released vapor is in question. Sensors can relatively easily detect and measure vapor concentration if the vapor is pumped through the sensor [Zhu et al. (2000)]. Still, to determine the vapor distribution by this method would be imprecise because it is impractical to collect and pump the vapor just from a specific location. Using the existing sensors, it is also difficult to determine the source size, and/or the depth and the horizontal location of a buried source. Thus, a predictive tool for any other vapor diffusing from underground objects to evaluate the required sensor sensitivity for any sensor

size, and the observation time, buried source location and for any type of porous media is required to be developed.

Some types of vapor sublimating from the original materials are relatively concentrated and easily adsorbed, which makes them ideal model materials. For example, naphthalene vapor, a typical polycyclic aromatic hydrocarbon with a unique smell, was used as a model material in several experimental works [Liscinsky et al. (2013); Rhead and Pemberton (1996); Cheng et al. (2004); Zhang et al. (2018)]. Solid naphthalene yields a relatively high vapor concentration since it sublimates at a relatively high rate. Its deposits in the form of white crystals can be detected to quantify the amount of vapor released from a porous medium. The albedo measurement or estimation was demonstrated to be an effective method to explore the surface texture, surface temperature variations, surface energy, etc. Such measurements either demand precise instruments, such as pyranometers [Payne (1972)] and scanning radiometers [King et al. (1986)], or just a photograph [Corripio (2004)]. Using the photography-based method is a convenient way to estimate the albedo value. However, it demands an albedo value of a known object as a reference point, i.e. it is impossible to establish the actual brightness values. Accordingly, it leads to imprecisions and errors when this method is used for vapor quantification. Since the albedo value is positive and proportional to the corresponding pixel intensity value [Troccoli and Allen (2006)], the intensity value can be obtained directly from a photograph. Thus, measuring the photograph pixel intensity values for vapor quantification purposes would be a more precise method.

2.2 Heat transfer in nonwovens

2.2.1 Mechanical properties of the nonwovens

(This section has been partially published in Zhang, W., Vilensky, R., Zussman, E., Yarin, A. L.

(2018). Adsorption and mass transfer in granular porous membranes/media due to inserted volatile materials. *International Journal of Heat and Mass Transfer*, 116, 248-258.)

The inter-fiber bonding area and/or bonding patterns in nonwovens fully determine such properties as the machine direction (MD) and cross-direction (CD) tensile stiffness (Young's modulus), elasticity, softness, compressibility, absorptivity, etc. These properties are determined by such factors as melting temperature and the degree of crystallinity and solidification when nonwovens are formed by meltblowing. When nonwovens are formed by solution blowing, the degree of solvent evaporation and fiber dryness and the degree of crystallinity dictate the final strength. In both cases of melt- and solution blowing of nonwovens, further strength is achievable by means of point-bonding, namely the thermal compression of bond area patterns across the nonwovens. Such bonding is driven by sintering and adhesion of the polymer fibers at the bond region, significantly increasing the physical strength of the nonwoven web.

Adhesion is the physical process of joining separate surfaces of materials (or fibers in a nonwoven [Michielsen et al. (2006)]) together through mechanical, chemical, or thermodynamic bonding. In the present case of thermal point-bonding of nonwovens, the polymers typically do not react and the adhesion and strength at such a bond point is driven by the diffusion and entanglement of polymer chains through the surfaces in contact [Michielsen et al. (2006); Brown (1994); Clarke (1996); Geoghegan et al. (1999); Jenkins et al. (2004)]. This diffusion process is due to the thermodynamically-driven reptation of polymer chains, resulting in their entanglement and formation of the adhesive strength at the interface [Brown (1994); Jenkins et al. (2004); Baldan (2012); Islam et al. (2010)]. In several important experiments such as [Clarke (1996); Baldan (2012)], it was observed that the diffusion of polymer chains is a two-step process. Initially, polymer chains quickly diffuse across the surfaces in contact, interlocking and leaving what are

referred to as “runners”, or un-entangled sections of the polymers, at the surface [Clarke (1996); Geoghegan et al. (1999)]. At this initial stage, most of the adhesive energy is gained and afterwards the system slowly relaxes toward an equilibrium with all ‘runners’ completely diffusing across the interface [Clarke (1996); Geoghegan et al. (1999)]. A notable theoretical work on the dynamics of the diffusion stages has been conducted in the literature. [O'Connor and McLeish (1994); O'Connor and McLeish (1993)].

Such understanding of the polymer diffusion and entanglement is already used industrially in the creation of point-bonded nonwoven webs [Michielsen et al. (2006)]. Accordingly, experiments with bonds of various contacting areas were conducted and discussed in the literature [Bhat et al. (2004)]. It is understood that processing times and point-bonding times should be chosen to allow melting of the crystalline regions in the nonwoven as well as a sufficient time for reptation and entanglement of interfused polymer chains across the fibers. The effect of thermal bonding on the microscopic level is akin to annealing at high temperature, past the glass transition temperature, and is used to enhance mechanical performance at the bond site. Various works have demonstrated such a phenomenon associated with thermal bonding of nonwovens as an increase in the crystal sizes [Bhat et al. (2004)]. In addition, the explanation of the crystallization behavior of PE and PBT, as well as the crystallized polymer structure and the degree of crystallinity is available in Refs. [Dangseeyun et al. (2004); Keller et al. (1954); Stein and Misra (1980); Lin et al. (2007); Hughes et al. (1989); Aggarwal and Tilley (1955)]. The changes in the degree of crystallinity of several other polymers caused by thermal bonding are available in the work of Hegde et al. (2008).

Furthermore, it is understood that pressure due to the point- bonding can increase the melting point of polymers due to the Clapeyron effect [Michielsen et al. (2006), Wang and

Michielsen (2002)]. Thermal degradation at the bond point has also been researched, leading to the conclusion that high bonding temperatures or long bonding times will result in deterioration of Young's modulus at the bond points [Fedorova et al. (2007); Wang and Michielsen (2001); Dasdemir et al. (2012)]. A further decrease in Young's modulus in a point-bonded nonwoven web can be also explained by the issues related to poor polymer compatibility. Adhesion between polymers is related to their miscibility, or often immiscibility of polymers brought in contact. The adhesion between dissimilar polymers is typically weak [Brown (1994); Islam et al. (2010)]. To address these limitations, bi-component fibers have been employed with the main aim of enhancing the mechanical strength of fibrous composite materials [Fedorova et al. (2007); Dasdemir et al. (2012)].

In the existing works, such processing conditions as temperature, bond pressure, and polymer micro-mechanics (reptations) and various other aspects of the point-bonding process have been addressed. However, the failure patterns at the bond periphery and their reasons remain mostly unexplored. In a point-bonded nonwoven, high-stiffness (point-bonded) domains are imposed in an elastic material of lower stiffness (the nonwoven web) as a means of increasing the overall mechanical properties. In this situation, it is of significant interest to understand whether such a stiff inclusion can act as a stress concentrator in the nonwoven web and lead to a premature failure due to over-bonding. An insight in these phenomena is of significant importance.

Elastic problems related to stretching of material with an inclusion (understood in the present work as a thermal bond) stem from the seminal work of Kirsch [Kirsch (1898)], who solved the planar problem on uniaxial stretching of an elastic material with a circular hole. The important developments motivated by the mechanics of composite materials can be found in Eshelby (1957); Eshelby (1959), which are the works that dealt with elastic inclusions. A more recent interest to

the problem is related to materials with nano-inclusions, where the stress field in an isotropic plane under uniaxial stretching with a circular inclusion was calculated in Deryugin and Lasko (2012). The approach of the latter work does not imply the complex elastic potentials, which significantly simplify calculations.

2.2.2 Cohesion/ adhesion of nonwovens

(This section has been partially published in Zhang, W., Yarin, A. L., Pourdeyhimi, B. (2019). Cohesion energy of thermally-bonded polyethylene terephthalate nonwovens: Experiments and theory. *Polymer Testing*, 78, 105984.)

When a modification is needed to improve the mechanical stability, wettability, or adhesion, the values of the surface energy, i.e., the adhesion or cohesion energy, should be characterized. Wang et al. (2009) gave a valuable guidance for the design and manufacturing of graphene films used in forensic applications based on their surface energy. Egitto and Matienzo (1990) related the improvement of wetting and adhesion of PTFE with the enhanced surface energy. Other sources in the literature revealed the importance of the evaluation of surface energy for the materials development.

The adhesion or cohesion energy of a thin film to a substrate can be measured by the wrinkled film method, film scratching, blister test, etc. In the blister test a film is detached from a substrate using the external force provided by a shaft pushing the film normally through a hole in the substrate. Several works on the blister test or its modifications are available. For example, Staszal et al. (2017) studied the adhesion energies of two polymer films after thermal bonding and polymer adhesion and sintering in compound nonwovens by employing blister test [Staszal et al.

(2018)]. Liechti and Shirani (1994) suggested blister tests of specimens with higher aspect ratio. The works that employed blister tests revealed the reliability of this method, as well as repeatability of its results, which is due to the fact that the blister test eliminates the edge effect.

The shape of a blister formed in the blister test, as well as the value of the force required to create such a blister can be used to calculate the adhesion or cohesion energy in the case of soft materials, which resist to blister formation predominantly by the elastic force resulting from stretching rather than from the bending stiffness. The corresponding theory was developed in the work of Lee et al. (2015). The thin film in the blister test can be described by the equation, which stems from the membrane equation and is related with the tensile properties of the thin film and the applied vertical force [Lee et al. (2015)].

2.2.3 Thermal bonding effects on nonwovens

Thermal calender bonding process is one of the most widely employed bonding methods in nonwovens manufacture due to it processes many advantages, such as relatively soft products and excellent economic efficiency [Russel (2006)]. During the industrial bonding process, the fabric properties could be tremendously influenced by the selected bonding parameters, such as bond area, bond size, the contact time of the fabric with the thermal calendar and the bonding temperature [Russel (2006)]. Thus, the bonding variables that could affect the structure and properties of nonwovens were studied in a number of works with different materials [Russel (2006); Zhang et al. (2018); Bhat et al. (2004); Hegde et al. (2008); Michielsen and Jain (2010)].

Bonding temperature is a very important bonding parameter. The mechanical properties are usually improved as the thermal bonding temperature increases up to a certain optimal value.

Beyond that value, the mechanical properties of the nonwovens decline [Zhang et al. (2018)]. In particular, a lower than the optimal temperature would lead to an insufficient fiber sintering, whereas a higher temperature would contribute to the thermal degradation of the polymer and nonwoven rupture at lower stretching stress [Fedorova et al. (2007); Kim et al. (2002)]. The rupture patterns of nonwovens in tensile tests were studied experimentally [Zhang et al. (2018); Wang and Michielsen (2001); Britton et al. (1984); Liao and Adanur (1999)], and it was shown that stiffened locations resulting from thermal bonds act as stress concentrators and rupture happens at their periphery when the bonded pattern is located at the center of a stretched specimen [Zhang et al. (2018)].

The mechanical properties of the fibrous materials in general, and the thermally-bonded nonwovens in particular, are closely related to the fiber-fiber interactions. The latter were studied in a number of works due to their importance to the fabric structural characterization and mechanical performance [Smith et al. (2003); Chandran and Barocas (2007); Wang and Sastry (2000)]. In particular, an image analysis algorithm was developed to record the fiber network topology [Amoroso et al. (2011); D' Amore et al. (2010)].

2.2.4 The Clapeyron effect

Polymer melting points at atmospheric pressure are well-known. It is expected that melting temperature should increase at higher pressures due to the Clapeyron effect [Russell (2006)], albeit to what extent is unknown. It has been stated that the melting temperature of nonwovens will not be increased greatly during commercial production [Michielsen et al. (2006)], detailed information is unavailable.

The thermodynamic Clapeyron-Clausius equation is used to describe the dependence of the phase-equilibrium temperature with pressure during condensation, melting, evaporation, etc. [Lobo and Ferreira (2001); Wayner (1999); Carey (1992); DasGupta et al. (1994); Gokhale et al. (2003)]. To elucidate the effect of pressure on the phase-change temperature, precision instruments were applied to different materials in several works. The Clapeyron effect was studied using temperature- controlled bath or pressure/ temperature controlled bath during crystal growth, and it was demonstrated to be significant [LaCombe et al. (1998)]. In the work of Muhr et al. (1982) and Warner (1975), a high-pressure differential thermal analyzer was employed to study the effect of hydrostatic pressure on phase transition. It was also shown that the melting point of isotactic polypropylene (iPP) can increase by about 10 °C at bonding pressure [Warner (1989)]. This result was obtained by employing the method of differential scanning calorimetry (DSC) and the thermal analyzer to scan the bond areas of the nonwoven. The literature survey shows that some accurate experimental results related to the Clapeyron effect are available, however, the methods employed were relatively complicated and expensive. Also, the Clapeyron effect on nonwovens was studied for a limited number of materials relevant in nonwovens, such as polypropylene (PP) [Warner (1989); Wunderlich (1986)], and there is a need to explore other relevant materials.

2.3 Heat and mass transfer during bio-mass burning in forest fires

Occupied about 30% world land area, the forest makes a significant contribution to the earth ecosystem, such as decreasing the content of carbon dioxide in the atmosphere and soil strengthening and provide various living resources for wildlife and human races. However, the forests around the world currently are being threatened by deforestation issues, which are caused by different reasons such as unsustainable logging and ranching. Besides human behaviors, forest

fire is another important reason can cause deforestation [Davis (1959); Chandler et al. (1983); Malamud et al. (1998)]. Usually, there are four main reasons can cause a forest fire [Scott (2000)]: lightning, sparks, vegetation spontaneous combustion, and volcanic eruptions. Due to forest fire is uncontrollable and will spread or propagate freely, it is extremely important to deeply understand the mechanism of the fire propagation in the forest (either in tree crown or tree trunk), the factors that affect the propagation progress and how these factors are related with each other.

In 20th century, several physical models were found to describe the mechanism of fire propagation from the several aspects, such as radiative transfer [Albini (1967); Albini (1985); Albini (1986)], heat transfer [Thomas (1967); Thomas (1971)] and energy flux conservation [Frandsen (1971)]. These theoretical models used to depict the flame transportation demands the known input parameters. However, some key input parameters, such as the flame height, are hard to measure under the natural condition and cannot always remain as constant. Also, the ingredients and properties of the flaming materials were various from location to location, season to season. Thus, the models of fire propagation cannot cover every issue and the limits still exist.

Besides the theoretical researching, experimental works are also conducted to study the fire propagation behavior, either under the natural condition or with the laboratory designed model experiments [Wagner (1964); Wagner (1973); Wagner (1977); Wagner (1988)]. Pine needles [Dupuy (1995); Dupuy et al. (2011)] and oaks leaves [Kane et al. (2008)], these common species in the forest were taken to burn to simulate the burning progress. The other nature variable conditions were also considered for the experimental designing, most commonly studied were slope effects, wind effects or the combination of these two factors [Viegas (2004); Morandini et al. (2001); Boboulos and Purvis (2009)]. However, these natural materials were stuffed in the beds to be burned and their packing densities are rarely considered. Secondly, the experimental

data obtained from burning leaves trials cannot fully to be used to describe the flame propagating in the real forest, i.e. the space between trees still needed to be considered.

Forest fire and the related problems of air pollution also attracted significant attention in the past. These problems are linked by pollutant emissions caused by large-scale forest biomass burning. Currently, biomass burning is a global issue that strongly affects air quality and life on earth [Crutzen and Andreae (1990)]. During the burning process, several gases, such as greenhouse gases and nitrogen oxides [Crutzen et al. (1979); Logan (1983); Watson et al. (1990)], are emitted into the atmosphere. A number of works are devoted to studies of the emissions accompanying biomass burning in specific locations [Chan (2017); Chen et al. (2017)]. In particular, the emissions from fresh vegetation or burning plants were studied. These studies sub-divided the burning progress of fresh vegetation into five main stages [DeBano et al. (1998); Lobert and Warnatz (1993)]: ignition, flaming, glowing, smoldering and extinction. The beginning phase of the flaming stage is called the drying/distilling stage. In this process, water vapor and volatile organic compounds are ejected directly from the vegetation heated over 100 °C [Lobert and Warnatz (1993)]. The other stages involve complicated chemical reactions and contribute to the emission of different pollutants in the form of combustion products. Even though several works were conducted to study of the burning stages, the distillation progress was largely unexplored [Chakrabarty et al. (2010); Yokelson et al. (1997); Simoneit et al. (1993); Reid et al. (2005)].

When vegetation is burning, sometimes vapor jets are observed being ejected from the plants, such as burning wet wood during camping or after throwing fresh coconut shell directly into the flame. Similar jet ejections were explored in relation to thermosprays [Vestal (1983)] and flash evaporation [Miyatake et al. (1981)]. However, most of the works related to vegetation burning only focus on the emission product species, the amounts of the emission products and the

kinetic mechanisms of chemical reactions, rather than on the physical aspects of the ejection preceding emission formation. Also, no information is available, as to our knowledge, even on an estimate of the mass of the ejection/emissions issued during the distillation stage.

CHAPTER 3

RESEARCH OUTLINE

3.1 Adsorption and mass transfer in granular porous media

(This section has been previously published in Zhang, W., Vilensky, R., Zussman, E., Yarin, A. L. (2018). Adsorption and mass transfer in granular porous membranes/media due to inserted volatile materials. *International Journal of Heat and Mass Transfer*, 116, 248-258)

The adsorption kinetics of three different materials: camphor, naphthalene, and 2,4-Dinitrotoluene (DNT) were explored. These chemically different materials with significant differences in volatility were chosen to elucidate the common mechanisms of their physisorption in porous media and to establish a novel method which allows one to use such model materials as camphor and naphthalene for predictions relevant to such low volatility materials as DNT, etc. Accordingly, the experimental results were rationalized in the framework of the adsorption/desorption theory to establish the kinetic and equilibrium adsorption/desorption parameters. It should be emphasized that the transient adsorption/desorption theory developed in the present work is novel. Experiments were conducted at different temperatures below melting points of three volatile substances, with morphologies of the clusters of the adsorbed molecules being explored and the adsorbed mass measured versus time. Two experimental methods were implemented. The first setup revealed the kinetics of adsorption/desorption of different substances onto the sand surface and enabled an estimate of the kinetic constants, and the second setup provided an additional insight regarding the simultaneous processes of diffusion and adsorption/desorption within granular media. The theoretical/numerical predictions are shown to

be in good agreement with the experimental data, as well as the agreement between the two experimental methods used to measure the adsorbed mass on sand was quite satisfactory. In particular, this work contributes to the detection methods based on the removal of minuscule amounts of the adsorbed material delivered by diffusing vapor from a sublimating volatile source, which is hidden in porous medium/under a porous membrane. This means that the ultimate goal of the present work is in the fundamental understanding of the physical processes involved in such cases, which is important for the development of the appropriate sensors.

3.2 Detection of vapor released from sublimating materials encased in porous media

(This section has been previously published in Zhang, W., Zussman, E., Yarin, A. L. (2018). Detection of vapor released from sublimating materials encased in porous medium. *International Journal of Heat and Mass Transfer*, 118, 1357-1372.)

Detection of materials encased in porous media is important in many applications and can be attempted via sensing vapor sublimating from them. Development of such sensors requires evaluation of vapor concentration expected at the free surface from materials encased at different depths. For these aims, experiments are conducted with a model material, naphthalene, which is relatively easy to detect at any depth from the free surface of porous media. Another aim of these experiments is to develop comprehensive theories which are applicable to any sublimating material, any sensor size, and the observation time, and for any type of porous media. Accordingly, the data acquired using the model experimental material (naphthalene buried in sand or clay) is used here for verification of the theory.

An additional aim is related to the question whether it is possible to amplify the vapor flux reaching the free surface by means of suppression of its partial adsorption in the bulk. Using sand

as a porous medium of interest, it is shown that it is possible to achieve this goal by dip coating of sand in polymer solution with a subsequent drying. In a modified sand with a dramatically reduced surface area of the grains smoothed by the polymer coating, vapor adsorption is dramatically suppressed, while vapor flux toward the free surface is dramatically increased, thus increasing the chances of detection.

3.3 Rupture mechanism of nonwoven being stretched

(This section has been previously published in Zhang, W., Staszal, C., Yarin, A. L., Shim, E., Pourdeyhimi, B. (2018). Point-bonded polymer nonwovens and their rupture in stretching. *Polymer*, 146, 209-221.)

The present section aims at the experimental investigation and theoretical modeling of the physical phenomena responsible for thermal bonding of polymer fibers in nonwovens and their effect on such mechanical properties as the nonwoven stiffness, the yield stress, the stress at failure, toughness, and the entire stress-strain curve. Here, experiments are conducted to understand the effect of point bonding in nonwovens on the mechanical performance as well as on failure patterns. In the experiments, two types of nonwovens were explored: Polybutylene Terephthalate (PBT) nonwoven and Polybutylene Terephthalate (PBT)/Polyethylene (PE) (80/20) nonwoven. Special attention was paid to the effect of the bonding pattern (e.g. circular or rhombic) on the nonwoven failure patterns in stretching. A theory is also given using the complex elastic potentials (i.e. the Goursat functions) in the framework of the general approach of the planar problem of the theory of elasticity. It was shown that failure happens at the periphery of stiffened bonds. The theory predicted tensile stress concentration up to 140% of the applied tensile stress in that area, which was responsible for the failure modes observed experimentally.

3.4 Cohesion energy of thermally-bonded nonwovens

(This section has been previously published in Zhang, W., Yarin, A. L., Pourdeyhimi, B. (2019). Cohesion energy of thermally- bonded polyethylene terephthalate nonwovens: Experiments and theory. *Polymer Testing*, 78, 105984.)

This section of the work aims at the experimental and theoretical investigation of the cohesion energy which can be achieved in the thermal calendar bonding of polymer nonwovens. Polyethylene terephthalate (PET) samples were used in the experiments. Tensile tests were conducted with the as-received PET nonwovens and thermally-bonded PET nonwovens. Thermal bonding was conducted under five temperatures: 160 °C, 170 °C, 180 °C, 190 °C, or 200 °C. The mechanical properties, Young`s modulus, the yield stress, the maximum stress before sample failure and the toughness were measured. Blister tests were conducted aimed at measuring the cohesion energy of thermally-bonded PET nonwovens. The pushing shaft velocities of 2 mm/ min and 10 mm/ min were selected in the blister test. In addition, the theoretical description of the calendar bonding in the nip and of the forces acting on a nonwoven beyond the calendar nip is given. It is used to theoretically evaluate the cohesion energy of nonwovens due to thermal bonding in the nip. The predicted cohesion energy was estimated to be of the order of 4.2 J /m², which is plausible for the experimental data corresponding to the lowest bonding temperature of 160 °C. On the other hand, at the higher bonding temperatures the experimentally measured cohesion energy was of the order of 10 J/ m², which can probably be attributed to the enhanced reptational entanglement at the elevated temperatures.

3.5 Thermal bonding patterns effect on mechanical properties of nonwovens

Here, the work aims at exploring the effect of the thermal bonding patterns on the mechanical properties of nonwovens. This study of thermal bonding patterns is focused on the thermal bond location and size and in the nonwoven specimens. Tensile tests were conducted, and the corresponding tensile properties were obtained for further analysis. The effect of the thermal bond location and area is studied in detail. Theory for estimating the fiber-fiber intersections under a single thermal bond of any shape was developed. The numbers of fiber-fiber intersections were calculated for the thermal bonds used in the current work based on the established theory.

3.6 Characterization of the Clapeyron effect

The work in this section is aiming at the experimental investigation of the effect of an increased thermal bonding pressure on the melting points of three polymers used in nonwovens. Namely, this work aims at quantifying the Clapeyron effect in these polymers. Three polymers, polybutylene terephthalate (PBT), polyethylene terephthalate (PET), and polypropylene (PP) (already received in the form of nonwovens), were used in the present experiments. A simple novel method of measurement of the melting points of such nonwoven under different pressures is proposed and developed. The results revealed: (i) the melting point of PBT nonwovens increased by 11.36 °C when the applied pressure was increased up to 277.79 atm; (ii) the melting point of the PET nonwovens increased by 7.79 °C when the applied pressure increased up to 104.86 atm; (iii) the melting point of PP nonwovens increased by 5.36 °C when the applied pressure was increased up to 104.86 atm. The results are discussed in light of the existing literature.

3.7 Explosive- like ejections formed from plant stem in fire

In the work described in this section, freshly-cut and ethanol-immersed *Epipremnum aureum* stems were used as experimental materials to study the water vapor and volatiles ejection from biomass burning at the distillation stage of a forest fire. The explosive-like ejections were observed in the experiments with horizontal stems subjected to the surrounding flame, and the results were quantified and explained theoretically. Also, horizontal syringe needles filled with either water or ethanol and subjected to the surrounding flame were used in model experiments as a stem substitute to separate the effect of the water from that of combustible volatiles modeled by ethanol. The temperature of the explosive-like ejections ejected from the horizontal stems or needles subjected to the flame was estimated. The predictions of the proposed theory estimating the vapor/volatile mass ejections were compared with the experimental data and a good agreement was revealed.

3.8 Flame propagation of canopy fire in a model system

To study the effects of spatial step, inclination angles and wind to the flame propagation velocity, i.e. experimentally simulate the fire spread in the forest, model experiments were designed and conducted in the laboratory. Cotton-tipped applicators, pure or dipped in ethanol, were applied as the flame source. Flir T1030sc IR camera and a DSLR camera were employed for the recording of the flame propagation progress. The flame propagation velocity, as well as flame morphologies, at various conditions were calculated and shown.

CHAPTER 4

ADSORPTION AND MASS TRANSFER IN GRANULAR POROUS MEMBRANES/MEDIA DUE TO INSERTED VOLATILE MATERIALS

(This chapter has been previously published as Zhang, W., Vilensky, R., Zussman, E., Yarin, A. L. (2018). Adsorption and mass transfer in granular porous membranes/media due to inserted volatile materials. *International Journal of Heat and Mass Transfer*, 116, 248-258.)

4.1 Introduction

In this chapter, we focus on the elucidation and understanding of the vapor transfer process within granular porous membranes and media, where simultaneous processes of adsorption/desorption and diffusion take place. The developed setup, methods and materials used for the experiments are introduced in section 4.2. The proposed theory is shown in section 4.3. Obtained experimental results, as well as the comparisons with the theoretical predictions, are shown in section 4.4. Conclusions are drawn in section 4.5.

4.2 Experimental: Materials and methods

4.2.1 Materials

Three different substances: camphor, naphthalene and 2,4- Dinitrotoluene (DNT) were used as an adsorbate (see Figure 4.1), while sand was used as an adsorbent. Naphthalene was purchased from J. T. Baker Chemicals, (CAS No 91-20-3). Camphor and DNT were obtained from Sigma Aldrich. Chloroform, chloroform D and acetone were purchased from Bio-Lab Ltd. (AR).

Sand samples with grain sizes of 0.225 ± 0.05 mm and about 0.5 mm (for sand used in setups I & II and setup III, respectively; cf. Figure 4.2) were employed. The measured permeability of the sand was about 58 Darcy (setups I & II) and 9-12 Darcy (setup III). Sand characterization for setup III including particle sphericity and layer permeability and porosity is described in detail in Appendixes A and B. Prior to use, the sand was heated to 200 °C for 5 h to remove any residues of organic materials. Non-woven cellulose cloth (Smith Detection Inc.) was used as a separator membrane, placed between two compartments in a vertical sand column in experimental setups I & II. The measured permeability of the cloth was about 0.5 Darcy.

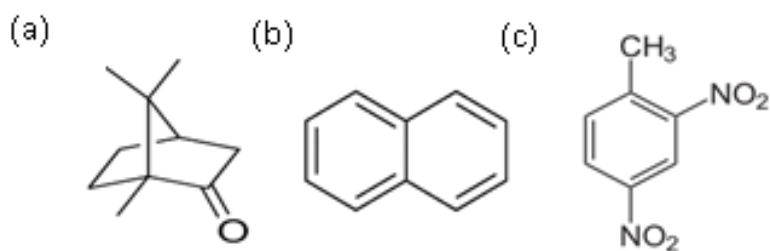


Figure 4.1 Chemical structure of the adsorbates: (a) Camphor, (b) Naphthalene, and (c) 2,4-Dinitrotoluene (DNT).

4.2.2 Experimental setups

Three complementary experimental systems (see Figure 4.2) were implemented to study different aspects of mass transfer (the interplay between adsorption/desorption and diffusion) within granular media membraned (i.e., sand). Experimental setup I was designed to reveal the kinetics of adsorption/desorption of different substances onto the sand surface and enable an estimate of the kinetic constants. Experimental setup II provided an additional insight regarding the simultaneous processes of diffusion and adsorption/desorption within granular media.

Experimental setup III revealed the morphology of deposited vapor on a glass substrate as a function of temperature gradient and distance from the substance reservoir, as well as introduced another method of measurement of the adsorbed vapor mass in comparison with setups I and II, as described below.

4.2.2.1 Setup I

A close system made of an aluminum cylinder (the inner diameter of 23 mm, the height of $L = 20$ mm) consists of 2 compartments with air at atmospheric pressure, separated by a cellulose membrane. A tested volatile substance (~ 2 g) is located at the bottom of the lower compartment and a thin layer of sand (0.2 g) is uniformly spread on top of the membrane. In both the lower and the upper compartments vapor was fully saturated. Thus, this system could be treated as a batch “reactor”, where vapor adsorbs onto the sand surface under a constant saturated vapor pressure, and since there is no vapor concentration gradient, diffusion is fully excluded and the adsorption/desorption process can be singled out and studied alone. The measurements of the adsorbed vapor mass on sand were conducted using UV–VIS spectrophotometer or $^1\text{H-NMR}$, as described below.

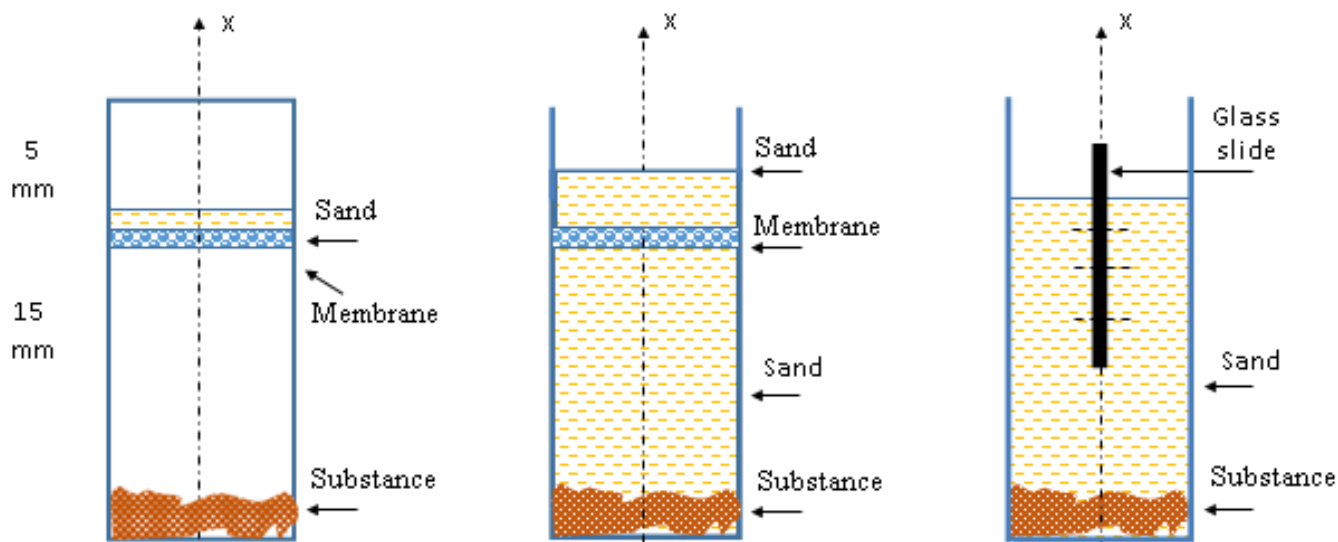


Figure 4.2 Schematics of the experimental setups. (a) Setup I is a closed system which consists of 2 compartments separated by a membrane. A thin layer of sand is placed on top of the membrane, with a sublimating substance located at the bottom of the lower compartment. The adsorbed vapor in sand can be measured taking samples and analyzing them using UV–VIS spectrophotometer or ¹H-NMR. (b) In setup II the sublimating substance is located at the bottom of a sand column. A membrane is located ~3 mm below the sand/air interface. Sand located above the membrane is open to atmosphere. Samples can be taken from this upper sand layer and the amount of the adsorbed vapor on sand can be measured at different time moments using UV–VIS spectrophotometer or ¹H-NMR. (c) In setup III, the volatile substance is located at the bottom of a sand column, which is opened to the atmosphere. A glass is mounted vertically, at the center of the column. Vapor deposit morphologies on the slide were optically observed at heights A, B and C after the slide had been withdrawn from the sand column. Also, samples of sand were taken for analysis and rinsed, while the removed deposit weighed for comparison with the data from setup II.

4.2.2.2 Setup II

An open system made of an aluminum cylinder (the inner diameter of 23 mm, the height of $L = 20$ mm). This setup was used to study the mass transfer of sublimating substances buried within a porous media in cases where the adsorption/desorption processes and diffusion proceed simultaneously, i.e., in distinction from setup I, vapor diffusion is not excluded in this case. In this setup a thin layer of a volatile analyte (1 g) was placed at the bottom of the lower compartment and dry sand was loaded on top of it forming a sand column (~18 mm in height). A cellulose membrane was located ~3 mm below the sand/air interface. The sand located above the membrane

(~2 g) was sampled at different time moments to quantify the amount of the adsorbed substance on sand. The experiments with different duration were done with new samples of pure sand below and above the membrane. Here, as in setup I the measurements of the adsorbed vapor mass on sand were conducted using UV–VIS spectrophotometer or $^1\text{H-NMR}$, as described below.

4.2.2.3 Setup III

This setup was used to observe the morphology of deposited vapor on a glass slide. A thin layer of camphor or naphthalene was placed at the bottom of a beaker. On top of this layer, ~2.3 cm height of sand was placed and a glass slide was inserted into the sand layer vertically. Parafilm with small holes was used to cover the beaker. The bottom of the setup was kept at 50 °C for at least 5 h. Sand samples were taken for the analysis of the adsorbed vapor during this time. Namely, they were weighed. Then, they were rinsed in either acetone or chloroform to remove as much as possible the absorbed camphor or naphthalene. After that, the samples were weighed again and the weight difference of the samples before and after rinsing was attributed to the adsorbed material.

4.2.3 Methods

Quantitative results obtained with setups I and II were primarily based on UV–VIS absorption measurements and $^1\text{H-NMR}$ analyses. For all the three volatile substances studied at each time moment of interest, sand was removed from the cellulose membrane and soaked in a suitable solvent in order to extract the adsorbed material. Then, the solution was filtered through Whatman filter paper (mesh size 1250) and the resulting filtrate was analyzed using UV–VIS spectrophotometer (Shimadzu, UV-1800), or $^1\text{H-NMR}$. In all cases, a calibration curve relating known concentrations to the measured absorbance values were constructed. The naphthalene and DNT filtrates were analyzed using UV–VIS, while in the case of camphor, because of its very low

UV–VIS absorbance signal, measurements were performed by $^1\text{H-NMR}$. Initially, sand was soaked in 10 ml chloroform-D for 2 h, then the solution was filtered and the resulting filtrate was analyzed using $^1\text{H-NMR}$. The $^1\text{H-NMR}$ spectrum produces several peaks, while for quantification three main peaks were analyzed: $\delta = 1.85, 0.93$ and 2.1 ppm. These peaks were integrated and averaged to give the amount of adsorbed camphor. We chose nitromethane as a standard, which has a single peak at $\delta = 4.5$ ppm (s, 3H).

The amounts of adsorbed naphthalene and DNT were quantified using UV–VIS. In the case of naphthalene, sand was soaked in 10 ml chloroform for 2 h, then the solution was filtered and the resulting filtrate was analyzed using UV–VIS at the wavelength of 278 nm. For DNT extraction, sand was soaked in 10 ml acetone, stirred for 2 h and then filtered. The obtained filtrate was reacted with NaOH 1.5M 5% (v/v) solution to form Meisenheimer complex. The color of the solution was changed from transparent to blue and the solution was analyzed using UV–VIS at a wavelength of 560 nm.

4.3 Theoretical background

When studying the mass transfer and the adsorption/desorption processes of vapor of a sublimating volatile substance, buried in a granular porous media, such as sand, the equilibrium adsorbed vapor mass M_{ads} can be evaluated as

$$M_{\text{ads}} = \rho S_{\text{total}} h_0 N_e \quad (4.1)$$

where ρ is the density of the adsorbate, S_{total} is the total surface area of porous media, h_0 is the monolayer thickness, and N_e is the average equilibrium number of the adsorbed layers if they would be uniformly smeared over the sand grain surfaces.

For weighing method used in setup III, the maximum adsorbed mass of naphthalene is $M_{\text{ads}} = 0.05453$ g at room temperature, $M_{\text{ads}} = 0.03939$ g at 50 °C, $M_{\text{ads}} = 0.04830$ g at 74.3 °C, and $M_{\text{sand+ads}} = 9.6632$ g. The maximum adsorbed mass of camphor is $M_{\text{ads}} = 0.01952$ g at room temperature, $M_{\text{ads}} = 0.01863$ g at 50 °C, $M_{\text{ads}} = 0.06453$ g at 74.3 °C, $M_{\text{ads}} = 0.04848$ g at 100 °C, and $M_{\text{sand+ads}} = 9.6632$ g. For the UV-VIS spectroscopy method used in setup II, the maximum adsorbed mass of naphthalene is $M_{\text{ads}} = 0.00045$ g at room temperature, $M_{\text{ads}} = 0.00085$ g at 50 °C, and $M_{\text{sand+ads}} = 2.0000$ g.

The monolayer thickness used for the evaluation is taken as $h_0 = 10^{-10}$ m. The specific surface area measured by the BET method [Brunauer et al. (1938)] was found as $S_{\text{total}} = 10 \text{ m}^2/\text{g}$. This relatively high value is attributed to the fact that sand particles reveal a net of pits and pores, the openings of which are visible in SEM images (cf. Figure 4.3).

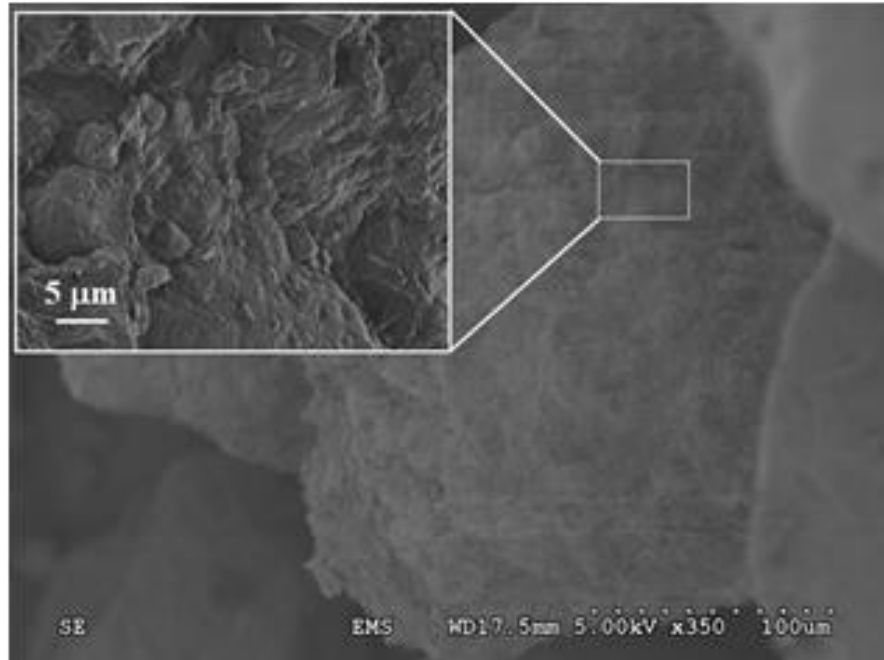


Figure 4.3 HR-SEM image of a sand particle. The inset shows the surface at a larger magnification.

Then, the average number of the adsorbed layers predicted by Eq. (4.1) would be about $N_e \approx 1$. In such cases, the adsorption-desorption kinetics could be described in the framework of the Langmuir approach [Langmuir (1918), Langmuir (1916)]. Namely, assume that vapor resulting from sublimation of a certain substance surrounds a solid surface of another compound (sand). Consider first an adsorption/desorption of vapor at the surface of the solid compound (sand). Denote a free vapor molecule as F, an empty site (without vapor molecule) at the solid surface as E, and a site at the surface with an adsorbed vapor molecule as A. Also, assume that the adsorbed vapor can form only a monolayer at the solid surface, as is corroborated by the value $N_e \approx 1$ evaluated from the measurements, as described above. Then, the adsorption/desorption process at the solid surface can be present as the following reaction scheme,



Denote the part of sites occupied by vapor molecules at the surface as θ , whereas $(1-\theta)$ is accordingly, the available part. Then, the vapor balance equation near the surface reads

$$\frac{dC}{dt} = -k_f C(1-\theta) + k_b \theta \quad (4.3)$$

where C is the vapor concentration in the bulk near the surface with the units $1/\text{cm}^3$. The “reaction” constants k_f and k_b corresponding to the forward (adsorption) and backward (desorption) “reactions” [cf. Eq. (4.2)] have units $1/\text{s}$ and $1/(\text{cm}^3 \cdot \text{s})$, respectively.

If a steady-state has been achieved, then the derivative $dC/dt = 0$, and according to Eq. (4.3) we arrive at the Langmuir adsorption isotherm [Langmuir (1918), Langmuir (1916)]

$$\theta_{eq} = \frac{(k_f / k_b)C_{eq}}{1 + (k_f / k_b)C_{eq}} \quad (4.4)$$

where subscript eq denotes the values of the parameters at the equilibrium conditions.

On the other hand, in the absence of the adsorption/desorption equilibrium the balance between the rate of decrease in the concentration of the free vapor molecules C and the increase in the part of the occupied sites θ can be established using the following considerations. Denote the surface concentration of the adsorbed vapor molecules as C_a with the units of $1/\text{cm}^2$, and assume that the adsorption/desorption process happens at a surface of a pore of diameter d . Then, the balance of vapor in the bulk and at the pore surface is given by

$$-\frac{d(C\pi d^3 / 6)}{dt} = \frac{d(C_a \pi d^2)}{dt} \quad (4.5)$$

It should be emphasized that an adsorbed vapor molecule occupies a known area S_0 at the pore surface, and its value is approximately equal to $16.2 (\text{\AA})^2$ [Guiochon et al. (2006)]. Therefore, the total number of sites at the pore surface is equal to $\pi d^2 / S_0$, and thus, Eq. (4.5) yields

$$\frac{d\theta}{dt} = -\frac{S_0 d}{6} \frac{dC}{dt} \quad (4.6)$$

where $\theta = [C_a \pi d^2 / (\pi d^2 / S_0)]$.

It should be emphasized that the system of Eqs. (4.3) and (4.6) fully describes the two physical characteristics C and θ of the adsorption/desorption process.

Vapor concentration in porous medium could also depend on vapor diffusion in the pores. Therefore, in the one-dimensional case of interest here, Eqs. (4.3) and (4.6) take the following form

$$\phi \frac{\partial C}{\partial t} = D \frac{\partial^2 C}{\partial x^2} - k_f C(1-\theta) + k_b \theta \quad (4.7)$$

$$\frac{\partial \theta}{\partial t} = -\frac{S_0 d}{6} [-k_f C(1-\theta) + k_b \theta] \quad (4.8)$$

where D is the vapor diffusion coefficient and ϕ is the porosity. Also, x is the coordinate normal to the membrane plane.

In the case where saturated vapor concentration C_w is sustained at one side of the sand layer $x = 0$, and vapor is removed by sufficiently strong air blowing on the other side of the sand layer $x = \delta$ (where $C=0$), the initial and boundary conditions for the system of Eqs. (4.7) and (4.8) read, respectively,

$$t = 0: C = C_w \text{ at } x = 0, C = 0 \text{ at } x > 0; \theta = 0 \text{ at } x \geq 0 \quad (4.9)$$

$$t > 0: C = C_w \text{ at } x = 0; C = 0 \text{ at } x = \delta \quad (4.10)$$

This is the case corresponding to setups II and III.

The adsorbed mass of the substance $M(t)$ in the sand layer as a function of time is found using solutions of the problem (4.7)- (4.10) as

$$M(t) = \frac{\mu_v}{N_A} DA \int_0^t \left(-\frac{\partial C}{\partial x} \Big|_{x=0} + \frac{\partial C}{\partial x} \Big|_{x=\delta} \right) dt \quad (4.11)$$

where μ_v is the molecular weight of vapor, N_A is Avogadro's number, and A is the cross-sectional area of the experimental cylinder, or beaker containing the sand layer.

The solution of the problem (4.7)- (4.10) tends to the steady state,

$$\theta(x) = \frac{(k_f / k_b) C(x)}{1 + (k_f / k_b) C(x)}, \quad C(x) = C_w \left(1 - \frac{x}{\delta} \right) \quad (4.12)$$

whereas according to Eq. (4.11) the value of M saturates, since $\partial C / \partial x \equiv -C_w / \delta$ in the steady state.

In the case where saturated vapor concentration C_w is sustained on both sides of the sand layer and vapor diffusion is much faster than the adsorption/desorption process (which applies to the experimental setup I), the problem described by Eqs. (4.7) and (4.8) reduces to the following equation

$$\frac{d\theta}{dt} = -\frac{S_0 d}{6} \left[-k_f C_w (1-\theta) + k_b \theta \right] \quad (4.13)$$

Its solution subjected to the initial condition $t=0, \theta=0$, reads

$$\theta = \frac{k_f C_w}{k_b + k_f C_w} \left\{ 1 - \exp \left[-\frac{S_0 d}{6} (k_b + k_f C_w) t \right] \right\} \quad (4.14)$$

Then, Eq. (11) yields the following expression for the adsorbed mass

$$\frac{M(t)}{M_{\max}} = \frac{k_f C_w}{k_b + k_f C_w} \left\{ 1 - \exp \left[-\frac{S_0 d}{6} (k_b + k_f C_w) t \right] \right\} \quad (4.15)$$

At equilibrium, $M_{\text{eq}} / M_{\max} = k_f C_w / (k_b + k_f C_w)$, where $M_{\max} = \rho h_0 S_{\text{total}}$, is the maximum mass adsorbed in the case when all the adsorption sites would be occupied.

It should be emphasized that for the further comparison with the experimental data it is convenient to transform the main results of the present section to the dimensionless form rendering parameters dimensionless using the following scales: C_w for C , δ^2 / D for t , δ for x and $(\mu_v / N_a) C_w A \delta$ for M , and introducing the following dimensionless groups

$$K_f = k_f \frac{\delta^2}{D}; \quad K_b = k_b \frac{\delta^2}{D C_w}; \quad K_\theta = \frac{S_0 d C_w}{6} \quad (4.16)$$

Then, Eqs. (7)-(11) corresponding to setups II and III take the following form

$$\frac{\partial \bar{C}}{\partial \bar{t}} = \frac{1}{\phi} \left[\frac{\partial^2 \bar{C}}{\partial \bar{x}^2} - K_f \bar{C}(1-\theta) + K_b \theta \right] \quad (4.17)$$

$$\frac{\partial \theta}{\partial \bar{t}} = K_\theta \left[K_f \bar{C}(1-\theta) - K_b \theta \right] \quad (4.18)$$

$$\bar{t} = 0: \bar{C} = 1 \text{ at } \bar{x} = 0, \bar{C} = 0 \text{ at } \bar{x} > 0; \theta = 0 \text{ at } \bar{x} \geq 0 \quad (4.19)$$

$$\bar{t} > 0: \bar{C} = 1 \text{ at } \bar{x} = 0; \bar{C} = 0 \text{ at } \bar{x} = 1 \quad (4.20)$$

$$\bar{M} = \int_0^{\bar{t}} \left[-\frac{\partial \bar{C}}{\partial \bar{x}} \Big|_{\bar{x}=0} + \frac{\partial \bar{C}}{\partial \bar{x}} \Big|_{\bar{x}=1} \right] d\bar{t} \quad (4.21)$$

where overbars denote dimensionless parameters.

Also, Eq. (4.15) corresponding to setup I can be transformed to the following dimensionless form

$$\bar{M}_a = 1 - \exp(-\bar{t}_a) \quad (4.22)$$

where $\bar{M}_a = M / (M_{eq} M_{max})$ and $\bar{t}_a = t / [(S_0 d / 6)(k_b + k_f C_w)]^{-1}$.

4.4 Results

4.4.1 Experimental setup I

The following experiments were performed at room temperature ~24 °C. In setup I, the substances' adsorption takes place on a very thin layer of sand subjected to the saturated vapor pressure on both sides, and vapor diffusion is essentially excluded. Thus, Eq. (4.12) reduces to the classical Langmuir equation with the adsorption and desorption coefficients, $k_{ads} = k_f (S_0 d / 6)$

and $k_{des} = k_b (S_0 d / 6)$, respectively. The adsorption kinetics for all three volatile substances used in the experiments with setup I was measured and the results are shown in Figure 4.4.

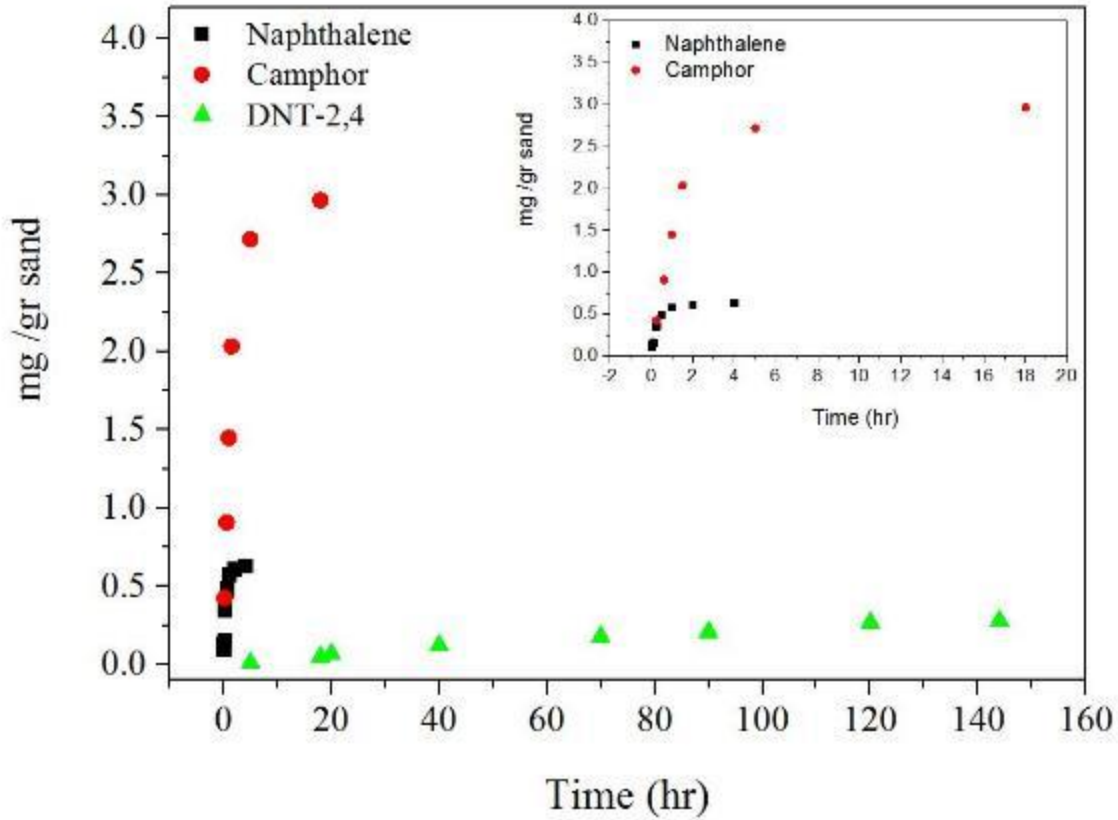


Figure 4.4 Adsorbed amount of naphthalene, camphor, and 2,4-DNT vs. time, at $\sim 24^\circ\text{C}$. The inset shows the adsorption of naphthalene and camphor during the first 20 h.

The experimental data for all the volatile substances from Figure 4.4 can be collapsed to a single dimensionless master curve according to Eq. (4.22), as shown in Figure 4.5. This allows one to establish the adsorption/desorption kinetics parameters of all the volatile substances listed in Table 4.1.

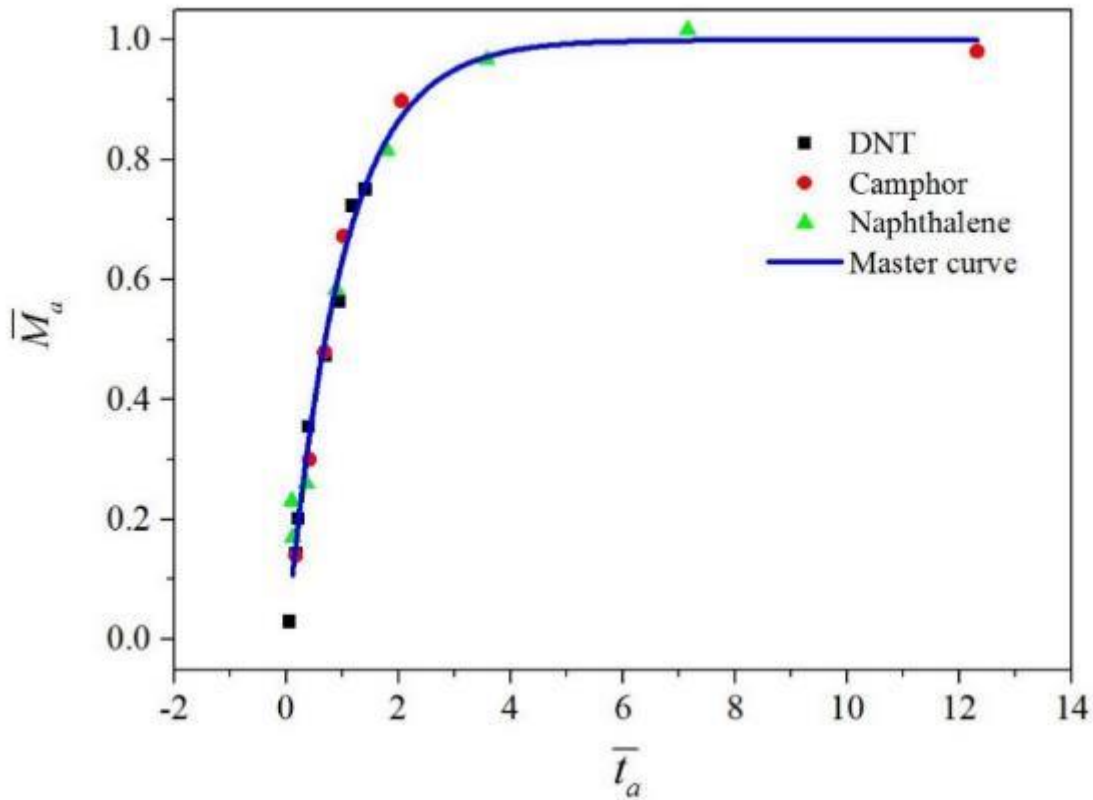


Figure 4.5 Normalized experimental adsorption data for the three substances: naphthalene, camphor and 2,4-DNT (shown by symbols) reduced to a single master curve according to Eq. (4.22).

It is seen that the equilibrium dissociation constant, $K_d = k_{des} / k_{ads}$ of camphor and 2,4-DNT is two orders of magnitude lower than that of naphthalene, implying a considerably higher affinity of the first two substances to sand surface. This can be explained by the polarity of camphor and DNT molecules which leads to an enhanced interaction with sand surface. On the other hand naphthalene molecules are non-polar making the naphthalene-sand interactions unfavorable. The adsorption rate, $R \sim k_{ads} P_{sat}$, where P_{sat} is the partial pressure, of naphthalene and camphor, is very high compared to that of 2,4-DNT, primarily because of a significantly higher vapor pressure

of the first two substances (the k_{ads} values for all the three substances were comparable, see Table 4.1).

Table 4.1 The adsorption/desorption kinetics constants and the equilibrium constant for the three volatile substances studied. The saturated pressure P_{sat} was used to find the values of C_w .

Material	P_{sat} [atm]	C_w [1/cm ³]	K_d [M]	k_{ads} [1/M×s]	k_{des} [1/s]
Naphthalene @24°C	10^{-4}	2.5×10^{15}	2.7×10^{-5}	30.9	8.28×10^{-4}
Naphthalene @50°C	1.1×10^{-3}	2.7×10^{16}	2.7×10^{-5}	76	2.07×10^{-3}
Camphor @24°C	2.4×10^{-4}	5.9×10^{15}	8.6×10^{-7}	17.8	1.54×10^{-5}
DNT-2,4 @24°C	10^{-6}	2.5×10^{13}	1.6×10^{-7}	10.8	1.76×10^{-6}

4.4.2 Experimental setups II and III

In the experimental setup II, naphthalene was used first as a target substance at 24 °C. In this system both diffusion and adsorption/desorption occur simultaneously and the evolution in time of the adsorbed vapor mass is described by the dimensionless Eqs. (4.17)- (4.21). These equations were integrated numerically using the semi-discretization of the spatial second derivative on the right-hand side of Eq. (4.17) and the numerical marching according to the Kutta-Merson algorithm. The results are depicted in Figures 4.6- 4.11. In particular, Figure 4.6 compares the predicted values for two pore size, $d=0.001$ and 0.0002 cm, with the experimental data for naphthalene at 24°C for two pore size. It can be seen that as d decreases, the mass of the adsorbed naphthalene increases. The comparison of the experimental data to simulations performed for $d=0.0002$ cm revealed good agreement. This is attributed to a larger surface area corresponding to smaller pores.

It should be emphasized that the simulations were conducted with the values of the kinetic adsorption/desorption parameters established in subsection 4.4.1 and listed in Table 4.1. Figure 4.7 presents the experimental data and the simulated results for naphthalene at 24 °C for two porosity values, $\phi = 0.3$, and 0.8 for the pore diameter $d = 0.0002$ cm. Good fitting of the experimental data is seen at $\phi = 0.3$.

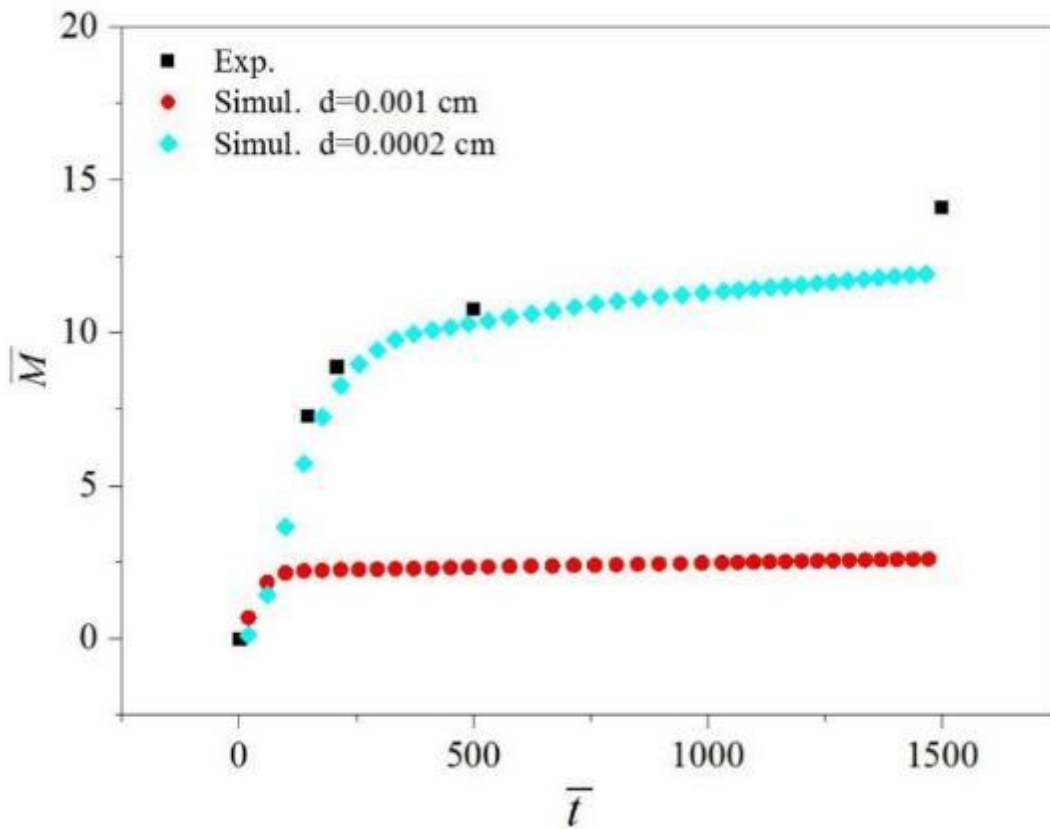


Figure 4.6 Absorbed mass of naphthalene at 24 °C versus time for two pore diameters, $d=0.001$ and 0.0002 cm. Black symbols correspond to the experimental data, red and blue symbols – to the numerical simulations.

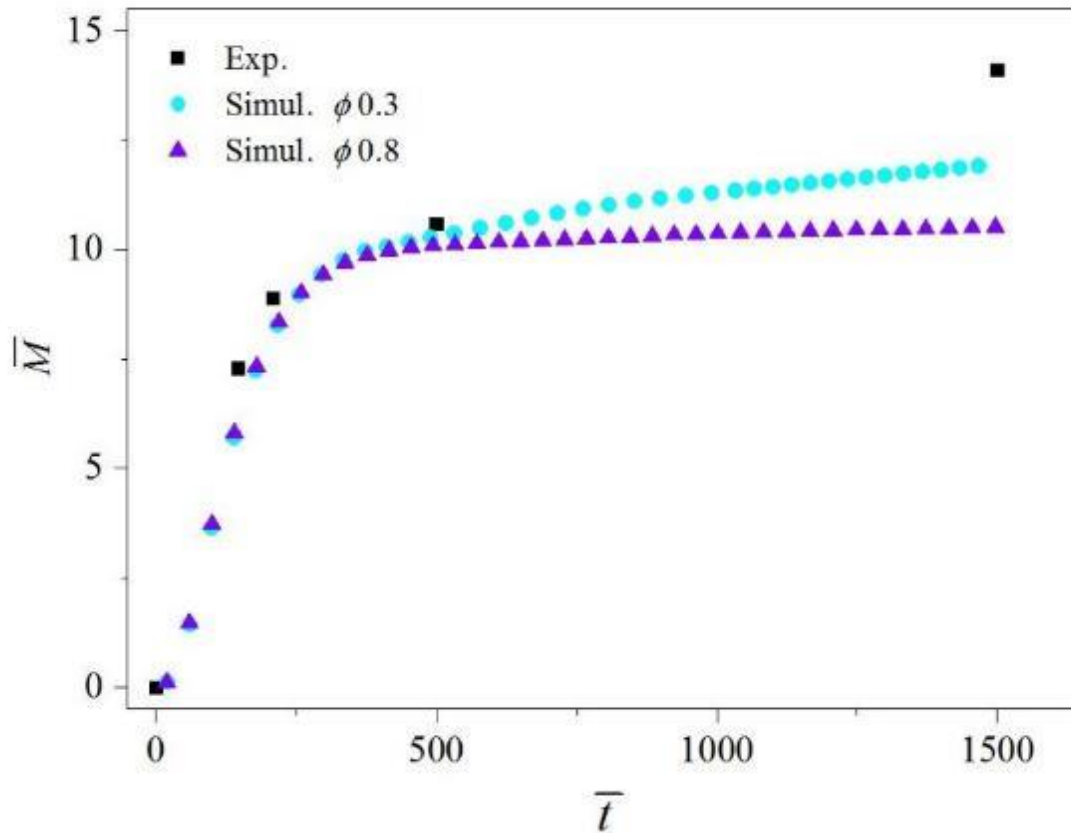


Figure 4.7 Absorbed mass of naphthalene at 24 °C versus time at $d=0.0002$ cm and two values of porosity, $\phi=0.3$ and 0.8 . Black symbols correspond to the experimental data, pink and blue symbols – to the numerical simulations.

Figure 4.8 depicts the experimental data for naphthalene obtained at 50 °C using setups II and III. Comparison of the experimental data obtained using setup II and III is satisfactory. No simulations were done in the present case, since the situation when the cylinder bottom is sustained at an elevated temperature, while its open top is at room temperature is non-isothermal, which is not accounted for by the current theoretical model (4.17) - (4.21). Its generalization for the non-isothermal cases will be done in future work.

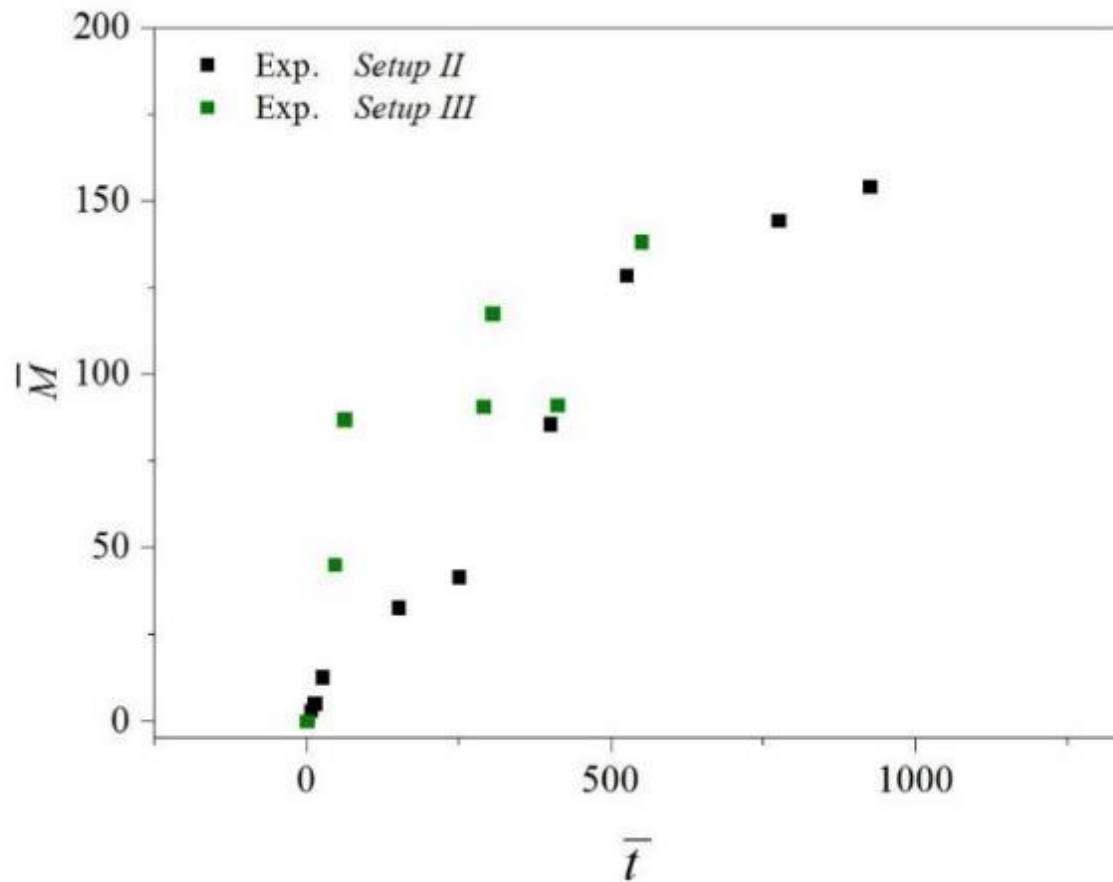


Figure 4.8 Absorbed mass of naphthalene at 50 °C measured experimentally using setups II and III (the results are shown by symbols the corresponding colors listed in the panel).

It should be emphasized that the following parameter values were used in the present subsection to render parameters dimensionless for setups I, II and III:

Setup II at 24 °C:

$$\delta = 1.8 \text{ cm}, A = 4.15 \text{ cm}^2, D = 0.0187 \text{ cm}^2 / \text{s}, C_w = 2.47 \times 10^{15} \text{ [1/cm}^3\text{]}, S_o = 2 \times 10^{-15} \text{ [cm}^2\text{]}$$

Setup III at 24°C:

$$\delta = 2.3 \text{ cm}, A = 23.5 \text{ cm}^2, D = 0.0187 \text{ cm}^2 / \text{s}, C_w = 2.47 \times 10^{15} \text{ [1/cm}^3\text{]}, S_o = \times 10^{-15} \text{ [cm}^2\text{]}$$

Setup II at 50°C:

$$\delta = 1.8 \text{ cm}, A = 4.15 \text{ cm}^2, D = 0.0224 \text{ cm}^2 / \text{s}, C_w = 2.47 \times 10^{16} [1 / \text{cm}^3], S_o = \times 10^{-15} [\text{cm}^2]$$

4.4.3 Experimental setup III: Morphological observations

In this setup, the morphology of the deposits of two volatile substances, camphor and naphthalene, were observed on the inserted vertical glass slides as a function of depth. The experiments were conducted for at least 5 h at 50 °C. The observed morphologies of camphor and naphthalene deposits adsorbed on vertical glass slides are shown in Figures 4.9 and 4.10, respectively. In Figure 4.9, clusters /crystals of camphor are observed on a glass slide, primarily at point A, which is located near the sand/air interface. In the case of camphor, as the depth decreases, i.e. the distance from the beaker bottom where a volatile substance is located, increases, a higher camphor deposition is observed (cf. Figure 4.9). This enhanced deposition of camphor vapor near the sand/air surface is attributed to a lower temperature at the surface. In the case of naphthalene, no apparent trend was observed regarding the deposition behavior as a function of the depth from the free surface (cf. Figure 4.10). In general, the results obtained in this setup indicate that the temperature gradient controls the vapor deposition, which requires generalization of the theoretical model for the non-isothermal case, which is currently underway. In addition, the morphologies of naphthalene and camphor crystals formed on horizontal glass slides located on top of the experimental setup, in the absence of sand, are shown in Figures 4.11 and 4.12.

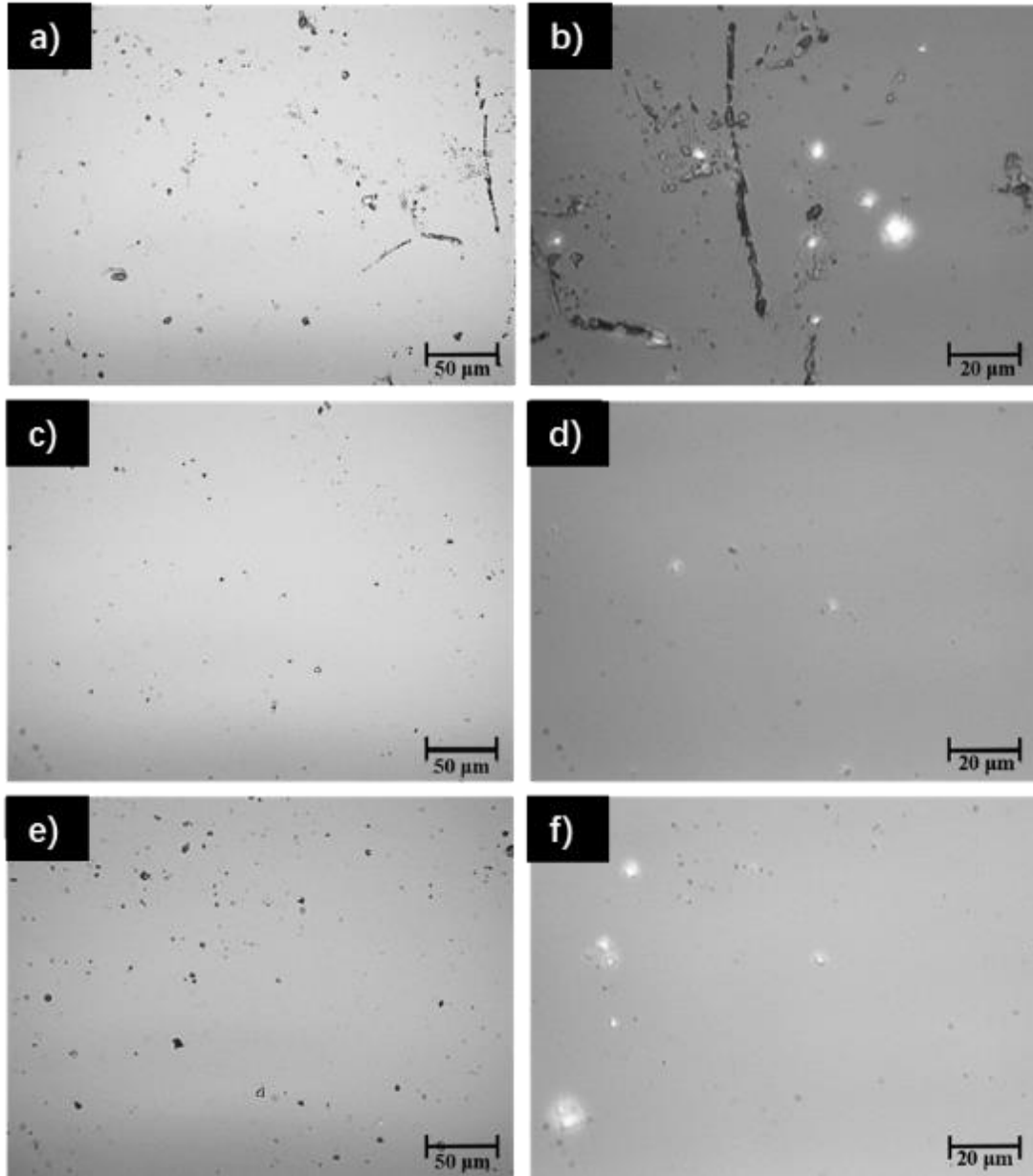


Figure 4.9 Morphology of camphor deposits on a vertical glass slide. Optical images (at magnifications $\times 50$ and $\times 20$) were taken after the slide had been withdrawn from the sand column, at three positions A=20 mm, B=10 mm and C=3 mm measured from the lower end of the glass slide (cf. Figure 4.2). (a) Position A ($\times 20$), (b) Position A ($\times 50$), (c) Position B ($\times 20$), (d) Position B ($\times 50$), (e) Position C ($\times 20$), and (f) Position C ($\times 50$).

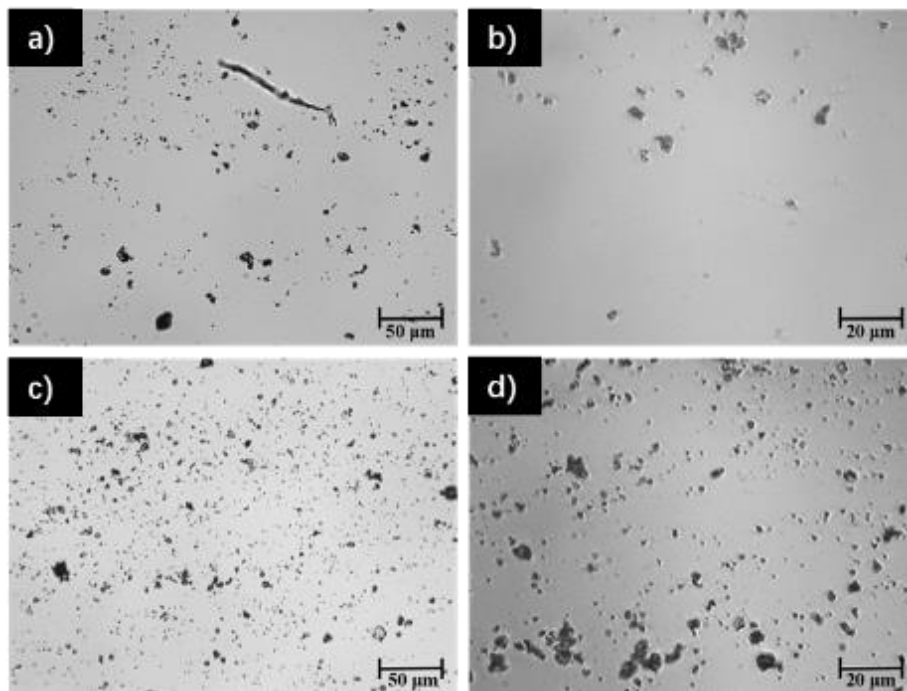


Figure 4.10 Morphology of naphthalene deposits on a vertical glass slide. Optical images (at magnifications $\times 50$ and $\times 20$) were taken after the slide had been withdrawn from the sand column, at two positions, A=15 mm, and B=5 mm, measured from the lower end of the glass slide (cf. Figure 4.2). (a) Position A ($\times 20$), (b) Position A ($\times 50$), (c) Position B ($\times 20$), and (d) Position B ($\times 50$).

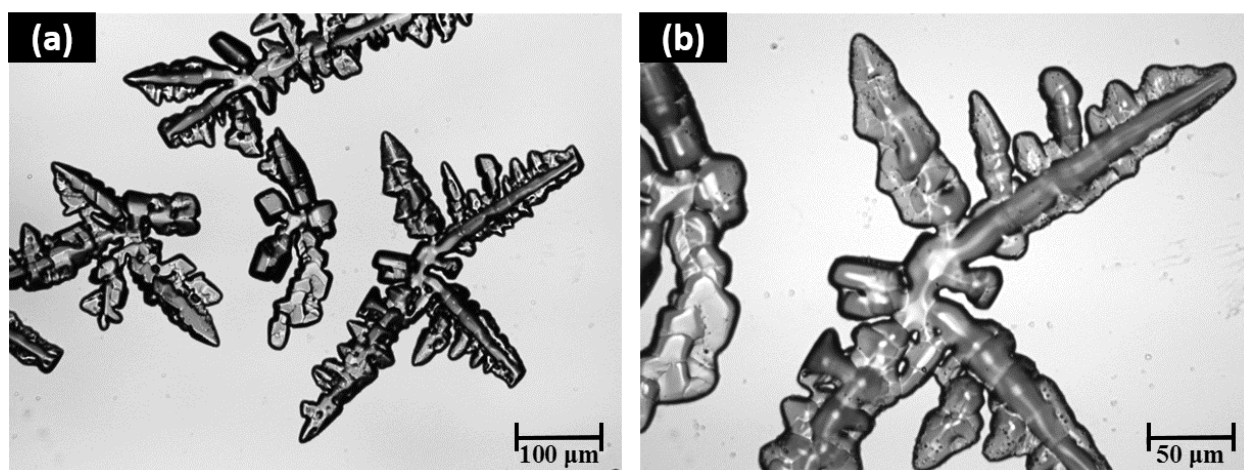


Figure 4.11 Morphology of camphor deposits adsorbed on glass slides. (a) The $\times 10$

magnification, and (b) The $\times 20$ magnification.

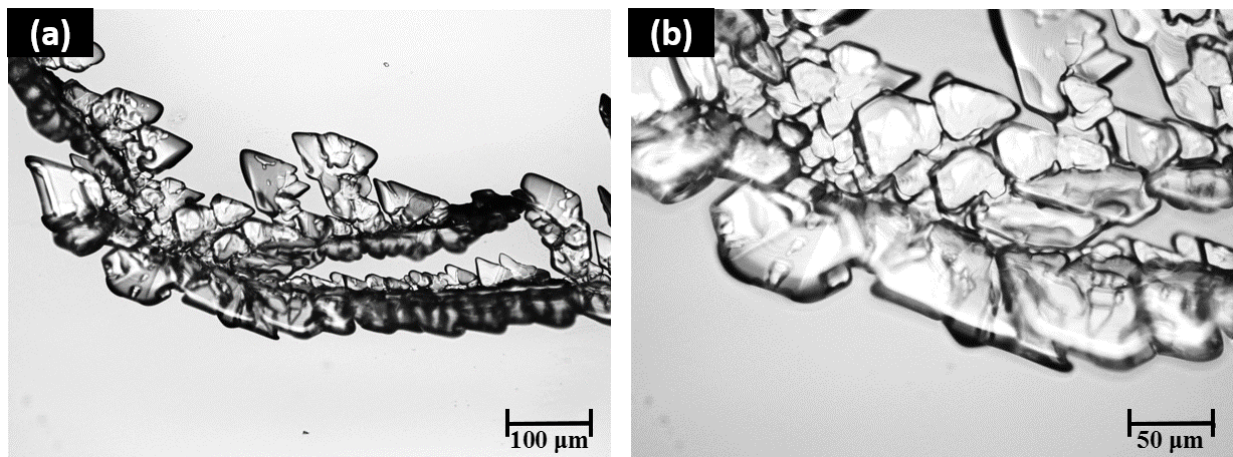


Figure 4.12 Morphology of naphthalene deposits adsorbed on glass slides. (a) The $\times 10$ magnification, and (b) The $\times 20$ magnification.

4.5 Conclusions

Experiments with setup I where the diffusion process is negligibly small compared to the adsorption/desorption processes revealed in conjunction with the theoretical model for this experiment the kinetic parameters responsible for the adsorption/desorption of three different volatile substances: camphor, naphthalene, and 2,4-Dinitrotoluene (DNT). It was shown that the data for all the three substances can be collapsed onto a single dimensionless master curve, which essentially can be applied to any other volatile substances to facilitate the development of the detection methods for them.

Experiments with setups II and III were conducted under the conditions where both the diffusion and the adsorption/desorption processes are important simultaneously. The measured adsorbed vapor mass as a function of time in these experiments was predicted in the numerical

simulations which employed the kinetics constants established using the experimental data and modeling for setup I. The agreement of the theoretical/numerical predictions with experimental data was good during the entire process of vapor deposition under these realistic conditions, which makes the proposed model a useful tool for description of multiple forensic situations associated with different volatile substances in addition to those studied in the present work.

Preliminary results for non-isothermal cases ascertain the importance of the temperature distribution on the adsorption/desorption rate and the adsorbed mass in general. In such cases, the experimental data obtained by two different methods of the adsorbed mass analysis in setups II and III were in good agreement with each other. These data will facilitate future generalization of the theory for the non-isothermal cases.

CHAPTER 5

DETECTION OF VAPOR RELEASED FROM SUBLIMATING MATERIALS ENCASED IN POROUS MEDIA

(This chapter has been previously published as Zhang, W., Zussman, E., Yarin, A. L. (2018). Detection of vapor released from sublimating materials encased in porous medium. *International Journal of Heat and Mass Transfer*, 118, 1357-1372)

5.1. Introduction

In the present chapter, the experiments with a naphthalene ball located in the original sand, where it sublimates and its vapor is adsorbed and diffuses through the pores toward the free surface where the detection takes place, are described in section 5.2. Similar experiments with a naphthalene ball located in kaolinite (clay) are described in section 5.3. The theoretical description of the process is given in section 5.4, and its comparison with the experimental data is discussed in section 5.5. Experiments with naphthalene sublimation and diffusion in modified sand (coated with polymer or after it underwent another surface treatment) are covered in section 5.6. Conclusions are drawn in section 5.7.

5.2 Experiments with original sand

5.2.1 Materials and experimental setup

The volatile material used in this work is naphthalene, which was purchased from Enoz. Its purity was 99.95%. The 1.9 cm naphthalene balls were used as received. Another volatile material used was camphor balls of 1.9 cm, which were formed from Frontier camphor powder.

Sand purchased from Quikrete was used as a model granular porous medium. It was pre-treated by rinsing in ethanol before being used in the experiments to eliminate impurities. Then, the wet sand was fully dried under 100 °C and sieved with 0.212 mm to 1.4 mm sieves. Such sand, which had not undergone any surface modification, except the elimination of impurities, is termed as the original sand. Kaolinite was purchased from Halaeveryday.

A hotplate was used, and a copper plate of 12"×12"×0.093" in dimensions was located on its surface in order to maintain the uniform surface temperature. A polycarbonate tank (14 cm×13 cm×22.5 cm) to be filled with sand was located on top of it and the tank bottom temperature was sustained at 78 °C (close to the melting temperature of naphthalene which is 80.26 °C) to speed up the experiments. A naphthalene ball was placed at the tank bottom, and after that, the tank was filled with sand. Four different heights of sand filling (or vice versa, four different depths of the naphthalene ball location) were used, namely, h=3.0 cm, 4.5 cm, 5.5 cm, and 7.0 cm. After 1 h, the temperature in the tank reached a steady value and then a 3M transparent film (13 cm×12 cm×0.05 cm) was placed at the free surface of the sand layer to collect naphthalene vapor, which reached the surface. It was found that the naphthalene vapor was deposited on the film in the form of white crystals.

At the beginning of any experiment, there was a relatively long delay time during which no naphthalene deposition on the film was observed at all. Such a delay cannot be attributed to diffusion. Indeed, the diffusion delay would be of the order of h^2/D , where D is the diffusion coefficient of the naphthalene vapor in air. Taking for the estimate $h=7.0$ cm and $D=0.1$ cm²/s, the

diffusion delay would be of about 8 min, whereas the observed delay was about $t_{\text{delay}}=161$ h. Therefore, the observed delay was due to vapor adsorption on sand grains in the bulk. Only after the adsorption process had saturated, vapor could reach the surface, and deposit on the film on the surface in the form of white crystals. Once the crystals started to appear on the film, 10 h of continuous experiment was conducted, in which the crystalline deposit was photographed every 2 h. Due to the insolubility of naphthalene in water, the transparent film was gently washed by D.I. water to remove the attached sand particles before each image was taken. Image J software was used to analyze the crystal images collected over time.

5.2.2 Experiments results

A 1.9 cm naphthalene ball was located in the middle of the tank bottom. In separate experiments the original sand filled the tank up to the heights $h=3.0$ cm, 4.5 cm, 5.5 cm, and 7.0 cm. The corresponding images of the films on the free surfaces of these sand layers recorded at several subsequent time moments for the height $h=3.0$ cm are shown in Figure 5.1. It shows that in the case of $h=3.0$ cm crystals of naphthalene on the film become visible in the middle, i.e. above the source (the naphthalene ball buried in the sand) after a delay $t_{\text{delay}}=12$ h. During the delay time, no deposit was collected at the surface, which means that the entire vapor flux was adsorbed in the sand bulk on the grain surfaces. Only when the adsorption process was fully saturated, vapor could diffuse to the free surface and form the deposit there. The time listed in the caption of Figure 5.1 is reckoned from this delay time. It should be emphasized that the crystal clusters seemingly continued to grow, i.e. the deposit density increased in time.

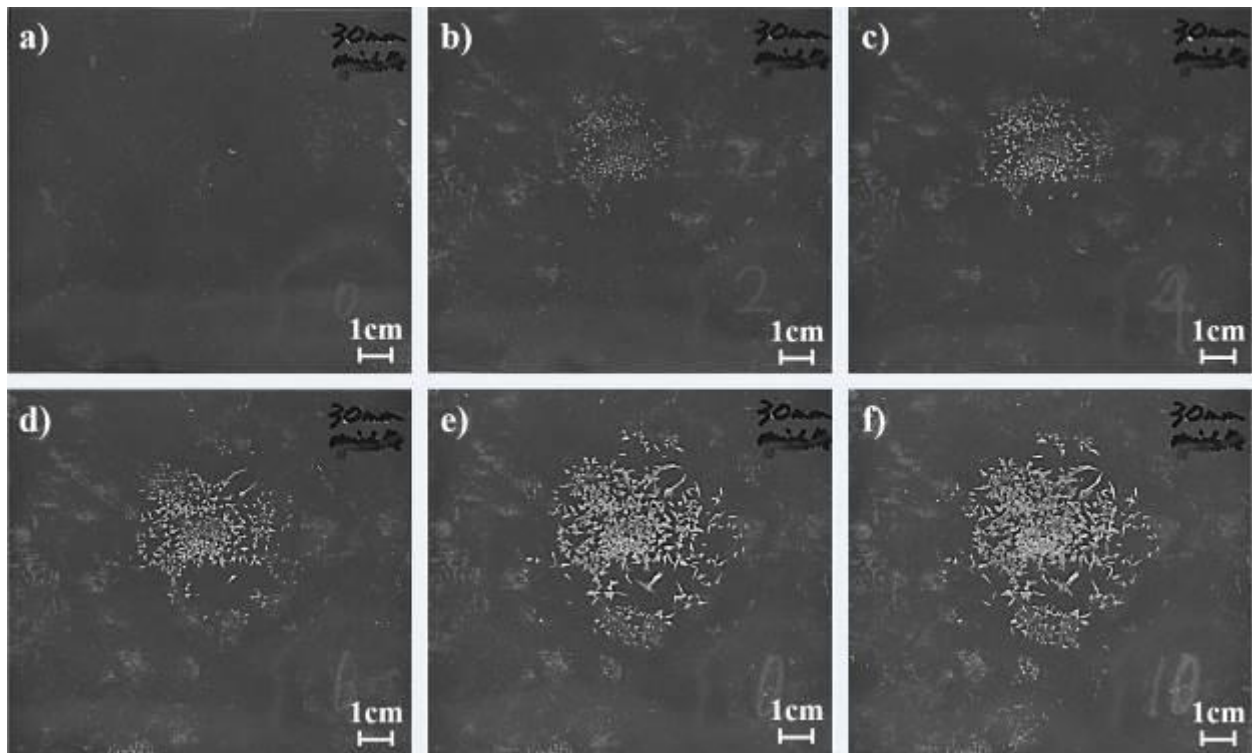


Figure 5.1 Morphology of naphthalene crystal deposits on transparent film at the free surface in the case of a 1.9 cm naphthalene ball buried in the middle under $h=3$ cm of the original sand: (a) at $t=0$, (b) at $t=2$ h, (c) at $t=4$ h, (d) at $t=6$ h, (e) at $t=8$ h, (f) at $t=10$ h. The time is reckoned from the delay time $t_{\text{delay}}=12$ h.

The area occupied by the naphthalene crystal deposits was outlined as shown, for example, in Figure 5.2 and measured by counting the number of pixels inside. The cumulative results for all four heights of sand layer for the entire time of deposit observation (10 h in all the above-mentioned experiments) are shown in Figure 5.3. It is seen that at least in the case of $h=3$ cm the area growth had saturated in 8 h (after the corresponding delay time $t_{\text{delay}}=12$ h). At higher values of h , the area saturation seemingly has not been reached, maybe because the area was not measured accurately enough to distinguish the peripheral fringes.

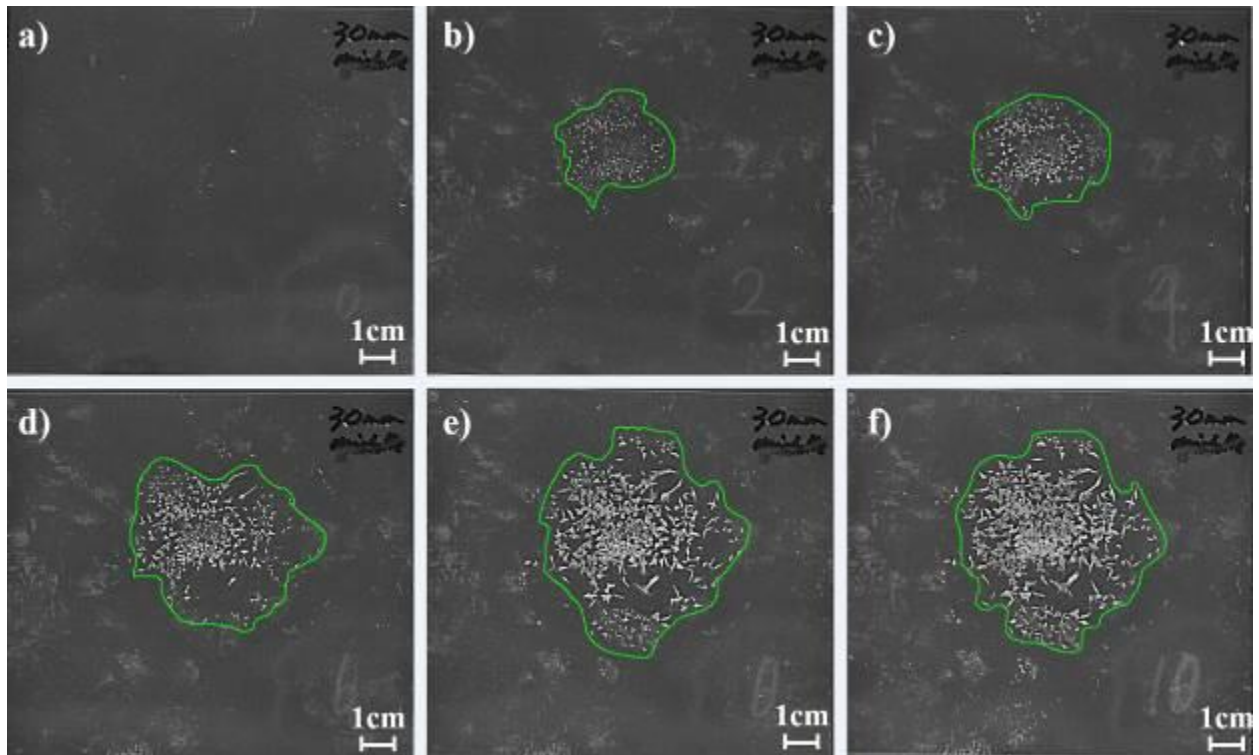


Figure 5.2 Measurement of the deposit surface area using the green outlines. The case of a 1.9 cm naphthalene ball buried in the middle under $h=3$ cm of the original sand: (a) at $t=0$, (b) at $t=2$ h, (c) at $t=4$ h, (d) at $t=6$ h, (e) at $t=8$ h, (f) at $t=10$ h. The time is reckoned from the delay time $t_{\text{delay}}=12$ h.

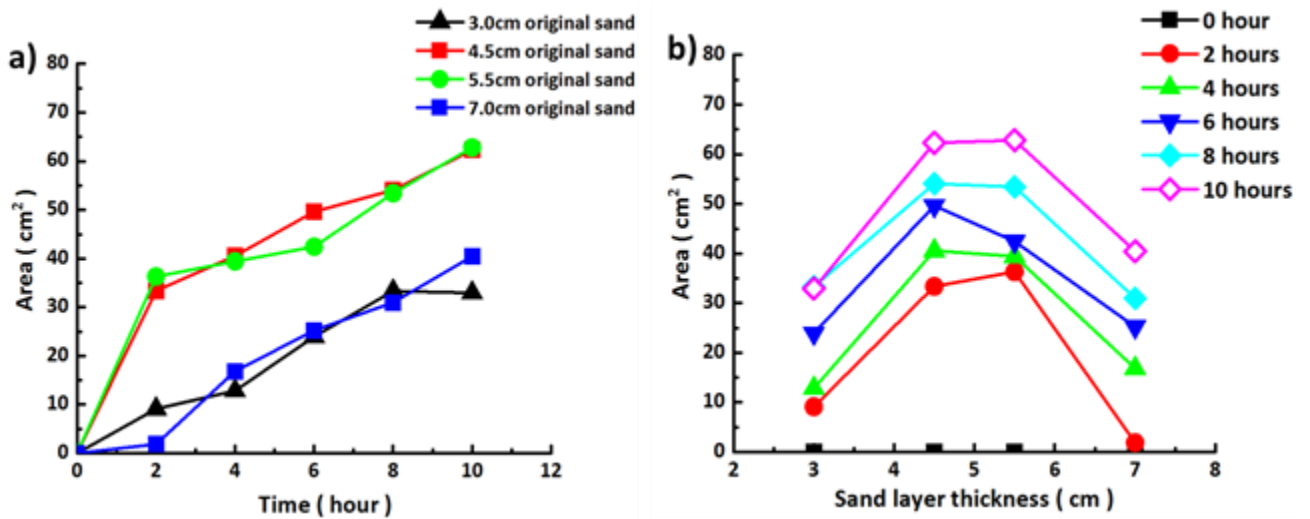


Figure 5.3 The measured deposit area for naphthalene crystal deposition. The case of the original sand, and a 1.9 cm naphthalene ball buried in the middle. (a) The area versus time, with time being reckoned from the delay times. (b) The area versus sand layer thickness. The experimental data is shown by symbols and spanned by lines.

5.2.3 Quantification of the amount of collected crystals

The amount of naphthalene crystalline deposit collected on the film on the free surface of sand layers was quantified via grayscale image intensity. The films with deposited naphthalene crystals were photographed using a DSLR camera with the setting of $f = 7.1$ and $1/5$ exposition time. All images were taken under the same conditions and settings. The intensity values of each pixel in the deposition area of naphthalene crystals were measured by the open software Image J. The area occupied by the deposited crystals varied in time and with the thickness of the sand layer (cf. Figure 5.3).

The original images were converted into 8-bit grayscale images. Then, the intensity values in the deposition area with deposited crystals and at the blank locations on the same film were measured. After that, the histograms of these two pixel intensities were plotted (cf. Figure 5.4). The horizontal axis of the histogram represents the pixel intensity values, which range from 0 to 255, and the vertical axis of the histogram represents the corresponding number of pixels. The image in Figure 5.4a corresponds to Figure 5.2b. At location 1 (cf. Figure 5.4a), where the crystals were observed, the pixel intensity value varies from 18 to 205 (cf. Figure 5.4b), and the mean intensity value is 30.7683 ± 12.0811 . No crystals were formed at location 2 (cf. Figure 5.4a), and the corresponding intensity values range from 22 to 51 (cf. Figure 5.4c), while the mean intensity value is 26.6578 ± 1.5948 . The values measured at location 2 were considered as the background,

which means that the latter pixel intensity values should be withheld from those measured at location 1. Then, the result represents the intensity value of the crystals. This procedure was applied to all experimental images.

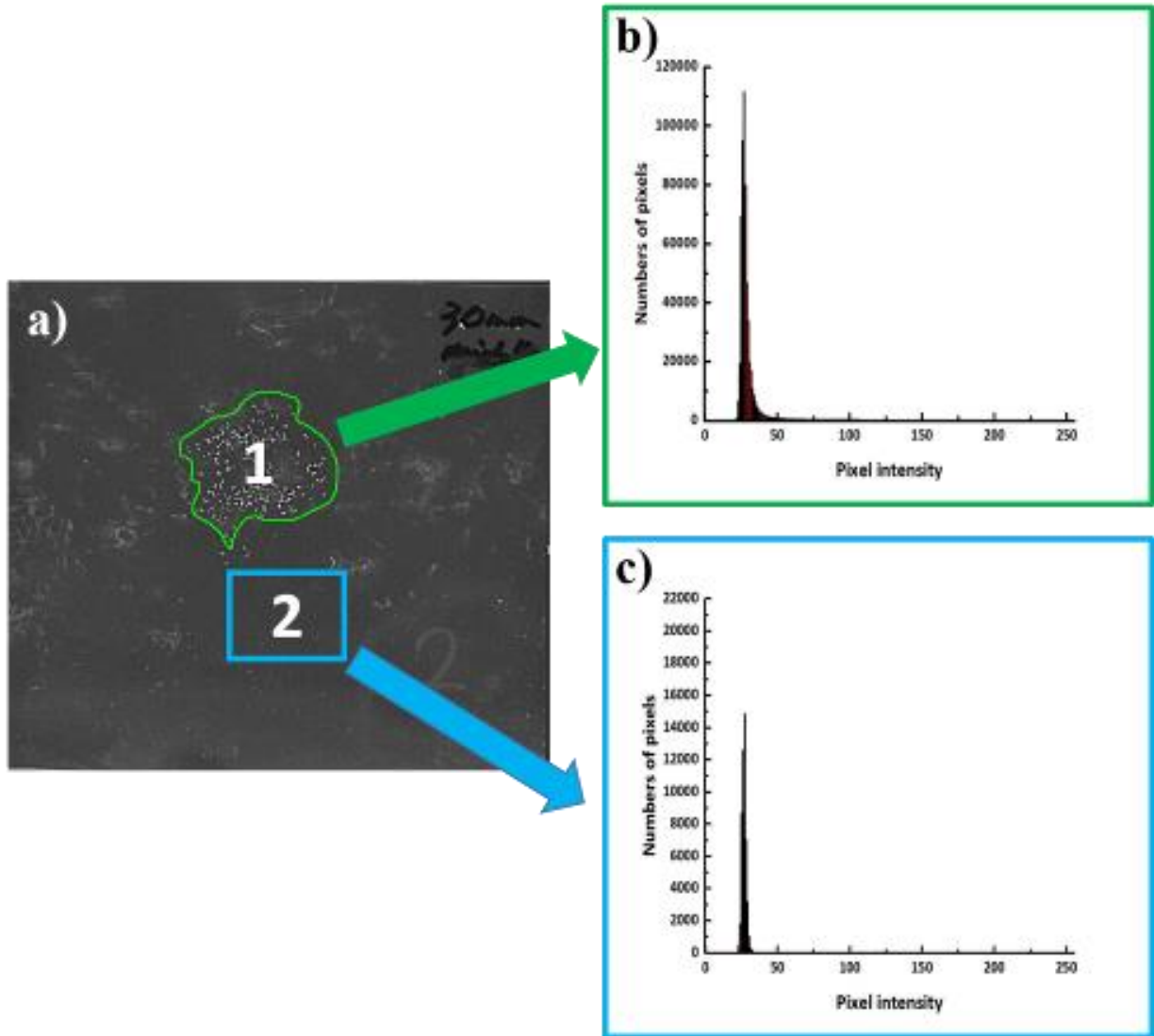


Figure 5.4 Measurement process of pixel values. a) The image corresponds to Figure 5.2b. b) Histogram of pixel intensity versus number of pixels at position 1. c) Histogram of pixel intensity versus number of pixels at position 2.

After measuring all pixel values of the deposited crystals, as described above, the total intensity values were calculated by summing all pixel values, and then divided by the corresponding deposition area to obtain the value of the total pixel intensity per unit deposition area. Thus calculated total pixel intensity per unit area is depicted in Figure 5.5 for different times and sand layer thicknesses.

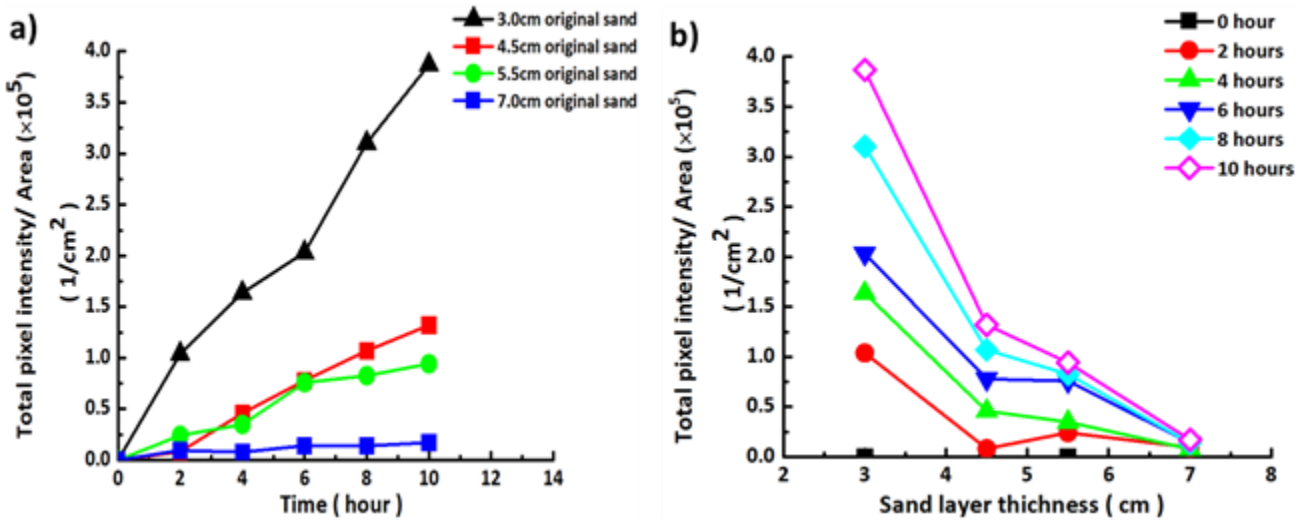


Figure 5.5 Total pixel intensity per unit area covered with naphthalene crystals. A 1.9 cm naphthalene ball was buried in the middle. The experiments with the original sand. (a) Total pixel intensity per unit area versus time, with time being reckoned from the delay times. (b) Total pixel intensity per unit area versus sand layer thicknesses. The experimental data is shown by symbols and spanned by lines.

It should be emphasized that measuring albedo by using photography-based methods is widely used in research and applications. However, this method can result in errors and inaccuracies being applied to quantify vapor deposition. To compare the accuracy of the albedo method and the present image intensity method, an image taken in the experiments was used and

a white paper was applied as the albedo value reference, whose value is 0.95 [Carpenter and Reddi (2012)]. The values of the albedo and the corresponding total image intensity were measured at locations A and B (Figure 5.6), whose areas were 1cm^2 and 0.3 cm^2 , respectively. Note that the ratio of the value of an unknown object albedo to the value of a reference object albedo equals to the ratio of the brightness of the unknown object to the brightness of the reference object, and the brightness of a grayscale image is the average intensity value of all pixels in the image. At location A, the brightness value was measured as 43.507 ± 30.815 , the albedo value was 0.31, and the total image intensity per unit area measured was 6208153 cm^{-2} . At location B, the brightness value was measured as 31.000 ± 24.557 , the albedo value was 0.22, and the total image intensity per unit area measured was 561916 cm^{-2} . It is seen that the albedo values corresponding to locations B and A vary by only 41%, while the intensity values per unit area vary by the factor of 10 (about 1000%). These values show that the albedo method is much less sensitive to the physical changes than the image intensity method used in the present work.

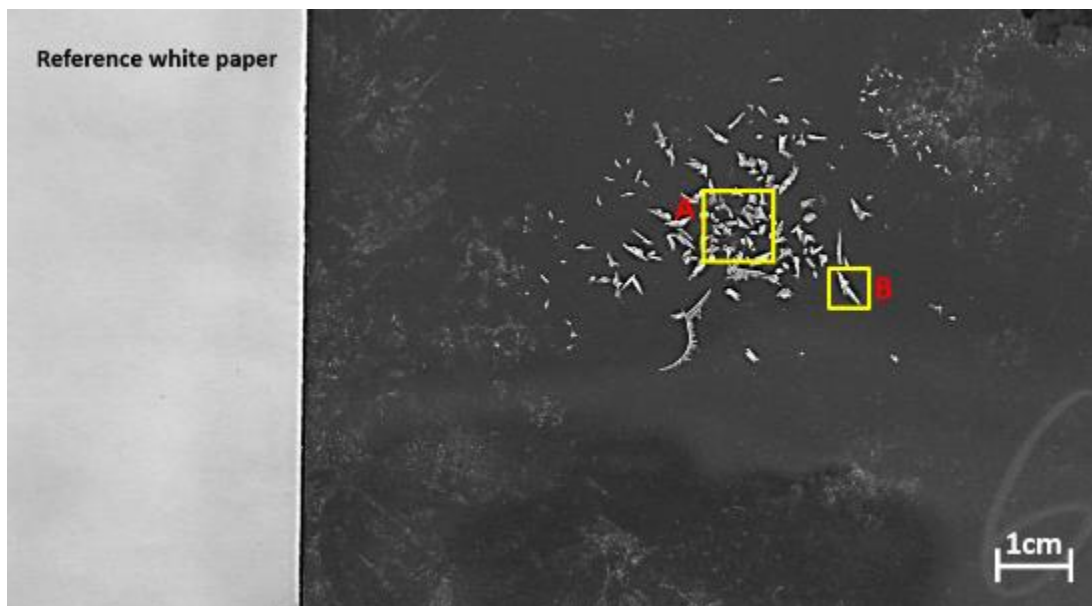


Figure 5.6 Comparison of the albedo method and the image intensity method. Squares indicate

locations A and B used in the measurements.

5.2.4 Correlation of the image intensity with the deposited vapor mass

In this subsection, the correlation of the deposited vapor mass with the image intensity is established. For this goal, nine naphthalene balls of the same diameter of 1.9 cm were placed in nine separate beakers. Then, layers of $h=2.0$ cm thickness of sand were filled up in the beaker, and the bottom temperature of the beakers was sustained at 78°C (below the melting temperature of naphthalene of 80.26°C) to speed up the experiments. Nine transparent films, which were the same as in the previously described experiments, were placed on top of sand to collect the naphthalene crystals formed by the deposited vapor. The film weights were measured at 1 h, 1.5 h, 2 h, and 2.5 h. The pure film weight was withheld from the measured values to find the weight of the deposited vapor as a function of time. Simultaneously, the total pixel intensity and deposition area were measured, as described in subsections 5.2.2 and 5.2.3. The mass of these crystals was linked to the total pixel intensity, as shown in Figure 5.7. The linear fit of the measured deposited mass m to the total intensity is given by the function $m = 6.61 \times 10^{-10} I_t + 0.0005$, and the standard deviations of the slope and intercept are 1.18×10^{-10} and 0.0001, respectively. The free term in this correlation is negligibly small and the correlation reduces to

$$m = 6.61 \times 10^{-10} I_t \quad (5.1)$$

which was used in the data processing, where m is the vapor mass in g and I_t is the total pixel intensity values.

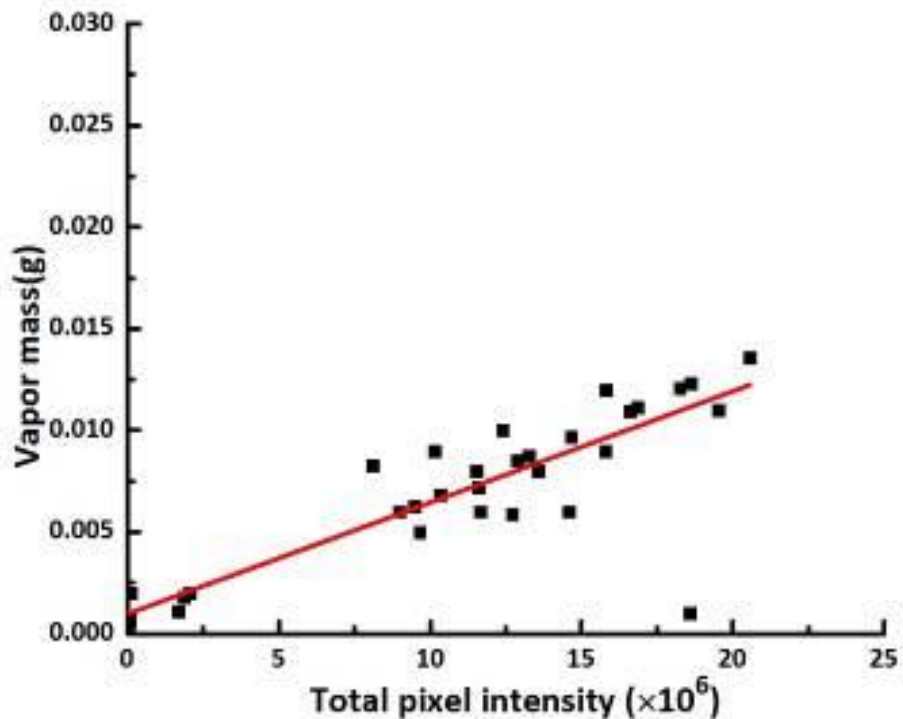


Figure 5.7 Deposited vapor mass versus the total intensity. The red line is the linear fit.

In addition to the experiments with naphthalene balls located at the bottom center, data was collected in the cases where the vapor source was located under the original sand off-center. These data are not discussed here for the sake of brevity.

5.3 Experiments with kaolinite

Kaolinite is an earthy, very soft white clay mineral. SEM images reveal that this clay has a plate-like structure (Figure 5.8). Air and moisture could occupy the pores between kaolinite plates. When kaolinite has been dried, only air would be contained in the pores and the mass M of a certain volume of kaolinite would be

$$M = V_{\text{pore}}\rho_{\text{air}} + V_{\text{clay}}\rho_{\text{clay}} \quad (5.2)$$

where V_{pore} is the volume of pores, V_{clay} is the volume of kaolinite plates, ρ_{air} is the air density and ρ_{clay} is the kaolinite density.

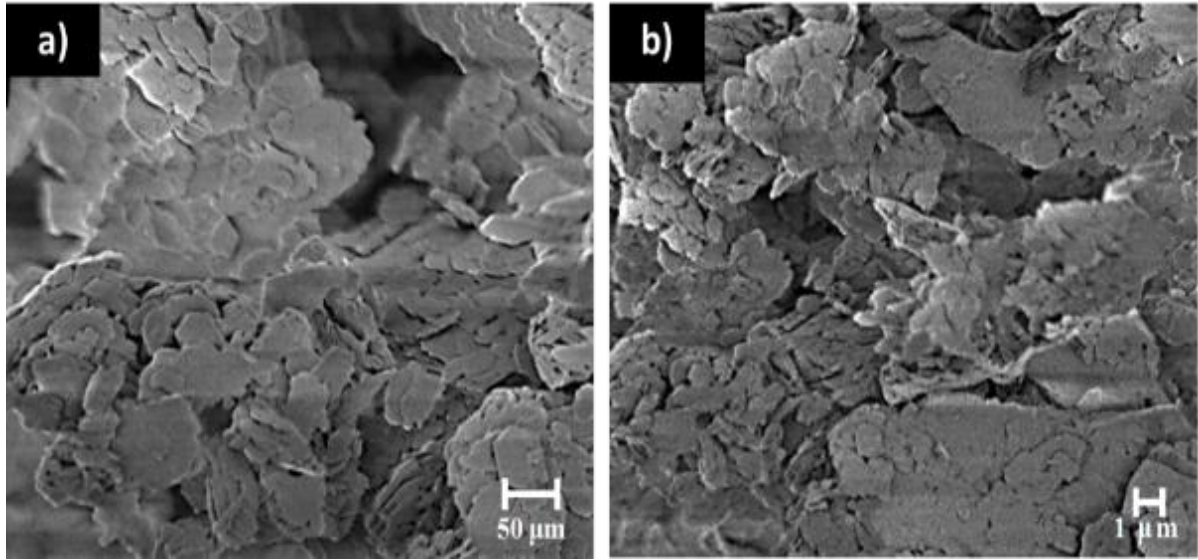


Figure 5.8 SEM images of plate-like structure of kaolinite.

In this section, four compacted kaolinite clay layers of thicknesses $h=3.0$ cm, 4.5 cm, 5.5 cm, and 7.0 cm were employed. The porosity of a sample of tightly compacted kaolinite was found as 40.3% . Thus, to maintain the same porosity for four different kaolinite samples (of different thicknesses) used in the experiments, dried kaolinite mass was chosen according to Eq. (5.2). The clay was dried under $100\text{ }^{\circ}\text{C}$ for 2 h. In the experiments, 397.3 g of clay was used in the $h=3.0$ cm case, 596.0 g of clay was used in the $h=4.5$ cm case, 728.5 g of clay was used in the $h=5.5$ cm case and 927.1 g of clay was used in the $h=7.0$ cm case. The 1.9 cm naphthalene balls were buried in the middle of the tank bottom, and transparent films described in section 5.2 were used to collect naphthalene depositions at the free surface of clay layers. After naphthalene crystals were first

detected on the film, experiments up to 6 h -long were conducted to collect naphthalene crystals. Morphologies of the crystals at different time moments during the experiment with the kaolinite clay layer of $h=3.0$ cm are shown in Figure 5.9.

The amount of crystals found in the experiments with kaolinite was larger than the amount in the corresponding experiments with the original sand in section 5.2, and also the time t_{delay} increased. On the other hand, the naphthalene crystal size in the experiments with kaolinite was smaller compared to the experiments with the original sand in section 5.2.

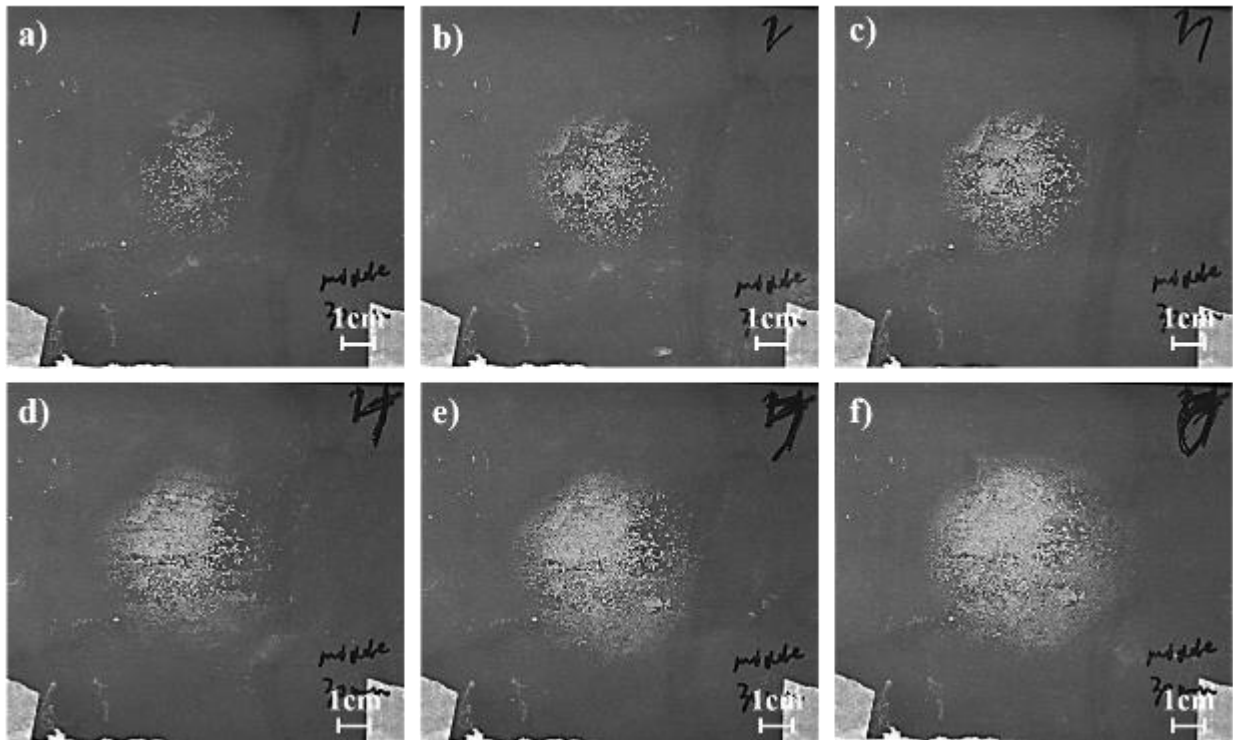


Figure 5.9 Morphology of naphthalene crystal deposits on transparent film at the free surface in the case of a 1.9 cm naphthalene ball buried in the middle under $h=3.0$ cm of kaolinite: (a) at $t=1$ h, (b) at $t=2$ h, (c) at $t=3$ h, (d) at $t=4$ h, (e) at $t=5$ h, (f) at $t=6$ h. The time is reckoned from the delay time $t_{\text{delay}}= 19$ h.

The area of the film with deposited crystals in the case of kaolinite porous medium obtained in 6 h reckoned after the delay time is shown in Figure 5.10. The largest area values obtained at $t=6$ h in the cases of $h=3.0$ cm and 7.0 cm in the experiments with kaolinite are larger than those at $t=8$ h and 10 h in the cases of $h=3.0$ cm in 7.0 cm, respectively, in the experiments with the original sand. However, the largest values obtained in the cases of $h=4.5$ cm and 5.5 cm in the experiments with the original sand at $t=10$ h are larger than those obtained in the corresponding experiments with kaolinite.

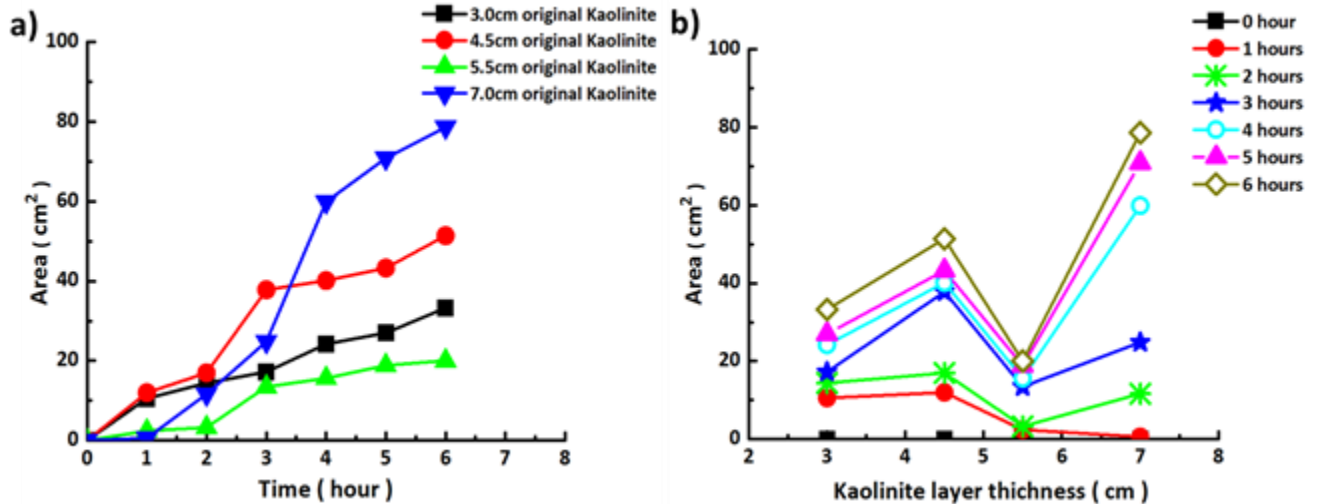


Figure 5.10 The measured area of the naphthalene crystal deposition. The case of the kaolinite porous medium, and a 1.9 cm naphthalene ball buried in the middle of the tank bottom. (a) The area versus time, with time being reckoned from the delay times. (b) The area versus the kaolinite layer thickness. The experimental data is shown by symbols and spanned by lines.

The values of the total intensity per unit area with the deposited crystals in four cases in the experiments with kaolinite are shown in Figure 5.11. The values obtained in each case of the

layer thickness and each time moment in the experiments with kaolinite are larger than the corresponding values in the experiments with the original sand (cf. Figures 5.5 and 5.11).

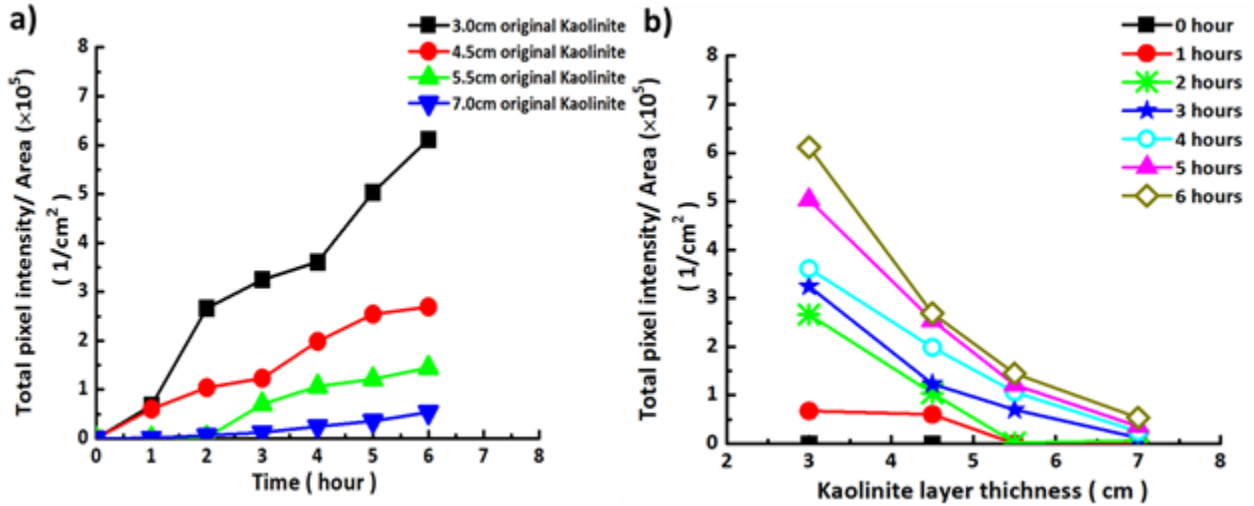


Figure 5.11 Total pixel intensity per unit area covered with naphthalene crystals. A 1.9 cm naphthalene ball was buried in the middle of the tank bottom. The experiments with the kaolinite layers. (a) Total pixel intensity per unit area versus time, with time being reckoned from the delay times. (b) Total pixel intensity per unit area versus the kaolinite layer thickness. The experimental data is shown by symbols and spanned by lines.

5.4 Theoretical

Assume that the adsorption/desorption of vapor on porous medium grains has already saturated, and the vapor transport in the pores is determined only by pure diffusion. In steady-state the diffusion equation reads

$$\frac{1}{r} \frac{\partial}{\partial r} \left(r \frac{\partial c}{\partial r} \right) + \frac{\partial^2 c}{\partial z^2} = 0 \quad (5.3)$$

where c is vapor concentration, r is the radial coordinate, z is the vertical coordinate, and we assume an axially-symmetric process corresponding to a source buried in a porous medium in the middle of the tank bottom.

Assume that a round vapor source of radius a is located at $z=0$ (at the bottom) with the center at $r=0$ (in the middle of the bottom). Over the source, the vapor concentration is known as $f(r)$, which corresponds to sublimation, where c_w is the saturated sublimation concentration. Then, the boundary conditions for Eq. (5.3) read

$$c|_{z=0} = f(r), \quad \text{e.g.} \quad f(r) = \begin{cases} c_w & \text{at } r < a \\ 0 & \text{at } r > a \end{cases} \quad (5.4)$$

$$c|_{r \rightarrow 0} < \infty \quad (5.5)$$

$$c|_{r \rightarrow \infty, z \rightarrow \infty} < \infty \quad (5.6)$$

Here we imply that the porous medium extends to infinity in the radial and vertical direction, which forms a singular problem. The assumption that the medium extends to infinity is justified by the fact that the source (naphthalene ball) size is sufficiently smaller than the tank size ($2a=1.9$ cm versus 13 cm). The assumption that the medium extends to infinity formally holds when the layer thickness h is much larger than the source size, which is better fulfilled with $h=7$ cm. However, the comparison of the theory with the experimental data discussed below shows that this approximation still works when h approaches $2a$.

The solution of this singular problem possesses a continuous eigenvalue spectrum v and is found using the variable of separation method as

$$c = \int_0^{\infty} M_v e^{-vz} J_0(vr) dv \quad (5.7)$$

where $J_0(\bullet)$ is the Bessel function of the first kind of zero order. The Eq. (5.7) already satisfies Eq. (5.3) and the boundary conditions (5.5) and (5.6). The coefficient M_v is found using the boundary condition, Eq. (5.4)

$$c|_{z=0} = f(r) = \int_0^\infty M_v J_0(vr) dv \quad (5.8)$$

This yields

$$M_v = v \int_0^\infty f(\rho) \rho J_0(v\rho) d\rho \quad (5.9)$$

where ρ is a dummy variable.

In particular, using the function $f(r)$ from Eq. (5.4), and combining Eqs. (5.7) and (5.9), we arrive at

$$c = c_w \int_0^\infty e^{-vz} v J_0(vr) \int_0^a \rho J_0(v\rho) d\rho dv \quad (5.10)$$

The inner integral in Eq. (5.10) is easily evaluated, and Eq. (5.10) yields the following solution of the problem

$$c = c_w a \int_0^\infty e^{-vz} J_0(vr) J_1(va) dv \quad (5.11)$$

At the axis of the vapor 'jet' rising by diffusion, i.e. at $r=0$, the integral in Eq. (5.11) can be evaluated analytically, which yields vapor distribution over the vertical axis z as

$$c|_{r=0} = c_w \left[1 - \frac{z}{\sqrt{z^2 + a^2}} \right] \quad (5.12)$$

Accordingly, the vapor flux along the axis is found as

$$-D \frac{\partial c}{\partial z} \Big|_{r=0} = \frac{D c_w a^2}{(z^2 + a^2)^{3/2}} \quad (5.13)$$

where D is the diffusion coefficient.

Therefore, at a distance z from the source, at a small central area S during time t the following mass m is expected to be deposited on an inserted (or an overlying) film

$$m = \frac{Dc_w a^2 St}{(z^2 + a^2)^{3/2}} \quad (5.14)$$

This prediction is compared below with the experimental data for the deposit masses collected on the overlying films at different distances z from the sublimating vapor source.

Note that the empirical Antoine equation,

$$\log_{10} p = A - \frac{B}{T + C} \quad (5.15)$$

is used to evaluate the saturated pressure of naphthalene. Here p is pressure in mm Hg, T is the temperature in $^{\circ}\text{C}$, and A , B , and C are the material-specific constants. Using the physical parameters from references [Weast et al. (1988); Yaws (2015)], in particular, $A = 6.89116$, $B = 1551.4785$, and $C = 168.879$, one can evaluate that saturated sublimation pressure of naphthalene at 78°C is $p = 4.2869$ mm Hg, which equals to 571.5396 Pa. Applying the ideal gas law, the saturated sublimation concentration of naphthalene in the air at 78°C is evaluated as $c_w = 2.5 \times 10^{-5}$ g/cm³.

The diffusion coefficient of naphthalene vapor in open air D_0 in cm²/s at 101.325 kPa is given by the following formula [Goldstein and Cho (1995)]

$$D_0 = 0.0681 \left(\frac{T}{298.16} \right)^{1.93} \left(\frac{1.013 \times 10^5}{p_{\text{atm}}} \right) \quad (5.16)$$

where T is temperature in $^{\circ}\text{K}$. The corresponding diffusion coefficient in porous medium D in cm²/s could be calculated as [Davidson and Trumbore (1995)]

$$D = D_0 \varepsilon^{4/3} \quad (5.17)$$

where ε is the porosity of a dried porous medium. Hence, the diffusion coefficient of naphthalene vapor in the dried sand with porosity $\varepsilon=0.191$ (19.1%) filled with air at 352.15 °K (78 °C) is 0.0104 cm² / s , and in kaolinite layer with porosity $\varepsilon = 0.403$ (40.3%) filled with air at 352.15 °K (78 °C) is 0.0279 cm² / s .

5.5 Comparison of the theory with experimental data

In terms of the deposited vapor mass, determined by Eq. (5.1), the experimental data from Figure 5.5 for the original sand layers is shown in Figures 5.12 and 5.13 in comparison with the theoretical predictions given by Eqs. (5.14)- (5.17). The agreement is reasonable for all the sand layer thicknesses and time moments.

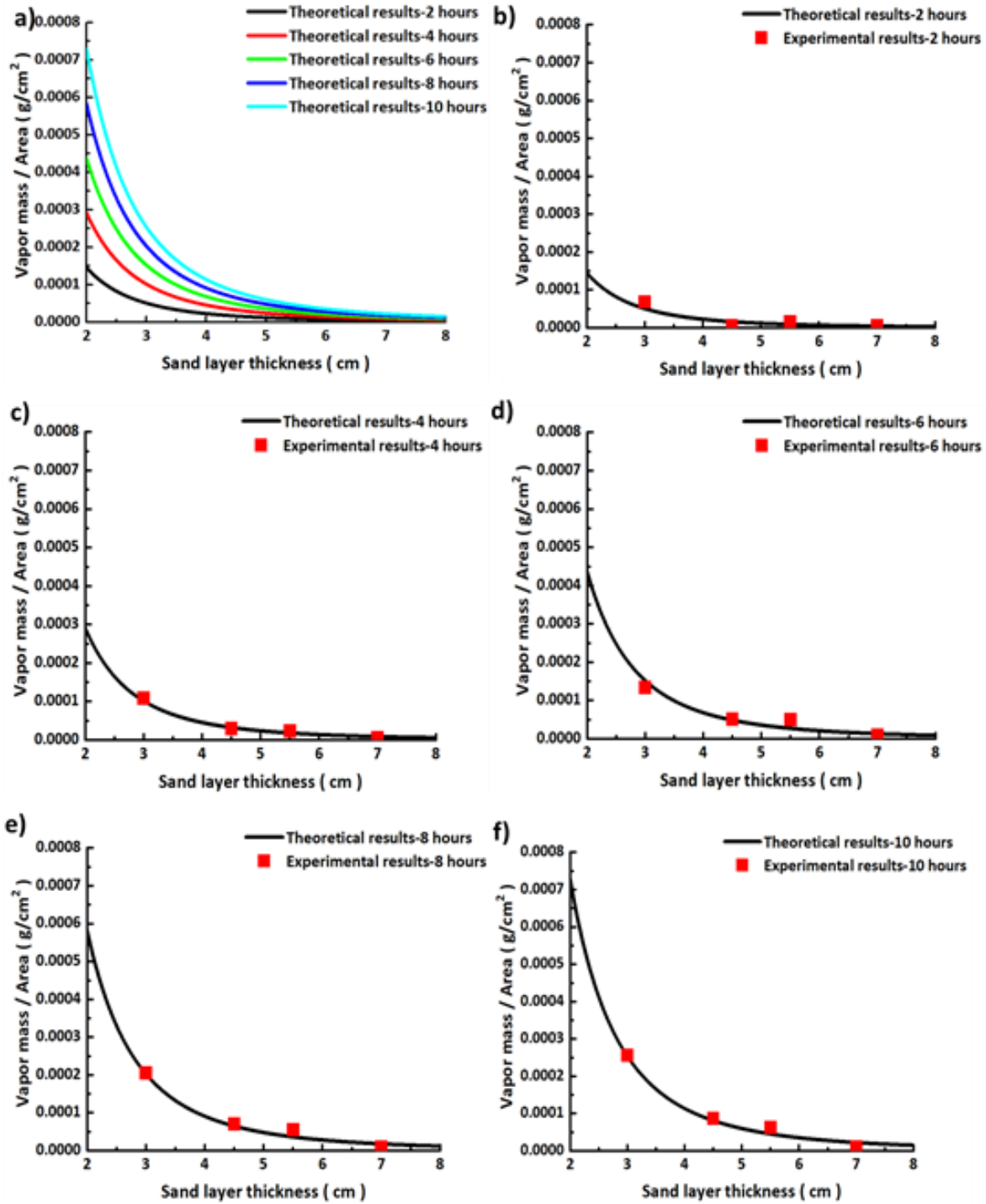


Figure 5.12 Naphthalene vapor mass per unit area versus the original sand layer thickness at different time moments after the adsorption/desorption process has been saturated, and vapor transport is fully determined by diffusion. (a) Theoretical results at different time moments listed

in the panel. The deposited mass distribution versus the sand layer thickness. In the following five panels the theoretical results are shown separately by lines, while the corresponding experimental data - by symbols. (b) $t = 2$ h. (c) $t = 4$ h. (d) $t = 6$ h. (e) $t = 8$ h. (f) $t = 10$ h.

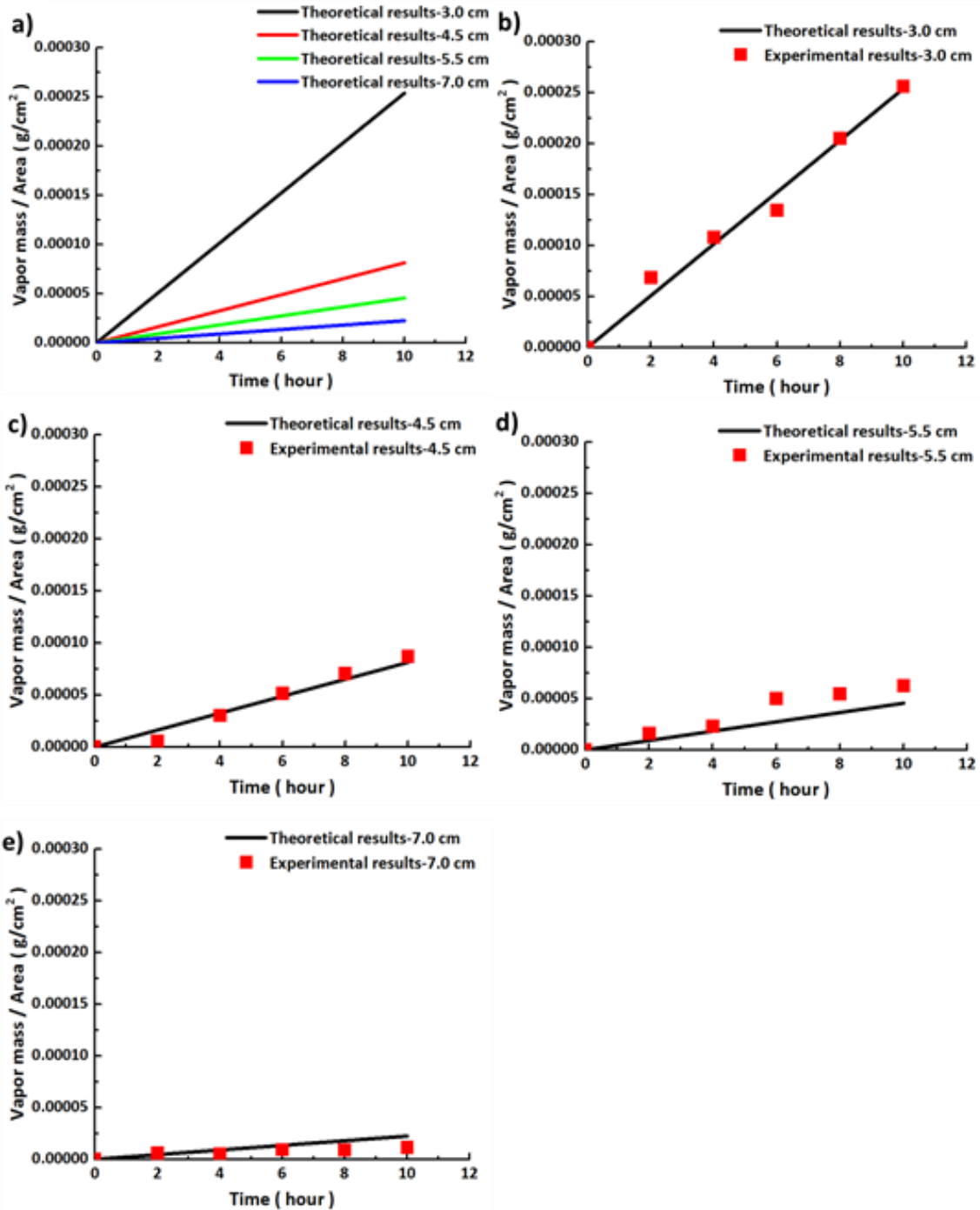


Figure 5.13 Naphthalene vapor mass per unit area versus time after the adsorption/desorption process has been saturated, and vapor transport is fully determined by diffusion at different thicknesses of the original sand layers. (a) Theoretical results at different sand layer thicknesses listed in the panel. In the following four panels the theoretical results are shown separately by lines, while the corresponding experimental data - by symbols. (b) Sand layer thickness of 3.0 cm. (c) Sand layer thickness of 4.5 cm. (d) Sand layer thickness of 5.5 cm. (e) Sand layer thickness of 7.0 cm.

The experimental data from Figure 5.11 for the kaolinite layers is shown in Figure 5.14 and Figure 5.15 in comparison with the theoretical predictions given by Eqs. (5.14)- (5.17). The agreement is reasonable for all the kaolinite layer thicknesses and time moments.

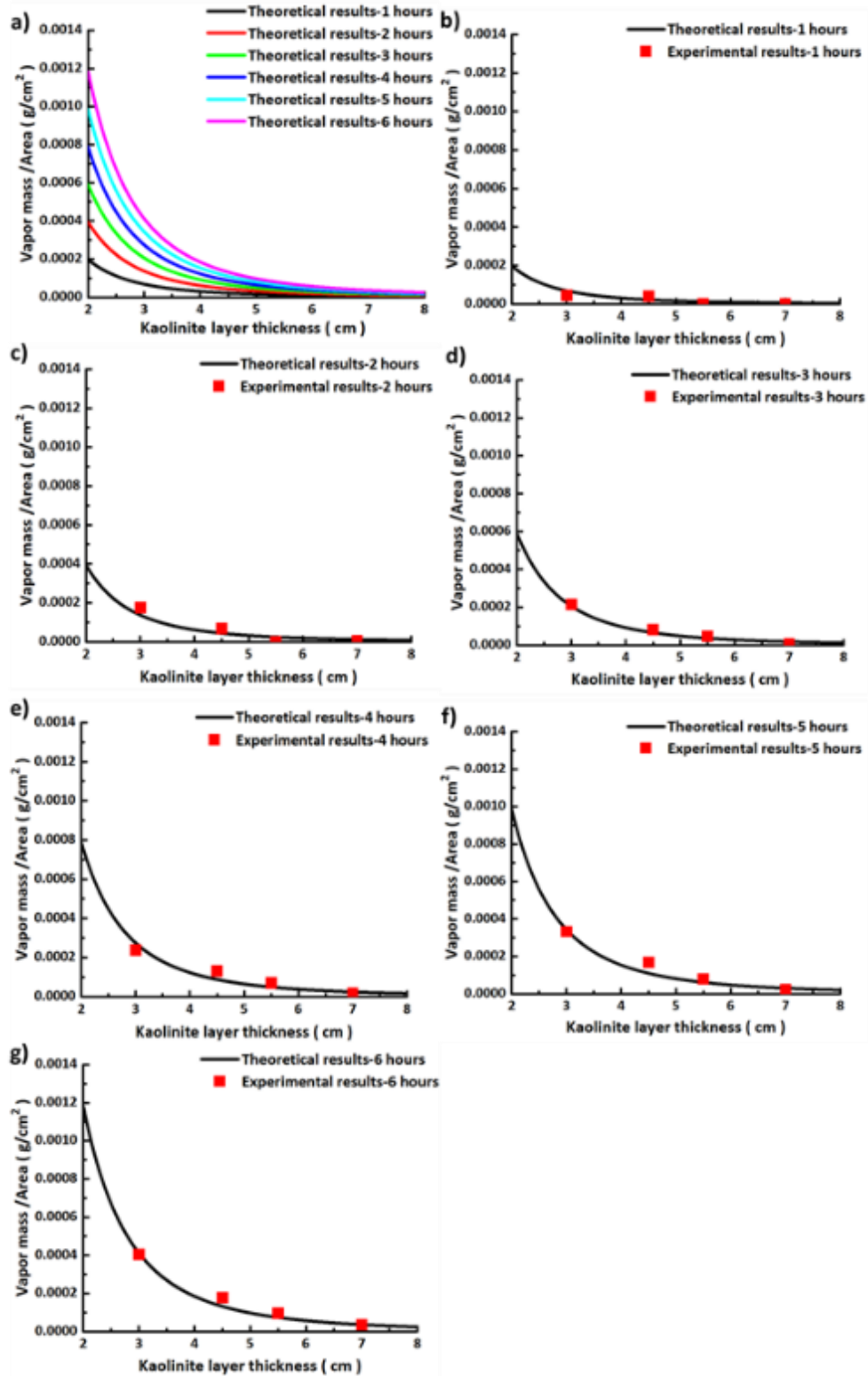


Figure 5.14 Naphthalene vapor mass per unit area versus the kaolinite layer thickness at different time moments after the adsorption/desorption process has been saturated, and vapor transport is

fully determined by diffusion. (a) Theoretical results at different time moments listed in the panel. The distribution of the deposited mass per unit area versus kaolinite layer thickness. In the following six panels the theoretical results are shown separately by lines, while the corresponding experimental data - by symbols. (b) $t = 1$ h. (c) $t = 2$ h. (d) $t = 3$ h. (e) $t = 4$ h. (f) $t = 5$ h. (g) $t = 6$ h.

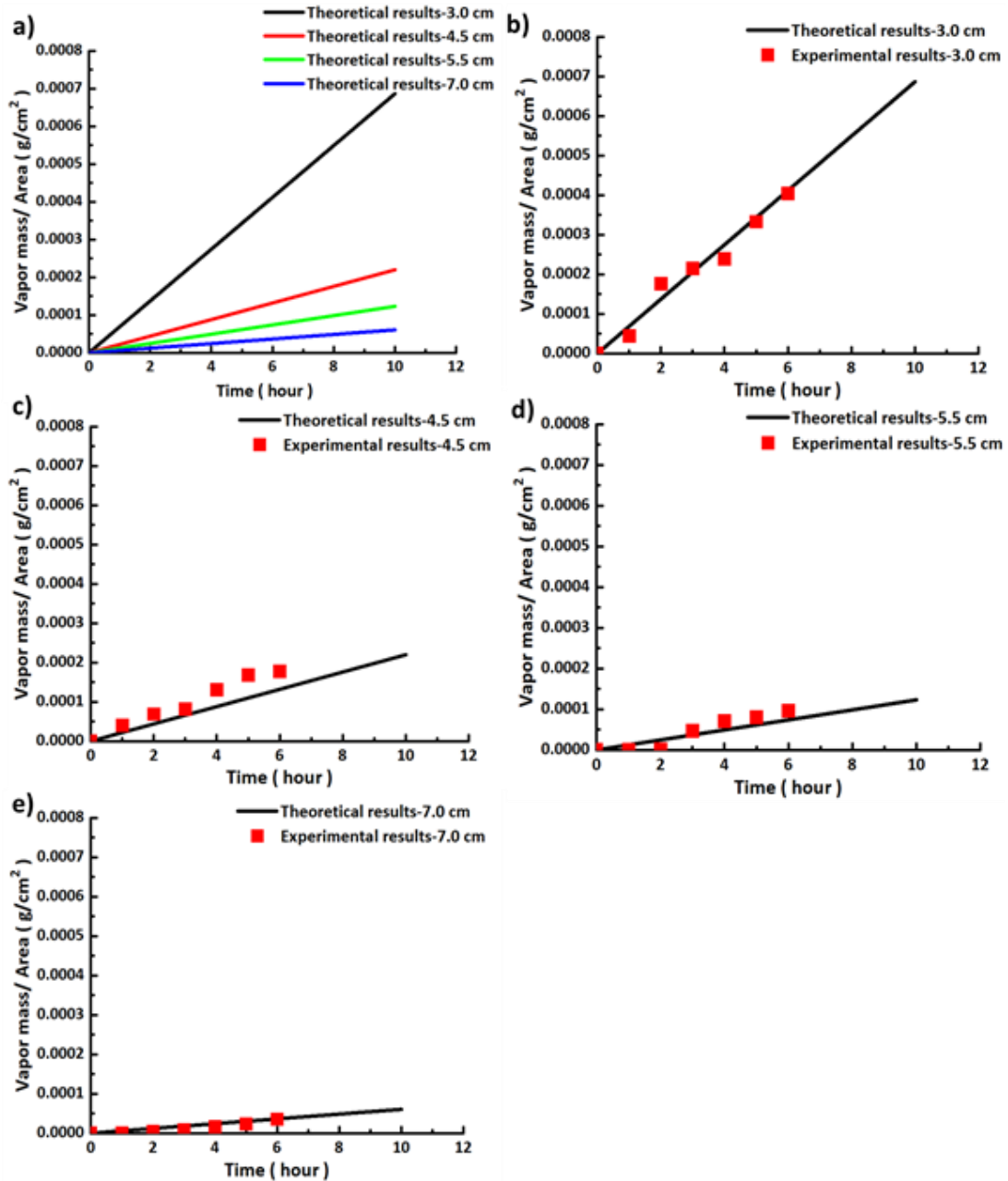


Figure 5.15 Naphthalene vapor mass per unit area versus time after the adsorption/desorption

process has been saturated, and vapor transport is fully determined by diffusion at different thicknesses of the kaolinite layers. (a) Theoretical results at different kaolinite layer thicknesses listed in the panel. In the following four panels the theoretical results are shown separately by lines, while the corresponding experimental data - by symbols. (b) Kaolinite layer thickness of 3.0 cm. (c) Kaolinite layer thickness of 4.5 cm. (d) Kaolinite layer thickness of 5.5 cm. (e) Kaolinite layer thickness of 7.0 cm.

It should be emphasized that Figures 5.12 and 5.13 show the mass of naphthalene vapor released from sand layer deposited on transparent film covering the beakers per unit area. No saturation has been reached in any of these cases and currently there is no available information (either theoretical or experimental), which can allow one to evaluate the maximum possible mass collected on transparent film if the naphthalene ball would last forever.

5.6 Experiments with sand with coated grains

In this section vapor transport is studied using sand with coated grains, i.e. modified in comparison with the original sand studied in sections 5.2 and 5.5. Four different kinds of coated sand are used: sand with grains coated by naphthalene molecules, sand with grains coated by camphor molecules, sand after silanization process (hydrophobic) and sand with grains coated by a polymer. Only the latter case (polymer coating) is discussed in detail here, whereas the cases of sand with grains coated by naphthalene molecules, sand with grains coated by camphor molecules, and sand after silanization process are omitted from the discussion for the sake of brevity.

Polyacrylonitrile (PAN, (molecular weight 150 kDa) is a synthetic, semi-crystalline organic polymer. Evaporating a droplet of 5 wt% PAN dissolved in N,N-dimethylformamide (DMF) at

room temperature for a long enough time on a glass slide on a shaker, a very thin transparent film could be formed (Figure 5.16). Also, being dipped into PAN solution and dried, the original sand grains stayed apart and were wrapped by a thin polymer film. This film covered the fractal-like structures on the sand grains and made them much smoother (see SEM images in Figure 5.17), thus reducing the number of potential adhesion sites at the sand grain surface.



Figure 5.16 Transparent film formed after evaporating 0.1 g droplet of 5 wt% PAN solution in DMF.

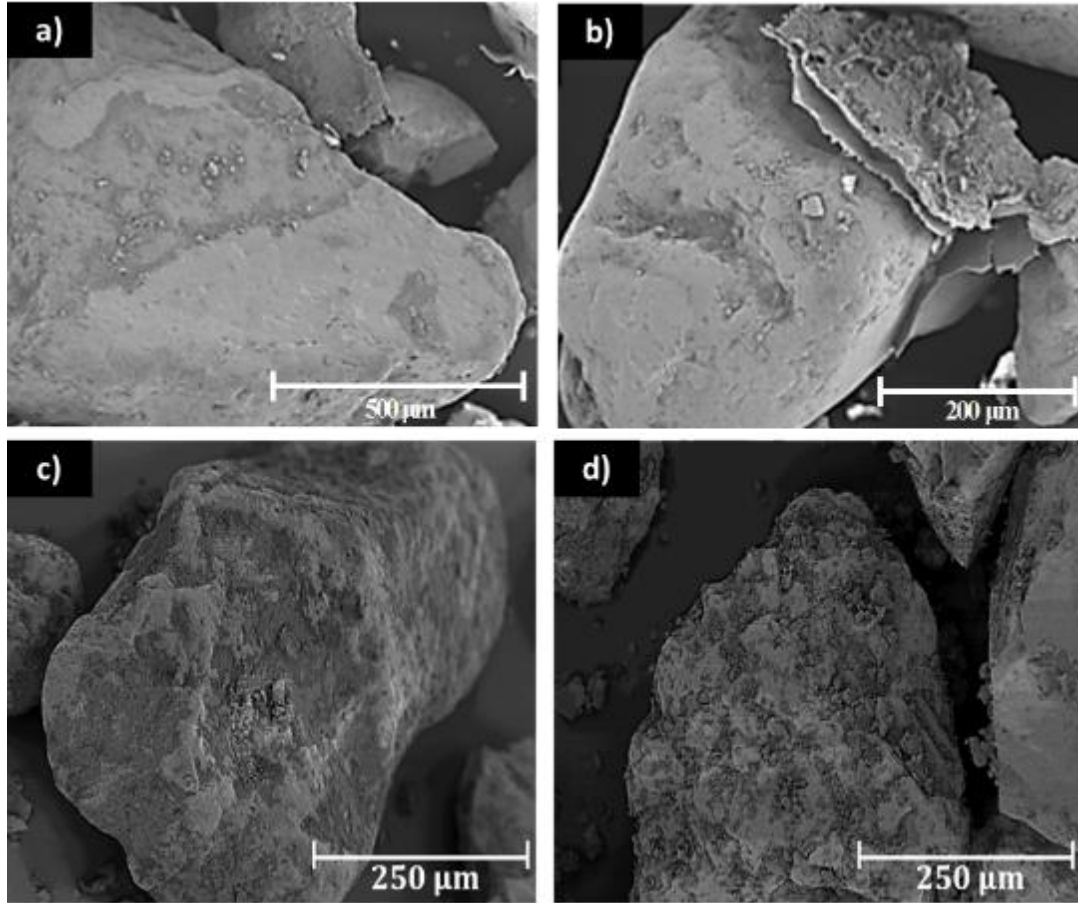


Figure 5.17 (a) and (b) SEM images of sand grains after they were dipped into 5 wt% PAN solution and dried. The grains are covered by a thin PAN layer and are smoother than the original sand grains in panels (c) and (d).

The polymer-coated sand was prepared using the pretreated original sand, which was dipped into 5 wt% PAN solution, fully dried, gently crushed and sieved. Both PAN and DMF were purchased from Sigma- Aldrich. The sieve opening selected was in the 0.212 mm to 1.4 mm range. Note that no DMF was left in the sand coating after drying. The average thickness of PAN coating on sand particles was approximately $\ell = 10 \mu\text{m}$.

Four PAN-coated sand layers with thicknesses of $h=3.0$ cm, 4.5 cm, 5.5 cm, and 7.0 cm were used in the present experiments. A 1.9 cm naphthalene ball was used as a vapor source which was buried in the middle of the tank bottom. In the case of $h=3.0$ cm naphthalene crystals could be observed in 1.5 h; in the case of $h=4.5$ cm, naphthalene crystals could be observed in 2.5 h; in the case of $h=5.5$ cm naphthalene crystals could be observed in 3 h; in the case of $h=7.0$ cm naphthalene crystals could be observed in 4 h. The observed morphologies of crystals in the case of the $h=4$ cm layer at different times are shown in Figure 5.18.

In these four experiments, the film areas occupied by the deposited crystal increase as time increases. The size of the clusters formed in the experiments with the PAN-coated sand is larger than those observed in the corresponding experiments with the hydrophobic sand. However, the number of crystals deposited in experiments with the PAN-coated sand is less than in the corresponding experiments with the original sand (cf. section 5.2).

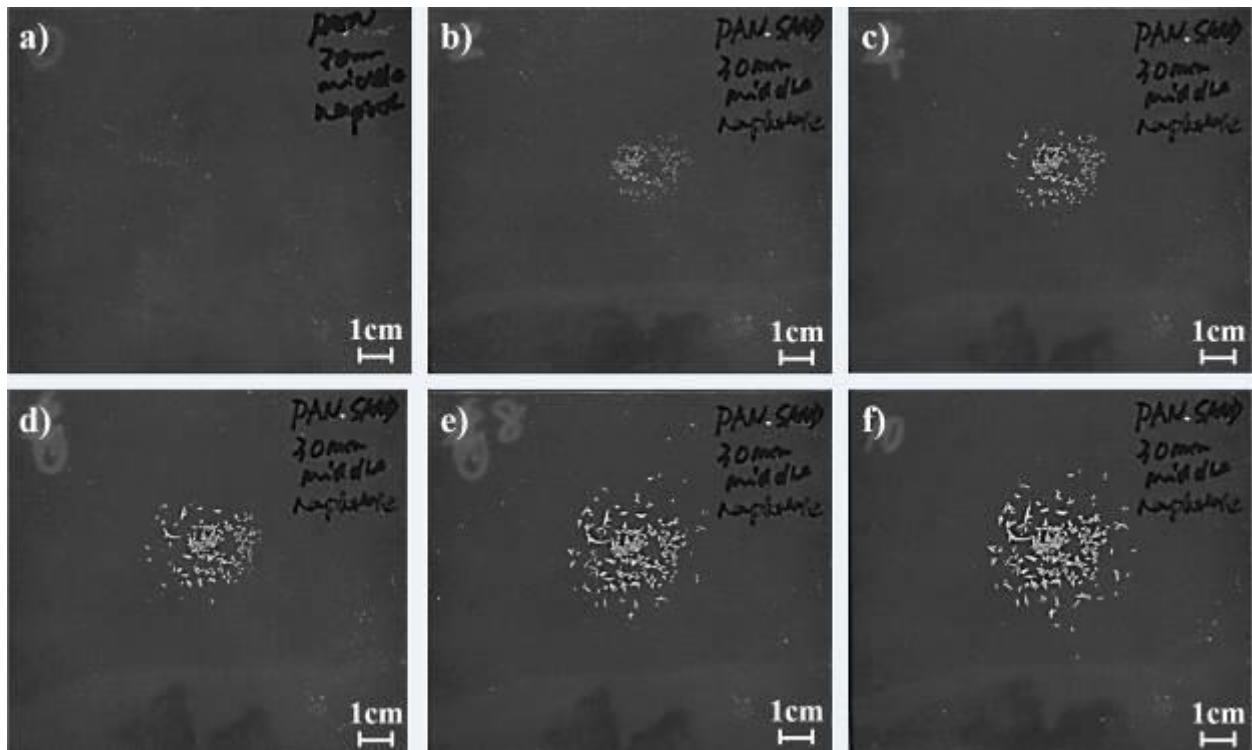


Figure 5.18 Morphology of naphthalene crystal deposits on transparent film at the free surface in the case of a 1.9 cm naphthalene ball buried in the middle of the tank bottom under $h=3.0$ cm of the PAN-coated sand: (a) at $t=0$, (b) at $t=2$ h, (c) at $t=4$ h, (d) at $t=6$ h, (e) at $t=8$ h, (f) at $t=10$ h. The time is reckoned from the delay time $t_{\text{delay}}=1.5$ h.

The area of the film with the deposited crystals in the case of the PAN-coated sand obtained within 10 h reckoned after the delay times is shown in Figure 5.19. The area values measured in the case of the PAN-coated sand were the largest among the three types of sand explored in this work (including the original sand and the hydrophobic sand, cf. section 5.2).

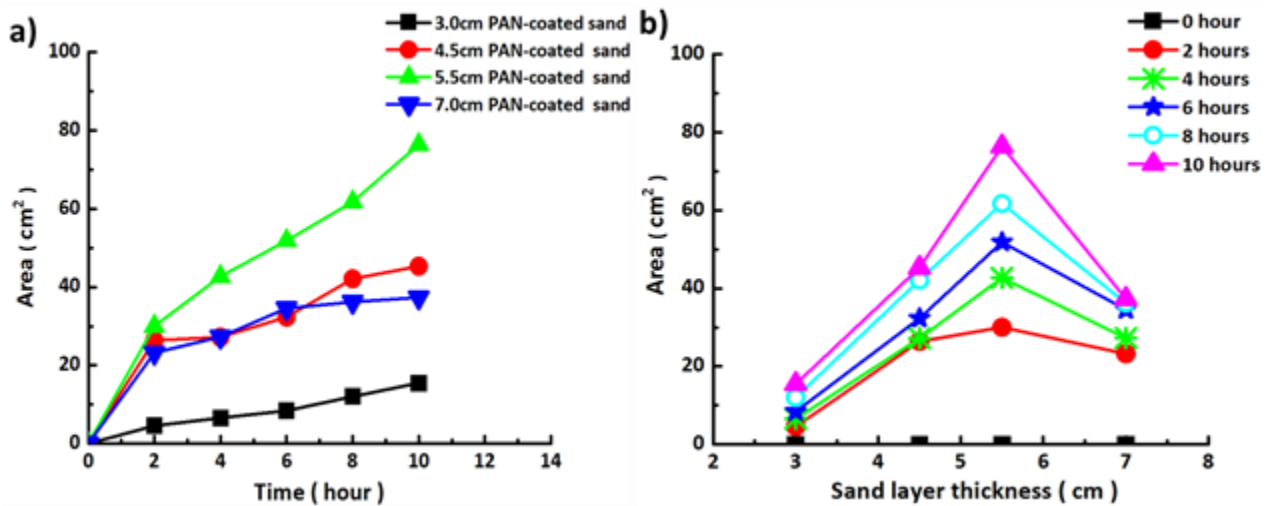


Figure 5.19 The measured deposit area of the naphthalene crystals deposition. The case of the PAN-coated sand, and the naphthalene ball buried in the middle of the tank bottom. (a) The area versus time, with time being reckoned from the delay times. (b) The area versus the thickness of the PAN-coated sand layers. The experimental data is shown by symbols and spanned by lines.

The values of the total pixel intensity per unit area covered with the deposited crystals in all the cases explored using the PAN-coated sand are shown in Figure 5.20. The largest values of the total pixel intensity per unit area obtained in the experiments with the PAN-coated sand are smaller than the corresponding values in the experiments with the original sand (cf. section 5.2) and larger than the corresponding values in the experiments with the hydrophobic sand.

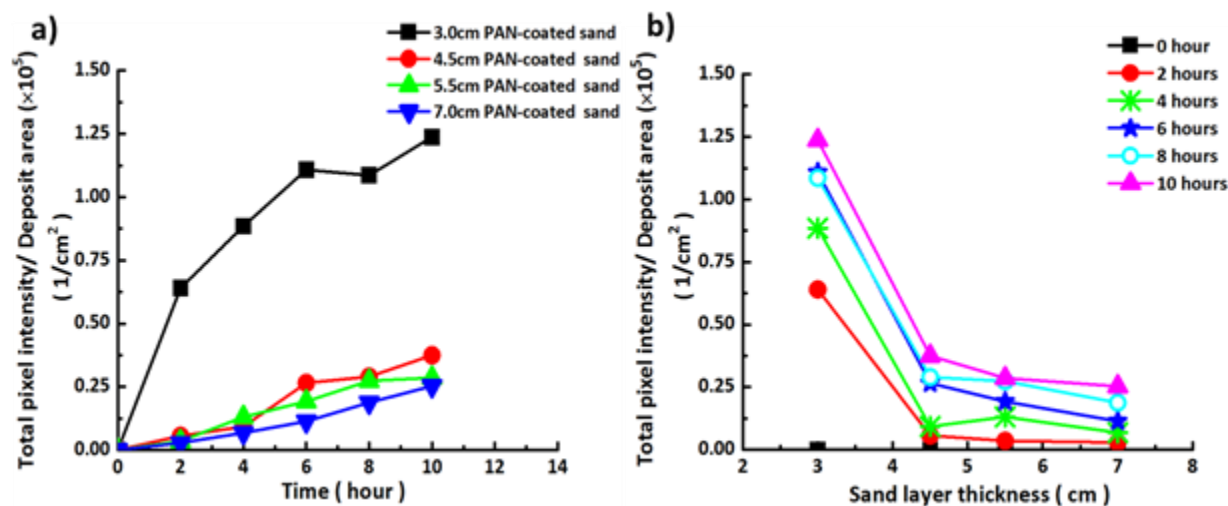


Figure 5. 20 Total pixel intensity per unit area covered with naphthalene crystals. The naphthalene ball was buried in the middle of the tank bottom. The experiments with the PAN-coated sand. (a) Total pixel intensity per unit area versus time, with time being reckoned from the delay times. (b) Total pixel intensity per unit area versus sand layer thickness. The experimental data is shown by symbols and spanned by lines.

The values of the total pixel intensity per unit area in all the cases studied using the original sand (section 5.2), the hydrophobic sand and the PAN-coated sand are summarized in Figure 5.21. It is clear that the delay time could be decreased by modifying sand, especially after coating it with 5 wt% PAN solution, in comparison to the delay time corresponding to the original sand. The delay

time results from the adsorption of naphthalene vapor on sand grains, which precludes vapor release to the free surface. Accordingly, the prolonged adsorption of vapor on sand grains delays its detection at the free surface.

The very fact that the presence of PAN coating results in a faster vapor release to the free surface means that such coating significantly diminishes retainment of the vapor inside sand layer. Therefore, if there would be any adsorption of naphthalene vapor on PAN, it would be much less than on sand. Also, vapor diffusion into PAN layer is hardly a factor. Indeed, the characteristic time of such diffusion $\tau_D \sim \ell^2 / D_{PAN}$, with D_{PAN} being the diffusion coefficient in solid PAN, is of the order 10 h, since $D_{PAN} \sim 10^{-10} \text{ cm}^2 / \text{s}$ [Fieldson and Barbari (1993)]. This time is longer than the delay in the significant vapor release to the free surface. Therefore, significant accumulation of naphthalene vapor inside PAN layer is excluded. On the other hand, coating sand grains (e.g. with PAN layer) significantly decreases the surface area of individual sand grains available for the adsorption, since the grain surface is dramatically smoothed, as seen in Figure 5.17 in the revised version. Therefore, vapor almost immediately reaches by diffusion the free surface (Figure 5.21) where it can be detected.

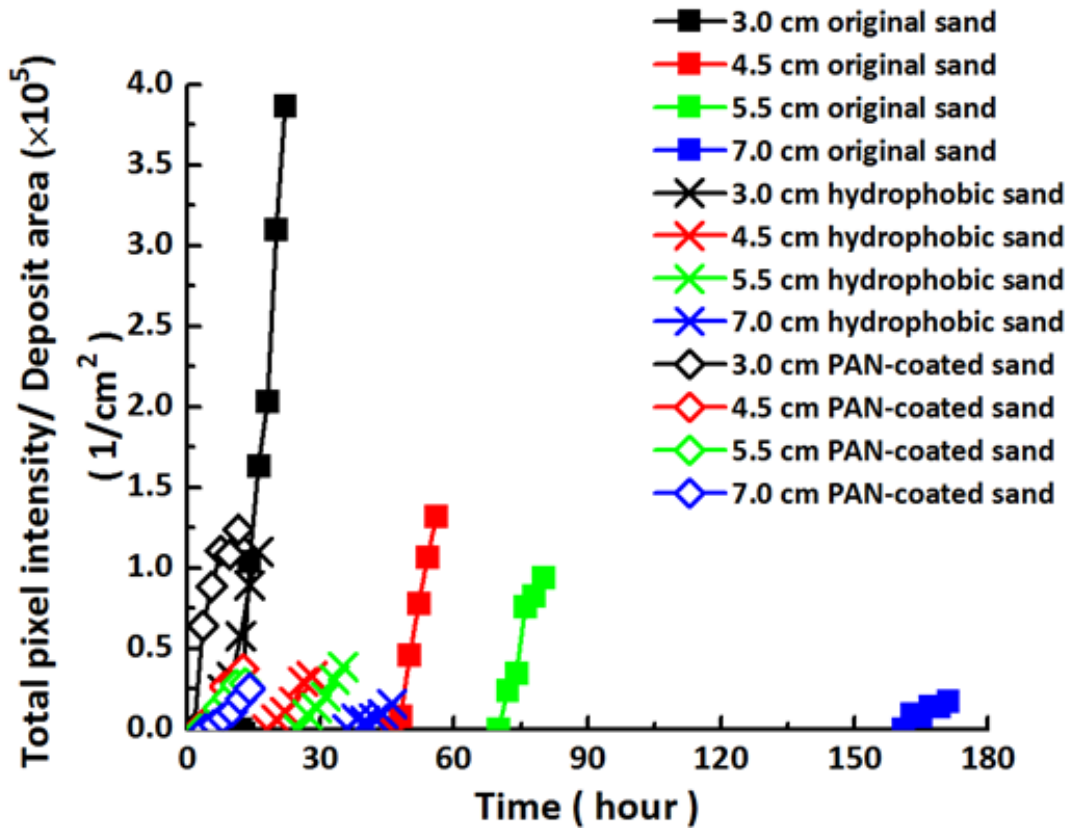


Figure 5. 21 Total pixel intensity per unit area covered with naphthalene crystals. A 1.9 cm naphthalene ball was buried in the middle of the tank bottom. The experiments with the original sand, the hydrophobic sand and the PAN-coated sand. The experimental data is shown by symbols and spanned by lines.

5.7 Conclusions

A method of measurement of vapor mass deposited by vapor sublimated from a buried source and diffused through a porous media, such as sand or a kaolinite layer is proposed. The theory predicting mass deposition on a detector located at the free surface is also proposed and compared with the experimental data with the original sand and kaolinite layers. The agreement of the theoretical predictions with the experimental data is rather good. In addition, the experiments with two kinds of modified sands were conducted: with the hydrophobic sand with a thin

trimethylsilanol layer at the grain surfaces, and with the polymer-coated sand with a thin PAN layer at the grain surfaces. It is shown that the deposited layers make the grains smoother and significantly diminish the surface area available for molecular adsorption. The latter significantly accelerates the release of the vapor sublimating from the buried source to the free surface where it can be detected.

CHAPTER 6

SENSING UNDERGROUND GAS RELEASE

6.1 Introduction

The focus of the present chapter is primarily forensic. Namely, the detection of materials located in ground at a certain depth by measuring traces of gases or vapors released from them and filtrating to the surface through such porous media as soil or sand. Due to the special recognizable odor and sublimation property, naphthalene is considered as a useful material for very accurate measurements. The developed theory is shown in section 6.2. The designed experiments and the experimental results are shown in section 6.3 and discussed in section 6.4. The conclusions are drawn in section 6.5.

6.2 Theoretical

Assume that the adsorption/desorption of gas on the ground material is saturated sufficiently fast, and the gas transport process is determined by pure diffusion. In the simplest one-dimensional case the diffusion equation reads

$$\frac{\partial C}{\partial t} = D \frac{\partial^2 C}{\partial x^2} \quad (6.1)$$

where t is time, x is the coordinate in the vertical direction, C is concentration of gas in ground, and D is the diffusion coefficient of the gas in ground.

Assume that the gas source is located at $x=0$, where gas concentration is known. Then, the first boundary condition for Eq. (6.1) reads

$$x = 0, \quad C = C_w \quad (6.2)$$

with C_w being a known concentration in depth.

Let a sensing device with volume V and surface area in contact with the ground S is located at the surface at $x=h$, where h is the depth of the gas source. Then, one can calculate the mass of gas collected by the sensor in time, and thus relate the mass flux with gas concentration inside the sensor as

$$-\int_0^t D \frac{\partial C}{\partial x} \Big|_{x=h} S dt = C|_{x=h} V \quad (6.3)$$

Eq. (6.3) forms the second boundary condition required to solve Eq. (6.1).

Assume that before sensing started, the gas concentration field with an unblocked access to the surrounding atmosphere (with no sensor on the ground surface) had reached a steady-state distribution, i.e.

$$t = 0, \quad C = C_w \left(1 - \frac{x}{h} \right) \quad (6.4)$$

Eq. (6.4) forms the initial condition required for Eq. (6.1) and implies that the initial gas concentration at the surface was negligibly small before the sensor was applied at $t=0$.

Render Eqs. (6.1)- (6.4) dimensionless using h as the scale for x , h^2/D – as the scale for t , and C_w – as the scale for C . Then, the dimensionless problem reads

$$\frac{\partial \bar{C}}{\partial \bar{t}} = \frac{\partial^2 \bar{C}}{\partial \bar{x}^2} \quad (6.5)$$

$$\bar{t} > 0: \quad \bar{x} = 0, \quad \bar{C} = 1; \quad \frac{d\bar{C}}{dt} \Big|_{\bar{x}=1} = -\frac{h}{H} \frac{\partial \bar{C}}{\partial \bar{x}} \Big|_{\bar{x}=1} \quad (6.6)$$

$$\bar{t} = 0: \quad \bar{C} = 1 - \bar{x} \quad (6.7)$$

In Eqs. (6.5)- (6.7) overbars denote dimensionless variables, and in (6.6) $H=V/S$ is the effective

height of the sensor. It is seen that in the dimensionless form the sensor reading $\bar{C}|_{\bar{x}=1}(\bar{t})$ is fully determined by a single dimensionless group h/H .

Eq. (6.5) was semi-discretized on lines $\bar{x} = \bar{x}_i$ ($i=1, \dots, N$), which makes it a system of the inter-related ordinary differential equations (ODEs) in time

$$\frac{d\bar{C}_i}{dt} = \frac{(\bar{C}_{i+1} + \bar{C}_{i-1} - 2\bar{C}_i)}{\Delta\bar{x}^2} \quad (6.8)$$

with $\Delta\bar{x} = (\bar{x}_{i+1} - \bar{x}_i)$ being equal for all the values of i .

The $(N+1)$ 'th ODE is provided by the second boundary condition (6.6). The inter-related system of $(N+1)$ ODEs is solved numerically starting from the initial condition (6.7) using the Kutta-Merson method. The results are discussed below in comparison with the experimental data.

6.3 Experimental

6.3.1 Materials

Naphthalene used as the volatile material in this work was purchased from Enoz[®], its purity was 99.95%. Sand bought from Quikrete was used as a model granular porous medium and pre-treated by rinsing in ethanol before being used in the experiments to eliminate impurities. Then, the wet sand was fully dried and sieved. The sieve opening selected was in the 0.212- 1.4 mm range. Sphericity of the sand particles was measured as 0.8281 as described in Appendix A. The permeability of a sand layer was measured as $k_s = 1.01 \times 10^{-11} \text{ m}^2$, and its porosity was found as $\varepsilon = 0.191$ (cf. Appendix B).

6.3.2. Experimental setup

A layer of naphthalene of the thickness of 4 mm was located at the bottom of two Pyrex[®] glass bottles of diameters 70 mm and 100 mm and heights L of 135 mm and 225 mm, respectively (the bottles had a slightly curved generatrix, so the bottom diameters are given here). Layers of sand of different heights h , 25 mm, 35 mm, 45 mm and 100 mm were located over the naphthalene layer. The top of the glass bottle was sealed. As a result, the free space of the glass bottle of the height $H=L-h$ was used as a sensor of naphthalene vapor sublimated from the buried naphthalene 5 mm-thick layer and diffused through the sand layer to the surface. Sensidyne 153U naphthalene detector tubes and a gas sampling pump was used for measuring the naphthalene concentration over the sand surface. The tubes were inserted through a small opening (4.83 mm) in the glass bottle top cover, after removing a plastic plug from it.

Four different sand layer - to the sensor height ratios h/H were explored in the present experiments at room temperature. The 250 ml glass bottle was used for measurements at $h/H=0.238, 0.368$ and 0.529 . The 1000 ml glass bottle was used for measurements at the ratio $h/H=0.833$. It should be emphasized that in the present measurements the sand layers were thinner than the blank space in the bottles above them.

Naphthalene vapor diffusion through sand is accompanied by its adsorption/desorption on the surfaces of sand particles. Accordingly, to exclude the influence of the adsorption/ desorption process on the current measurements, the deposited sand layers over the naphthalene layer inside a glass bottle were left for at least 24 h to achieve the adsorption/desorption equilibrium. This means that an equilibrium thickness of naphthalene adsorbed on sand particles was achieved first, and thus measurements of the vapor flux to the surface were unaffected by the adsorption/desorption process.

To prevent vapor leakage during the experiments, an annulus rubber was placed between the cap and the bottle, Para film was wrapped outside the entire bottle, Dow Corning® RTV Sealant was used to seal the gap between the cap and the plastic plug in the cap.

Vapor probes were taken as described below. For that, the sealant and the plastic plug were removed. One side of the naphthalene detector tube was inserted into the blank space of the glass bottle 1 cm over the sand layer and the other side of the detector tube was attached to the sampling pump. Pulling the sampling pump handle, 100 ml vapor probes were taken from the bottle. The vapor was pumped through the detector tube and, as a result, the detector tube color would change from pale yellow to brown. Reading at the maximum point of the stained layer revealed the naphthalene vapor concentration (in ppm) in the probe taken from the blank space of the bottle. When one experiment was finished, the vapor remained inside the bottle would be vacuumized to assure no influence from the remaining sublimated naphthalene vapor on the next experiment, which was started anew, but with a different duration of time before a probe would be taken.

6.3.3 Data processing and saturated pressure of naphthalene vapor

The naphthalene detector tube reading in ppm was converted into mg/m³ by the following formula Detected concentration (mg/m³) = X × 5.235 mg/m³ where X is the dimensionless number of ppm read by the tube. The saturated sublimation pressure of naphthalene in the air was evaluated by the Antoine equation

$$\log_{10} P = A - \frac{B}{T + C} \quad (6.9)$$

where P is pressure in mm Hg, T is the temperature in °C, A, B, and C are the material-specific constants. Using the data from [Yaws (2015)], A = 6.89116 °C, B = 1551.4785 °C, and

$C = 168.879$ °C, one can evaluate that saturated sublimation pressure of naphthalene at 25 °C as $P = 0.0774$ mm Hg, which equals to 10.3192 Pa. Applying the ideal gas law, the saturated sublimation concentration of naphthalene in the air is evaluated as 532.9 mg/m³, which approximately equals to 101 ppm.

6.3.4 Experimental results

Naphthalene detector tubes readings in ppm at different time were collected and the results are shown in Figure 6.1. Each symbol in Figure 6.1 corresponds to a reading from a separate experiment. It is emphasized that naphthalene concentration in the sensor (the blank space of the glass bottle) increases as the collection time increases for all four sand layer height ratios studied. At the height ratio of 0.238, the naphthalene concentration reached a maximum in 4 h, as is shown in Figure 6.1a, which is approximately equal to the saturation value of 101 ppm. At the height ratio of 0.368, the naphthalene concentration also reached the maximum corresponding to the saturation value in 4 h, as is seen in Figure 6.1b. At the height ratio of 0.529, the naphthalene concentration reached the maximum corresponding to the saturation in 6 h, as is shown in Figure 6.1c. At the height ratio of 0.833, the naphthalene concentration reached the saturation maximum only in 18 h, cf. Figure 6.1d. An increase in the sand layer thickness diminishes the vapor concentration at any given time moment and delays reaching the saturation.

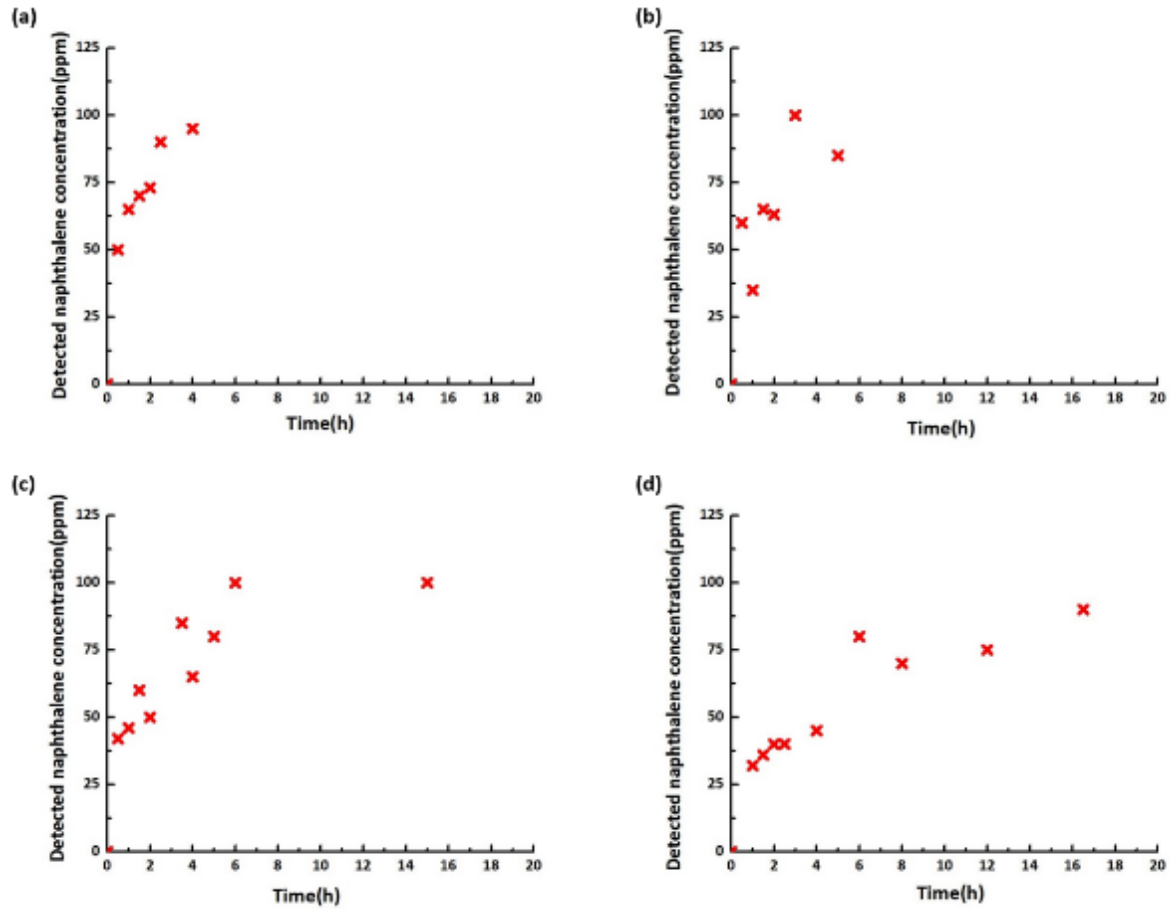


Figure 6. 1 Naphthalene concentration in the sensor space at different sand height ratio versus time. (a) The height ratio of 0.238. (b) The height ratio of 0.368. (c) The height ratio of 0.529. (d) The height ratio of 0.833.

6.4 Discussion: Comparison of the theoretical predictions with the experimental data

The diffusion coefficient of naphthalene vapor in air D_0 in cm^2/s at 101.325 kPa is given by the following formula [Keumnam et al. (1992)]

$$D_0 = 8.17708 \times 10^{-7} T^{1.983} \quad (6.10)$$

where T is temperature in $^{\circ}\text{K}$; the formula is valid between 287.65°K and 327.11°K , and the

diffusion coefficient is in cm^2/s . The corresponding diffusion coefficient in a porous medium D_s in cm^2/s could be calculated as [Davidson and Trumbore (1995)]

$$D_s = D_0 \varepsilon^{4/3} \quad (6.11)$$

where ε is the porosity of a dried porous medium. Hence, the diffusion coefficient of naphthalene vapor in the dried sand with porosity $\varepsilon=0.191$ (19.1%) filled with air at 298.65°K is $0.00725 \text{ cm}^2/\text{s}$.

Following the theoretical section time and vapor concentration measured in the experiments are rendered dimensionless as $\bar{t} = t D_s / h^2$ and $\bar{C} = C / C_w$, where C_w is the saturated concentration of naphthalene vapor.

The experimental data from Figure 6.1 is replotted in the dimensionless form and compared with the theoretical predictions obtained by solving the problem (6.5)- (6.7) in Figure 6.2. The agreement of the theoretical predictions with the experimental data in Figure 6.2 is quite reasonable for all the sand height –to sensor height ratios.

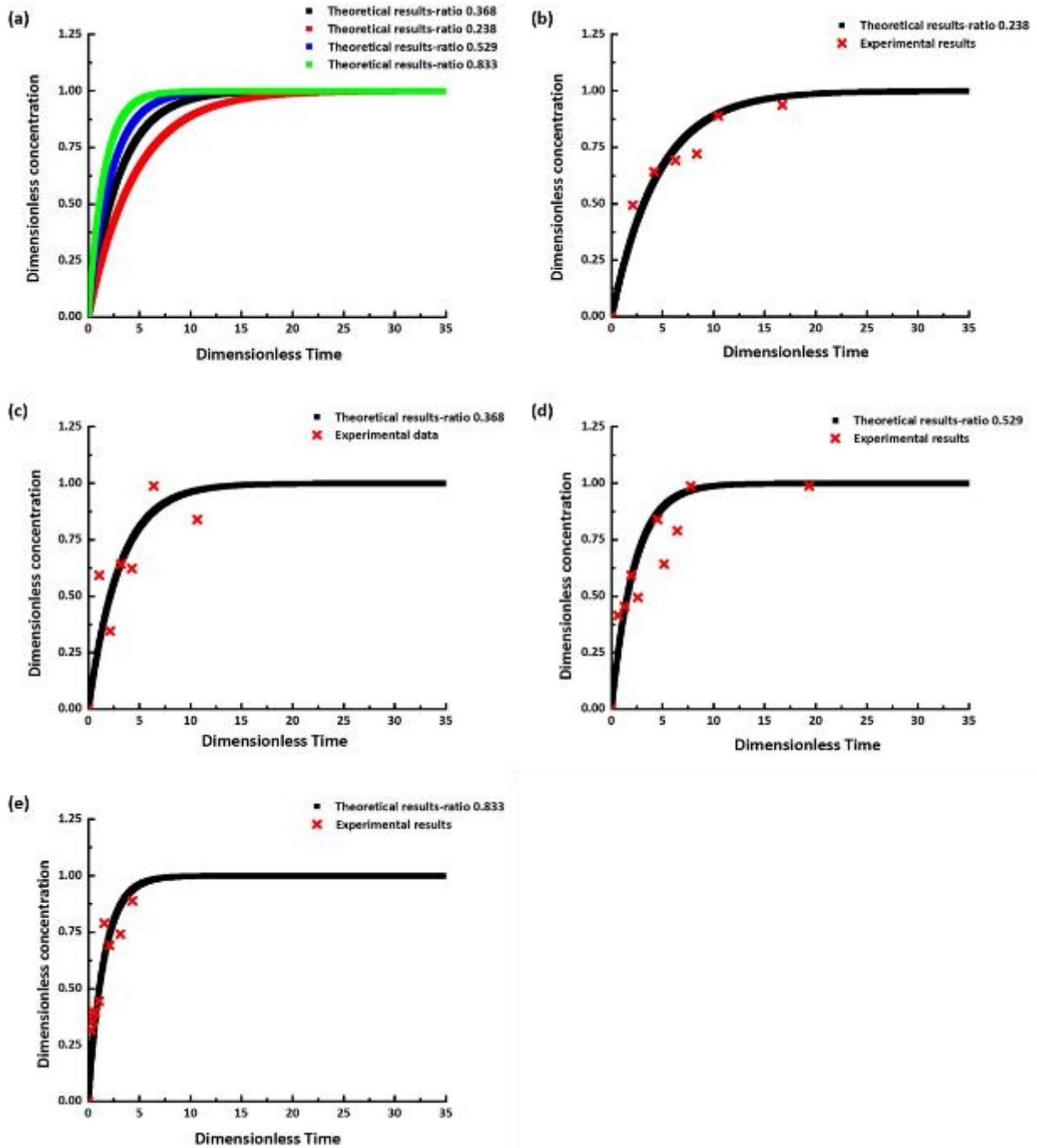


Figure 6. 2 Naphthalene vapor concentration versus time at different sand height ratios: the comparison between the theory and the experimental data. (a) Theoretical results at four different sand layer height ratios listed in the panel. In the following four panels the theoretical results are shown separately by lines while the corresponding experimental data - by symbols. (b) The height

ratio of 0.238. (c) The height ratio of 0.368. (d) The height ratio of 0.529. (e) The height ratio of 0.833.

6.5 Conclusions

The proposed theory of sensing of naphthalene vapor diffusing through sand layers is verified by the experimental data at four sand-to-sensor height ratios. Accordingly, the theory can be used as a predictive tool for any other vapor diffusing from underground objects to evaluate the required sensor sensitivity for any sensor size, and the observation time, and for other types of soil (not necessarily sand).

CHAPTER 7

HEAT-TRANSFER IN POINT-BONDED POLYMER NONWOVENS AND THEIR RUPTURE IN STRETCHING

(This chapter has been previously published as Zhang, W., Staszal, C., Yarin, A. L., Shim, E., Pourdeyhimi, B. (2018). Point-bonded polymer nonwovens and their rupture in stretching. *Polymer*, 146, 209-221.)

7.1 Introduction

The present chapter aims at further understanding the effect of thermal point-bonding inclusions on nonwoven webs as a means of increasing mechanical performance. The materials and setups used in the experiments, as well as the tensile testing process, are shown in detail in section 7.2. The obtained results are discussed in section 7.3 and the conclusions were drawn in section 7.4.

7.2 Experimental

7.2.1 Materials

Two meltblown nonwoven mats were chosen for this work, Polybutylene Terephthalate (PBT) (which will be designated as PBT nonwoven from here on) as well as a nonwoven composed of a mixture of 80 % Polybutylene Terephthalate and 20 % Polyethylene (PE) (which will be designated as PBT/ PE 80/20 nonwoven from here on). The PBT nonwoven had the basis weight of 100 GSM (gram per square meter basis weight) with the average measured thickness of 0.33

mm. The PBT/ PE 80/20 nonwoven had the basis weight of 75 GSM with the average measured thickness of 0.30 mm. The nonwovens tested were all cut into 15 mm × 90 mm rectangular samples from the nonwoven sheets in the same direction.

In the present work, the as-received nonwovens were pre-bonded using a standard point-bonding process. As will be discussed in the following section, further bonding was conducted by significantly larger circular and rhombic punches at the center of these nonwoven strips to understand the effect of bonding and the corresponding rupture pattern. Such an additional bond would be significantly stronger than the surrounding bonds as corroborated by the rupture patterns elucidated by the following results. Thus, it can be assumed that the minor pre-bonding had a minimal effect compared to the further bonding process used in this work.

7.2.2 Thermal bonding

In the present section, the nonwovens were further thermally bonded using the setup depicted in Figure 7.1a.

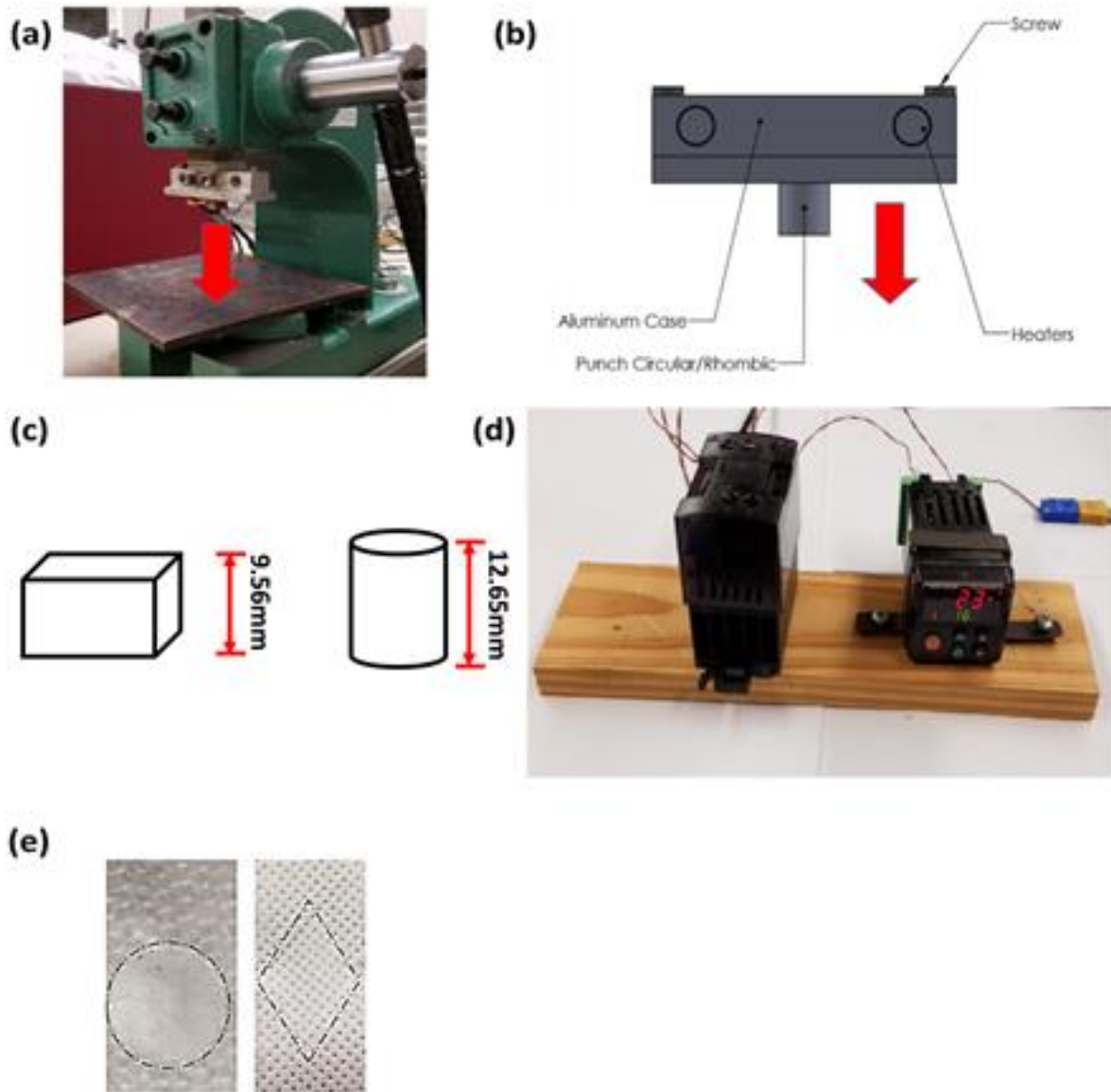


Figure 7. 1 (a) Thermal bonding setup for the additional bond patterning with the aluminum case attached and used for point bonding. (b) Schematic of the aluminum case with an interchangeable thermal punch inserted. (c) Schematic of two types of thermal punches, rhombic and circular. (d) The temperature controller (Watlow EZ-ZONE). (e) Example of PBT nonwoven sample with a single circular bond pattern as well as a single rhombic bond pattern formed by the setup of panel (a).

The main part of the setup was an Arbor press used to advance and compress a nonwoven using an aluminum case containing interchangeable heated punches (either circular or rhombic in cross-section) (cf. Figure 7.1a and 7.1b). The diameter of the circular punch was 12.60 mm and its surface area was 124.59 mm², whereas the rhombic punch had a length of 18.90 mm, width of 12.65 mm, and the total surface area of 119.54 mm² (cf. Figure 7.1c). The aluminum case and the interchangeable punch were heated using an embedded cartridge heater (CSH- 201200/120 V). A thermocouple (Omega model 5TC-PVC-T-24-180) was embedded in the various interchangeable punches. A temperature controller (Watlow EZ- ZONE) (cf. Figure 7.1d) was also included. Using such a configuration, the temperature of the front face of the interchangeable punches was regulated to various constant set temperatures for thermal bonding.

The heated interchangeable punch (either circular or rhombic) was advanced and contacted the central portion of the rectangular nonwoven samples and formed additional thermal bonding patterns on them. The contact time of the punch with the samples was maintained at 1 s. For the case of the PBT nonwovens, thermal bonding was conducted at constant temperature of 190 °C, whereas for the case of the PBT/PE 80/20 nonwovens, the constant temperatures chosen were 110°C as well as 120°C. These temperatures were chosen to ensure full thermal bonding (the melting point of PBT is 220°C [Mandal (2009)] and of PE is 110- 126°C [Mandal (2009)]). An example of a PBT nonwoven bonded with either circular or rhombic punch is shown in Figure 7.1e.

7.2.3 Tensile tests of bonded nonwovens

Tensile tests of the original and the additionally bonded samples were conducted using an Instron machine (model 5942) with a 100 N load cell to obtain the entire stress-strain curves of the

as-obtained original PBT nonwovens and the PBT/ PE 80/20 nonwovens as well as those which underwent thermal punching as described in subsection 7.2.2. The sample was clamped firmly in place by pneumatic clamps with an initial test length of 40 mm and advanced at a rate of 2 mm/min. For each type of samples tested, 10 tensile trials were conducted.

The Young's modulus and yield stress was determined from the acquired data using the following phenomenological Green's equation fitted to the acquired stress-strain curves [Kirsch (1898); Eshelby (1957)]

$$\sigma_{xx} = Y \tanh\left(\frac{E}{Y} \varepsilon_{xx}\right) \quad (7.1)$$

Here σ_{xx} is the tensile stress, ε_{xx} the tensile strain, E the Young's modulus, and Y the yield stress. The equation, due to the assumption of perfect plasticity was fitted to the experimental data so that the elastic region was approximated first with a minimum coefficient of determination R^2 of at least 0.999.

The toughness T of the nonwoven samples, i.e. the specific energy associated with tensile deformation was given using the following equation:

$$T = \int \sigma_{xx} d\varepsilon_{xx} \quad (7.2)$$

7.2.4 Imaging

Images of nonwovens were taken by a DSLR camera with a setting of $f= 3.5$ and 1/60 exposition time. All images were taken under the same conditions.

7.3 Results and discussion

7.3.1 Results of the tensile tests of the as-received nonwovens as well as the bonded nonwovens

Tensile tests were conducted using the as-received PBT nonwovens and PBT/ PE 80/20 nonwovens. Several examples of stress-strain curves for these nonwovens are shown in Figures 7.2 and 7.3.

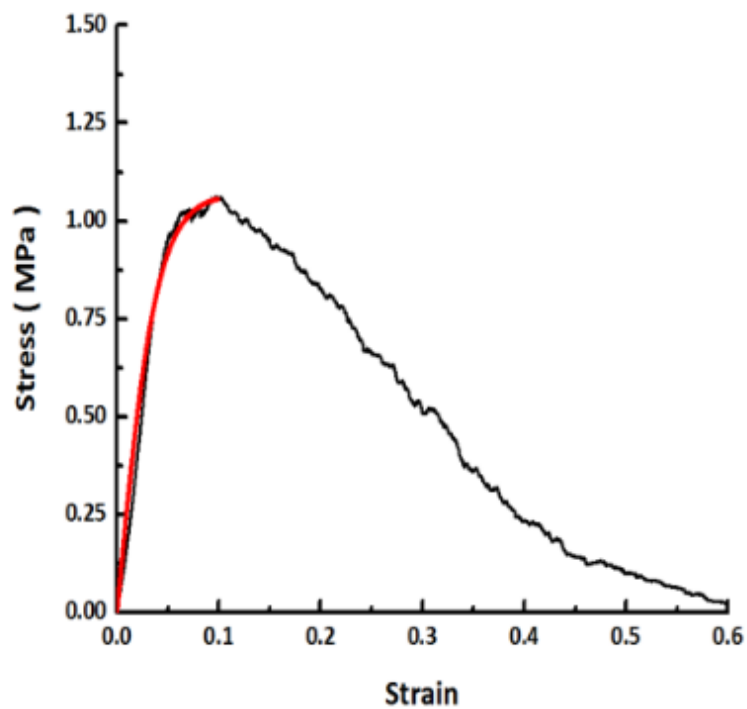


Figure 7. 2 An example of the stress-strain curve of the as-received PBT nonwovens measured in tensile tests. The data is shown by the black curve, the phenomenological Green equation (7.1) fit by the red curve.

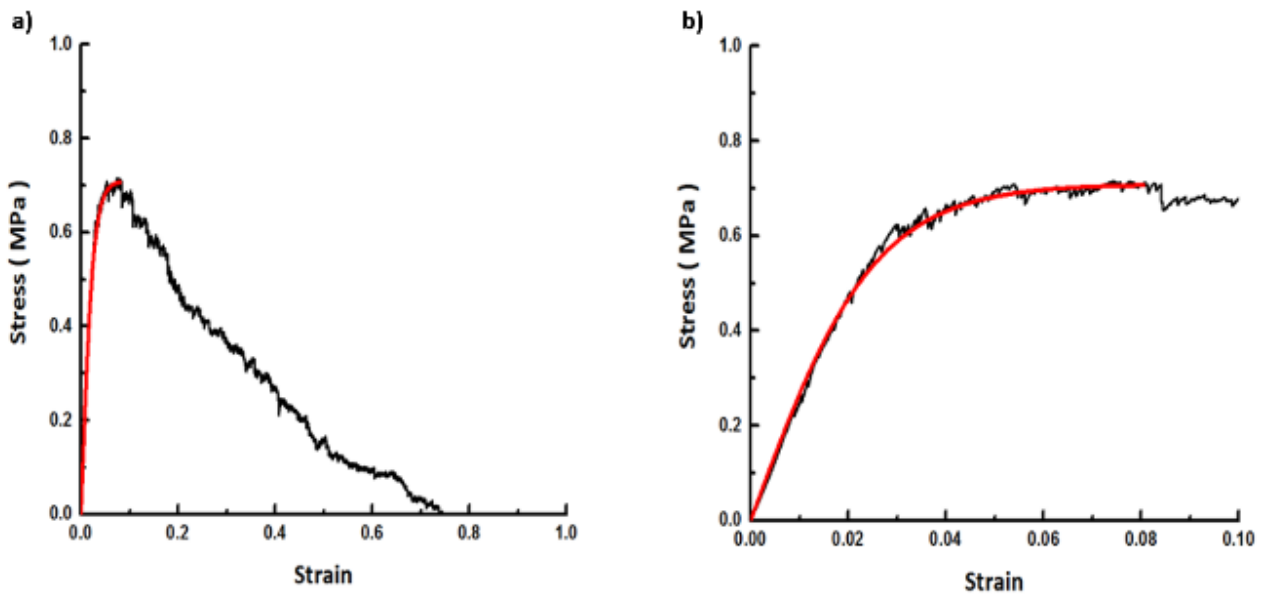


Figure 7. 3 (a) An example stress-strain curve of the as-received PBT/ PE 80/20 nonwovens measured in tensile tests. The data is shown by the black curve, the phenomenological Green equation (7.1) fit- by the red curve. (b) A zoomed-in view of the elastic section followed by the perfectly plastic section.

From the obtained results from the tensile tests, the average Young's modulus E and yield stress Y revealed by the phenomenological Eq. (7.1) were found. Also, the toughness T as revealed by Eq. (7.2) for both the as-received PBT nonwoven as well as the as-received PBT/ PE 80/20 nonwoven was determined. In addition, maximum stress at failure σ_{\max} was found. These results are presented in Table 7.1 and depicted in Figure 7.4.

Table 7. 1 Average mechanical properties of as-received PBT and PBT/PE 80/20 nonwovens.

Nonwoven type	Average Young's modulus E (MPa)	Average yield stress Y (MPa)	Average toughness T (MPa)	Average maximum at failure σ_{max} (MPa)
As- received PBT	34.521 ± 6.133	1.169 ± 0.104	0.320 ± 0.066	1.167 ± 0.098
As- received PBT/PE 80/20	27.397 ± 10.520	0.646 ± 0.137	0.410 ± 0.090	0.628 ± 0.119

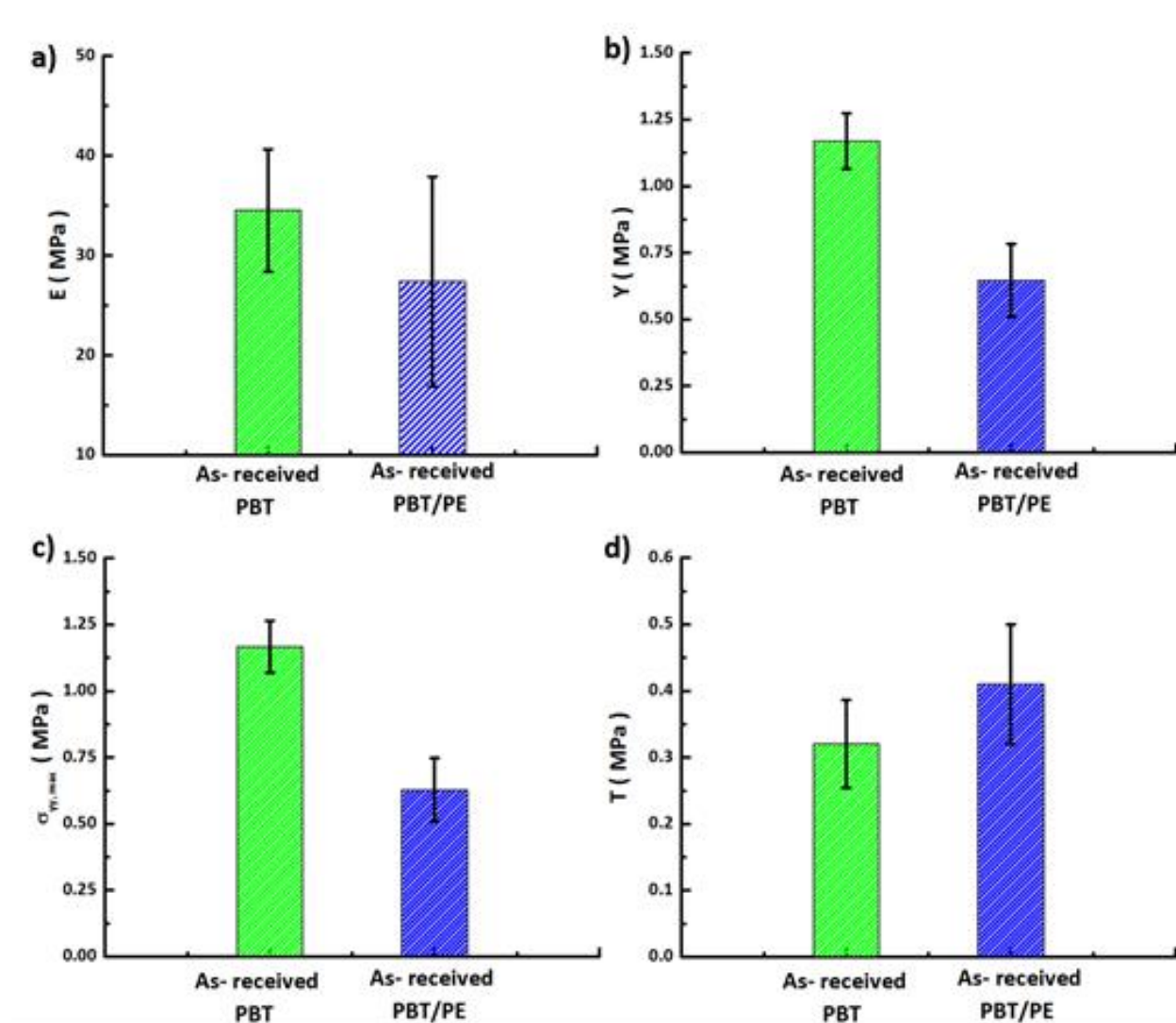


Figure 7. 4 Mechanical properties in the tension of the as-received PBT and PBT/PE 80/20 nonwovens. (a) Average values of Young's modulus E. (b) Average values of the yield stress Y.

(c) Average values of the maximum stress ($\sigma_{xx, \max}$). (d) Average values of the toughness (T).

As seen in Table 7.1 and Figure 7.4, the as-received PBT nonwovens revealed a higher Young's modulus E , the yield stress Y , and the maximum stress σ_{\max} than those of the PBT/ PE 80/20 nonwovens. On the other hand, the toughness (T) of the as-received PBT/ PE 80/20 nonwovens was higher than that of the as-received PBT nonwovens, which is related to a prolonged plastic deformation of the former prior to the failure. Furthermore, the as-received PBT/ PE 80/20 nonwovens also revealed a section of a perfectly plastic behavior at which the tensile stress practically plateaus and Green's equation approximates the data very accurately (Figure 7.3b).

7.3.2 Results of the tensile tests of the thermally bonded nonwovens

Tensile tests were conducted with PBT nonwovens and PBT/ PE 80/20 nonwoven samples modified by a single circular thermal bond as well as by a single rhombic thermal bond. For the case of the PBT nonwoven, thermal bonding was conducted at a temperature of 190 °C, as for the PBT/ PE 80/20 nonwovens the bonding temperatures chosen were 110 °C as well as 120 °C. Several examples of stress-strain curves for these nonwovens bonded with a circular and rhombic bond are shown in Figures 7.5 and 7.6.

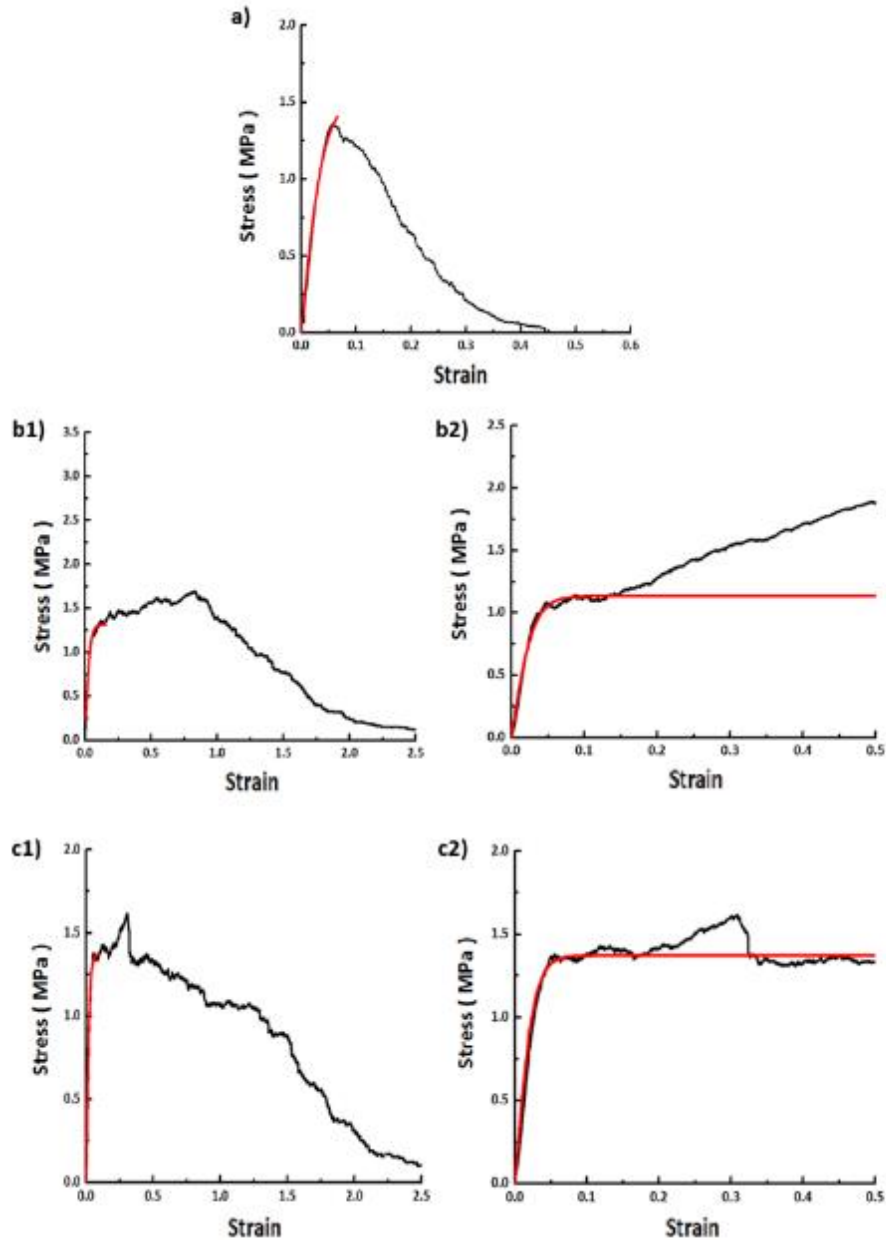


Figure 7. 5 Examples of the stress-strain curves of the nonwoven samples bonded with an additional single circular bond. (a) The PBT nonwoven bonded by a circular bond at 190 °C. (b1) The PBT/ PE 80/20 nonwoven bonded by a circular bond at 120 °C and (b2) a zoomed-in view of the elastic region. (c1) The PBT/ PE 80/20 nonwoven bonded by a circular bond at 110 °C and (c2) a zoomed-in view of the elastic region. The data is shown by the black curves, the Green equation fit- by the red curves.

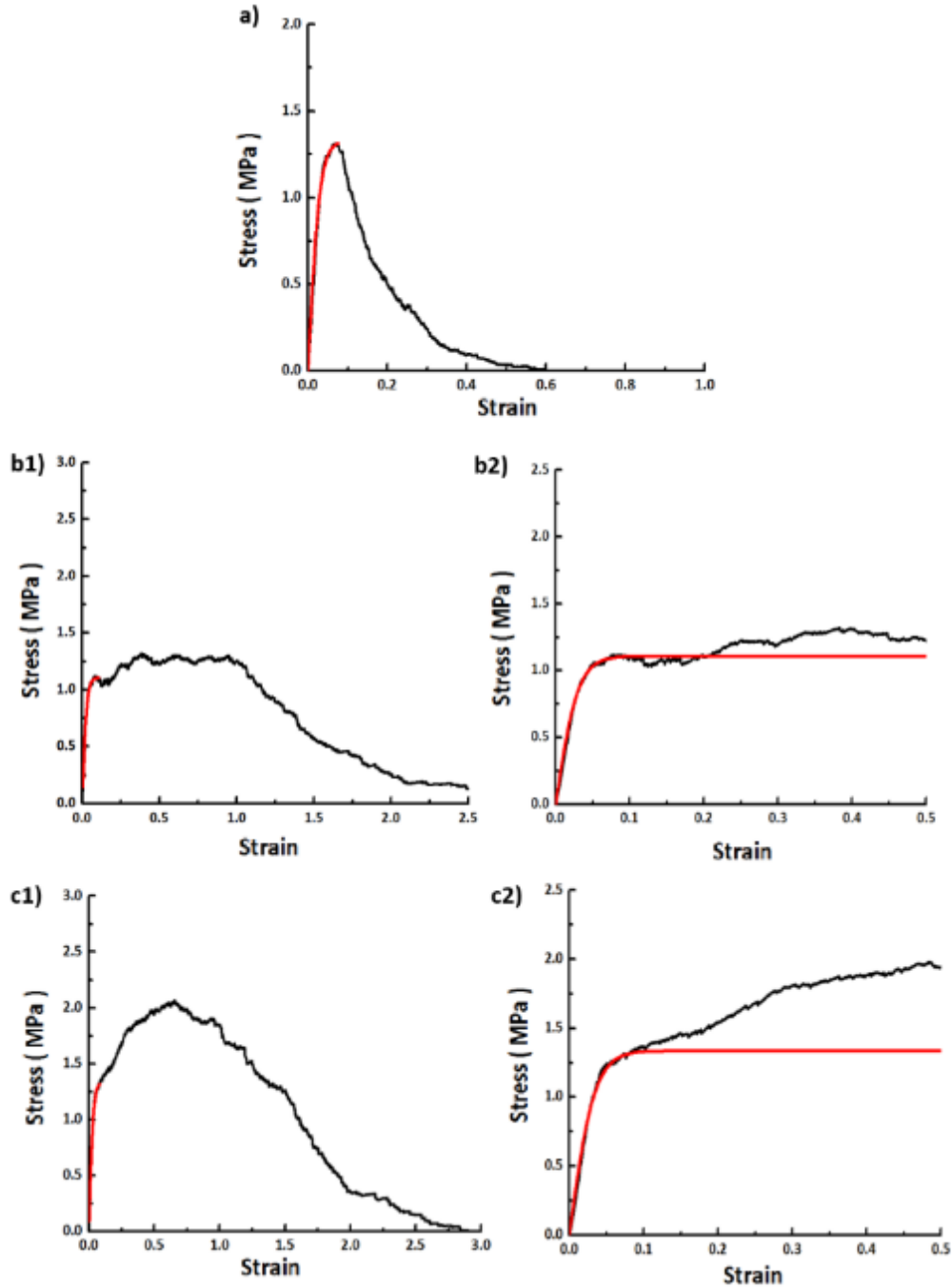


Figure 7. 6 Examples of the stress-strain curves of the nonwoven samples bonded with an additional single rhombic bond. (a) The PBT nonwoven bonded by a rhombic bond at 190 °C. (b1) The PBT-PE nonwoven bonded by a rhombic bond at 120 °C and (b2) a zoomed-in view of the elastic region. (c1) The PBT/ PE 80/20 nonwoven bonded by a rhombic bond at 110 °C and (c2) a

zoomed-in view of the elastic region. The data is shown by the black curves, the Green equation fit- by the red curves.

From the stress-strain curves obtained for the PBT nonwovens as well as the PBT/PE 80/20 nonwovens, both thermally bonded with the circular punch as well as the rhombic punch, the average Young’s modulus E, the yield stress Y, toughness T, and the maximum stress at failure σ_{max} were determined. These results are presented in Table 7.2. In Figures 7.7 and 7.8, the results for these mechanical properties for the as-received nonwovens are compared to those of the thermally bonded nonwovens.

Table 7. 2 Average mechanical properties of bonded PBT and PBT/PE 80/20 nonwovens.

Nonwoven name	Average Young’s modulus E (MPa)	Average yield stress Y (MPa)	Average toughness T (MPa)	Average maximum stress at failure σ_{max} (MPa)
Circular bonded PBT	36.847 ± 4.699	1.455 ± 0.288	0.289 ± 0.052	1.364 ± 0.230
Rhombic bonded PBT	41.200 ± 5.652	1.355 ± 0.288	0.254 ± 0.040	1.310 ± 0.202
110 °C Circular bonded PBT/ PE 80/20	36.057 ± 10.346	1.117 ± 0.194	2.222 ± 0.395	1.127 ± 0.193
110 °C Rhombic bonded PBT/ PE 80/20	41.657 ± 7.787	1.209 ± 0.240	2.527 ± 0.638	1.198 ± 0.263
120 °C Circular bonded PBT/ PE 80/20	37.856 ± 7.382	1.273 ± 0.216	2.477 ± 0.890	1.260 ± 0.215
120 °C Rhombic bonded PBT/ PE 80/20	40.932 ± 5.401	1.241 ± 0.224	2.410 ± 0.626	1.226 ± 0.197

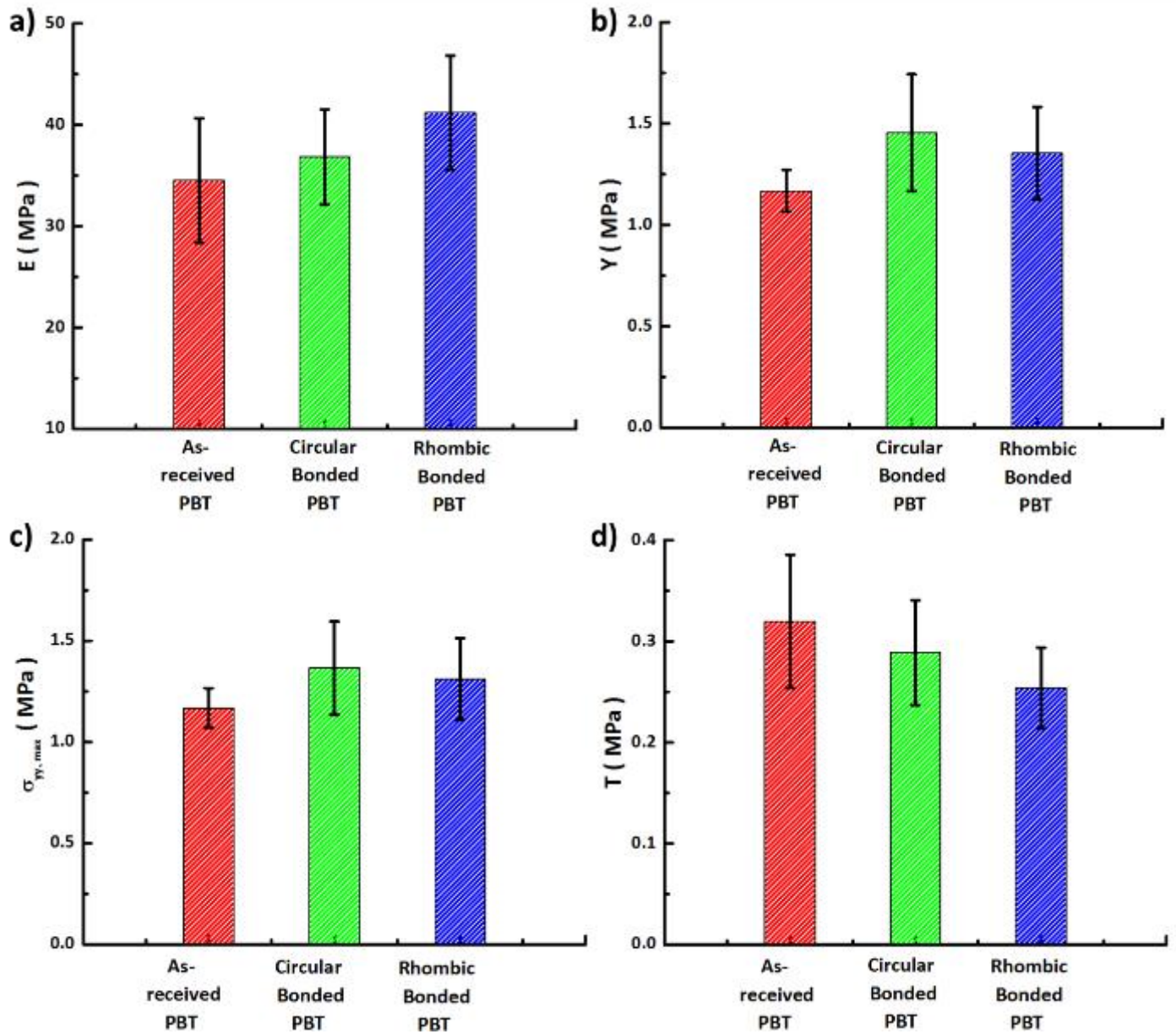


Figure 7. 7 Mechanical properties of the as-received PBT nonwovens, PBT nonwovens with an additional single circular bond imposed at 190 °C, and PBT nonwovens with an additional single rhombic bond imposed at 190 °C. (a) Average values of Young`s modulus. (b) Average values of the yield stress. (c) Average values of the maximum stress at failure. (d) Average values of toughness.

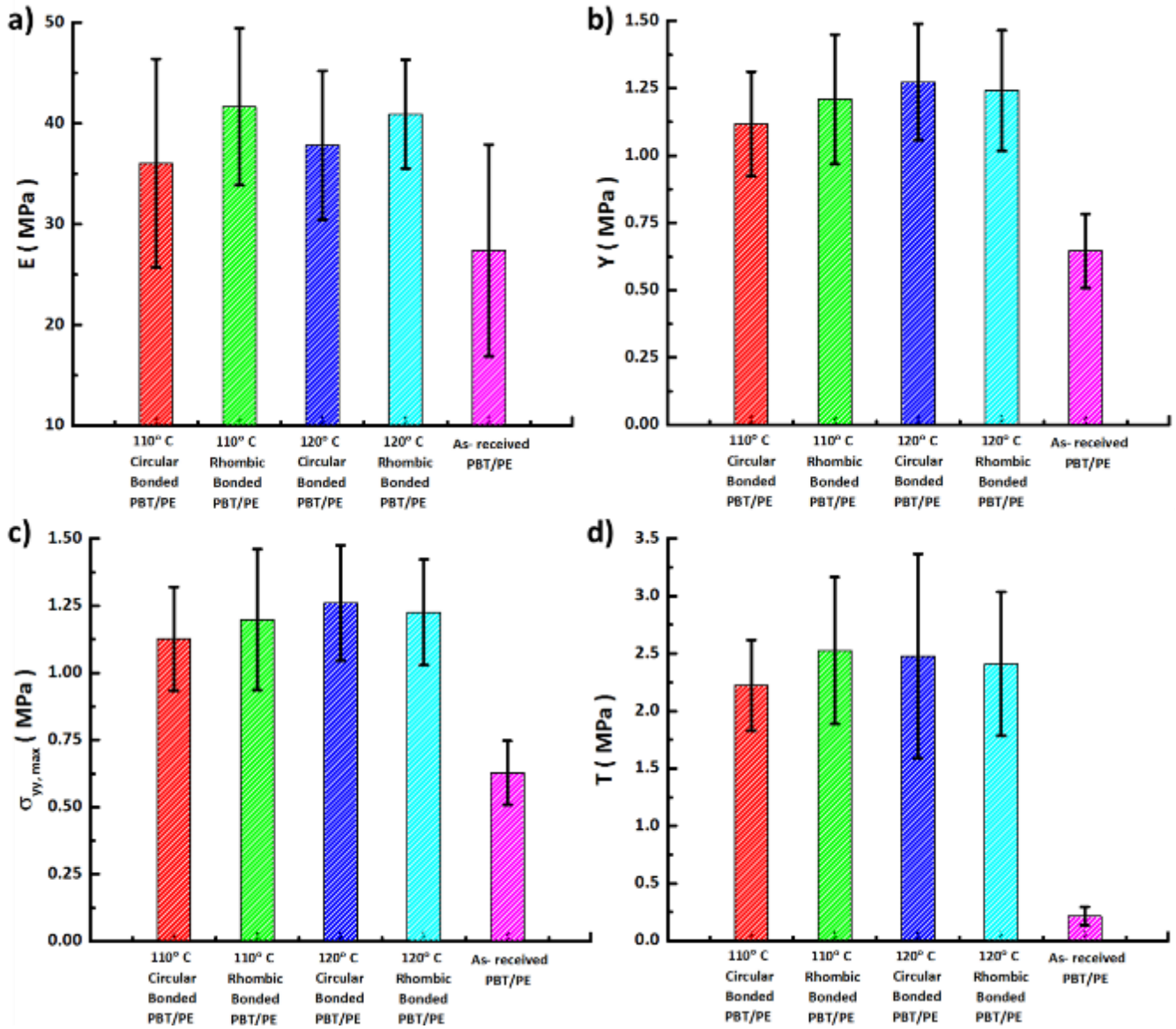


Figure 7. 8 Mechanical properties of the as-received PBT/PE 80/20 nonwovens in comparison with those bonded at 110 °C and 120 °C with a single circular or rhombic bond. (a) Average values of Young's modulus. (b) Average values of the yield stress. (c) Average values of the maximum stress. (d) Average values of toughness.

From the results presented in Figures 7.7 and 7.8, various conclusions on the effect of bonding can be made. For the case of both PBT nonwovens as well as PBT/PE 80/20 nonwovens,

an additional circular or rhombic bond will increase Young's modulus, the yield strength, and the maximum stress as compared to the as-received nonwovens. However, in the case of the PBT nonwovens, the additional bonds decreased the toughness.

Such a decrease in the toughness of the PBT nonwoven samples can be explained by the fact that a thermal bond acts as a stress concentrator inside the nonwoven sample. As will be corroborated by the theoretical stress fields in subsection 7.3.4, the increased stresses at the bond periphery are observed when an inclusion of a higher stiffness (the thermal bond) is added to the nonwoven. Due to such inclusions, the nonwoven stiffness increased overall. However, the bonds acted as stress concentrators and led to an earlier failure and as a result, a decrease in toughness. Furthermore, comparing the toughness of the PBT nonwoven with a circular bond to that with a rhombic bond, the increased stresses at the bond periphery of the rhombic shape compared to the circular one also led to a further decrease in the toughness. Such phenomena will be further discussed in the following subsection 7.3.3.

For the case of the PBT/PE 80/20 nonwoven, a decrease in toughness was not observed. In this nonwoven, bonding was conducted to only melting point of PE (110-129°C [Mandal (2009)]) which bonded the web of PBT. Such a bonding allowed for the high stresses at the bond periphery to be alleviated in the PBT/ PE 80/20 nonwoven. This alleviation in the rupture in the nonwoven was likely caused by the breaking of the PBT/PE 80/20 bond and a slowed failure leading to an increase in the overall toughness of the nonwoven.

The overall increase in the yield stress, and the maximum stress as well as the decrease in Young's modulus in the case of the circular punch, as opposed to the rhombic punch, is likely a manifestation of the fact that the area of the circular bond is slightly larger than that of the rhombic bond (the area of the circular bond is 124.59 mm² and that of the rhombic one is 119.54 mm²).

Accordingly, comparing the results for these two types of bonds, one can conclude that a larger bonding area facilitates an increase in the yield stress and the maximum stress values before failure, albeit decreases Young's modulus.

Comparing bonding the PBT/ PE 80/20 nonwovens at 110 °C to that at 120 °C for either circular bonds or rhombic bonds, one is tempted to conclude that the higher bonding temperature results in a minimal overall increase in the mechanical properties. However, due to the large standard deviation in the results obtained, no clear conclusion can be made.

7.3.3 Rupture patterns

The rupture patterns at the bond periphery in the bonded nonwovens can be clearly seen after tensile tests. The as-received PBT nonwoven before and after testing as well as those with the circular- and rhombic-shaped bonds are shown in Figure 7.9. The as-received PBT/ PE 80/20 nonwovens before and after tensile tests as well as those with the circular- and rhombic-shaped bonds at 110 °C and 120 °C are shown in Figure 7.10. Only a single sample of rupture of each nonwoven is shown here for the sake of brevity.

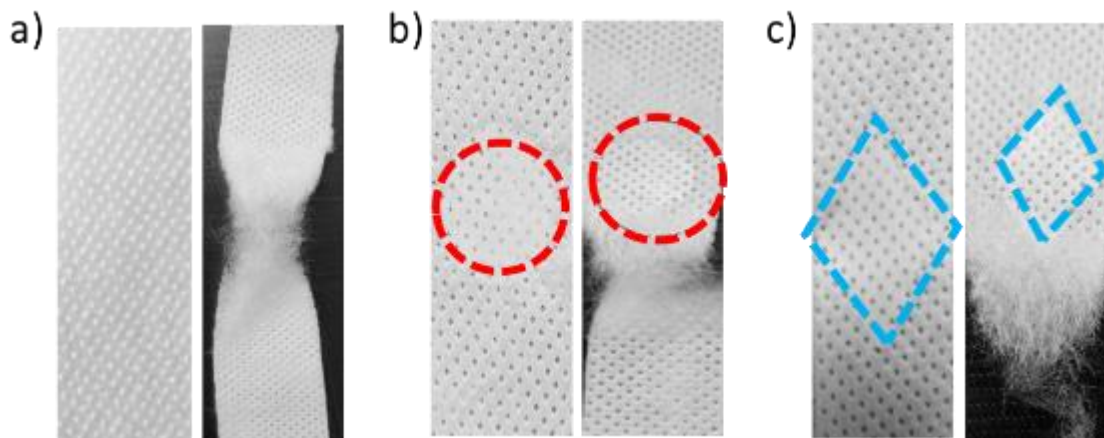


Figure 7. 9 Examples of the effect of stretching in tensile tests on rupture patterns. (a) The as-

received PBT nonwoven before and after tensile test, (b) the PBT nonwoven with a circular bond before and after tensile test, and (c) the PBT nonwoven with a rhombic bond before and after tensile test. The red and blue dashed lines encompass the bond pattern implemented on the circular bonded as well as rhombic bonded samples.

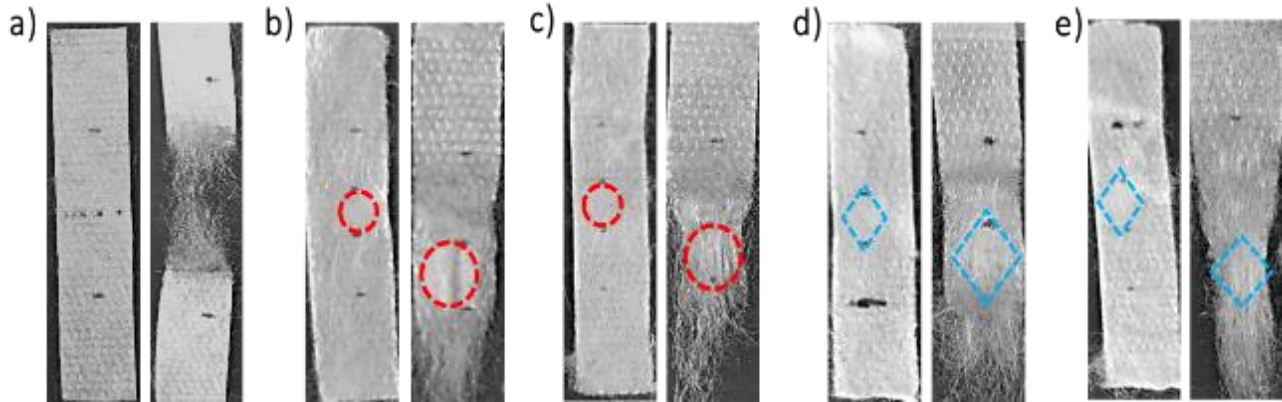


Figure 7. 10 Examples of the effect of tensile test on rupture patterns. (a) The as-received PBT/PE 80/20 nonwoven before and after tensile test, (b) the PBT/PE 80/20 nonwoven with a 110 °C circular bond before and after tensile test, (c) the PBT/PE 80/20 nonwoven with a 120 °C circular bond before and after tensile test, (d) the PBT/PE 80/20 nonwoven with a 110 °C rhombic bond before and after tensile test, and (e) the PBT/PE 80/20 nonwoven with a 120 °C rhombic bond before and after tensile test. The red and blue dashed lines encompass the bond pattern implemented on the circular bonded as well as rhombic bonded samples. Black dots and horizontal lines on the samples were drawn to facilitate the experiments and do not represent holes.

From the failure patterns depicted in Figures 7.9 and 7.10, it is seen that rupture in the as-received nonwoven samples occurred at the center due to the elongation in tensile tests. However, for the bonded samples, the rupture happens around the bond periphery (see Figures 7.9b- 7.9c and 7.10b- 7.10e). Note that such rupture patterns around the periphery were observed in all 10

samples in the tests conducted for the circular punches as well as the rhombic punches in the PBT-nonwoven and also the PBT/PE 80/20 nonwoven. Such a result further corroborates the results related to sample toughness discussed in subsection 7.3.2. There it was observed that failure at the bond periphery was due to the stress concentration caused by the bonds. Furthermore, this phenomenon leads to a decrease in toughness of the PBT nonwovens.

7.3.4 Theoretical prediction of the stress concentration and rupture location

The theoretical solutions of the problem on the stress distributions surrounding a circular thermal bond obtained in Appendix C and providing insights into the experimentally observed failure patterns are illustrated below. As an example, the parameter values used were: the ratio of the Young's moduli of the bond and the surrounding matrix $E_2/E_1=10$, the Poisson's ratios of the bond and the surrounding matrix $\nu_1=1/2$, $\nu_2=0.4$, respectively, and the ratio of the stretching stress to Young's modulus of the matrix $\sigma/E_1=0.1$. In all the figures below the coordinates and displacements are rendered dimensionless by the radius of the inclusion circle (the bond) R , and the stresses-by the stretching stress σ .

Figure 7.11 shows the field of displacement v in the y -direction and Figure 7.12 shows the field of displacement u in the x -direction in material 1 plotted using Eqs. (C19)- (C21), (C26) and (C27) from Appendix C.

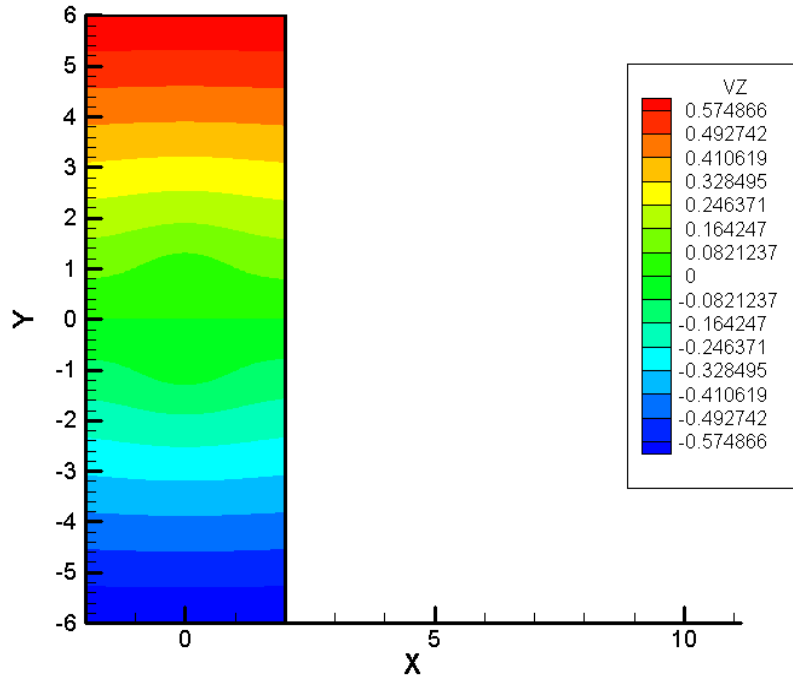


Figure 7. 11 The field of displacement v.

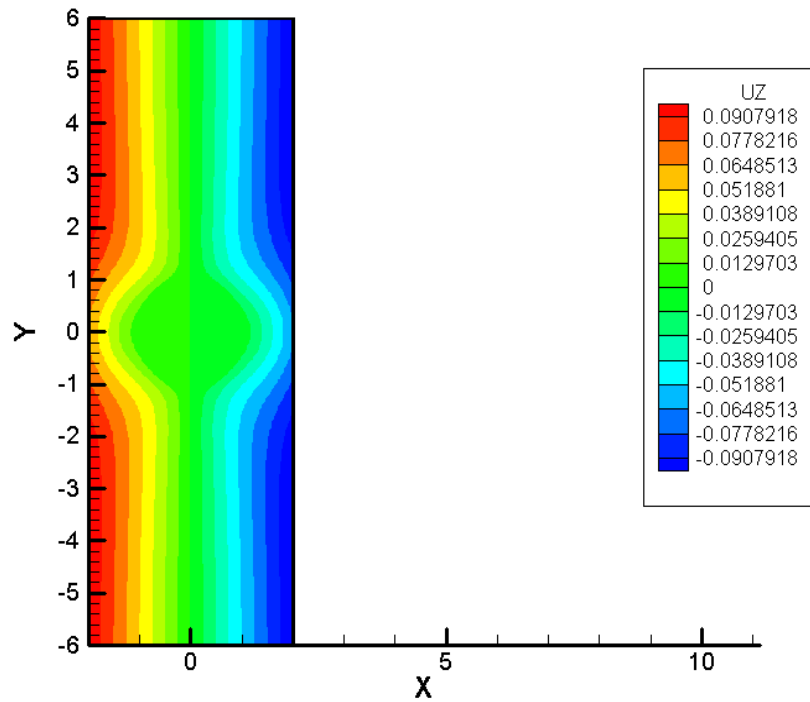


Figure 7. 12 The field of displacement u.

Figure 7.13 shows the displacement in the direction of stretching in the outer material along

the direction of stretching y plotted using Eq. (C29) from Appendix C.

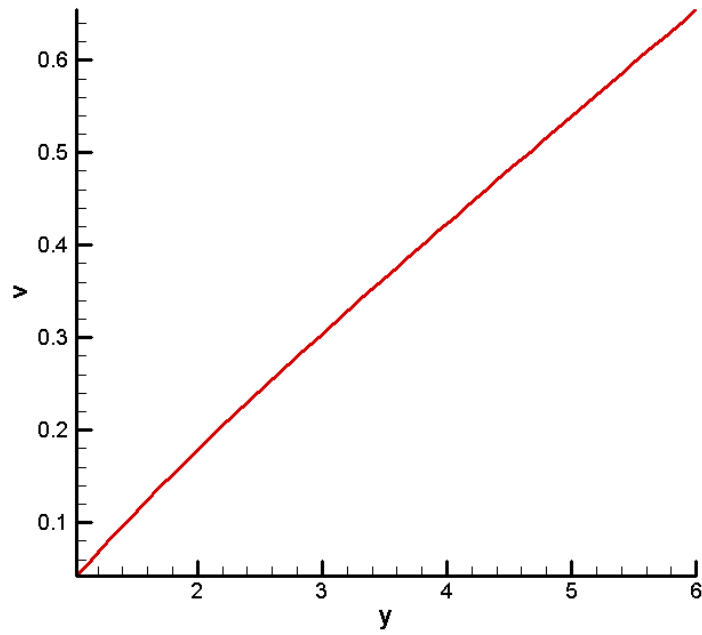


Figure 7. 13 Displacement v in material 1 along the stretching axis.

The stress fields in the entire material 1 and the inclusion 2 plotted using Eqs. (C31)- (C41) from Appendix C are shown in Figures 7.14- 7.16.

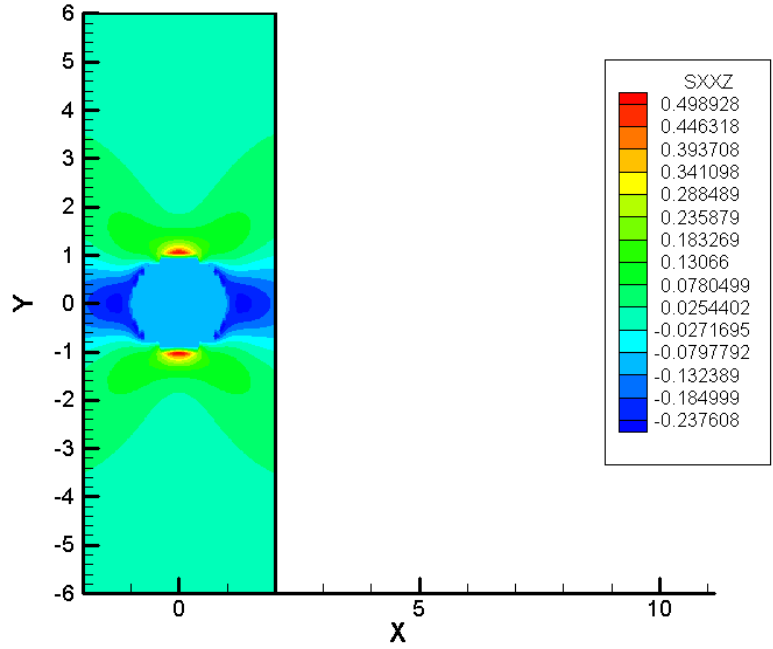


Figure 7. 14 The stress field σ_{xx} .

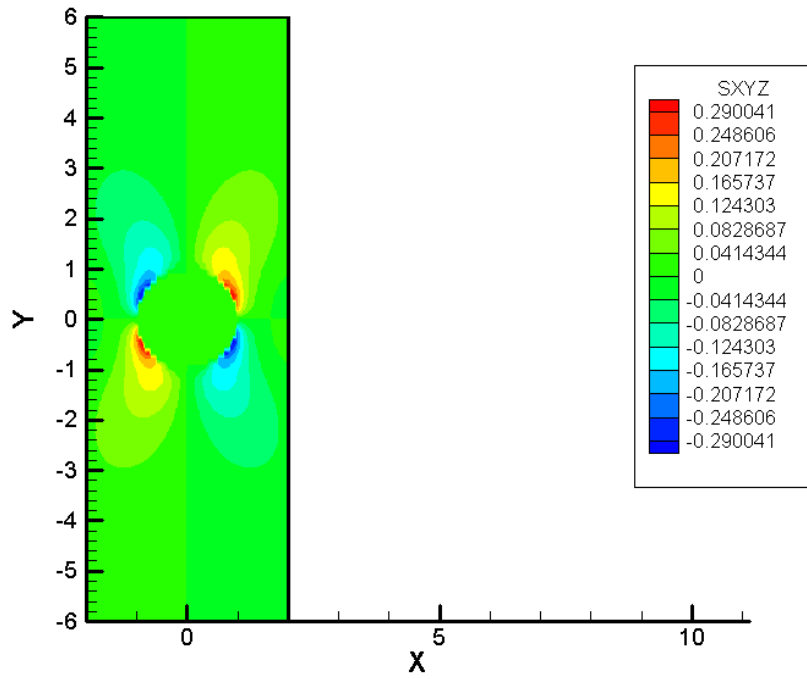


Figure 7. 15 The stress field σ_{xy} .

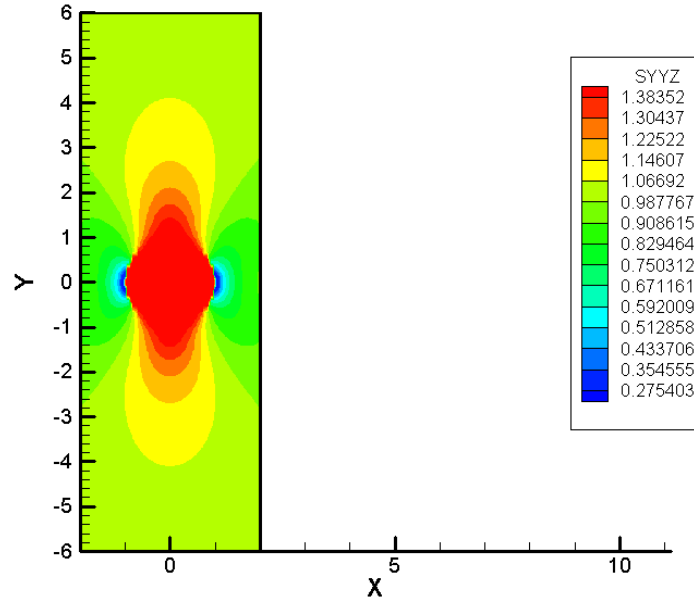


Figure 7. 16 The stress field σ_{yy} .

The stretching stress σ_{yy} near the inclusion in Figure 7.16 exceeds the stretching stress at infinity by about 40%. These results show that a thermal bond acts as a stress concentrator, which triggers rupture at its periphery. Comparing this prediction to the experimental results, it is implied that such a stress concentration led to an early failure of a bonded PBT nonwoven and as a result, a decrease in its toughness. Moreover, the failure patterns at the bond peripheries in Figures 7.9 and 7.10 are also in a qualitative agreement with this prediction.

It should be emphasized that a dramatic increase in the crystallinity of the bond point and the corresponding increase in the value of E_2 would likely lead to a further increase in stress at the bond point periphery during stretching. Such an increase in the stress would lead to an early rupture at the periphery, as the results of the tensile tests and the theory demonstrate. This prediction also agrees with the work [Michielsen et al. (2006)] where it was demonstrated that there exists an optimum bonding temperature corresponding to a desirable increase in the mechanical strength of nonwovens.

7.4 Conclusions

The experimental investigation in tensile tests of the effect of the additional thermal bonds on two types of nonwovens, PBT nonwoven and PBT/PE 80/20 nonwoven, elucidated the effect of thermal bonding on the overall mechanical performance. It was found that the addition of a bond, either circular or rhombic, increased the nonwoven stiffness, the yield strength, and the maximum stiffness for both types of nonwovens tested. However, when a PBT nonwoven was bonded, a decrease in toughness was observed. Such a decrease was due to an increased stress at the bond periphery (the stress concentration there) facilitating failure. A theory was also presented which demonstrated that thermal bonds act as stress concentrators, increasing the tensile stress up to 140% at the bond periphery. Such an increase in tensile stress can and does trigger failure at the bond periphery as revealed by the failure patterns experimentally.

In the PBT/PE 80/20 nonwovens, a further increase in the toughness of the nonwoven samples was apparent, which was significantly different from the phenomena observed in the PBT nonwovens. This occurred because during bonding of PBT/PE 80/20 nonwovens, only PE fibers melted and bonded the un-melted PBT fibers, interlocking the web. Due to such interlocking, these bonds would compensate for the increased stress at the bond periphery. Here, these bonds would most likely slowly rupture during tensile tests and as a result, lead to an overall increase in the toughness of such material.

Due to the larger bonding area of the circular bond in comparison to that of the rhombic bond, an increase in the yield stress and the maximum stress at failure was observed in the former case. Such an increased area can also explain a lower Young's modulus resulting from the rhombic bonding.

CHAPTER 8

HEAT-TRANSFER AND COHESION ENERGY OF THERMALLY- BONDED NONWOVENS: EXPERIMENTS AND THEORY

(This chapter has been previously published as Zhang, W., Yarin, A. L., Pourdeyhimi, B. (2019). Cohesion energy of thermally- bonded polyethylene terephthalate nonwovens: Experiments and theory. *Polymer Testing*, 78, 105984.)

8.1 Introduction

The present chapter aims at measurements and theoretical evaluation of the cohesion energy resulting from calendar bonding of nonwovens. The experimental part is described in section 8.2. In particular, the tensile properties of the nonwovens are measured in subsection 8.2.1. This data is required in the subsequent blister test, which is described in subsection 8.2.2. The theories associated with the thermal calendar bonding process and the estimate of the adhesion or cohesion energy are presented in section 8.3, where the comparison with the experimental data is also discussed. Conclusions are drawn in section 8.4.

8.2 Experimental

8.2.1 Tensile tests of the as-received and thermally-bonded PET nonwovens

The materials used in the current work were polyethylene terephthalate (PET) nonwovens. The as-received PET nonwovens have the base weight of 18.25 GSM (gram per square meter) with

the average measured thickness (1 layer) of 0.24 mm. The melting temperature and glass transition temperature of PET are 250 °C and 80 °C, respectively [Mandal (2009)]. The density of PET is 1.32 g/cm³ [Mandal (2009)]. Tensile tests were conducted with as-received and thermally-bonded PET nonwovens.

The thermal bonding setup employed here was similar to the one used in the literature in Zhang et al. (2018) (cf. Figure 8.1). In brief, in this setup an aluminum casing was installed in an Arbor press and could only be moved in the vertical direction. An interchangeable heated punch was attached to the aluminum casing. The rectangular punch used in the present work had a length of 50.8 mm, width of 24.5 mm, and the total area of 1244.6 mm². A 1 mm in diameter hole was drilled within the stainless-steel punch (cf. Figure 8.2b). A cartridge heater (CSH- 201200/120V) was embedded in the casing and connected to the temperature controller, which could regulate the front temperature of the interchangeable punch. A thermal couple (Omega model 5TC- PVC-T-24-180) connected to the controller was inserted into the hole of the punch. The bonding temperature was selected as 160 °C, 170 °C, 180 °C, 190 °C, and 200 °C. The contact time of the thermal punch with nonwoven samples was maintained around 1 s.

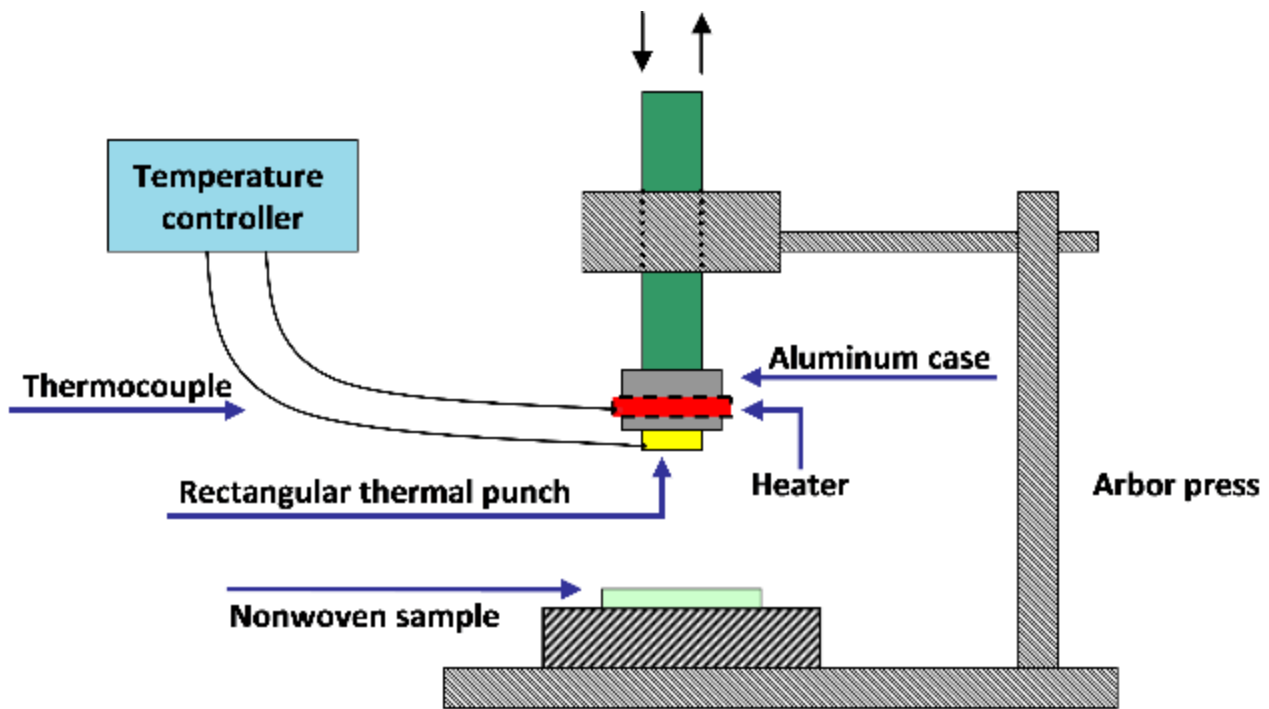


Figure 8. 1 Schematic of the thermal bonding setup.

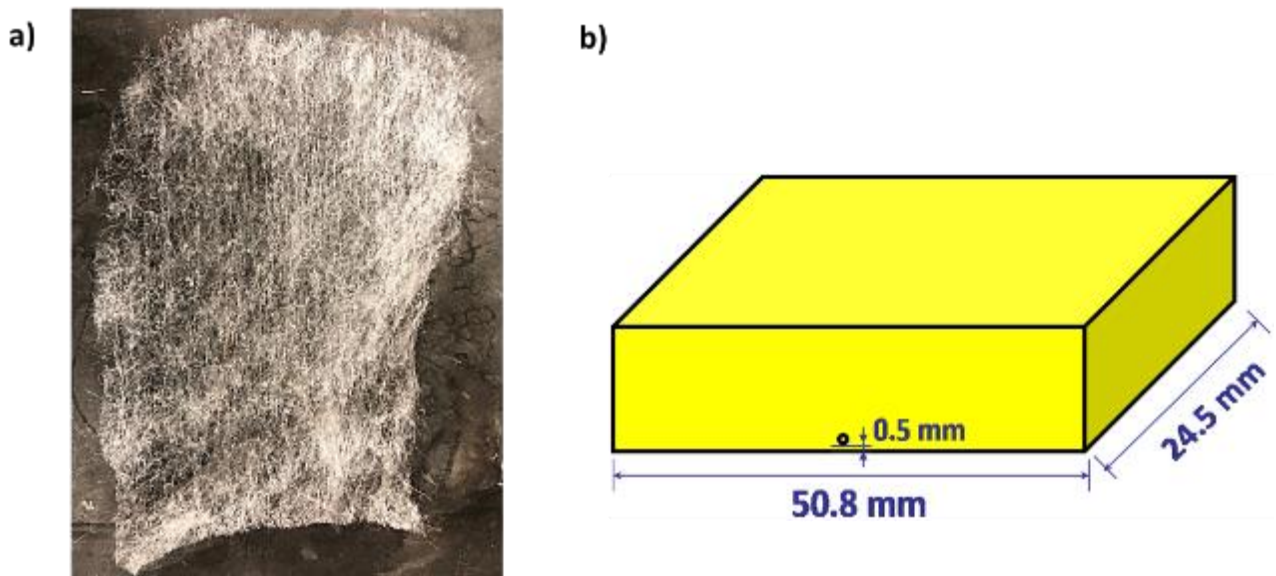


Figure 8.2 (a) A single layer of the as-received nonwovens. (b) Schematic of the rectangular thermal punch.

Tensile tests of the as-received and thermally-bonded PET nonwovens were conducted

with the Instron machine (model 5942) equipped with a 100 N load cell to obtain the entire stress-strain curves. The as-received PET nonwovens (cf. Figure 8.2a) were stacked into eight layers, which could guarantee uniformity of the tested samples, and used in the tensile tests. They were cut from the nonwoven sheets in the machine direction as specimens with the dimension of 22 mm in width and 90 mm in length. Also, the as-received nonwovens were stacked in six layers. These specimens were thermally bonded together and then used in tensile tests. In particular, in the experiments all six layers were bonded with the bonding time being 1 s. It should be emphasized that the six instead of eight layers of nonwovens were used for the thermal bonding process, because eight layers were too thick for that process. Thus, the layer number was reduced. The dimensions of the specimens of thermally-bonded nonwovens were 50.8 mm× 24.5 mm, which was identical to the dimensions of the thermal punch.

The materials used in the present experiments were received directly from the industrial partners and are non-uniform. To make uniform specimens required for the analysis of the experimental data using the existing theory of the tensile test and avoid the influence of the non-uniformity, eight layers of non-bonded nonwovens were used to evaluate the mechanical properties. For the thermally bonded specimens, only six layers of nonwovens were required for sufficient uniformity. It should be emphasized that the initial length and the numbers of layers used in the experiments were dictated by the size of the thermal punch and the subsequent blister test.

In the tensile tests the samples were clamped by pneumatic clamps of the Instron. The initial length of the specimens between the grips was 40 mm for the as-received specimens (without prior thermal bonding), and 30 mm for the thermally-bonded specimens due to the difference in their original dimensions. Ten trials were conducted in each type of experiments. The tensile test rate was 2 mm/ min. The Young`s moduli and the yield stress values were determined

from the data by fitting the phenomenological Green's equation [Green (1956)].

$$\sigma_{xx} = Y \tanh\left(\frac{E}{Y} \varepsilon_{xx}\right) \quad (8.1)$$

where σ_{xx} is the tensile stress, ε_{xx} the tensile strain, E is Young's modulus, and Y is the yield stress.

The maximum stress before failure σ_{max} and toughness τ of the nonwoven samples were also obtained in the current work similarly to the work of Zhang et al. (2018). Note that toughness is found via integration of the stress-strain curve and characterizes the ability of the material to 'absorb' energy during deformation. The average values of the above-mentioned mechanical properties of the as-received and thermally-bonded PET nonwovens are listed in Table 8.1. Examples of stress-strain curves for as-received and thermally-bonded nonwovens are shown in Figure 8.3. Note that the standard deviations obtained based on measurements of 10 specimens in each case are in line with those recorded for the other nonwovens [Yarin et al. (2014); Yarin et al. (2019)], which are highly inhomogeneous materials, in distinction from regular plastics. Nonwovens are inherently non-uniform materials with the chaotic internal structure. Even though macroscopically uniform (in thickness) specimens were prepared from the original industrial materials, it is impossible to guarantee that exactly the same number of fibers will be sintered during thermal bonding. This explains the non-monotonous variation of Young's modulus with bonding temperature in Table 8.1.

Table 8.1 Mechanical properties of the as-received and thermally- bonded PET nonwovens.

Measurements were repeated at least 10 times in each case and used to obtain these results.

	Average Young`s modulus E (MPa)	Average yield stress Y (MPa)	Average maximum stress at failure σ_{max} (MPa)	Average toughness τ (MPa)
As-received PET	0.541±0.292	0.108±0.045	0.103±0.044	0.048±0.021
160 °C thermally-bonded PET	14.400±2.282	1.165±0.328	3.084±0.708	0.987±0.173
170 °C thermally-bonded PET	26.102±3.410	1.159±0.306	3.704±0.470	1.040±0.247
180 °C thermally-bonded PET	18.328±4.465	1.873±0.079	3.978±0.746	1.157±0.341
190 °C thermally-bonded PET	27.211±2.772	1.960±0.327	4.442±0.249	1.364±0.402
200 °C thermally-bonded PET	19.414±0.700	3.037±0.550	4.265±0.133	1.327±0.059

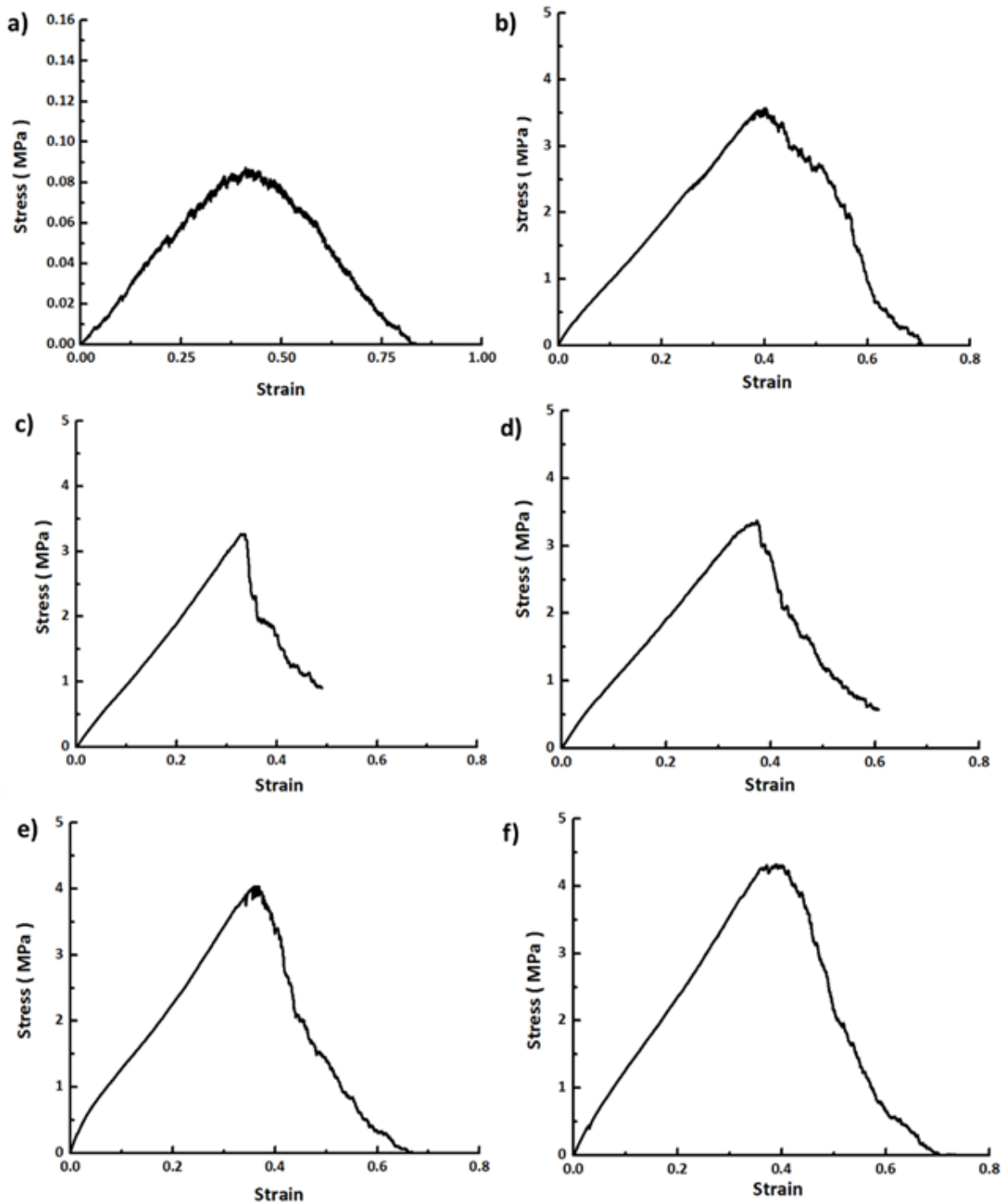


Figure 8.3 Examples of the stress-strain curves of the as-received and thermally- bonded nonwoven samples. (a) The as-received PET nonwovens. (b) The PET nonwovens thermally-bonded at 160 °C. (c) The PET nonwovens thermally- bonded at 170 °C. (d) The PET nonwovens

thermally- bonded at 180 °C. (e) The PET nonwovens thermally- bonded at 190 °C. (f) The PET nonwovens bonded at 200 °C.

8.2.2 Blister tests of thermally- bonded PET nonwovens

8.2.2.1 Thermal cohesion of PET nonwovens and optical observations

In the present subsection, the cohesion energy of PET nonwovens bonded at different temperature was measured using blister tests. The nonwovens were cut in the machine direction into rectangles of 38.1 mm×63.5 mm in size directly from the as-received PET nonwoven mats and folded into three layers. A through hole of 3.1 mm in diameter was punched at the center of the three layers of the as-received nonwoven specimens (denoted as mat A in Figure 8.4). On top of mat A, additional three layers of the same-size as-received PET nonwovens (denoted as mat B in Figure 8.4) were placed. Then, mat A and mat B were thermally bonded together and the non-bonded (peripheral, see Figure 8.4) part was trimmed. The thermal bonding setup employed here was described in subsection 8.2.1. The average thickness of the bonded six layers in the sample used was measured as 0.36 mm.

It should be emphasized that in the blister test the shaft diameter is 1 mm, the hole diameter is 3.1 mm, whereas the specimen size is 50.8 mm × 24.5 mm, which is more than an order of magnitude larger than the two previous sizes. This is the standard acceptable size ratio for the membrane analysis used for the data interpretation. Moreover, the blister diameter was ~ 10 mm, also sufficiently larger than the shaft and the hole.

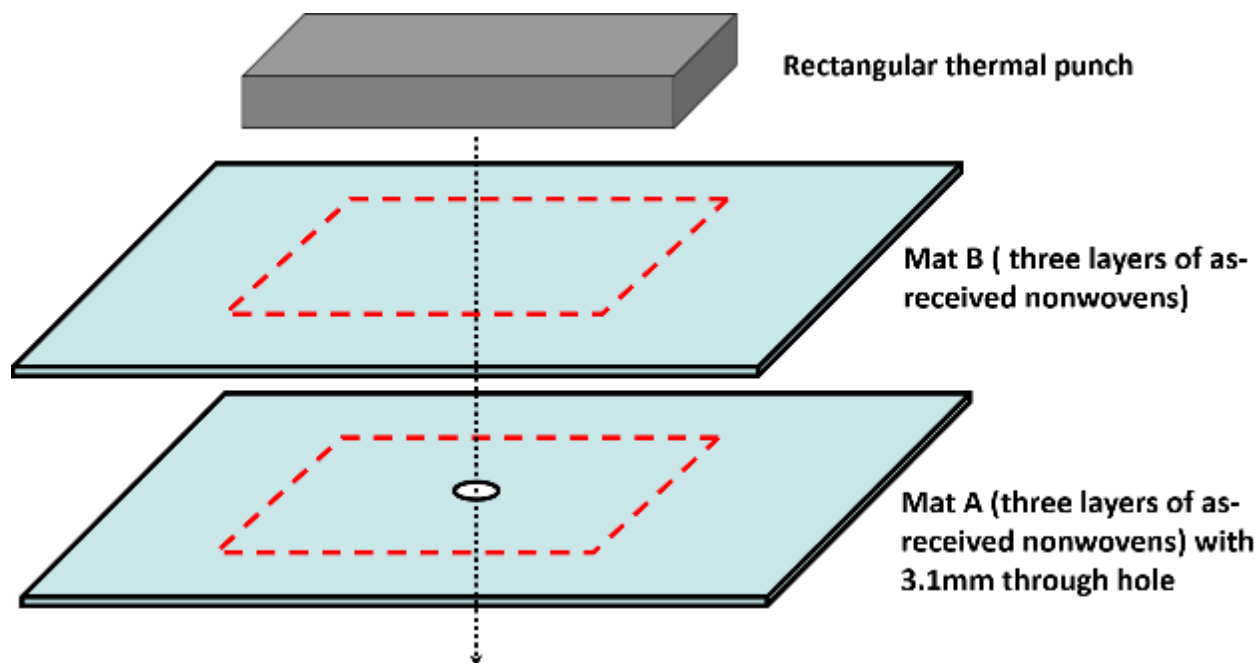


Figure 8. 4 Thermal bonding process used for PET nonwovens. Mat B was placed on the top of mat A, which had a 3.1 mm through hole at the center. Then, both mats were thermally bonded together by the rectangular thermal punch. The red dashed lines encompass the bonding area. The non-bonded part (outside the red dashed line) was trimmed after the thermal bonding process.

Hitachi S-3000N scanning electron microscope (SEM) was employed to image the as-received (cf. Figures 8.5a and 8.5b) and thermally- bonded PET nonwovens (cf. Figures 8.5c- 8.5f and 8.6a- 8.6f). The fibers in the as-received PET nonwovens were not bonded to each other. The average diameter of the individual PET fibers in the PET nonwovens was measured to be about 15.23 μm . After the as-received PET nonwovens were thermally bonded, the fibers under the bonding punch were sintered. It should be emphasized that the thermal bonding temperature was lower than the melting point of PET. It had been noticed that more fibers deformed and sintered as the thermal bonding temperature increased.

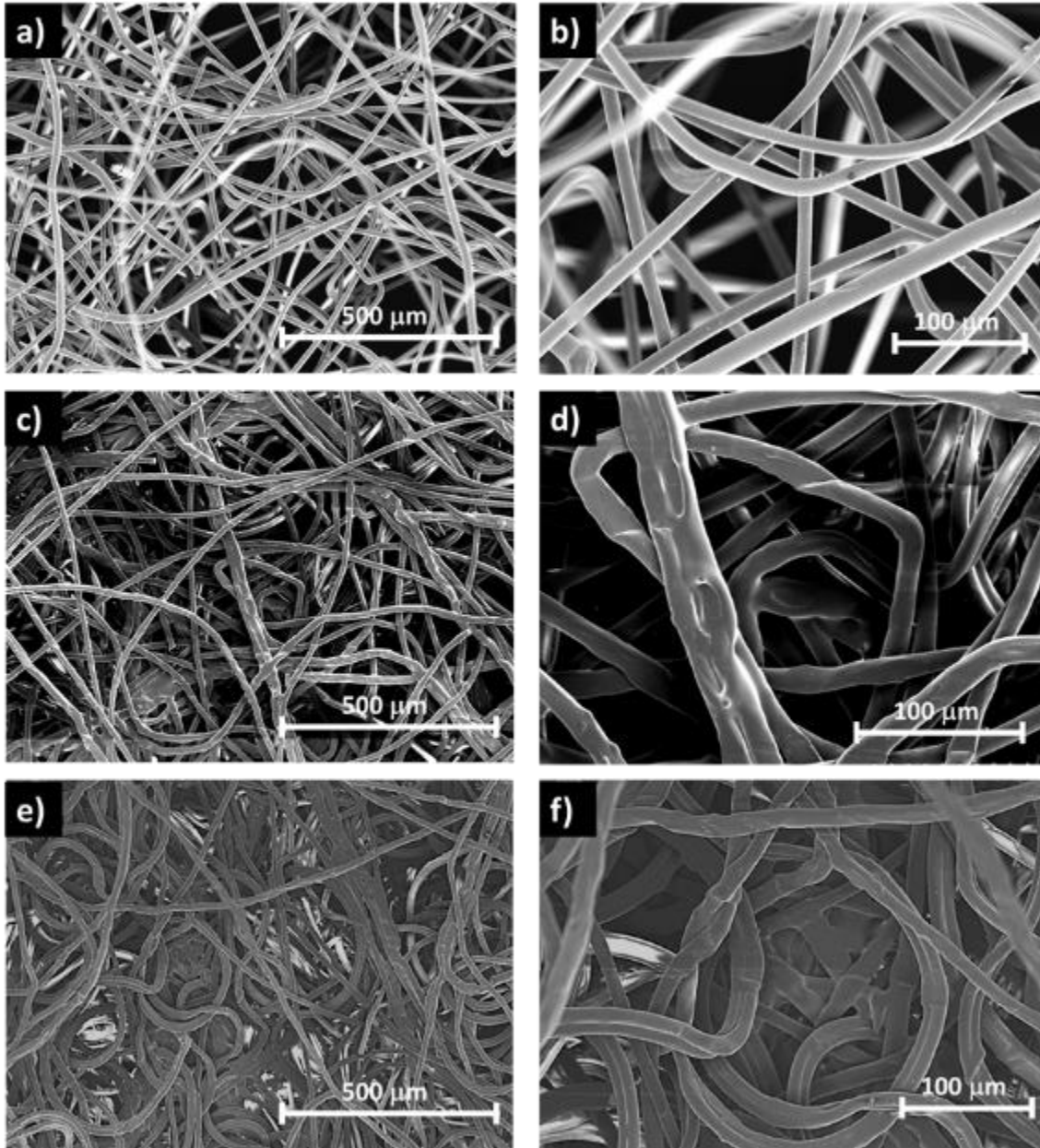


Figure 8. 5 SEM images of the as-received and thermally- bonded PET nonwovens. (a) and (b) The as-received PET nonwovens. (c) and (d) PET nonwovens thermally bonded at 160 °C. (e) and (f) PET nonwovens thermally bonded at 170 °C.

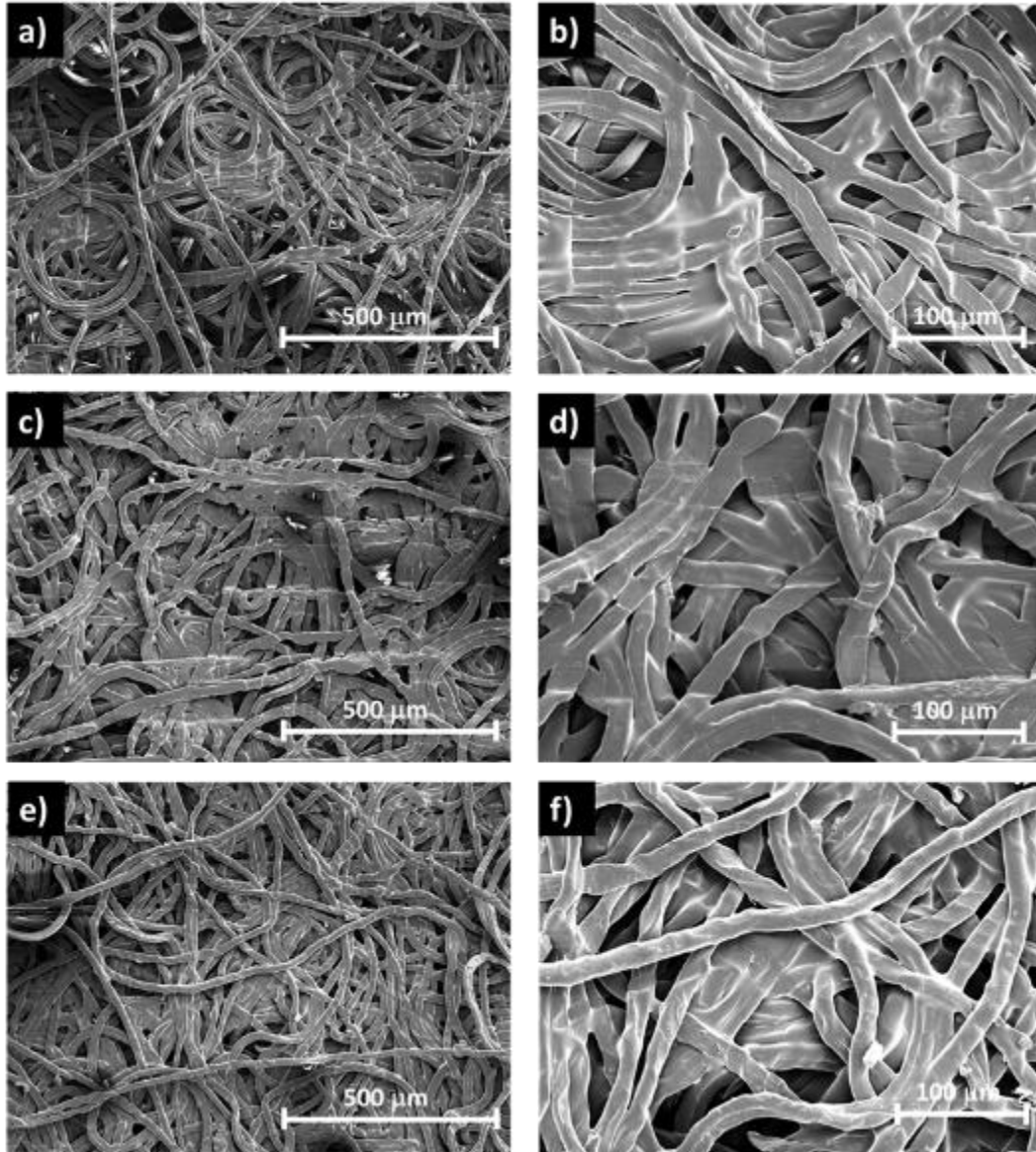


Figure 8. 6 SEM images of PET nonwovens thermally bonded at different temperatures. (a) and (b) PET nonwovens thermally bonded at 180 °C. (c) and (d) PET nonwovens thermally bonded at 190 °C. (e) and (f) PET nonwovens thermally bonded at 200 °C.

8.2.2.2. Blister tests of thermally- bonded PET nonwovens

After thermal bonding, the bonded nonwoven samples were fixed on steel substrates by using the double-sided Scotch tape and gently pressed by finger to ensure firm attachment to the tape (cf.

Figure 8.7). The steel substrates, the double-sided tape and mat A had concentric 3.1 mm holes at the center.

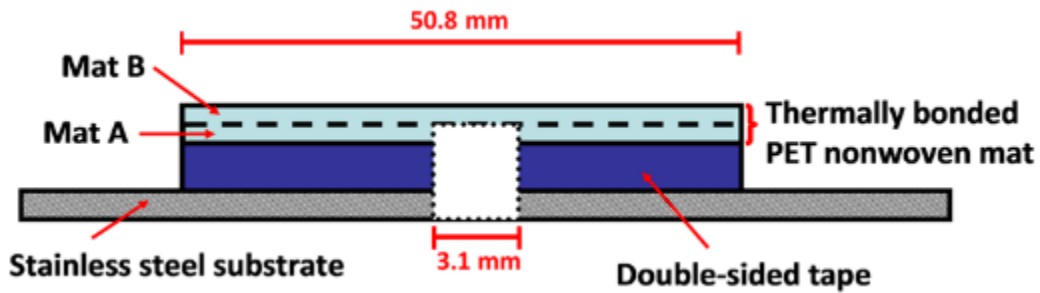


Figure 8. 7 The schematic of the prepared sample for the upcoming blister test. Thermally-bonded PET nonwoven mats were fixed by double-sided tape on the stainless-steel substrate. The steel substrates, the double-sided tape and mat A had concentric 3.1 mm holes at the center.

Blister tests were conducted using the Instron machine with a 500 N load cell to measure the cohesion energy of thermally-bonded PET nonwovens. A 1 mm in diameter shaft was attached to the 500 N load cell and advanced at two rates: 2 mm/ min or 10 mm/min. In each experiment, a blister would be ultimately formed due to the applied force imposed by the moving downward shaft and measured by the Instron (cf. Figure 8.8).

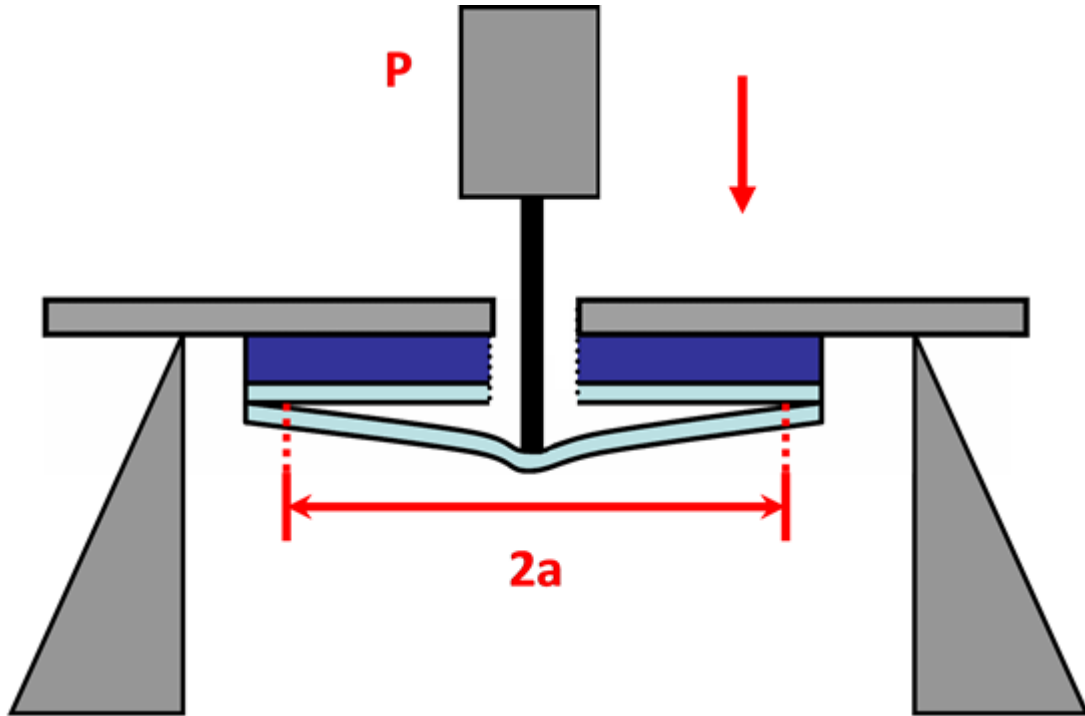


Figure 8. 8 Schematic of the blister test. The maximum force (P) before the failure of the nonwoven sample and the maximum blister diameter ($2a$) were measured.

Blister tests in each trial were interrupted when a nonwoven sample had failed. Blister formation was recorded using a Dino-Lite digital microscope. The videos obtained were analyzed by NCH editor and Image Pro Plus 7 (Media Cybernetics). Accordingly, the maximum blister diameter ($2a$) was measured. The examples of the final configurations of the blisters obtained from thermally-bonded at different temperatures PET nonwovens are shown in Figures 8.9 and 8.11. The examples of the load-extension curves are shown in Figures 8.10a and 8.12a. The corresponding measured values of the maximum blister diameter are shown in Figures 8.10b and 8.12b.

It should be emphasized that the poked blisters returned to the original configuration with zero deflection immediately, which manifests full reversibility, i.e., the immaterial plasticity and

viscoelasticity.

When blister tests were conducted at the rate of 2 mm/ min, the average values of the maximum blister diameter (2a) decreased as the thermal-bonding temperature increased. The reason for that was that PET nonwovens became stiffer at higher bonding temperatures, as illustrated by Figures 8.5 and 8.6. On the other hand, when blister tests were conducted at the rate of 10 mm/ min, the average values of the maximum blister diameter (2a) barely changed as the bonding temperature increased.

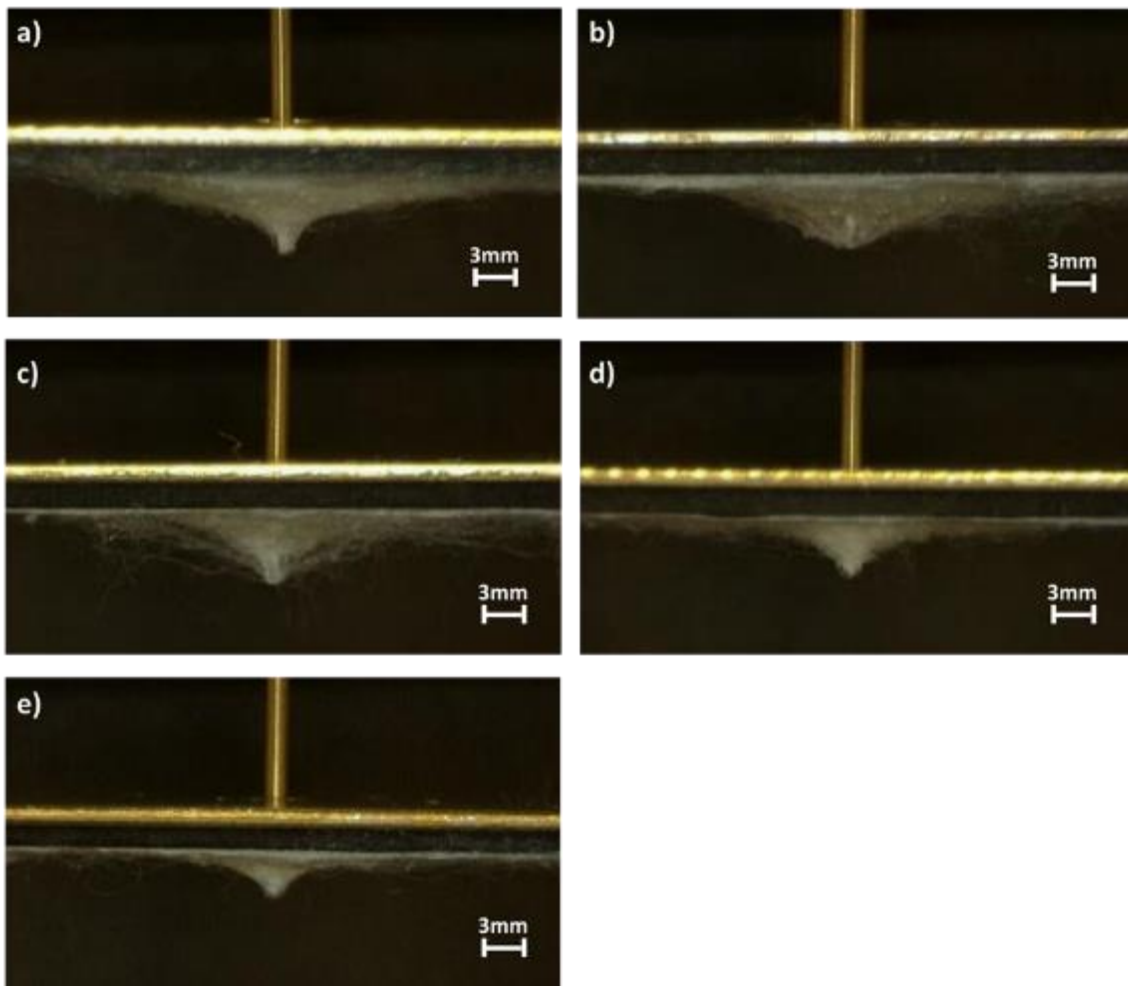


Figure 8. 9 Blister profiles of PET nonwovens obtained at the maximum force before the failure.

The nonwovens were thermally-bonded at different temperatures. The blister tests were conducted at the rate of 2 mm/min. (a) Bonding temperature of 160 °C. (b) Bonding temperature of 170 °C. (c) Bonding temperature of 180 °C. (d) Bonding temperature of 190 °C. (e) Bonding temperature of 200 °C.

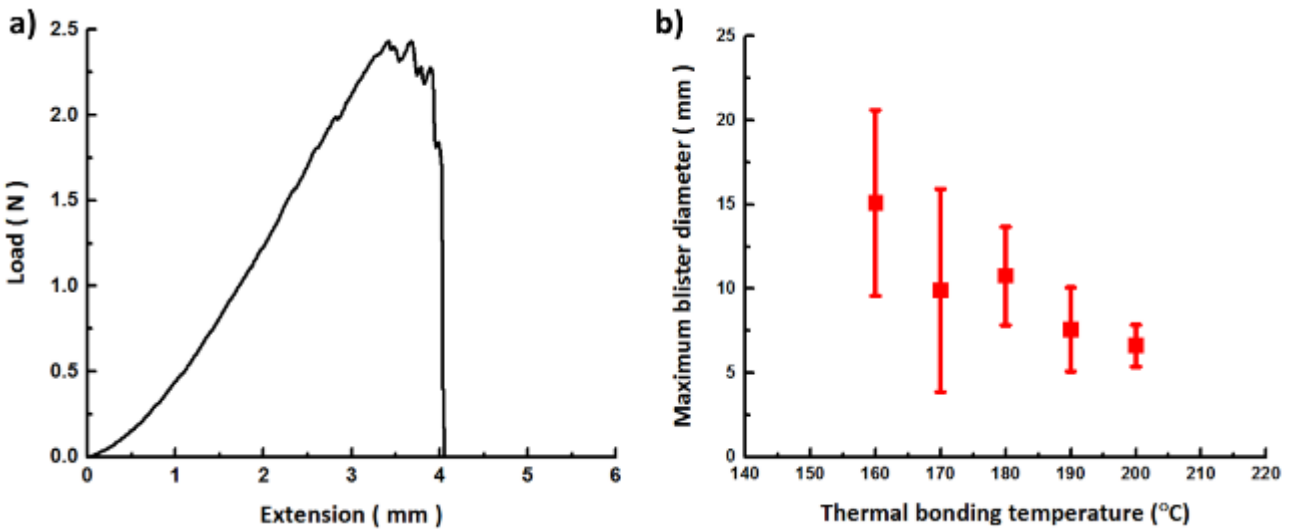


Figure 8. 10 (a) The load-extension curve. The thermal bonding temperature is 200 °C. (b) The maximum blister diameter versus bonding temperature. The blister tests conducted at 2 mm/ min.

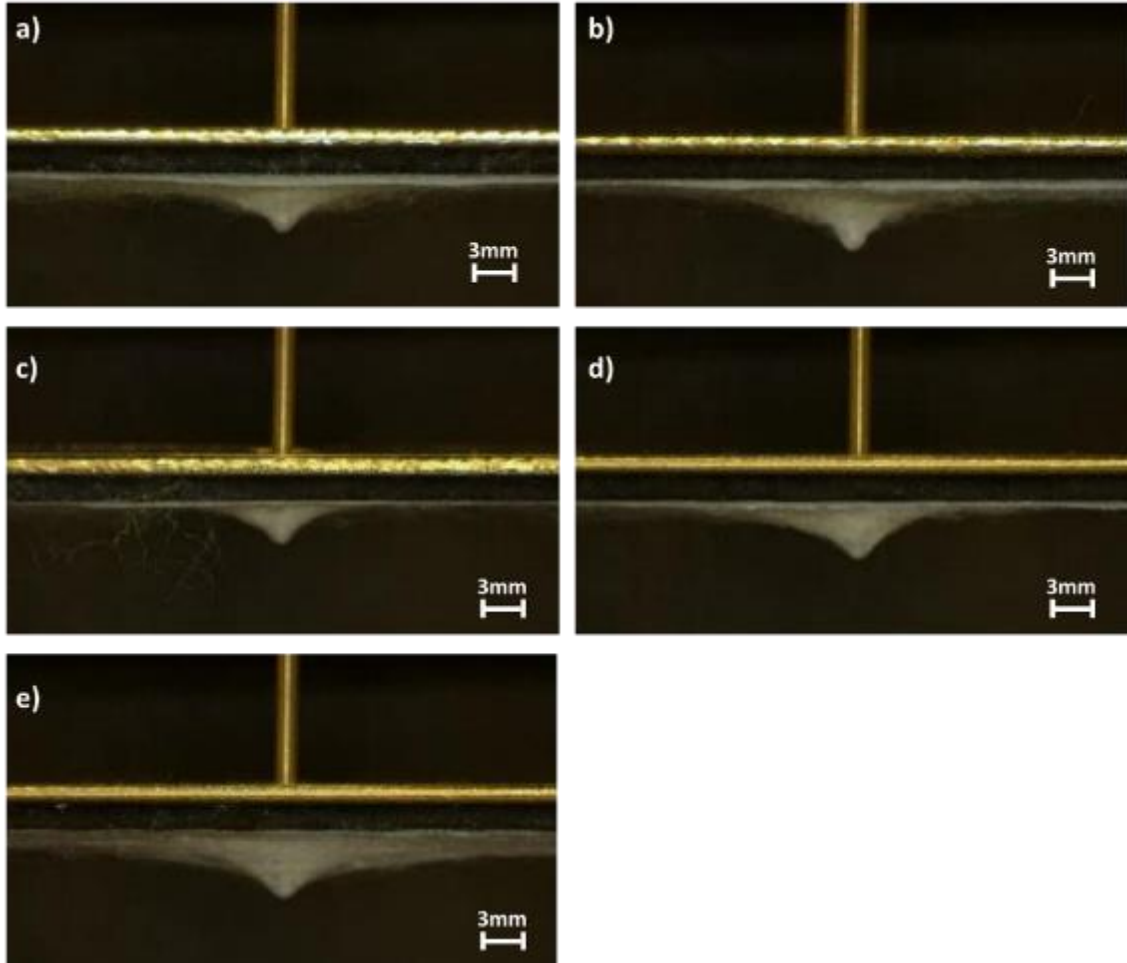


Figure 8. 11 Blister profiles of PET nonwovens obtained at the maximum force before the failure. The nonwovens were thermally- bonded at different temperatures. The blister tests were conducted at the rate of 10 mm/min. (a) Bonding temperature of 160 °C. (b) Bonding temperature of 170 °C. (c) Bonding temperature of 180 °C. (d) Bonding temperature of 190 °C. (e) Bonding temperature of 200 °C.

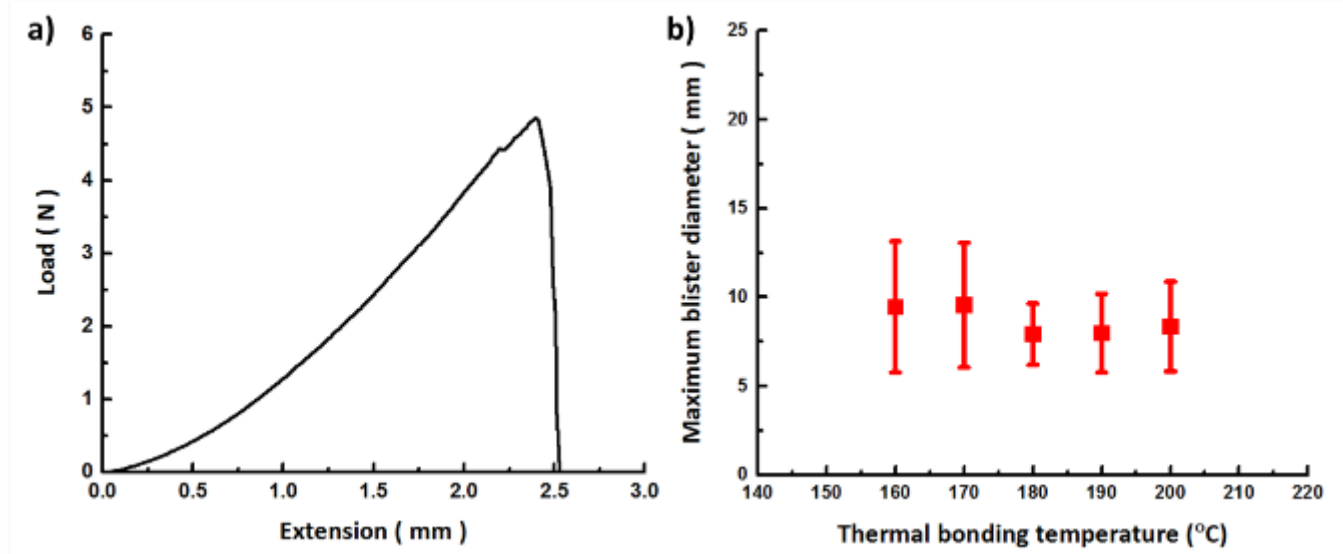


Figure 8. 12 (a) The load-extension curve. The thermal bonding temperature is 200 °C. (b) The maximum blister diameter versus bonding temperature. The blister tests conducted at 10 mm/ min.

The adhesion or cohesion energy of thermally-bonded nonwovens was found, similarly to the work of Staszal et al. (2017), by using the following expression derived by Lee et al. (2015)

$$T_{\text{cohesion}} = \frac{3}{8} \left(\frac{P^4}{\pi^4 E h a^4} \right)^{1/3} \quad (8.2)$$

where T_{cohesion} is the adhesion or cohesion energy, P is the peak load, E is Young's modulus of thermally-bonded PET nonwovens, h is the thickness of the folded three layers of thermally-bonded PET nonwovens, and a is the blister radius at the peak load [Yarin et al. (2019)].

It should be emphasized that Young's moduli E of the PET nonwovens thermally bonded under various conditions were measured in tensile tests in subsection 8.2.1. The average values of E in each case were used in Eq. (8.2). The corresponding average values of the cohesion energy of the thermally- bonded PET nonwovens are shown in Figure 8.13.

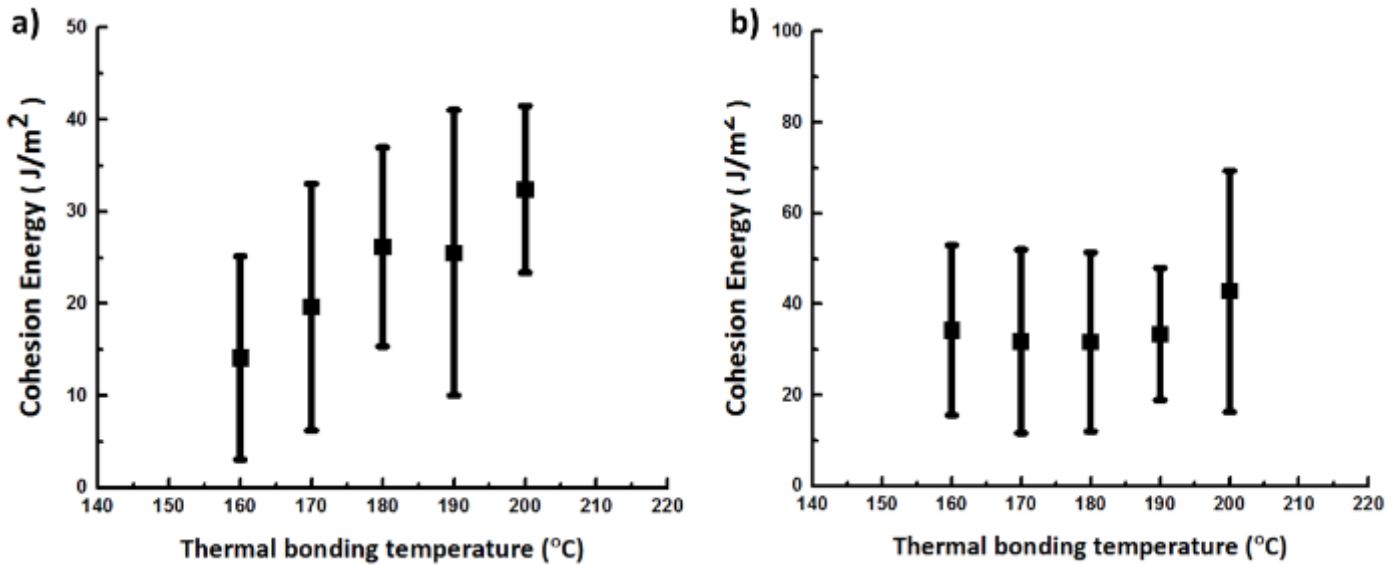


Figure 8.13 Cohesion energy of thermally- bonded PET nonwovens versus the bonding temperature. (a) Blister test conducted at the shaft rate of 2 mm/ min. (b) Blister test conducted at the shaft rate of 10 mm/ min.

According to the data obtained, the cohesion energy of the thermally- bonded PET nonwovens found from the tests with 2 mm/ min increased as the bonding temperature increased. On the other hand, the cohesion energy of the thermally- bonded PET nonwovens found from the tests with 10 mm/ min rate essentially reached a plateau.

The measured value of the cohesion energy are compared in subsection 8.3.5 with those predicted for calendar bonding in the nip.

8.3 Theoretical

8.3.1 Calendar bonding in the nip

Consider the first stage of calendar thermal bonding process, with the nonwoven layer

passing through a heated calendar nip with a velocity V . The calendar nip is between two cylindrical rollers of radius R . Note that the velocity $V=\omega R$, where ω is the angular velocity of the rollers. The rollers press against each other, and thus squeeze the nonwoven layer with a constant force F . Both cylindrical rollers are heated to a selected temperature T_c . Accordingly, when the nonwoven layer passes through the calendar nip it is heated up and compressed, with both effects facilitating thermal bonding. A sketch of the nonwoven layer entering the nip is shown in Figure 8.14. When two metal cylindrical rollers are pressed toward each other with a normal force F , they elastically flatten in the contact area, and the length of the straightened perimeter of a roller, $2a_c$ (cf. Figure 8.14), is given by the solution of the Hertz problem [Landau and Lifshitz (1970)]

$$2a_c = \frac{4}{\sqrt{\pi}} \sqrt{\frac{(1-\nu^2)}{E_r}} FR \quad (8.3)$$

where E_r is Young's modules and ν is Poisson's ratio of the calendar rollers, and F is the compression force per unit cylinder length.

The residence time (the dwell time), which is the characteristic time for the nonwoven to pass through the calendar nip reads

$$\tau_{\text{residence}} = \frac{2a_c}{V} \quad (8.4)$$

The heating of a nonwoven element in the nip is essentially conductive and one-dimensional and can be described by the following heat transfer problem

$$\frac{\partial T_p}{\partial t} = \alpha_T \frac{\partial^2 T_p}{\partial x^2} \quad (8.5)$$

where T_p is the polymer temperature, α_T is the thermal diffusivity of polymer fibers (since the thermal diffusivity of air is negligibly small compared to that of the polymers [Staszal et al. (2016)], t is time, and x is the coordinate normal to the nip.

Solutions of Eq. (8.5) is subjected to the following initial and boundary conditions

$$\begin{aligned} t=0: & \quad T_p = T^0; \\ t>0: & \quad x=0, T_p = T_c; \quad x = h_{\text{nip}}, T_p = T_c \end{aligned} \quad (8.6)$$

where $t=0$ corresponds to the moment when a material element enters the nip, h_{nip} is the nip thickness, T^0 is the initial temperature of the nonwoven layer, and T_c is the cylindrical roller temperature. Note that $T_c > T^0$, and both temperatures are supposed to be known.

The solution of the problem (8.5) and (8.6) is straightforward and found by the method of variable separation [Tikhonov and Samarskii (1990)]. It reads

$$\frac{T_c - T_p}{T_c - T^0} = \frac{4}{\pi} \sum_{n_{\text{odd}}=1}^{\infty} \frac{1}{n} \exp\left(-\frac{\pi^2 n^2 t \alpha_T}{h_{\text{nip}}^2}\right) \sin\left(\pi n \frac{x}{h_{\text{nip}}}\right) \quad (8.7)$$

Accordingly, the characteristic time of the nonwoven heating is

$$\tau_{\text{heating}} = \frac{h_{\text{nip}}^2}{\pi^2 \alpha_T} \quad (8.8)$$

To achieve a good calendar bonding of nonwovens, the residence time $\tau_{\text{residence}}$ should be larger than the heating time τ_{heating} . Thus, Eqs. (8.3), (8.4) and (8.8) yield the following condition of good calendar bonding

$$\frac{1}{4\pi^{3/2}} \frac{V h_{\text{nip}}^2}{\alpha_T} \sqrt{\frac{E_r}{(1-v^2)FR}} \leq 1 \quad (8.9)$$

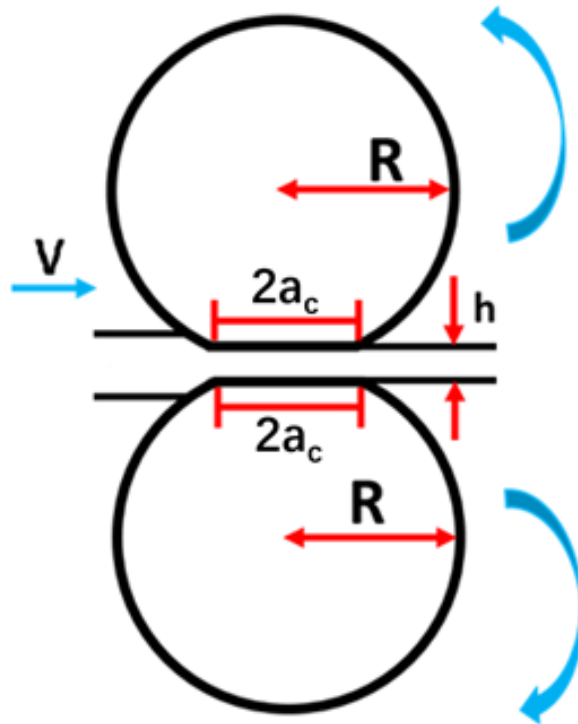


Figure 8. 14 Nonwoven passing through the calendar nip between two rollers.

8.3.2 Forces acting on nonwoven beyond calendar nip

Following the classical capstain theory of Euler, consider a section of a nonwoven layer which has already passed the calendar nip but still stays stuck to one of the rollers as depicted in Figure 8.15. The nonwoven layer is pulled to the right with force T , which is definitely a function of the polar angle $\Delta\alpha$, since friction $\Delta F_{\text{friction}}$ from the roller acts on the nonwoven section corresponding to the angle $\Delta\alpha$.

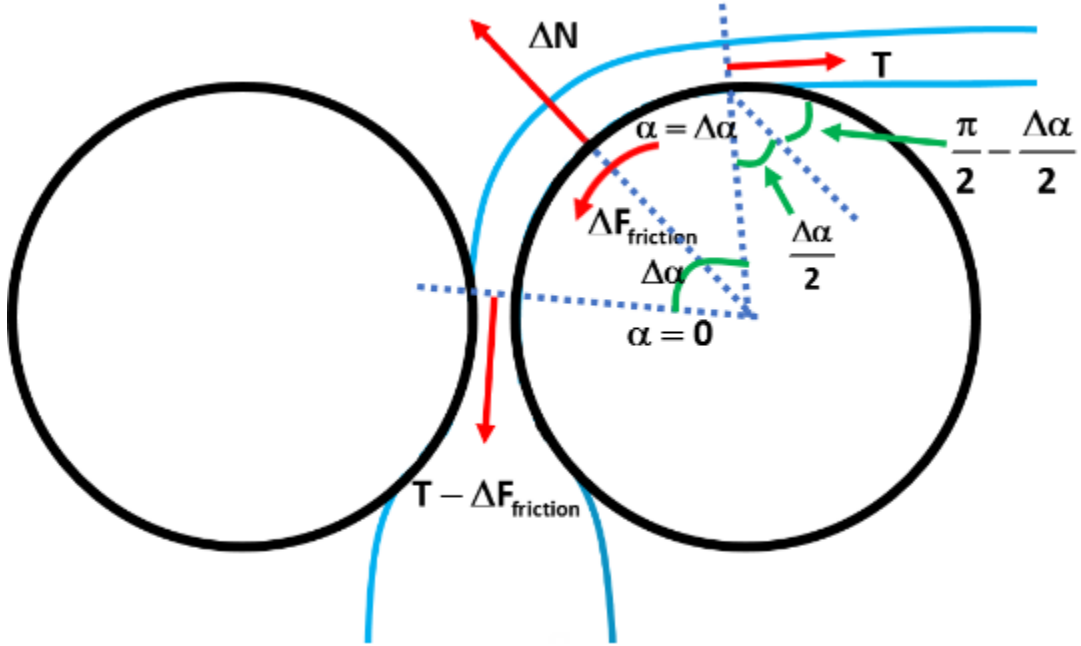


Figure 8. 15 Schematic of a nonwoven beyond the calendar nip. The angle $\Delta\alpha$ in this figure can be arbitrary (depending on the equipment used), and not necessarily 90° .

Consider a section of a nonwoven in contact with the roller corresponding to the angle $\Delta\alpha \ll 1$. The balance of forces acting on this section in the direction normal to the roller surface (the radial direction) reads

$$\Delta N = 2T \cos\left(\frac{\pi}{2} - \frac{\Delta\alpha}{2}\right) = 2T \sin\left(\frac{\Delta\alpha}{2}\right) \approx 2T \frac{\Delta\alpha}{2} = T\Delta\alpha \quad (8.10)$$

where ΔN is the compression force acting from the roller on the section of the nonwoven layer under consideration.

By the Amonton's law $\Delta F_{\text{frict}} = \mu\Delta N$, where μ is the friction coefficient. Thus, Eq. (8.10) yields

$$\Delta F_{\text{friction}} = \mu T\Delta\alpha \quad (8.11)$$

The friction force diminishes tension in the nonwoven, which is expressed as

$$\Delta T = -\Delta F_{\text{friction}} \quad (8.12)$$

according to the tangential projection of the force balance.

Then, Eqs. (8.11) and (8.12) yield

$$\frac{\Delta T}{T} = -\mu \Delta \alpha \quad (8.13)$$

Integrating the latter equation in the limit $\Delta \alpha \rightarrow 0$, one recovers the capstain (the Euler) equation

$$T = T_0 \exp(-\mu \alpha) \quad (8.14)$$

where T_0 is the tension in the nonwoven cross-section which has just left the nip.

Eqs. (8.10) and (8.14) yield the following expression for the compression force acting on the chosen section,

$$\Delta N = T_0 \exp(-\mu \alpha) \Delta \alpha \quad (8.15)$$

Integrating the latter equation in the limit $\Delta \alpha \rightarrow 0$, and accounting for the boundary condition $N=0$ at $\alpha=0$, one obtains the following expression for the distribution of the compression force experienced by the nonwoven in contact with the roller at $0 < \alpha < \alpha_*$,

$$N = \frac{T_0}{\mu} [1 - \exp(-\mu \alpha)] \quad \text{at } 0 < \alpha < \alpha_* \quad (8.16)$$

Note that this compressive force N will facilitate sintering, i.e., thermal bonding in the nonwoven section still in contact with the roller beyond the calendar nip up to an angle α_* .

A material element of a nonwoven in contact with the roller moves with an angular velocity ω , i.e., $\alpha = \omega t$, where time t is reckoned from the moment the element left the calendar nip.

Accordingly, Eq. (8.16) takes the form

$$N(t) = \frac{T_0}{\mu} [1 - \exp(-\mu\omega t)] \quad \text{at} \quad 0 < t < \frac{\alpha_*}{\omega} \quad (8.17)$$

8.3.3 Sintering area in thermal bonding

Consider sintering under the action of the compressive force acting on the nonwoven in contact with the roller beyond the calendar nip using the simplified two-dimensional model sketched in Figure 8.16, where the fiber radii are taken as a_0 and it is implied that the entire 'box' (an element in the nonwoven cross-section) is 1×1 in size and fully filled with the fibers. Thus, the number of fibers per unit length of the 'box' side is $n' = 1/2a_0$. Accordingly, the number of contacts per unit area of the 'box' bottom is $n = 1/4a_0^2$. Note that the units of n are cm^{-2} .

The compressive force ΔN acts on the surface $R\Delta\alpha$ of a nonwoven element, as considered in subsection 8.3.2, with R being the roller radius. Therefore, according to Eq. (8.15) the magnitude of the compressive stress acting on the nonwoven in contact with the roller beyond the calendar nip is

$$|\sigma'(t)| = \frac{T_0 \exp(-\mu\omega t)}{R} \quad \text{at} \quad 0 < t < \frac{\alpha_*}{\omega} \quad (8.18)$$

Note that the compressive stress σ' can also be expressed as

$$\sigma' = \sigma_{xx}(1 - m) \quad (8.19)$$

where m is the surface porosity and σ_{xx} is the real stresses acting in all contacts over a unit area of the 'box' bottom.

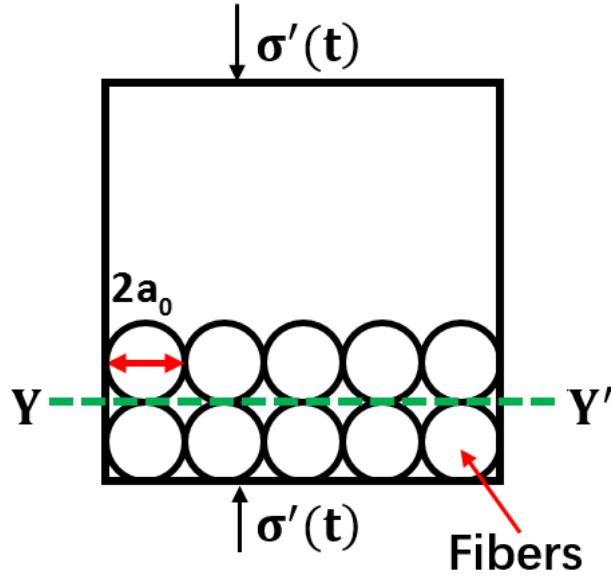


Figure 8. 16 Schematic of sintering (thermal bonding) under the action of compressive force acting on nonwoven.

Let the radius of a current contact area between two fibers be y (see Figure 8.17). It is implied that fibers are not necessarily parallel to each other, while their complicated contact area is reduced to an equivalent circle of radius y . Then, the cross-sectional area of the solid-solid contacts over the plane YY' in Figure 8.16 (cf. also Figure 8.17) would be

$$n\pi y^2 = 1 - m \tag{8.20}$$

The compressive force per unit contact, using Eqs. (8.19) and (8.20), is found as

$$f = \frac{|\sigma_{xx}|}{n} = \frac{|\sigma'(t)|}{(1 - m)n} = \frac{|\sigma'(t)|}{n^2\pi y^2} \tag{8.21}$$

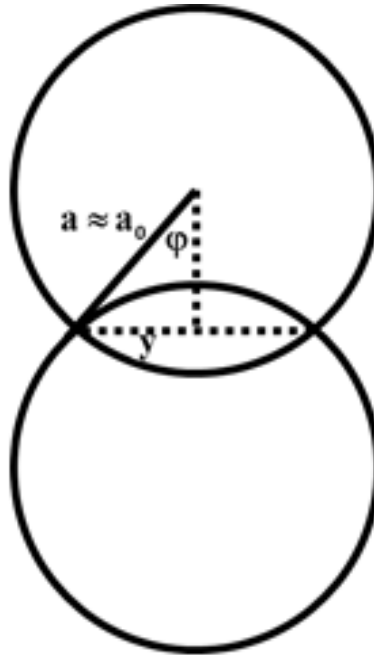


Figure 8. 17 Sintering of two fibers.

Then, the compressive stress magnitude at the contact of two individual fibers is

$$\sigma = \frac{|\sigma'(t)|}{n^2 \pi^2 y^4} \quad (8.22)$$

The power provided by such a compression through an individual contact reads

$$P_{\text{supplied}} = f \frac{d}{dt} [a_0 (1 - \cos \varphi)] \quad (8.23)$$

where the angle φ is defined in Figure 8.17.

Using Eq. (8.16), and considering the limit of $\varphi \ll 1$, one reduces Eq. (8.23) to the following form

$$P_{\text{supplied}} = \frac{|\sigma'(t)| a_0}{n^2 \pi y^2} \frac{d}{dt} \left(\frac{\varphi^2}{2} \right) \quad (8.24)$$

In the pseudo-plastic deformation regime, the stress-strain relation reads [Geguzin (2014);

Librovich and Yarin (1988)]

$$\sigma = K \left(\frac{d\varepsilon}{dt} \right)^w \quad (8.25)$$

where K and w are the rheological parameters of the pseudo-plastic power law, and the strain according to Eq. (8.24), in the limit $\varphi \ll 1$ is $\varepsilon = \varphi^2 / 2$.

The power supplied by the compression force is spent for dissipation. The power dissipated per unit volume reads

$$P_{\text{dissipation}} = 4\pi a_0^2 \ell K \left[\frac{d}{dt} \left(\frac{\varphi^2}{2} \right) \right]^{w+1} \quad (8.26)$$

where the equivalent length along two fibers which is sintered is denoted ℓ .

Since power supply is equal to the power dissipation, $P_{\text{supplied}} = P_{\text{dissipation}}$, according to Eqs. (8.24) and (8.26) one obtains

$$\frac{|\sigma'(t)| a_0}{n^2 \pi y^2} \frac{d}{dt} \left(\frac{\varphi^2}{2} \right) = 4K\pi a_0^2 \ell \left[\frac{d}{dt} \left(\frac{\varphi^2}{2} \right) \right]^{w+1} \quad (8.27)$$

Since $y \approx a_0 \varphi$ (cf. Figure 8.17) and $n^2 = 1/16a_0^4$, the contact area $S = \pi a_0^2 \varphi^2$ is found as

$$S^{1/w} \frac{dS}{dt} = \left[\frac{|\sigma'(t)| a_0^{3+2w} 2^w \pi^{w-1}}{K\ell} \right]^{1/w} \quad (8.28)$$

Substituting Eq. (8.18) into Eq. (8.28), transform it to the following form

$$\frac{dS^{1+1/w}}{dt} = \left(\frac{w+1}{w} \right) \left[\frac{T_0}{R} \frac{a_0^{3+2w}}{\ell} \frac{2^w \pi^{w-1}}{K} \right]^{1/w} \exp\left(\frac{-\mu\omega t}{w} \right) \quad (8.29)$$

In the isothermal case, e.g., when the nonwoven is still at the roller temperature $T_c = \theta_r$, and the rheological parameters $K = K(\theta_r)$ and $w = w(\theta_r)$ are constant, the sintered area $S(t)$ between two fibers sintered in the process of thermal bonding which continues beyond the calendar

nip at the roller surface is

$$S(t) = S_n \left\{ 1 + \left(\frac{a_0^2}{S_n} \right)^{(w+1)/w} \frac{2(w+1)}{\mu\omega} \left(\frac{T_0 a_0 \pi^{w-1}}{R \ell K} \right)^{1/w} \left[1 - \exp\left(-\frac{\mu\omega t}{w} \right) \right] \right\}^{w/(w+1)} \quad (8.30)$$

at $0 < t < \alpha_* / \omega$, where S_n is the sintered area that has been reached during thermal bonding inside the calendar gap and is still to be found.

In order to calculate S_n reached under the action of a constant compressive force P in the nip, one should use Eq. (8.28) with $|\sigma'(t)|$ being replaced by $|\sigma_0| = P/2a_c L$, where the flattened roller length $2a_c$ is obtained from the solution of the Hertz problem for cylinders Eq. (8.3), and L is the width of the calendar rolls. Then, Eq. (8.28) takes the form

$$S^{1/w} \frac{dS}{dt} = \left(\frac{P}{2a_c L} \frac{a_0^{3+2w} 2^w \pi^{w-1}}{K \ell} \right)^{1/w} \quad (8.31)$$

It should be emphasized that in Eq. (8.31) time t is reckoned from the moment an individual element of nonwoven has entered the nip. Integrating Eq. (8.31), we arrive at

$$\frac{wS^{(w+1)/w}}{w+1} = \left(\frac{P}{2a_c L} \frac{a_0^{3+2w} 2^w \pi^{w-1}}{K \ell} \right)^{1/w} t \quad (8.32)$$

The residence time (the dwell time) of an element in the nip is, as in subsection 8.2.1, $t = \tau_{\text{residence}} = 2a_c / V$, where the velocity $V = \omega R$. Thus, the value of the sintered area of an individual thermally- bonded contact at the exit from the nip S_n is found from Eq. (8.32) as

$$S_n = a_0^2 \left[\frac{4(w+1) a_c}{w V} \right]^{w/(w+1)} \left(\frac{P}{2a_c L} \frac{a_0 \pi^{w-1}}{\ell K} \right)^{1/(w+1)} \quad (8.33)$$

8.3.4 The effect of cooling on sintering area in thermal bonding

Consider the effect of cooling of the nonwoven when it is moving on the roller beyond the nip. Assume that the temperature θ of the nonwoven decreases due to air cooling according to the Newton law

$$\frac{d\theta}{dt} = -\beta(\theta - \theta_{\infty}) \quad (8.34)$$

where β is the heat transfer coefficient, i.e., $\beta = \beta(\theta_r)$, θ_r is the temperature near to the roller surface and θ_{∞} is the air temperature.

Since $K = K_0 \exp(U/\theta)$ [Librovich and Yarin (1988)] where K_0 is the pre-exponent of the consistency index K and U is the ratio of the activation energy to Boltzmann's constant (or to the universal gas constant depending on the definition of the activation energy), Eq. (8.29) takes the following form

$$\frac{dS^{(w+1)/w}}{dt} = \left(\frac{w+1}{w}\right) \left[\frac{T_0}{R} \frac{a_0^{3+2w}}{\ell} \frac{2^w \pi^{w-1}}{K_0} \right]^{1/w} \exp\left(-\frac{U}{w\theta} - \frac{\mu\omega t}{w}\right) \quad (8.35)$$

Note that integrating Eq. (8.34), one finds

$$\frac{\theta - \theta_{\infty}}{\theta_r - \theta_{\infty}} = e^{-\beta t} \quad (8.36)$$

or

$$\exp\left(-\frac{\mu\omega t}{w}\right) = \left(\frac{\theta - \theta_{\infty}}{\theta_r - \theta_{\infty}}\right)^{\mu\omega/w\beta} \quad (8.37)$$

It should be emphasized that in Eqs. (8.34)- (8.37) time t is reckoned from the moment when the material element of nonwoven left the calendar nip.

Using Eqs. (8.34) and (8.37), transform Eq. (8.35) to the following form

$$\frac{dS^{1+1/w}}{d\theta} = -\frac{1}{\beta} \left(\frac{1}{\theta - \theta_\infty} \right) \left(\frac{\theta - \theta_\infty}{\theta_r - \theta_\infty} \right)^{\mu\omega/w\beta} \left(\frac{w+1}{w} \right) \left[\frac{T_0}{R} \frac{a_0^{3+2w}}{\ell} \frac{2^w \pi^{w-1}}{K_0} \right]^{1/w} \exp\left(-\frac{U}{w\theta}\right) \quad (8.38)$$

By using the Frank-Kamenetskii transformation [Zeldovich et al. (1985)] in the case of a large activation energy of the pseudo-plastic flow, Eq. (8.38) can be integrated analytically, which yields

$$S(t) = S_n \left\{ 1 + \left(\frac{a_0^2}{S_n} \right)^{(w+1)/w} \left(\frac{1}{\beta} \frac{n+1}{n} \right) \left(\frac{T_0}{R} \frac{a_0^{3+2w}}{\ell} \frac{2^w \pi^{w-1}}{K_0} \right)^{1/w} \frac{w\theta_r^2}{U} \left\{ 1 - \exp\left\{ \frac{U}{n\theta_r^2} (\theta_r - \theta_\infty) [1 - \exp(-\beta t)] \right\} \right\} \right\}^{w/(w+1)} \quad (8.39)$$

Note that the dependence on the friction coefficient μ in Eq. (8.39) disappeared in comparison with Eq. (8.30). It should be emphasized that the area S_n is still given by Eq. (8.33), since in the case of good thermal bonding in the nip discussed in subsection 8.3.1, when $2a_c / V \gg h^2 / \alpha_T$ according to Eqs. (8.2) and (8.6), in the nip $\theta \approx \theta_r$.

8.3.5 Cohesion energy due to thermal bonding

Consider the cohesion stress σ_c between two material planes [Zimon (2012)]

$$\sigma_c = \frac{A}{6\pi H^3} \quad (8.40)$$

where A is the Hamaker constant and H is the inter-plane distance. This stress corresponds to the dispersion van der Waals forces and their detailed description can be found in Israelishvili (2011).

Similarly to Eq. (8.20), the effective solid-solid contacts correspond to the following part of the unit area

$$1 - m = \frac{S}{4a_0^2} \quad (8.41)$$

Then, according to Eqs. (8.40) and (8.41), the breaking strength of the material will be given as

$$\sigma_{\max} = \frac{AS_{\max}}{24\pi a_0^2 H^3} \quad (8.42)$$

rather than by σ_c (which would correspond to an intact contact area).

The work of separation W_{cohesion} is evaluated as $W_{\text{cohesion}} \approx \sigma_{\max} H$. Its value is approximately equal to 2γ , where γ is the effective surface tension.

Thus, the expected cohesion energy is

$$\bar{\sigma}_c = \frac{AS_{\max}}{24\pi a_0^2 H^3}, \quad W_{\text{cohesion}} = \frac{AS_{\max}}{24\pi a_0^2 H^2} \quad (8.43)$$

It should be emphasized that the detailed dependences for S_{\max} on time were found in subsections 8.3.2 and 8.3.3. Here, for the estimate, take the value of $S_{\max} / \pi a_0^2 \approx 1$ and $A = 10^{-18} \text{ J}$ (the latter is slightly increased compared to the standard value accounting for the fact that polymer-polymer cohesion is stronger than that of the lower molecular materials due to reptational motion and mixing of macromolecules near the interface). Also, take for the estimate the value of the inter-plane distance H based on the Burgers vector as, $H = 10^{-8} \text{ cm}$. Then, the cohesion energy is estimated from the second Eq. (8.43) as $W_{\text{cohesion}} \sim 4.2 \text{ J/m}^2$, which seems to be plausible at the lowest bonding temperature of $160 \text{ }^\circ\text{C}$ (cf. Figure 8.13a), where the measured value is $\sim 10 \text{ J/m}^2$. The values of the cohesion energy W_{cohesion} of thermally-bonded nanofiber mats in Staszal et al. (2017) were in the $1\text{--}10 \text{ J/m}^2$ range. The values of the cohesion energy of thermally-bonded PET nonwovens measured using bister tests in the present work in subsection 8.2.2.2 were on the scale of 10 J/m^2 at the bonding temperatures higher than $160 \text{ }^\circ\text{C}$. The lower theoretical value of the cohesion energy than those measured experimentally at the higher temperatures can probably be attributed to the fact that the present estimate does not account for the reptation-driven entanglement of macromolecular chains during fiber-fiber sintering [De

Gennes (1989); Ji and De Gennes (1993); Raphael and De Gennes (1992)], which can be strongly enhanced at the elevated temperatures. On the other hand, the potential energy losses for plastic deformation and their effect on the cohesion energy were negligibly small, because the blisters of Figures 8.9 and 8.11 completely disappeared after unloading and took the original shape, which shows that the blister tests were conducted in the purely elastic regime.

8.4 Conclusions

Tensile tests were conducted for the as-received and thermally-bonded PET nonwovens. The corresponding mechanical properties were obtained. The PET nonwovens were thermally bonded by the in-house lab-scale setup at five temperatures: 160 °C, 170 °C, 180 °C, 190 °C, and 200 °C, which were lower than the melting point of PET (260 °C). The observations revealed fiber-fiber sintering. The cohesion energy of thermally- bonded nonwovens was measured using blister tests. It was shown that the cohesion energy of thermally- bonded PET nonwovens increased as the bonding temperature increased when it was measured in the blister tests conducted at the shaft rate of 2 mm/ min. On the other hand, the values of the cohesion energy obtained in the blister tests conducted at the shaft rate of 10 mm/min were practically independent of the bonding temperature. The theory of calendar bonding in the nip developed in the present work revealed the values of cohesion energy of the order of 4.2 J/m². According to the experimental data in Figure 8.13, this value seems to be reasonable for thermal bonding at the temperature of 160 °C. On the other hand, at higher bonding temperatures the experimental values were of the order of 10 J/m². At these higher temperatures, the theory underestimates the cohesion energy probably because it does not account for the enhanced reptation-driven entanglement of macromolecular chains during fiber-fiber sintering. Figure 8.6 shows that the as-received PET nonwovens were sintered under the

bonding punch. However, it does not reveal any specific mechanism contributing to the cohesion energy. Moreover, strong sintering of thermally punched nonwovens to metal surfaces is also possible, which is the case with total exclusion of interleaving/entanglement through the interface. Therefore, it is of interest to evaluate the cohesion energy due to atomic force potential and compare to the experimentally measured values, as is done in the present work. The comparison mentioned above revealed a plausible estimate of the cohesion energy at the lowest bonding temperature of 160 °C, which shows that in this range the contribution of the atomic force potential to the cohesion energy is dominant. On the other hand, at the bonding temperatures higher than 160 °C the results show that the reptation-driven entanglement of macromolecular chains during fiber-fiber sintering becomes significant and cannot be neglected. The potential energy losses for plastic deformation and their effect on the cohesion energy are negligibly small, because the blisters of Figures 8.9 and 8.11 completely disappear after unloading and take the original shape, which attests that the blister tests are conducted in the purely elastic regime.

CHAPTER 9

THERMAL BONDING PATTERNS EFFECT ON MECHANICAL PROPERTIES OF NONWOVENS

9.1 Introduction

In the present chapter, the effect of the asymmetrically off-center located thermal bonds on the mechanical behavior of nonwovens in tensile tests is studied experimentally. The rupture pattern, the failure location, as well as the corresponding mechanical properties were elucidated. The experimental materials, thermal bonding setup, rupture patterns and the measured mechanical properties of the off-center thermally bonded nonwovens are described in detail in section 9.2. This section also reveals the effect of the bond area. The latter is studied in more detail in section 9.3, where the number of the pre-bonded and then sintered elements under bonds of certain shapes are measured and compared. A theory which evaluates the number of fiber-fiber intersections sintered under an arbitrary bond is given in section 9.4. The conclusions are drawn in section 9.5.

9.2 Experimental: Tensile test

9.2.1 Materials and thermal bonding setup

The material used in the current section was non-bonded Polypropylene (PP) nonwovens, which were provided by FiberVisions and used as received. The melting point of the as-received PP nonwovens was measured as 160 °C and the base weight was 40 GSM (gram per square meters). The thickness of a single layer of the as-received PP nonwovens was measured as 1 mm. The average value of the diameter of the PP fibers in the nonwovens was measured as 19.07 μm (cf.

Figure 9.1). The density of crystalline PP is 0.946 g/cm^3 [Mandal (2009)].

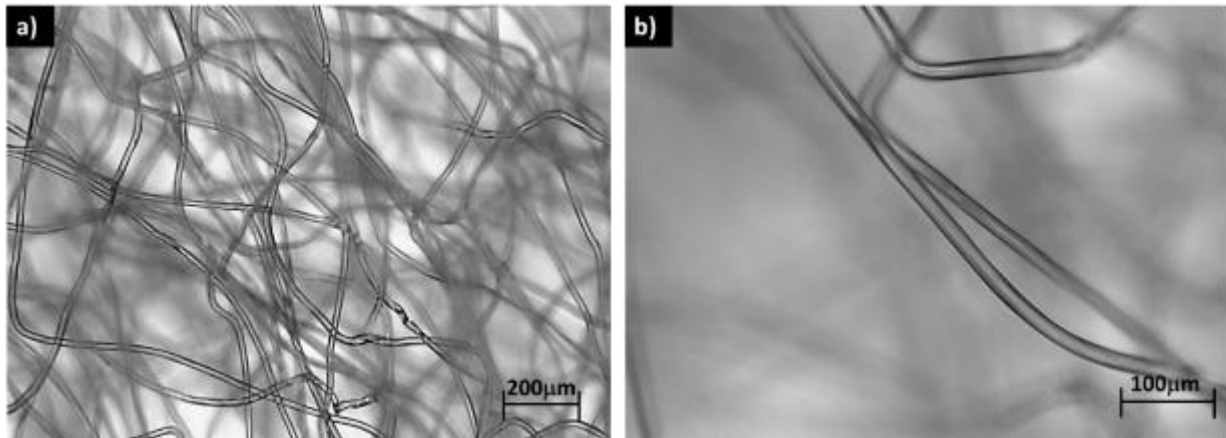


Figure 9. 1 Optical images of the PP fibers in the as-received nonwovens. (a) The $\times 4$ magnification. (b) The $\times 10$ magnification.

The thermal bonding setup here was the same one used in [Zhang et al. (2018)]. It employed the Arbor press and consisted of several separable parts: (i) an aluminum casing; (ii) a cartridge heater (CSH- 201200/120V); (iii) a stainless-steel thermal punch; (iv) a temperature controller; (v) a thermal couple (Omega model 5TC- PVC-T-24-180). Two shapes of thermal punch were employed in the present work similarly to [Zhang et al. (2018)]: a rectangular and a circular one. The rectangular thermal punch had a length of 50.8 mm, and a width of 24.5 mm. The diameter of the circular thermal punch was 12.6 mm. By pressing these two thermal punches against a nonwoven specimen, 762.0 mm^2 rectangular thermal bond and 124.59 mm^2 circular thermal bond could be made.

Tensile tests of PP nonwovens were conducted with the Instron machine (model 5942), which was equipped with a 500 N load cell. By employing this machine, the entire stress-strain curves could be obtained and used for further analysis. The as-received PP nonwovens were folded into three layers, thermally bonded and the resulting specimens were used in the tensile tests. The

specimens were cut from the PP nonwoven sheets along the machine direction. The dimensions of the prepared nonwoven specimens was 30 mm in width and 90 mm in length.

The bonding temperature was selected as 150 °C, which was lower than the melting point of PP. The contact time of the thermal punch with the PP nonwoven specimens was maintained, as before [Zhang et al. (2018)], around 1 s due to the limitations of the lab-scale setup. Three bonding types were studied in the present work: (i) circular thermal bonding located at the specimen center (denoted as type B thermal bond); (ii) circular thermal bonding located at a significantly off-center position of a nonwoven specimen (denoted as type C thermal bond); (iii) rectangular thermal bonding located at the center of a nonwoven specimen (denoted as type D thermal bond). The corresponding schematics are shown in Figure 9.2.

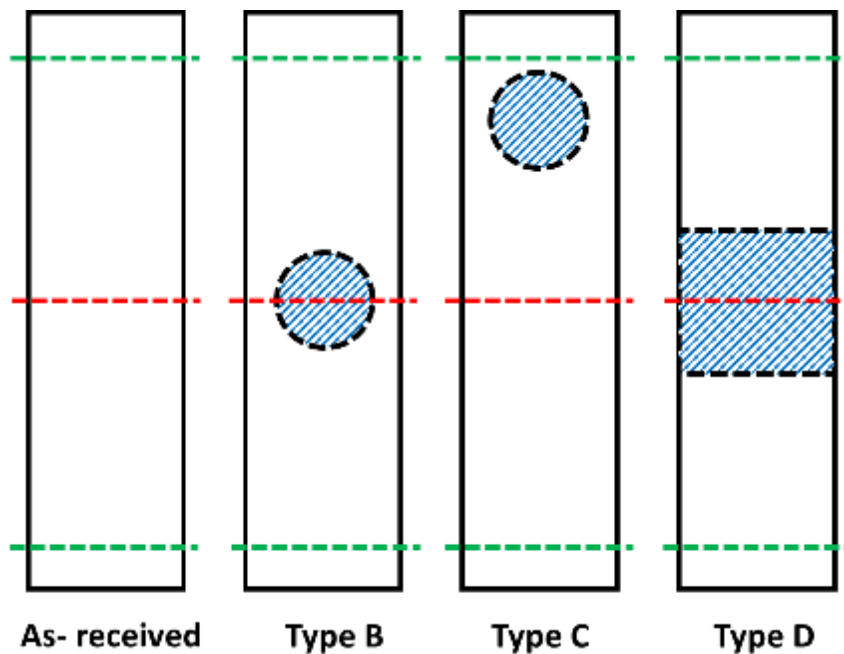


Figure 9. 2 The schematics of the as-received nonwoven and the nonwoven specimens with three types of thermal bonding patterns. Green dashed lines and red dashed lines indicated the positions

of the pneumatic grips and the centerline of the PP nonwoven specimens, respectively. The shaded circles or rectangle show the shapes and the locations of thermal bonds.

In the tensile tests, the specimens were clamped by the pneumatic grips of the Instron 5942 machine (as shown in Figure 9.2). The initial length of the specimens between the clamps was 70 mm. Ten trials were conducted for each experiment with the as-received and thermally bonded nonwovens. The tensile test rate was selected as 2 mm/min.

9.2.2 The rupture patterns of the as-received and thermally- bonded PP nonwovens

The rupture patterns of the as-received and thermally- bonded PP nonwovens after stretching in the tensile tests are shown in Figure 9.3. For the sake of brevity, only three examples (out of ten tested) of failed as-received and thermally- bonded nonwoven specimens are shown. From the failure pattern depicted in Figure 9.3a, one can conclude that the as-received PP nonwovens rupture at the center. For the nonwovens with the off-center type B thermal bond (cf. Figures 9.3b and 9.3c), the rupture also happened at the specimen center rather than at the thermal bond periphery, as it would be the case of thermal bonds located at the specimen center [Zhang et al. (2018)]. Figure 9.3d depicts the rupture pattern of the PP nonwovens with type D thermal bond. The failure happened in the middle place between the grip position and the rectangular bond periphery, which shows that the bond essentially served as a second (virtual) grip in this case, while rupture happened between at the center the real and virtual bond.

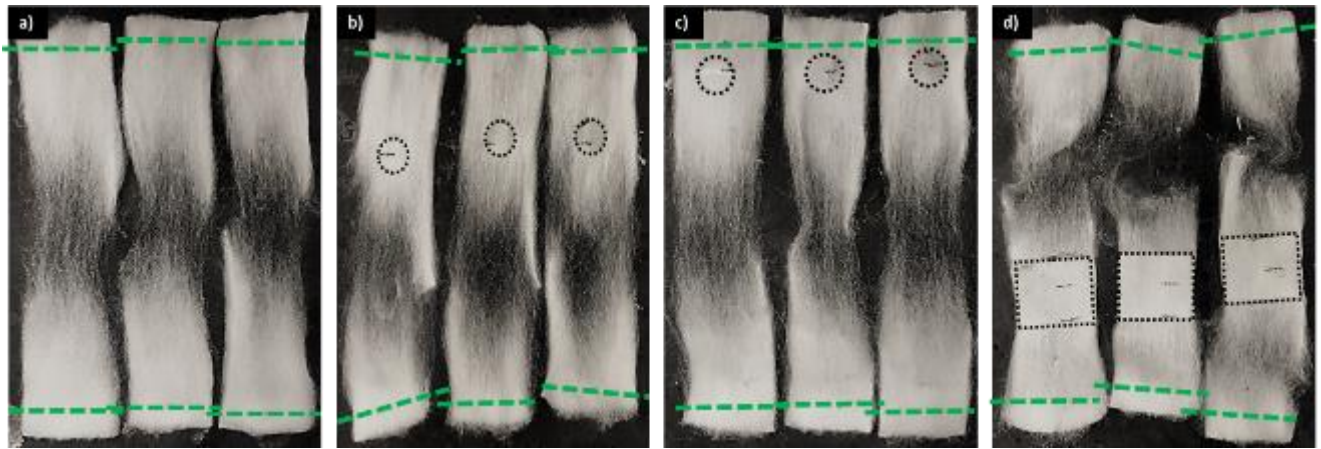


Figure 9. 3 The failure patterns of the as-received and thermally-bonded PP nonwovens. (a) The as-received PP nonwovens. (b) The PP nonwovens with type B thermal bond. (c) The PP nonwovens with type C thermal bond. (d) The PP nonwovens with type D thermal bond. Green dashed lines indicate the positions of the Instron grips. Black dashed lines encompass the thermal bonds.

9.2.3 Results of the tensile tests of the as-received and thermally- bonded PP nonwovens

The tensile tests were conducted with the as-received and thermally- bonded nonwovens. The corresponding stress-strain curves were obtained by using the Instron 5942 machine. They are presented in Figure 9.4.

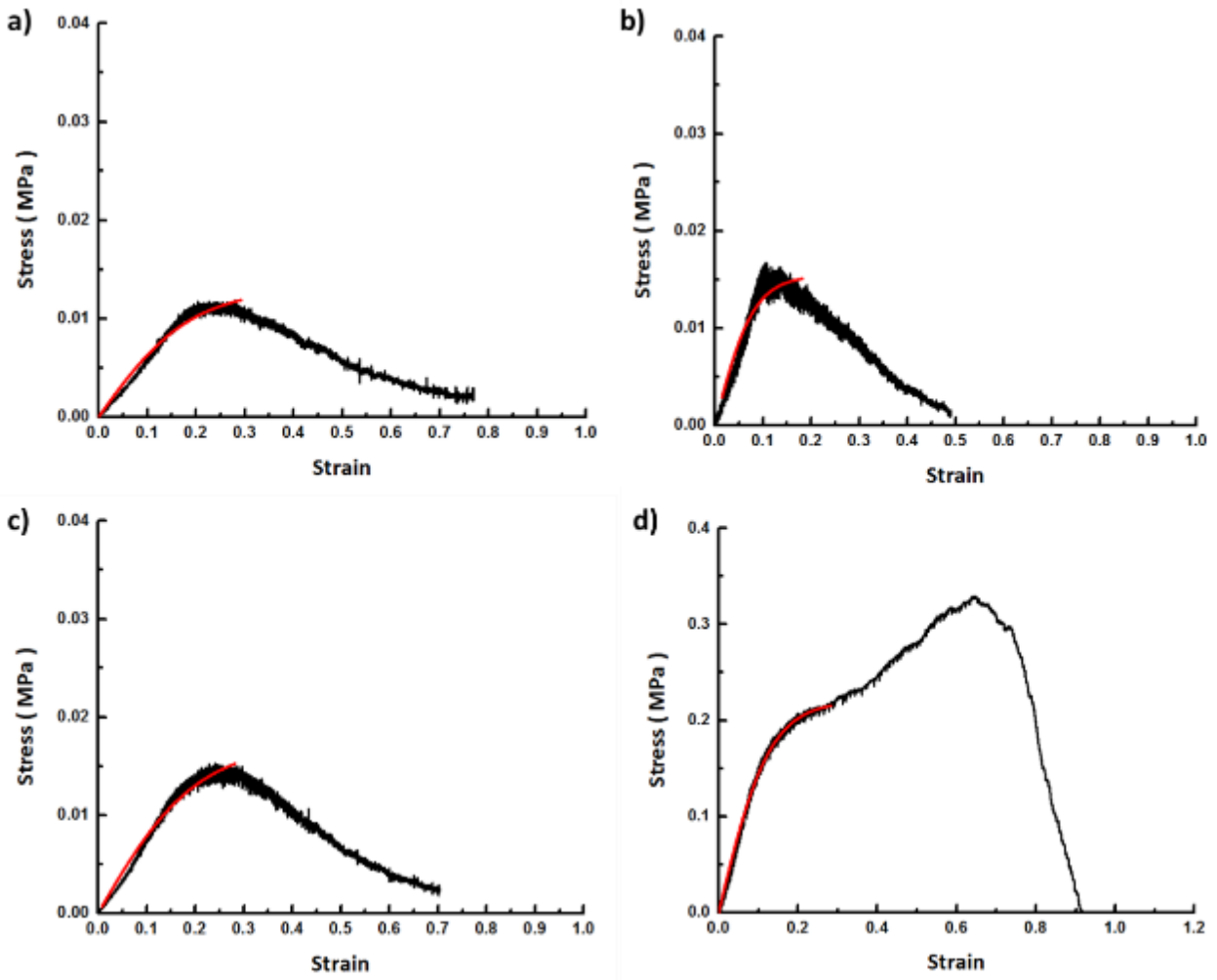


Figure 9. 4 Stress-strain curves of the as-received and thermally- bonded nonwovens measured in tensile tests. The experimental data is shown by black lines and fitted by the phenomenological Green`s equation, as shown by red lines. (a) The as-received PP nonwoven. (b) The PP nonwoven with type B thermal bond. (c) The PP nonwoven with type C thermal bond. (d) The PP nonwoven with type D thermal bond.

The experimental data was fitted by the phenomenological Green`s equation [Green (1956); Yarin et al. (2014)],

$$\sigma = Y \tanh\left(\frac{E}{Y} \varepsilon\right) \quad (9.1)$$

where E is Young's modulus, Y is the yield stress, σ is the tensile stress and ε is the tensile strain.

As a result of the fitting shown in Figure 9.4 the Young's moduli and the yield stresses of the specimens were determined. The maximum stress before failure and the toughness of the PP nonwoven specimens were also found. The values of these mechanical properties found from ten experimental trials in each case are presented in Figures 9.5 and 9.6.

The average values of the Young's moduli of the PP nonwovens with type B and type C thermal bonds were higher than those of the as-received nonwovens (cf. Figure 9.5a). This indicates that thermal bonds in the nonwoven specimens, at any location, would increase the nonwovens stiffness. The closer the thermal bond was located to the center (type B thermal bond), the higher was the Young's modulus (cf. with the type C thermal bond at the significantly off-center location; Figure 9.5a).

Compared the average values shown in Figures 9.5b- 9.5d, it is seen that the thermal bonding closer to the specimen center (type B thermal bond) would increase the yield stress, the maximum stress before failure and the toughness of the PP nonwovens. On the other hand, a significantly off-center location of the thermal bond (type C thermal bond) practically did not enhance these mechanical properties.

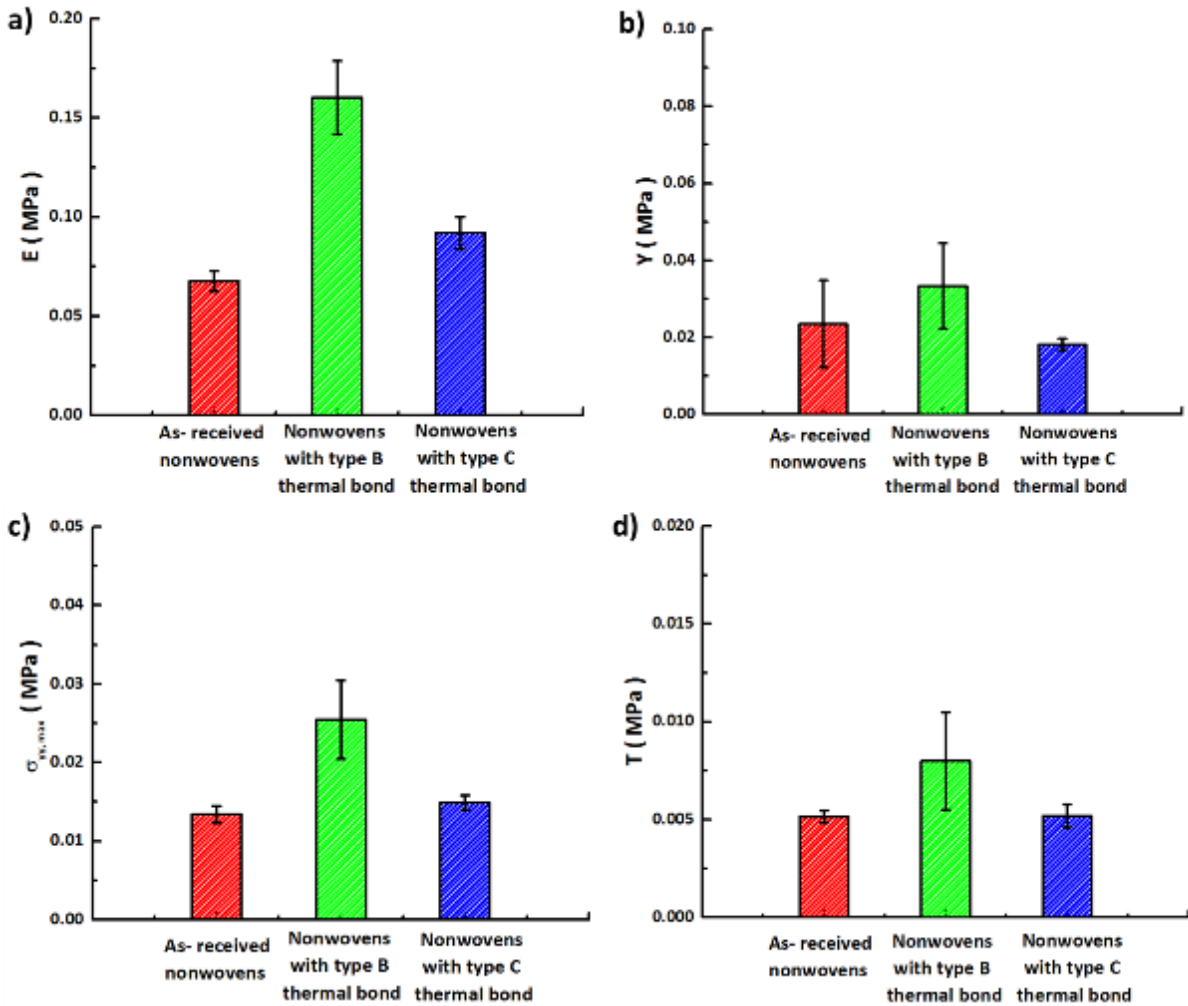


Figure 9. 5 Mechanical properties of the as-received PP nonwovens and those with type B and type C thermal bonds. (a) Average values of Young`s moduli. (b) Average values of the yield stress. (c) Average values of the maximum stress at failure. (d) Average values of the toughness.

The comparison with the nonwoven specimen with type D thermal bond, shown in Figure 9.6, reveals that all mechanical properties dramatically increase in this case because of the larger size of the thermal bond.

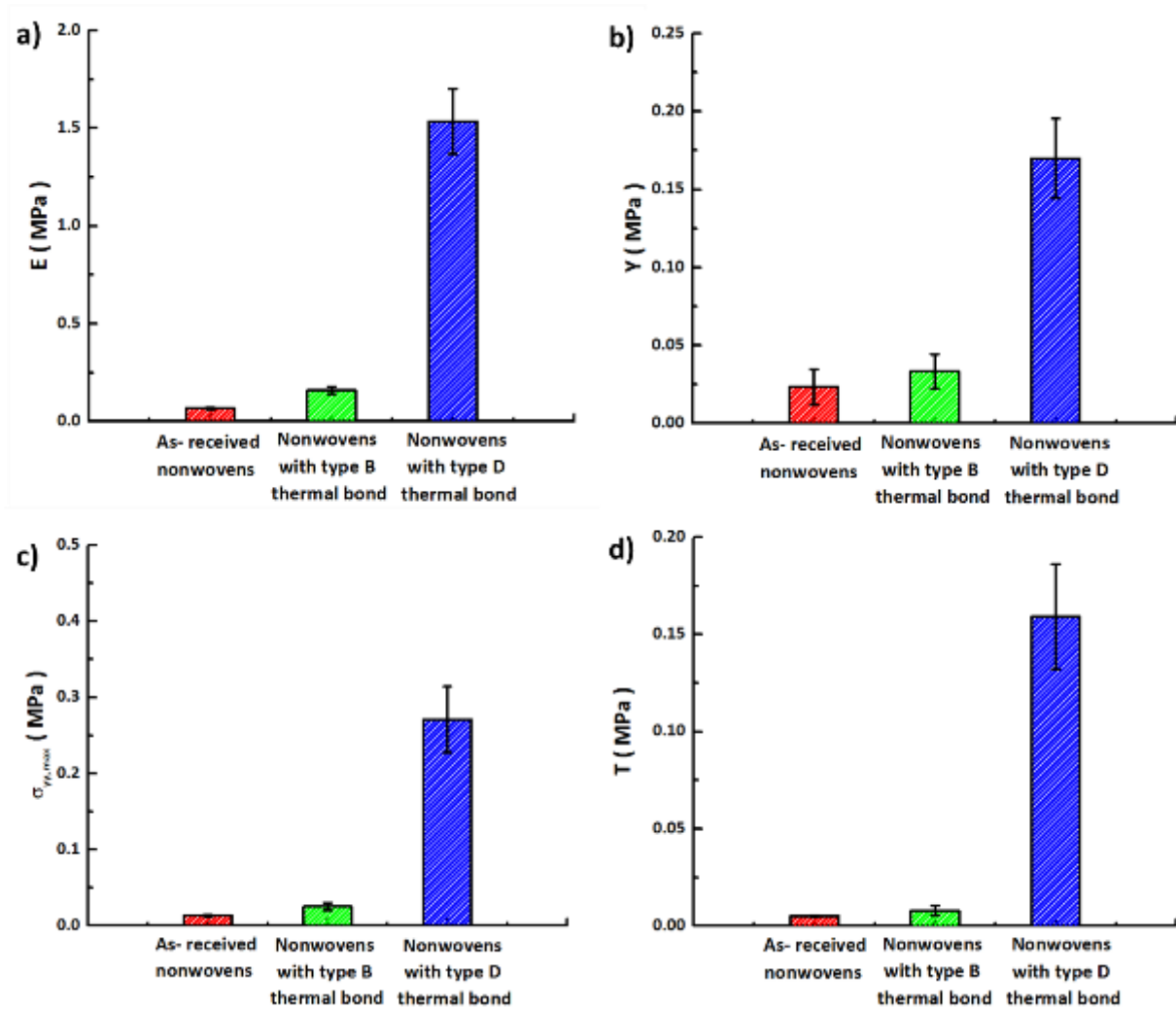


Figure 9. 6 Mechanical properties of the as-received PP nonwovens and those with type B and type D thermal bonds. (a) Average values of Young`s moduli. (b) Average values of the yield stress. (c) Average values of the maximum stress at failure. (d) Average values of the toughness.

9.3 Experimental: The effects of the thermal bond area

In this section, the experiments were designed for elucidating the effects of the thermal bond shape and area. The materials used here are light-weight Spunbond-Meltblown- Spunbond (SMS) nonwovens, which were provided by Halyard and used as received (cf. Figure 9.7a). These nonwovens were formed from polypropylene and had already been pre-bonded with RHT pattern

before they were received at UIC. The RHT pattern was shown in [Vogt (1976)]. Usually the bond area for the RHT pattern applied in industry varied from 5% to 30% of the fabric laminate web.

The thickness of light-weight RHT-bonded-pattern nonwoven was measured as 0.26 mm, and the base weight as 32.55 GSM (gram per square meters). The tested nonwovens were all cut from the nonwoven sheets into 15 mm × 90 mm rectangular specimens in the machine direction.

Additional single circular or rhombic thermal bonds were made on the light-weight nonwovens using the thermal bonding setup described in subsection 9.2.1. The bonding temperature was 150 °C. The total surface area of the heated punch used in this section was 124.59 mm² for the circular punch and 119.54 mm² for the rhombic punch. The as-received light-weight nonwoven specimen (cf. Figure 9.7a) and the specimen with additional single circular (cf. Figure 9.7b) or rhombic (cf. Figure 9.7c) thermal bond are shown in Figure 9.7.

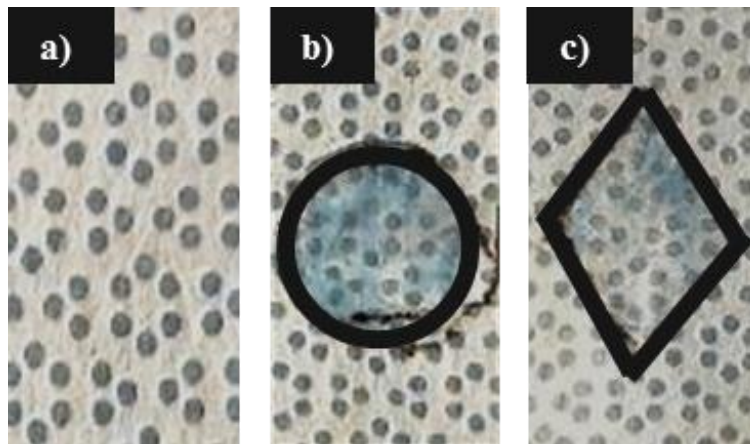


Figure 9. 7 Specimens of as-received light-weight RHT bonding pattern nonwoven, and of those with single circular bond pattern, as well as single rhombic bond. (a) The as-received light-weight RHT bonding pattern nonwoven specimen. (b) The light-weight nonwoven with single circular thermal bond. (c) The light-weight nonwoven with single rhombic thermal bond. The periphery of

the circular or rhombic thermal bond was highlighted by black lines.

The mechanical properties of the as-received light-weight nonwoven specimens as well as of those with single circular or rhombic bond were measured in tensile tests. The test setting parameters were the same as in the experiments in section 9.2. The results of tensile tests are shown in Figure 9.8.

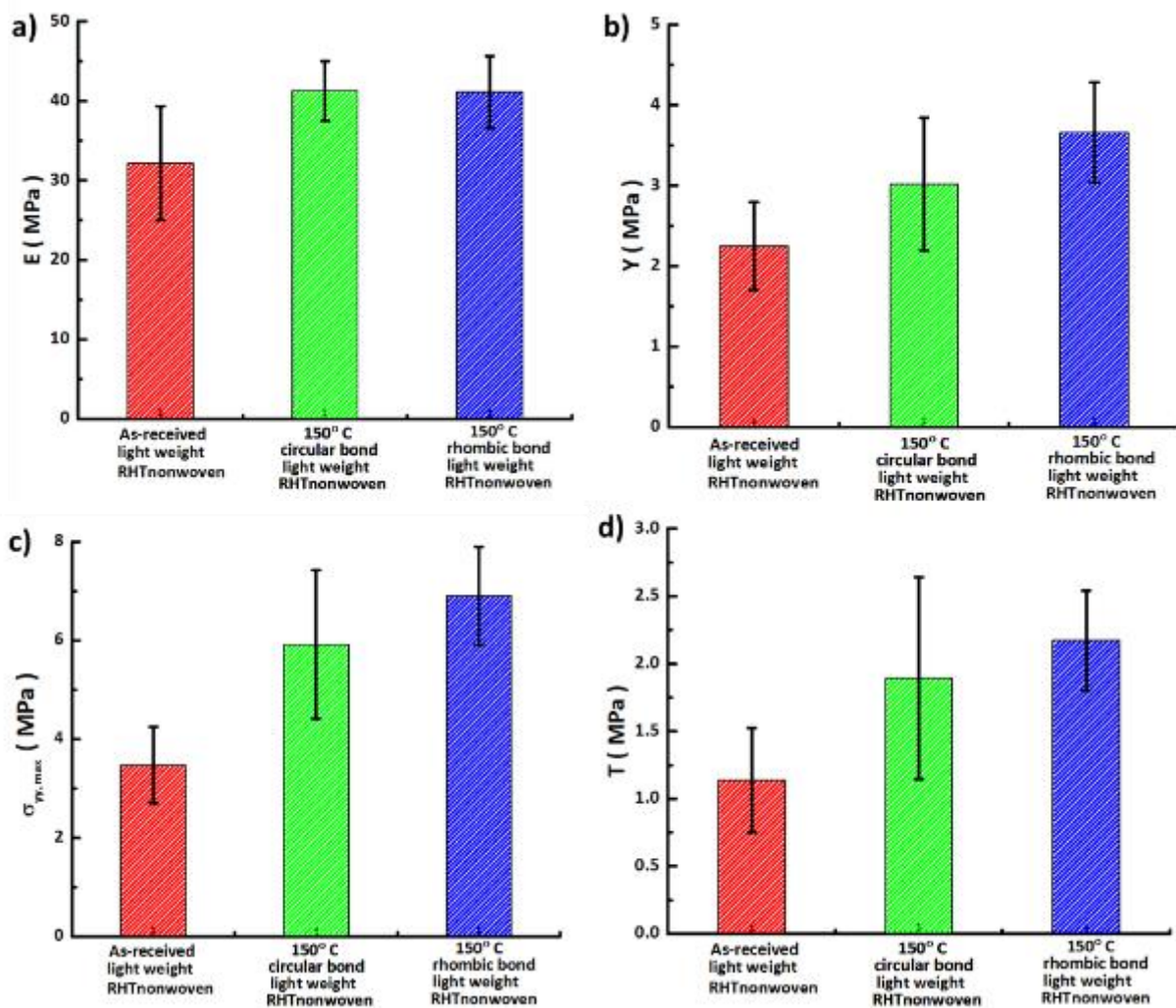


Figure 9. 8 Mechanical properties of the as-received light-weight SMS RHT pattern nonwovens in comparison with those bonded at 150 °C with a single circular or rhombic bond. (a) Average

values of Young's modulus. (b) Average values of the yield stress. (c) Average values of the maximum stress. (d) Average values of toughness.

Comparing the values of the mechanical properties shown in Figure 9.8, one concludes that the additional circular or rhombic thermal bonding increased the values of Young's modulus by 28.34%. It can also be noticed that the additional thermal bond, especially with the rhombic shape, significantly increased the other mechanical properties of the light-weight nonwovens. The value of the yield stress was increased by 34.30% because of the single circular thermal bond (124.59 mm²) and by 62.90% because of the single rhombic thermal bond (119.54 mm²) in comparison with the as-received material. According to Figure 9.8c, the strength at the failure of the light-weight nonwovens increased much higher because of the rhombic bond (by 98.99%) in comparison to the circular one because of the circular bond (by 70.45%). The toughness values of the light-weight nonwovens were also increased by ~66.46% and 91.20%, respectively, because of the single circular and rhombic thermal bond (cf. Figure 9.8d).

One possible reason for this dramatic change happened for this specific material caused by an addition single rhombic thermal bond in comparison to an additional single circular thermal bond is related to the fact the former incorporated (overlaid) a larger cumulative area of the original bonds relative to its own area. This fact is established in detail below in this section.

In the present study of the overlaid cumulative area of the original bonds under the additional single circular and rhombic bonds the light-weight nonwovens were used. The original bonds were blackened at the places where the additional thermal bonds were supposed to be done (cf. Figure 9.9a). The images of such nonwoven specimens were recorded by DSLR camera at $f = 7.1$ and $1/5$ s exposure time. The images of nonwoven specimens were processed with Image-Pro Plus 7.0 (Media Cybernetics) software (cf. Figure 9.9b) to measure the cumulative area of the

original bonds overlaid by the additional single thermal bonds.

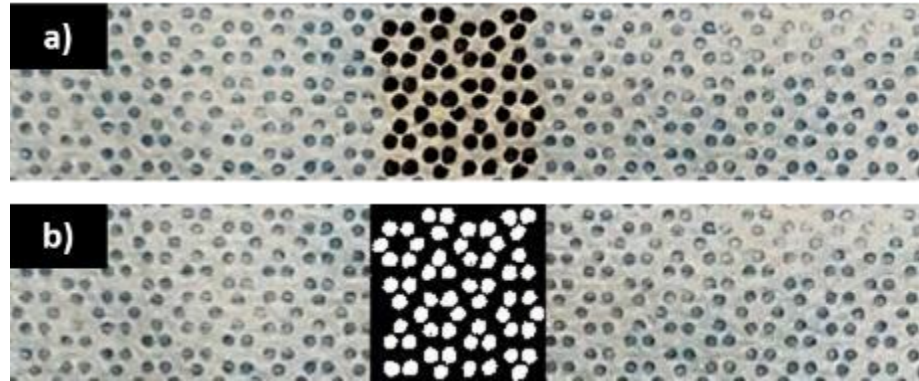


Figure 9. 9 (a) A specimen of the light-weight RHT pattern SMS nonwoven with blackened original bonds. (b) The corresponding processed specimen image. The specimen size is 15 mm × 90 mm.

The process for measuring the cumulative original bond area overlaid by an additional circular thermal bond was as follows. The black and white zone in Figure 9.9b, of the area of 251 mm², highlighted the original bonds outside and under the additional circular bond. The area of the additional circular bond is encompassed by the blue circle (cf. Figures 9.10a- 9.10e). This area is equal to 124.59 mm². The measurement started at the position where the blue circle, the boundary of the additional circular bond, leaned against the top left corner of the black and white zone (cf. Figure 9.10a). Then, the overlaid original thermal bonds inside this blue circle were filled with red color and their cumulative area at this position was calculated. Then, the blue circle was moved in steps by 0.1 mm downward in the vertical direction (cf. Figure 9.10b) until it leaned against the bottom left corner (cf. Figure 9.10c) and the measurements were done at each of them. Then, the blue circle was moved by steps of 0.1 mm in the horizontal direction (cf. Figure 9.10d) and the measurements were done as in Figures 9.10a- 9.10c. The final position is shown in Figure

9.10e where the blue circle leans against the bottom right corner. It should be emphasized that the additional bonding position on the nonwoven specimens that were used in the tensile tests were located in the present case in the middle of each specimen, and the measurement procedure described above took into account every possible position that the additional circular bond would occupy.

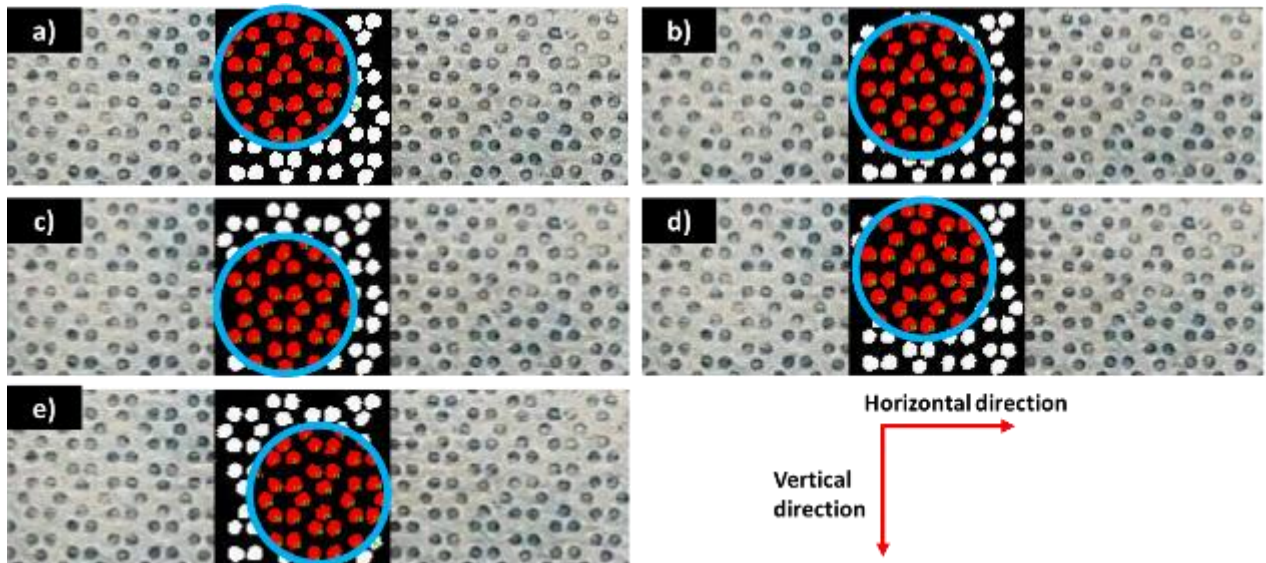


Figure 9. 10 Measurement procedure used to find the area ratio in the case of an additional circular thermal bond. (a) – (e) Various possible bonding positions within the black and white zone. The blue circles in panels (a) to (e) encompass the additional circular bond and the overlaid original bonds are shown in red.

The cumulative areas of the overlaid original bonds (the red bonds) was found from 255 positions encompassed by the blue circle within the black and white zone. The area ratios of the cumulative original bonds overlaid by the additional single circular thermal bond to the area of the latter were calculated as

$$\phi_{\text{circular}} = \frac{A_1}{A_2} \quad (9.2)$$

where A_1 is the cumulative area of the original bonds overlaid by the additional single circular thermal bond, A_2 is the area of the additional single circular thermal bond, and ϕ_{circular} is the corresponding area ratio.

The probability density function of the area ratios $f(\phi)$ is found as

$$f(\phi) = \frac{\sum_{j=1}^n \phi_j}{\sum_{i=1}^N \phi_i} \quad (9.3)$$

where n is the numbers of the area ratios in a specific range j are listed in Table 9.1. In this case $N=255$.

Table 9. 1 The numbers of the ratios of the cumulative area of the original bonds overlaid by the additional single circular thermal bond to the area of the latter in a specific ratio range.

Area ratio range	n
0.272-0.274	1
0.274-0.276	6
0.276-0.278	7
0.278-0.280	16
0.280-0.282	10
0.282-0.284	19
0.284-0.286	27
0.286-0.288	23
0.288-0.290	12
0.290-0.292	15
0.292-0.294	14
0.294-0.296	19
0.296-0.298	19
0.298-0.300	27
0.300-0.302	32
0.302-0.304	7

0.304-0.306	1
Total	255

Then the probability density function of the area ratios $f(\phi_{\text{circular}})$ is plotted in Figure 9.11.

The average area ratio value calculated using the probability density function as

$$\sum_{j=1}^{255} \phi_j f(\phi_j) = 0.286.$$

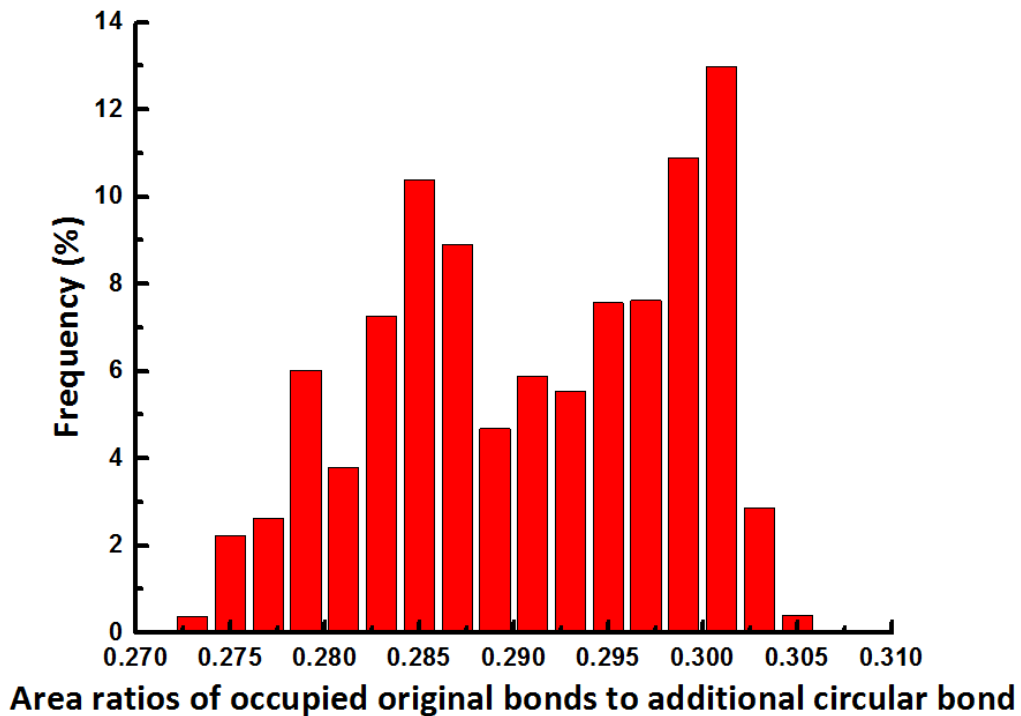


Figure 9. 11 The probability density function of the area ratios of the cumulative original bonds overlaid by the additional single circular thermal bond to the area of the latter.

Similar measurements were done for the additional rhombic bonds. The beginning and ending measuring positions are shown in Figures 9.12a and 9.12b. The area of the rhombic bond (18.9 mm in length and 12.7 mm in width) is encompassed by blue rhomboid and the area inside

was 119.54 mm². The cumulative areas of the overlaid original bonds (red bonds) was found separately from 160 positions within the black and white zone (318 mm² in area). Then, the area ratios of the cumulative original bonds overlaid by the additional single rhombic thermal bond to the area of the latter was calculated as

$$\phi_{\text{rhombic}} = \frac{A_3}{A_4} \quad (9.4)$$

where A_3 is the cumulative area of the original bonds overlaid by the additional single rhombic thermal bond, A_4 is the area of the additional single rhombic thermal bond, and ϕ_{rhombic} is the corresponding area ratio.

Then the probability density function of the area ratio is found by Eq. (9.3) and the corresponding values of n are listed in Table 9.2. In this case $N=160$.

Table 9. 2 The numbers of the ratios of the cumulative area of the original bonds overlaid by the additional single rhombic thermal bond to the area of the latter in a specific ratio range.

Area ratio range	n
0.290-0.292	1
0.292-0.294	1
0.294-0.296	8
0.296-0.298	9
0.298-0.300	7
0.300-0.302	13
0.302-0.304	15
0.304-0.306	13
0.306-0.308	11
0.308-0.310	9
0.310-0.312	18
0.312-0.314	8
0.314-0.316	11
0.316-0.318	18
0.318-0.320	4
0.320-0.322	13

0.322-0.324	1
Total	160

The corresponding probability density function of the area ratios was plotted versus is plotted in Figure 9.12c. The area ratio was in the 0.292 to 0.322 range, and the average area ratio

value was found as $\sum_{j=1}^{160} \phi_j f(\phi_j) = 0.308$.

The average value of the area ratio found for the additional rhombic bond was by 7.1% larger than that for the additional circular bond. This is in concert with the results shown in Figures 9.8.

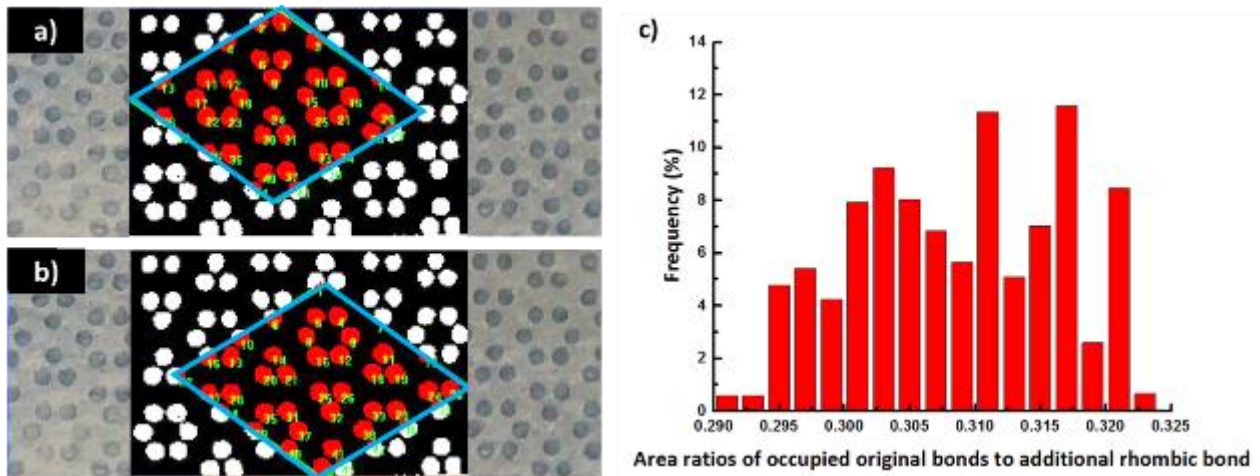


Figure 9. 12 Measurement of the area ratio in the case of an additional rhombic thermal bond configuration and the corresponding probability density function of the area ratio. (a) The beginning measuring position. (b) The ending measuring position. (c) The probability density function of the area ratio. The blue lines in panels (a) and (b) encompass the additional rhombic bond and the overlaid original bonds are shown in red.

9.4 Theoretical: The numbers of fiber-fiber intersections sintered under a single thermal bond

Consider a square of side length L . In a nonwoven it is crisscrossed by straight fibers. Some of them might belong to the same longer fiber or be located at different heights along with the nonwoven thickness. These distinctions are disregarded in the present consideration, as immaterial, and all the intersections projected on the same plane. Accordingly, the shortest fiber length crisscrossing the chosen square is $\ell_{\min} = 0$ and the longest one is $\ell_{\max} = \sqrt{2}L$, since the crisscrossing cannot be longer than the diagonal. Introduce the probability density function of fiber length over the square as $P(\ell)$. It should be normalized that

$$\int_0^{\sqrt{2}L} P(\ell) d\ell = 1 \quad (9.5)$$

Then, since all fiber lengths are equally probable, $P(\ell)$ does not depend on ℓ and thus,

$$P(\ell) = \frac{1}{\sqrt{2}L} \approx \frac{0.71}{L} \quad (9.6)$$

Denote the orientation probability density function of the fibers as $F(\theta)$, where θ is the polar angle centered at a fiber center. Since fibers in nonwovens practically do not possess directionality, i.e. they possess no ‘head’ and ‘tail’, the angle θ of interest belongs to the interval $-\pi/2 \leq \theta \leq \pi/2$.

Accordingly, the normalization condition requires

$$\int_{-\pi/2}^{\pi/2} F(\theta) d\theta = 1 \quad (9.7)$$

and all the angular directions are equally probably (the mat is assumed to be isotropic). Thus, $F(\theta)$ does not depend on θ and

$$F(\theta) = \frac{1}{\pi} \quad (9.8)$$

Let the number of the fiber centers per unit area be c , with the units of c being cm^{-2} . Consider a certain fiber of length ℓ and find the number of other fibers intersecting it. In the general case one can always consider this fiber of length ℓ being oriented ‘vertically’, and the normal direction to it being $\theta=0$. Then, if ‘another’ fiber of length ℓ_1 and the orientation θ has its center in the strip $\ell_1 \cos \theta \times \ell$ about the chosen one, it will intersect it. According, the number of fibers intersecting the chosen one is equal to

$$n = \int_{-\pi/2}^{\pi/2} d\theta \int_0^{\sqrt{2}L} d\ell_1 F(\theta) P(\ell_1) c \ell_1 \ell \cos \theta \quad (9.9)$$

Using Eqs. (9.6) and (9.8) and evaluating the integrals in Eq. (9.9), one obtains

$$n = \frac{\sqrt{2}}{\pi} c \ell L \quad (9.10)$$

The total number of the fiber-fiber intersections over the square area L^2 is equal to

$$N = \frac{1}{2} \int_0^{\sqrt{2}L} P(\ell) \frac{\sqrt{2}}{\pi} c \ell L d\ell = \frac{cL^2}{2\pi} \quad (9.11)$$

Note that the factor $1/2$ before the integral in Eq. (9.11) accounts for the fact that the intersection of a fiber A with a fiber B is identical with the intersection of the fiber B with the fiber A.

The average length of fibers over the square area L^2 is equal to

$$\bar{\ell} = \int_0^{\sqrt{2}L} \ell P(\ell) d\ell = \frac{L}{\sqrt{2}} \quad (9.12)$$

The mass of the fibers per unit area (a known parameter for nonwovens) M can be expressed as

$$M = \rho \bar{\ell} \pi a^2 c \quad (9.13)$$

where ρ is the polymer density, and a is the fiber cross-sectional radius.

Accordingly, from Eqs. (9.12) and (9.13) one finds

$$c = \frac{M\sqrt{2}}{\rho\pi a^2 L} \quad (9.14)$$

Substituting Eq. (9.14) into Eq. (9.11), one obtains the number of fiber-fiber intersections over the square area L^2

$$N = \frac{1}{\sqrt{2}\pi^2} \frac{ML}{\rho a^2} \quad (9.15)$$

The latter yields the number of the fiber-fiber intersections under any bond of area S on an 'isotropy square of side length L ' as

$$N = \frac{1}{\sqrt{2}\pi^2} \frac{MS}{\rho a^2 L} \quad (9.16)$$

Consider a single layer of PP nonwoven used in section 9.2 and thermally bonded by a circular, rhombic or rectangular thermal punch. Use the values described in section 9.2 for calculation, namely, the base weight of PP nonwoven as 40 GSM, the average diameter of a single PP fiber as 19.07 μm , and the density of PP polymer as 0.946 g/cm^3 .

For the circular thermal bond, the area of the bonded part in the nonwoven sample was 124.59 mm^2 . Thus, the numbers of the fiber-fiber intersection within this bond area is calculated as 371 based on Eq. (9.16). For the rhombic thermal bond, the area of the bonded part in the nonwoven specimen was 119.54 mm^2 , and ~364 fiber-fiber intersection within this bonding area can be present according to Eq. (9.16). For the rectangular thermal bond, the area of the bonded part in the nonwoven sample was 762.0 mm^2 . Hence, the numbers of the fiber-fiber intersection within this bonding area is calculated as 920 based on Eq. (9.16). The predicted increase in the number of the fiber-fiber intersections under the bonds of different shapes correlates with the measured increase in their maximum strength and toughness in the tensile tests (cf. Figure 9.6).

9.5 Conclusions

Polypropylene (PP) nonwovens were tested in the experiments using the as-received and thermally-bonded specimens. Circular and rectangular thermal punches were employed to thermally bond the nonwoven specimens. Three types of bonding patterns were formed with bonds being located at different off-center locations and having different areas. Tensile tests were conducted with the as-received and thermally-bonded PP nonwovens and the corresponding average values of the mechanical properties were obtained. Based on the experimental results, one can conclude that: (i) the closer-to-the-center thermal bond would enhance the mechanical properties of nonwovens, while the bond at a significantly off-center position practically did not affect these properties; (ii) the larger size of thermal bond significantly affects the mechanical properties of the PP nonwovens.

The additional single thermal circular or rhombic bonds were demonstrated to enhance the mechanical properties of the light-weight RHT pattern SMS nonwovens, especially of the light-weight ones. The additional rhombic bonds were more beneficial than the single circular ones and significantly increased the maximum stress at failure and toughness of the light-weight RHT pattern SMS nonwovens. This effect was linked to a larger area ratio of the cumulative area of the overlaid original bonds to that of the additional rhombic bond than to that of the additional circular one. The average value of the area ratio for the rhombic bond was by 7.1% larger than for the circular one. With additional single rhombic thermal bond, the average values of the maximum stress at failure and the toughness of the light-weight RHT SMS nonwovens were increased by 98.99% and 91.20%, respectively.

The number of the fiber-fiber intersections in PP nonwovens under a single thermal bond

was estimated based on the theory developed in the present work. The results calculated for the cases of circular, rhombic and rectangular thermal bonds used in the current work were 371, 364, and 920, respectively, which correlates with the measured enhancement of the mechanical properties caused by these bonds.

CHAPTER 10

METHOD OF CHARACTERIZATION OF THE CLAPEYRON EFFECT IN POLYMERS DURING HEATING-UP UNDER PRESSURE

10.1 Introduction

In the present chapter, a relatively simple method is proposed to study the Clapeyron effect for materials relevant in nonwovens. The novel inexpensive and straightforward method developed for this purpose is described in section 10.2. The experimental results are presented and discussed in section 10.3. Conclusions are drawn in section 10.4.

10.2 Experimental

The melting points of three types of nonwovens were tested in the present work: polybutylene terephthalate (PBT), polyethylene terephthalate (PET), and heavy-weight RHT pattern Spunbond- Meltblown- Spunbond polypropylene (PP), which were received from the Nonwoven Institute and Halyard, respectively. The as-received PBT and PP nonwovens were pre-bonded by a standard industrial process (cf. Figure 10.1a and 10.1c). The as-received PET nonwovens were not bonded (cf. Figure 10.1b). The thicknesses of a single layer of as- received PBT and PP nonwovens were measured as 0.56 mm and 0.40 mm, respectively. The PBT and PP samples used in the experiments were directly cut from the as-received nonwoven mats as square pieces with the areas of 1 mm², 4 mm², and 9 mm².

Instead of using the as-received PET nonwovens directly, several layers of such nonwovens were stacked together and thermally-bonded using an in-house-made setup. Then, PET samples

with the areas of 1 mm², 4 mm², and 9 mm² were cut from the thermally-bonded PET mats, whose thickness was measured as 0.48 mm. It should be emphasized that the purpose of the thermal bonding applied to PET nonwoven mats was to increase the uniformity of the samples facilitate the further experimental observations. The thermal bonding process and the selection of the thermal bonding temperature would not influence future experimental results. The thermal bonding setup used in the current work was described elsewhere [Zhang et al. (2018)]. The rectangular thermal punch, who had a length of 50.8 mm and width of 24.5 mm, was used for the thermal bonding process in the current work. The thermal bonding temperature was selected as 200 °C.

The setup (Figure 10.2) designed for observing the Clapeyron effect consisted of (i) a hotplate; (ii) the upper and lower aluminum cylinders; (iii) a thermocouple and a thermometer; (iii) iron cubes used as applied weight; (iv) the recording device; and (v) the light source. The Thermo Scientific hotplate was employed as the constant heat supply source and the working temperatures for the PBT, PET and PP nonwovens were set as 330 °C, 330 °C and 270 °C, respectively. The sizes of the two aluminum cylinders were 12.60 mm in diameter and 12.65 mm in height. A prepared nonwoven sample was placed between the two cylinders. The weight of the upper cylinder was measured as 12.75 g. There was a 1 mm diameter hole drilled on the side of the lower cylinder and the distance of the center of the hole to the top surface of the lower cylinder was 1 mm. An Omega thermocouple was inserted through this hole and connected to an Omega HH806AW thermometer. Due to the very small distance between the thermocouple position and the top surface of the lower cylinder, the temperature reading was designated as the temperature of the top surface of the lower cylinder, which was essentially, the sample temperature. Three iron cubes of different masses of 685.7 g, 1071.5 g, and 1102.3 g were employed to apply different

weight. Thus, different pressures were realized by the different combination of the applied weight and the sample area. Dino-Lite digital microscope was used as the recording device. The detailed schematic of the experimental setup and the magnified view of the gap between the upper and lower cylinders are shown in Figures 10.2a and 10.2b, respectively.

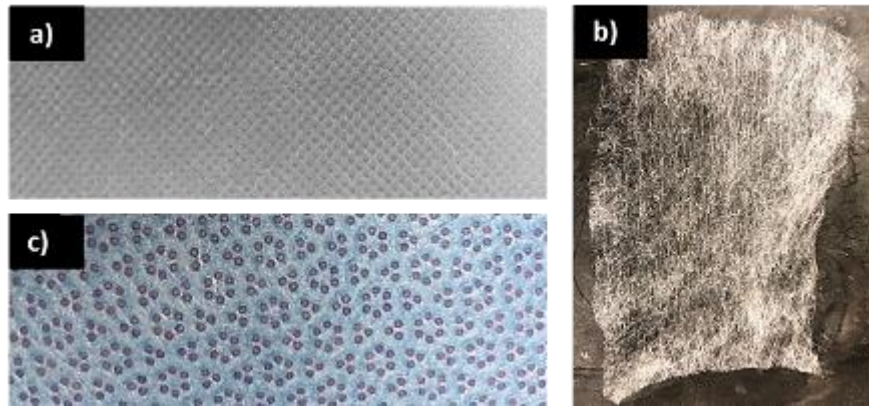


Figure 10. 1 As-received single layers of PBT, PET and PP nonwovens. (a) PBT; (b) PET; (c) PP.

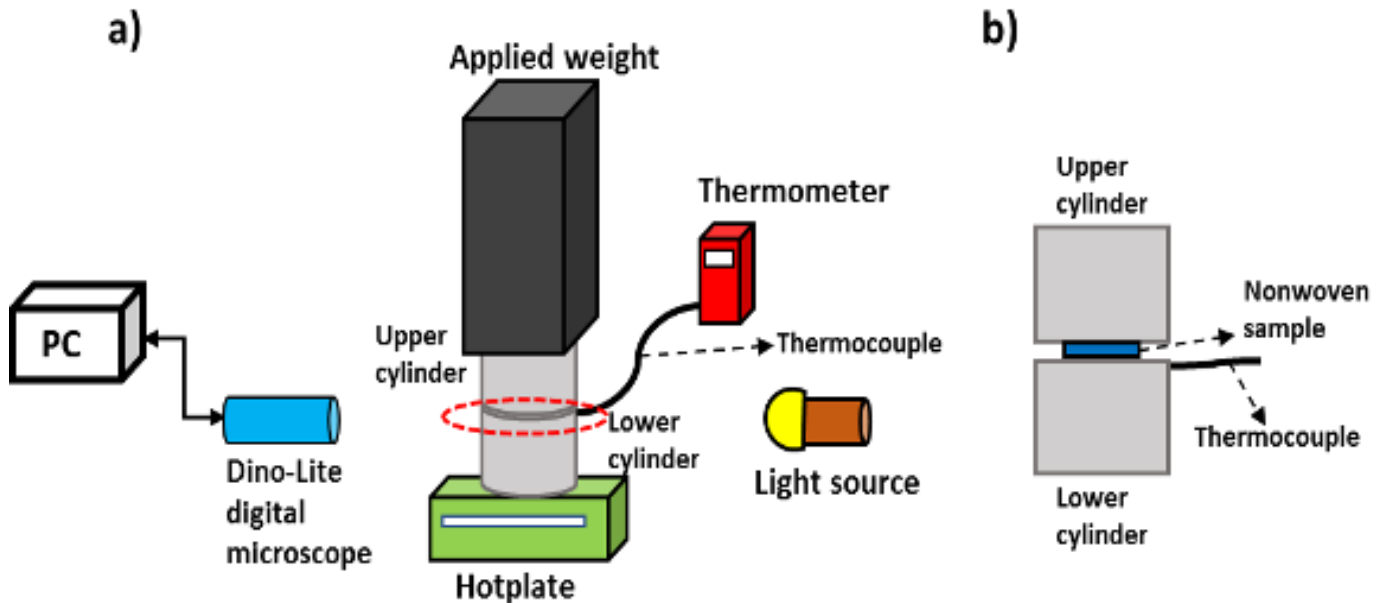


Figure 10. 2 Schematic of the experimental setup. (a) The entire setup. The red dashed oval in this

panel encompasses the domain zoomed-in in panel (b). (b) The magnified view of the gap between the upper and lower cylinder, where the nonwoven samples were located.

As the temperature of the top surface of the lower cylinder increased and reached the melting point of the nonwoven, the tested sample melted, the upper cylinder moved downward, and the sample height decreased since the molten sample was squeezed by the upper cylinder. The corresponding change in the inter-cylinder gap was recorded by a Dino-Lite digital microscope and analyzed. It should be emphasized that the top surface temperature of the lower cylinder, recorded by the thermometer, was still increasing during the melting process due to the heat supply from the hotplate. Thus, the melting point of the nonwovens was, essentially, the measured temperature at the moment when the upper cylinder started to move downward, i.e. the nonwoven started to melt. The experimental results are presented and discussed in section 10.3.

10.3 Experimental results and discussions

10.3.1 Melting of PBT, PET and PP nonwovens under the upper cylinder weight without additional applied weight

The nonwoven melting is a continuous process, and the sample height (equal to the measured inter-cylinder gap) kept decreasing during sample melting in the setup in Figure 10.2. Figure 10.3 illustrates the observations of the inter-cylinder gap during melting of a 9 mm² PBT nonwoven sample without an applied weight of the iron cubes, i.e. just under the upper cylinder weight. The sample height was measured by the open software ImageJ and marked in each image. The time interval from the moment the PBT nonwoven began to melt (cf. Figure 10.3a) to the moment it melted completely (cf. Figure 10.3e), was about 95 s. Similar observations were done when the additional weights (the iron cubes) were applied.

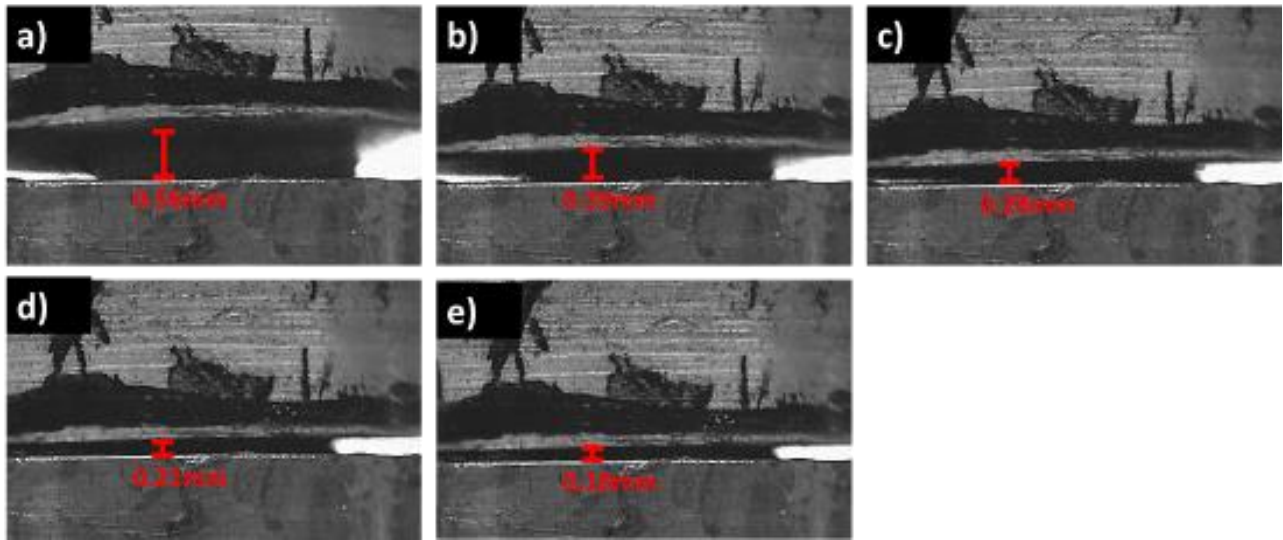


Figure 10. 3 Melting process of a PBT nonwoven sample without an applied weight at different time moments: (a) $t = 0$, the inter-cylinder gap is 0.56 mm. (b) $t = 25$ s, the inter-cylinder gap is 0.39 mm, (c) $t = 50$ s, the inter-cylinder gap is 0.28 mm, (d) $t = 75$ s, the inter-cylinder gap is 0.21 mm, (e) $t = 95$ s, the inter-cylinder gap is 0.18 mm.

Figure 10.4 shows the melting process of the 9 mm^2 thermally-bonded PET nonwoven sample without an applied weight. Starting from the moment when the sample began to melt (cf. Figure 10.4a) to the moment when the sample melted completely (cf. Figure 10.4e), the entire melting process took about 20 s. The thickness of the PET sample was observed to decrease from 0.48 mm to 0.25 mm. Similar observations were done for PET nonwoven loaded with additional applied weights. These results are discussed in subsection 10.3.3.

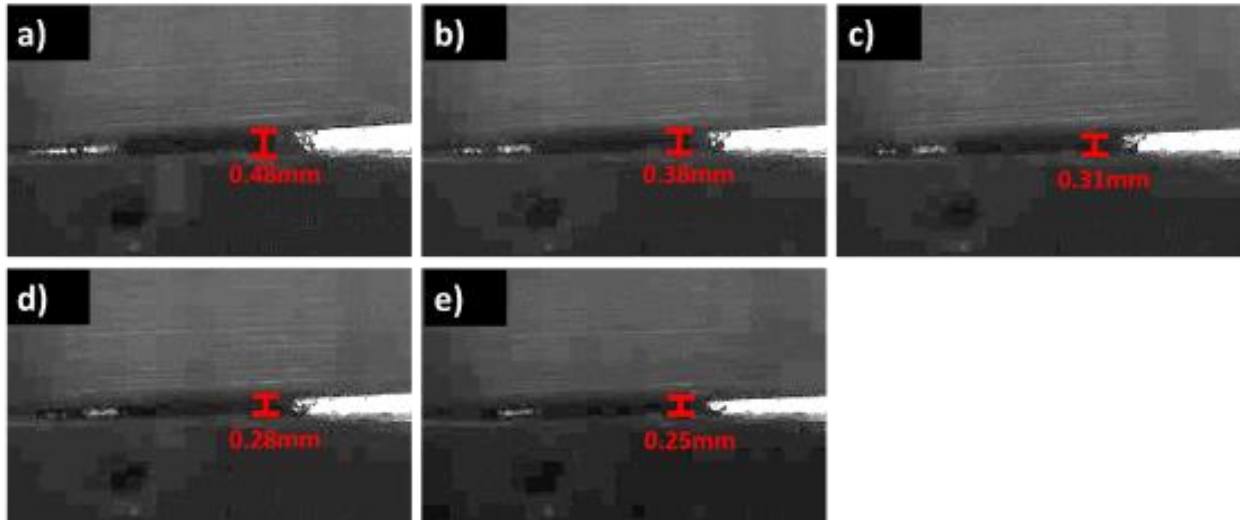


Figure 10. 4 Melting process of PET nonwoven sample without an applied weight at different time moments: (a) $t = 0$, the inter-cylinder gap is 0.48 mm; (b) $t = 5$ s, the inter-cylinder gap is 0.38 mm; (c) $t = 10$ s, the inter-cylinder gap is 0.31 mm; (d) $t = 15$ s, the inter-cylinder gap is 0.28 mm; (e) $t = 20$ s, the inter-cylinder gap is 0.25 mm.

Figure 10.5 shows the melting process of the PP nonwoven sample without an applied weight. From the moment the sample began to melt (cf. Figure 10.5a) to the moment the sample melted completely (cf. Figure 10.5e), it also took about 20 s. Similar observations were done for PP nonwoven loaded with the additional applied weights.

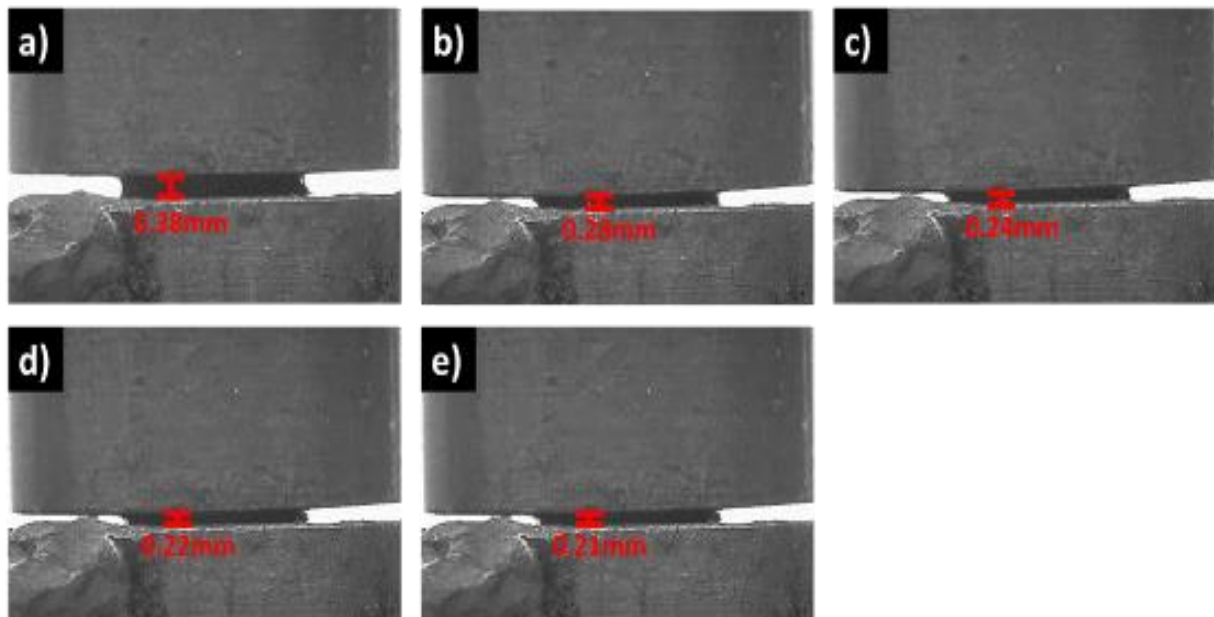


Figure 10. 5 Melting process of a PP nonwoven sample without an applied weight at different time moments; (a) $t=0$, the inter-cylinder gap is 0.38 mm. (b) $t=5$ s, the inter-cylinder gap is 0.28 mm. (c) $t=10$ s, the inter-cylinder gap is 0.24 mm. (d) $t=15$ s, the inter-cylinder gap is 0.22 mm. (e) $t=20$ s, the inter-cylinder gap is 0.21 mm.

10.3.2 Melting of PBT nonwovens under different applied weights (pressures)

The melting points of PBT nonwovens were measured with five values of the applied pressure: 0.14 atm (9 mm² sample with no applied weight, just under the upper cylinder weight), 11.65 atm (9 mm² sample with 1071.5 g applied iron cube and 12.75 g upper cylinder), 26.22 atm (4 mm² sample with 1071.5 g applied iron cube and 12.75 g upper cylinder), 104.86 atm (1 mm² sample with 1071.5 g applied iron cube and 12.75 g upper cylinder) and 277.79 atm (1 mm² sample with 2859.50 g applied iron cube and 12.75 g upper cylinder). Three experimental trials were conducted in each case, and the averaged results are shown in Figure 10.6. The red line in this figure indicates the corresponding fitting curve and the fitting equation is

$T = -10.065 \exp(-P / 23.269) + 230.101$, where P is applied pressure and T is the melting temperature.

Without an additional weight applied, the average value of melting temperature of PBT nonwovens was measured as 219.99 °C, which is close to the value of the melting temperature of 220 °C reported in the literature [Thomas and Visakh (2011)]. The melting points changed by about 4.31 °C as the applied pressure increased from 0.14 atm to 11.65 atm (cf. Figure 10.6). Accordingly, the rate gradient was 0.370 °C/atm. As the pressure increased from 11.65 atm to 26.22 atm, the melting point increased by about 2.45 °C, i.e. with the gradient of 0.168 °C/atm. When the pressure increased up to 104.86 atm, the melting point of the PBT nonwoven increased by about 2.77 °C, corresponding to a very low gradient of 0.035 °C/atm. At the pressure of 277.79 atm, the melting point of PBT nonwoven was 231.35°C, i.e. changing by about 1.83 °C, corresponding to a very low gradient of 0.011 °C/atm. The average gradient over the entire pressure interval was 0.041°C/atm. The observations revealed the extent of the Clapeyron effect for the PBT nonwovens. It should be emphasized that the effect weakened at higher pressures.

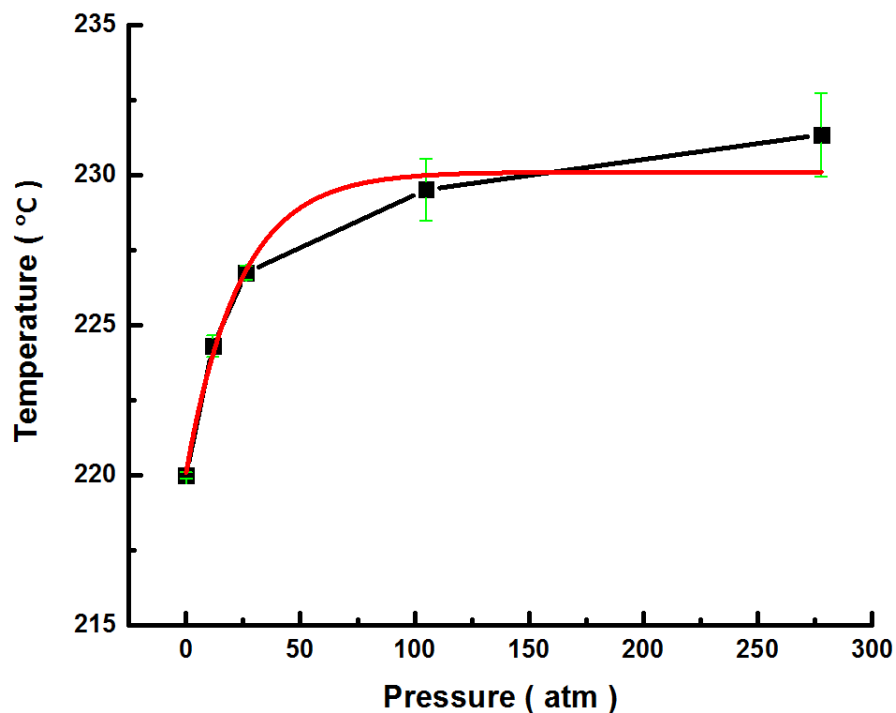


Figure 10. 6 Dependence of melting temperature on the applied pressure for the PBT nonwovens.

The sample height of the PBT nonwoven at the moments of the beginning and ending of the melting process under different applied weights are shown in Figure 10.7. The sample height was marked in each image. The changed in the sample height revealed the movement of the upper cylinder, which became possible due to the nonwoven melting. It should be emphasized that the rate of change of the sample height from the beginning moment (cf. Figures 10.7a1, 10.7b1, 10.7c1, 10.7d1 and 10.7e1) to the corresponding ending moments (cf. Figure 10.7a2, 10.7b2, 10.7c2, 10.7d2 and 10.7e2) with various applied pressures.

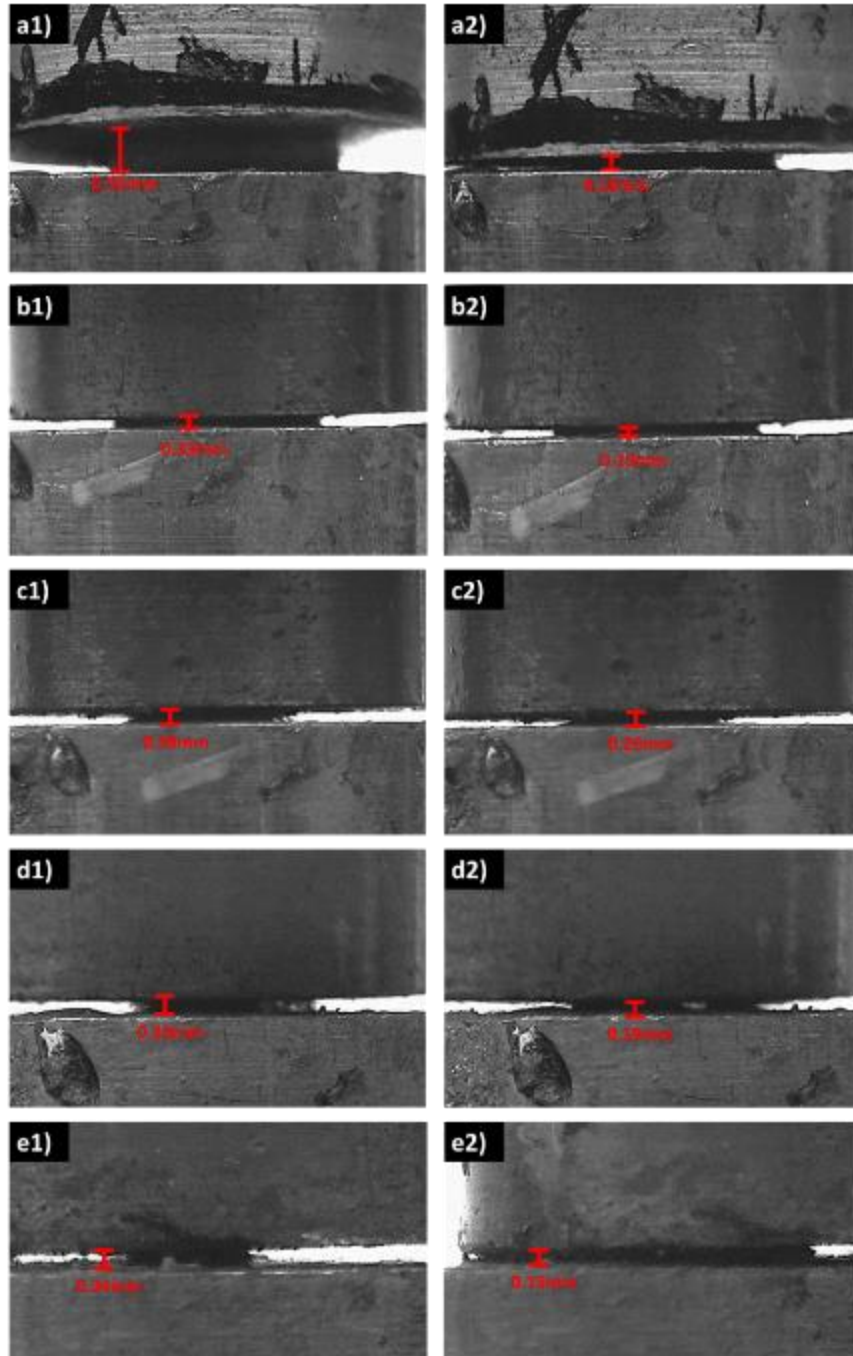


Figure 10. 7 Change in the sample height for the PBT nonwovens due to melting. Panels (a1) and (a2) show the 9 mm² sample with no applied weight at the beginning and ending moments of melting. Panels (b1) and (b2) show the 9 mm² sample with 1071.50 g of the applied weight, namely, under the pressure of 11.65 atm, at the beginning and ending moments of melting. Panels (c1) and (c2) show the 4 mm² sample with 1071.50 g of the applied weight, namely, under the pressure of

26.22 atm, at the beginning and ending moments of melting. Panels (d1) and (d2) show the 1 mm² sample with 1071.50 g of the applied weight, namely, under the pressure of 104.86 atm, at the beginning and ending moments of melting. Panels (e1) and (e2) show the 1 mm² sample with 2859.50 of the applied weight, namely, under the pressure of 277.79 atm, at the beginning and ending moments.

10.3.3 Melting of PET nonwovens under different applied weights (pressures)

The melting points of PET nonwovens were measured with four values of the applied pressure: 0.14 atm (9 mm² sample with no applied weight, just under the upper cylinder weight), 11.65 atm (9 mm² sample with 1071.5 g applied iron cube and 12.75 g upper cylinder), 26.22 atm (4 mm² sample with 1071.5 g applied iron cube and 12.75 g upper cylinder), and 104.86 atm (1 mm² sample with 1071.5 g applied iron cube and 12.75 g upper cylinder). Three experimental trials were conducted in each case, and the averaged results are shown in Figure 10.8. The red line in this figure indicates the corresponding fitting curve and the fitting equation is $T = -7.718 \exp(-P/10.772) + 256.801$, where P is the applied pressure and T is the melting temperature.

Without an additional weight applied, the average value of the melting temperature of PET nonwovens was measured as 249.18 °C, which is similar to the value of 250 °C reported in the literature [Thomas and Visakh (2011)]. The melting points changed by about 5.18 °C as the applied pressure increased from 0.14 atm to 11.65 atm (the rate gradient was 0.450 °C/atm). As the pressure increased from 11.65 atm to 26.22 atm, the melting point increased by about 1.28 °C (the gradient of 0.168 °C/atm). When the pressure increased to 104.86 atm, the melting point of the PET nonwoven increased by about 1.33 °C (the gradient of 0.017 °C/atm). The average gradient over

the entire pressure interval was calculated as 0.074 °C/atm. The experiments were conducted with the applied pressure up to 104.86 atm due to the limitations of the thickness changing observations.

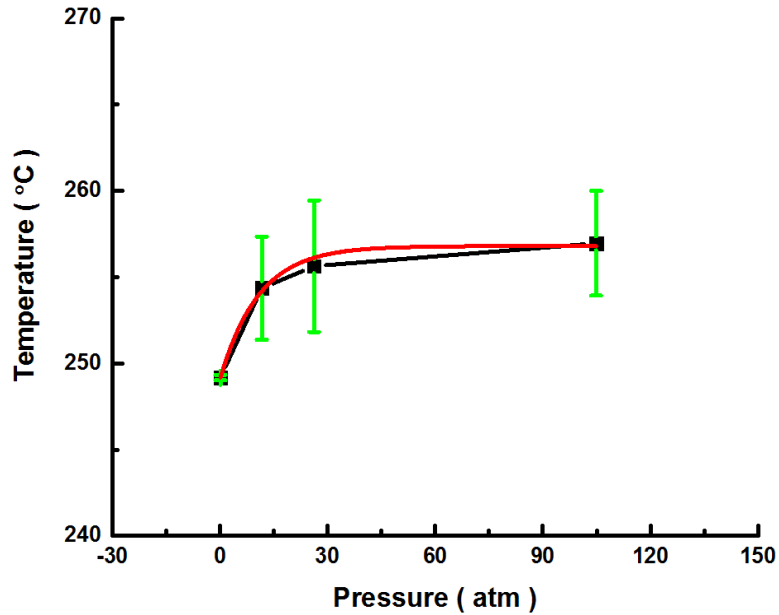


Figure 10. 8 Melting temperature dependence on pressure for the PET nonwovens.

The sample heights of the PET nonwoven at the moments of the beginning and ending of the melting process under different applied weights are shown in Figure 10.9. The sample height is marked in each image.

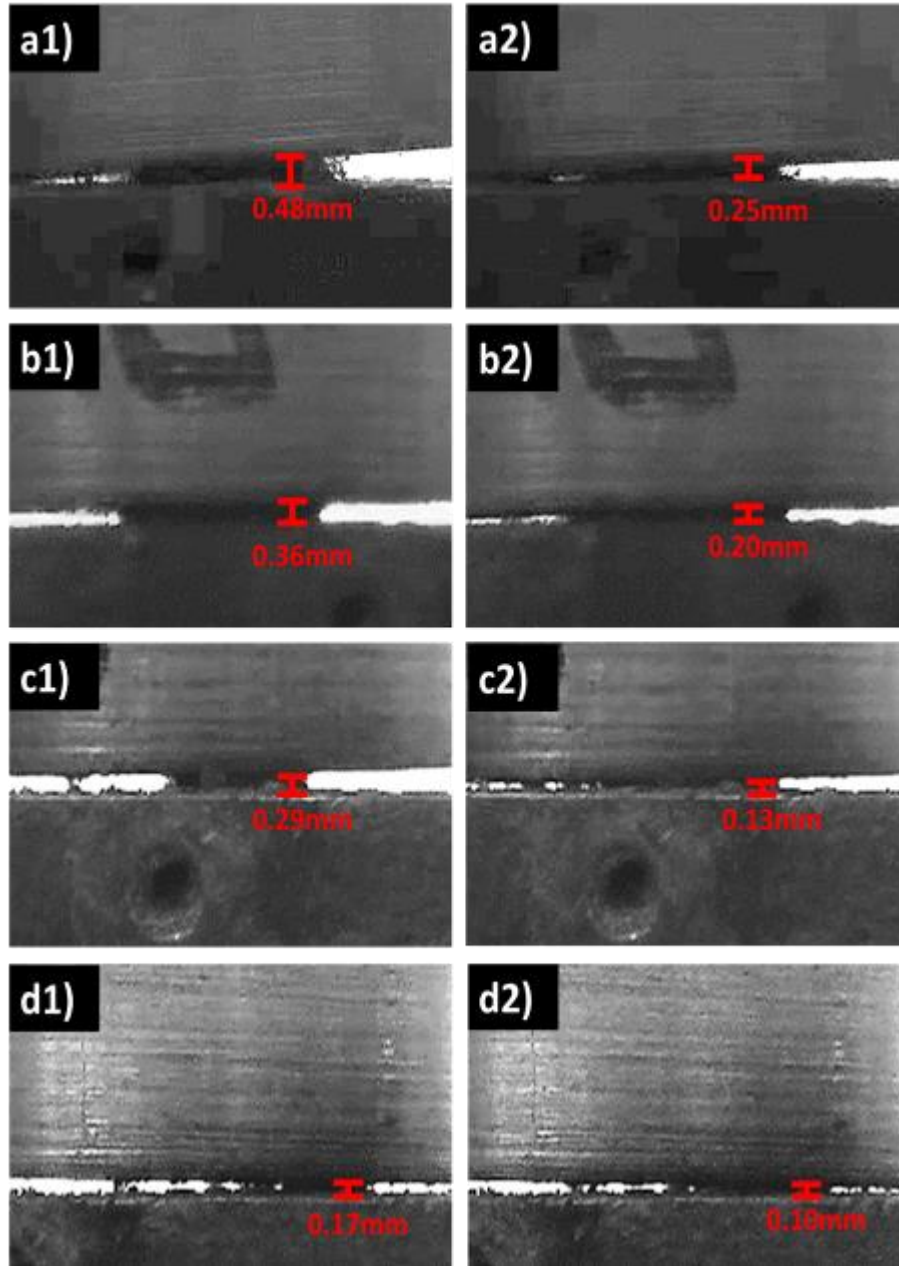


Figure 10. 9 Change in the sample height for the PET nonwovens due to melting. Panels (a1) and (a2) show the 9 mm² sample with no applied weight at the beginning and ending moments of melting. Panels (b1) and (b2) show the 9 mm² sample with 1071.50 g of the applied weight, namely, under the pressure of 11.65 atm, at the beginning and ending moments of melting. Panels (c1) and (c2) show the 4 mm² sample with 1071.50 g of the applied weight, namely, under the pressure of 26.22 atm, at the beginning and ending moments of melting. Panels (d1) and (d2) show the 1 mm²

sample with 1071.50 g of the applied weight, namely, under the pressure of 104.86 atm, at the beginning and ending moments of melting.

10.3.4 Melting of PP nonwovens under different applied weights (pressures) vs. PBT and PET nonwovens

The melting points of PP were measured under four different pressures, 0.31 atm (4 mm² sample with no applied weight, just under the upper cylinder weight), 11.65 atm (9 mm² sample with 1071.5 g applied weight and 12.75 g upper cylinder), 26.22 atm (4 mm² sample with 1071.5 g applied weight and 12.75 g upper cylinder) and 104.86 atm (1 mm² sample with 1071.5 g applied weight and 12.75 g upper cylinder). Three experimental trials in each case were conducted and the average melting temperature values are shown in Figure 10.10. The red line in this figure indicates the corresponding fitting curve, with the fitting equation being $T = -5.45 \exp(-P / 16.64) + 166.93$. The comparison of the melting temperature dependences on pressure for PBT, PET, and PP is shown in Figure 10.11.

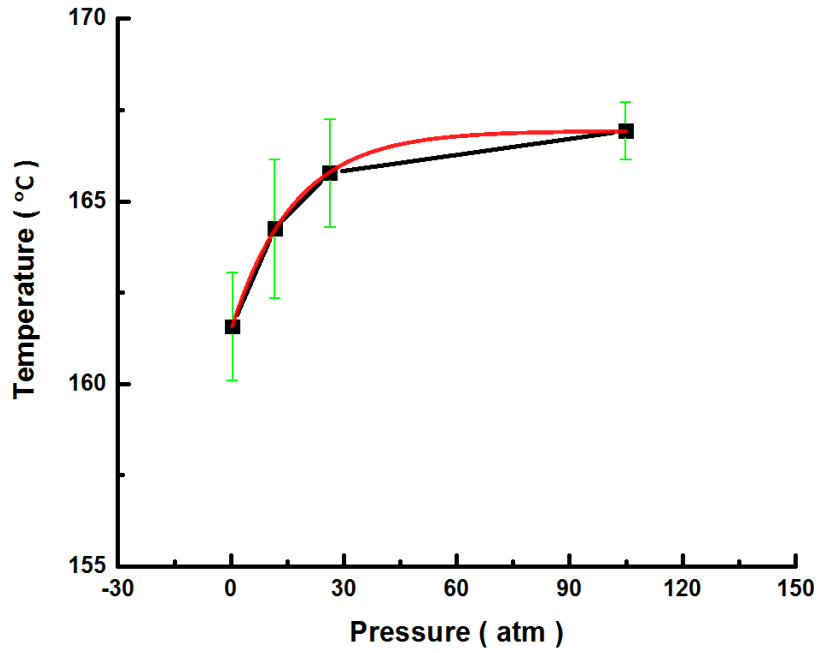


Figure 10. 10 Melting temperature dependence on pressure for the PP nonwovens.

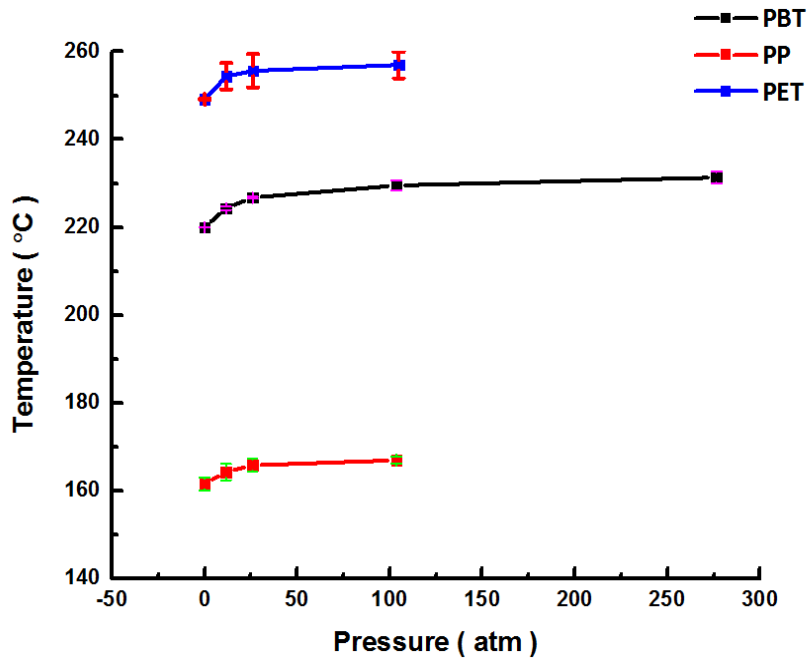


Figure 10. 11 Comparison of the melting temperature dependence on pressure for the PBT, PET and PP nonwovens.

The melting point of the PP nonwoven at 0.31 atm, 11.65 atm, 26.22 atm, and 104.86 atm was measured as 161.58 °C, 164.25 °C, 165.78 °C and 166.93 °C, respectively. According to the literature [Maier and Calafut (1998)], the melting point of commercial PP is in the 160 to 166 °C range. Thus, the melting temperature of PP obtained in the present work at 0.31 atm is reasonable. The melting gradient for PP in the 0.31 to 11.65 atm pressure range was found as 0.236 °C/atm. This value is smaller than the one corresponding to the PBT nonwovens. In the intervals from 11.65 atm to 26.22 atm and from 26.22 atm to 104.86 atm, the changing rates the gradient values for PP are 0.105 °C/atm and 0.015 °C/atm, respectively. These two values are also smaller than the corresponding values found for the PBT nonwovens. The average gradient over the entire pressure interval was 0.118 °C/atm.

As stated in [Warner (1989)], the actual melting point of PP would be increased about by 10 °C under the bond pins. According to the present experimental results, the melting point of the PP nonwoven increased by about 5.36 °C. The possible reason for the 4.64 °C temperature difference would be in the material difference. The isotactic PP was used in [Warner (1989)], while the PP nonwovens used in the present work were a commercial product, i.e. the atactic material, with the unknown crystallinity. It is clear that crystallinity would greatly influence the melting point of PP materials. It should be emphasized that the pressure rise in the experiments with the PP nonwovens was only up to 104.86 atm since the sample height change was relatively harder to observe at 277.79 atm. Accordingly, the method proposed in the present work revealed reliable results and is easy to implement and highly efficient.

The sample height of the PP nonwovens at the moments of the beginning and ending of the melting process at different applied weights (pressures) is seen in Figure 10.12. The sample height is marked in red in each image. It should be emphasized that the difference between the sample

heights at the beginning and ending moments decreases as the applied weight (pressure) increases.

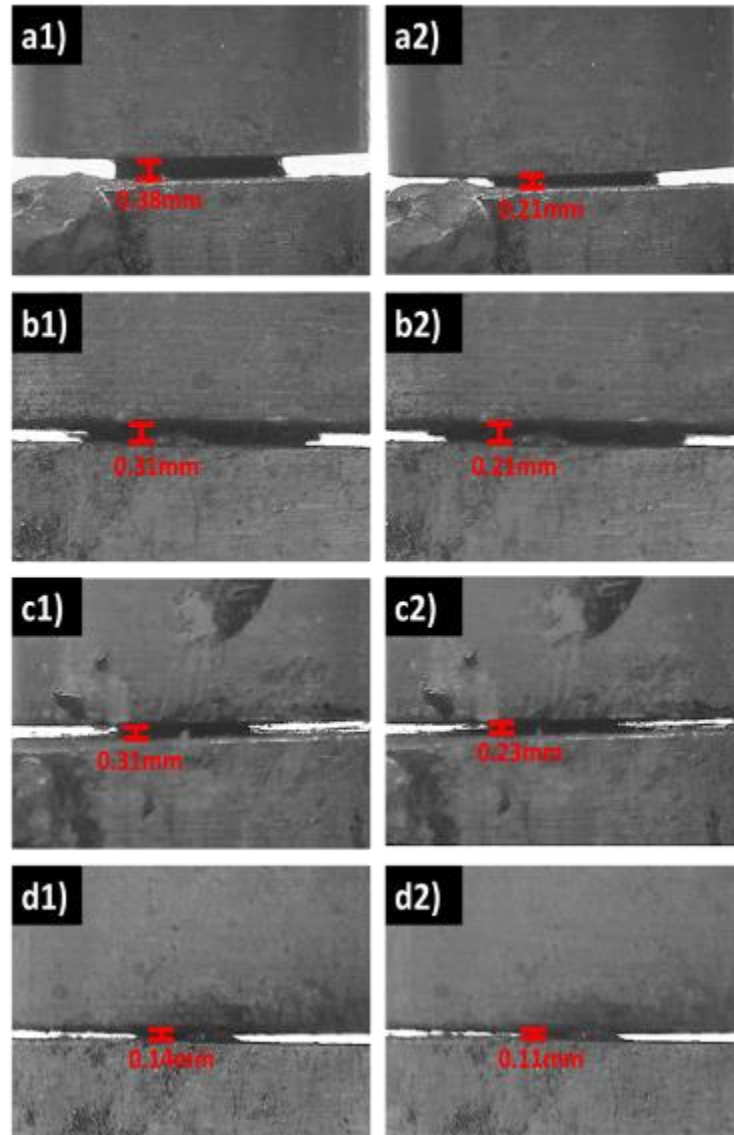


Figure 10. 12 Change in the sample height of the PP nonwovens due to melting. Panels (a1) and (a2) show the 4 mm² sample with only upper cylinder weight (the 0.31 atm pressure), at the beginning and ending moments of melting process, respectively. Panels (b1) and (b2) show the 9 mm² sample with 1071.50 g applied weight (the 11.65 atm pressure), at the beginning and ending moments of melting process, respectively. Panels (c1) and (c2) show the 4 mm² sample with

1071.50 g applied weight (the 26.22 atm pressure), at the beginning and ending moments of melting process. Panels (d1) and (d2) show the 1 mm² sample with 1071.50 g applied weight (the 104.86 atm pressure), at the beginning and ending moments of melting process.

10.4 Conclusion

A novel simple and straightforward method of measuring melting points of nonwovens/polymers subjected to different pressures was proposed. The method was implemented with the PBT, PET, and PP nonwovens, and the Clapeyron effect for them was quantified. Firstly, the melting point of the PBT nonwovens increased by about 11.36 °C when the applied pressure changed from 0.14 atm to 277.79 atm. Secondly, the melting point of the PET nonwovens increased by about 7.79 °C when the applied pressure changed from 0.14 atm to 104.86 atm. Thirdly, the melting point of the PP nonwovens increased by about 5.36 °C when the applied pressure changed from 0.31 atm to 104.86 atm. The results obtained were corroborated by comparison with the same existing data from literature and that the method proposed was found to be reliable and effective.

CHAPTER 11

EXPLOSIVE-LIKE EJECTIONS FORMED FROM PLANT STEM IN FIRE AND THE ESTIMATE OF VAPOR MASS EJECTION AT DISTILLATION STAGE OF FOREST FIRE

11.1 Introduction

In this chapter, the materials and the experimental setup are described in section 11.2. The observations of jets issued from burning vegetation are discussed in section 11.3. The model experiments with jets issue from liquid-filled needles engulfed in flame are described in section 11.4. The theory estimating the vapor mass issued at the distillation stage from burning fresh vegetation or liquid-filled needles engulfed in flame is presented and compared with the experimental data in section 11.5.

11.2 Materials and experimental setup

In this section, the details of experiments conducted with plant stems are described. The stems were collected from *Epipremnum aureum* (Golden Pothos), which is an evergreen vine and a commonly-found indoor plant (cf. Figure 11.1a). The diameter of *Epipremnum aureum* stem used in the experiments was around 3 to 4 mm. Fresh stems of *Epipremnum aureum* were also cut as 0.5 mm-thick slices which were observed using Olympus BX51 microscope. The cross-sectional stem microstructure observed using such slices is shown in Figure 11.2. The cross-sectional view clearly reveals that stems are comprised of a system of parallel channels filled with liquid, which might be water and/or volatiles or their mixture with water. In addition, fresh stems were also

immersed in ethanol for 20 h (cf. Figure 11.1c, which shows that both sides of stem became brown after that).



Figure 11. 1 Experimental materials. (a) The entire *Epipremnum aureum* plant. (b) A fresh-cut stem from the plant. (c) Both ends of a fresh-cut stem became brown after 20 h immersion in ethanol.

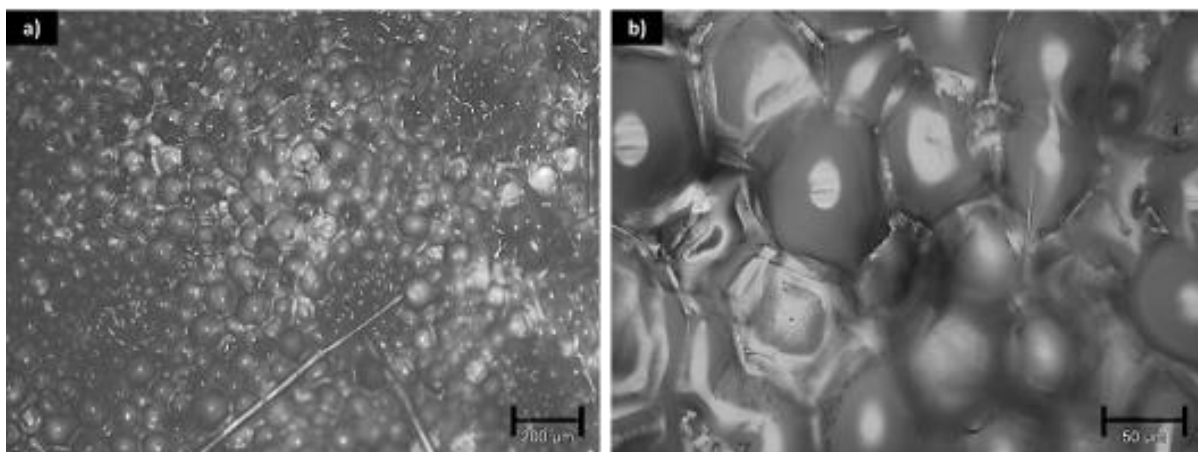


Figure 11. 2 Cross-sectional morphology of an *Epipremnum aureum* stem with liquid-filled channels visible. (a) ×4 magnification. (b) ×20 magnification.

A cotton dipped into pure ethanol was used as a flame source. All stems were cut into 6 cm-long samples, which were fixed horizontally using a clipper about 1 cm above the flame source (cf. Figure 11.3). A Phantom V210 high-speed camera and Flir T1030sc IR camera were employed for observations and recording of the overall process morphology and the temperature field.

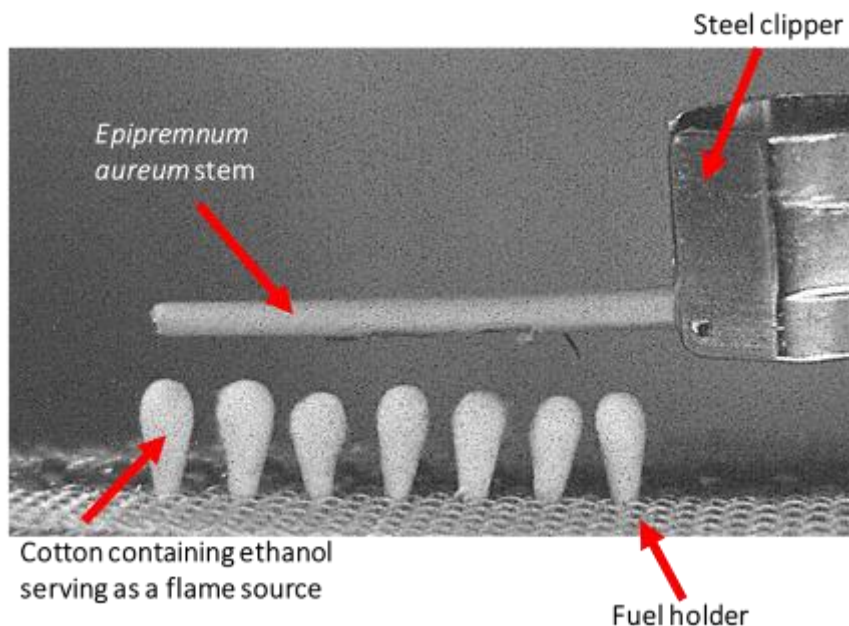


Figure 11. 3 Experimental setup.

11.3 Experiments conducted with stems

11.3.1 Experiments conducted with freshly-cut stems

In this experimental series with freshly-cut stems engulfed in flame, the resolution selected for the high-speed camera was 1008×416 pixels, the sampling rate was 200 fps, and the exposure time is $4900 \mu\text{s}$. It took about 0.7 s after the ignition for the flame to become fully developed and the stem to be engulfed in light blue flame about 6 cm of length in the horizontal direction (the time is reckoned from the moment of ignition of the first utmost left cotton-wrapped poll in Figure

11.3). After about 2 s from the ignition (cf. Figures 11.4a-11.4d) a small horizontal torch was noticed to be issued for about 1s from the left end of the stem (cf. Figure 11.4e). Then, a relatively violently ejection and the corresponding horizontal torch were observed for about 5s (cf. Figure 11.4f -11.4j). After the main ejection and the torch disappeared, a very small flame remained at the pre-notched incision at the stem center and several jets were also issued at several random locations over the stem surface (cf. Figure 11.4k- 11.4o). Some places locations were charred after the main ejection and torch have disappeared (cf. Figure 11. 4o). Additionally, it should be emphasized that red dotted lines depicted in Figure 11.4a-11.4c indicate the flame configuration and are to be compared with the further experimental results. The overall flame configuration was shaped by the natural convection.

The progress was also recorded by the IR camera simultaneously with the high- speed camera. Due to the limitations of the sampling rate of the IR camera, each image shown in Figure 11.5 does not correspond to the exactly the same time moment as those in Figure 11.4. It should be emphasized that the color bars in these images do not show a well-defined temperature due to the unknown emissivity of the burning vegetation. The temperature estimate will be discussed in section 11.5.

It is clearly seen that the stem was located at the practically constant temperature during the burning progress indicated by the red color (cf. Figure 11.5a-11.5d). The temperature of the horizontal vapor jets issued from the stem, corresponding to green color, was lower than that of the burning fuel.

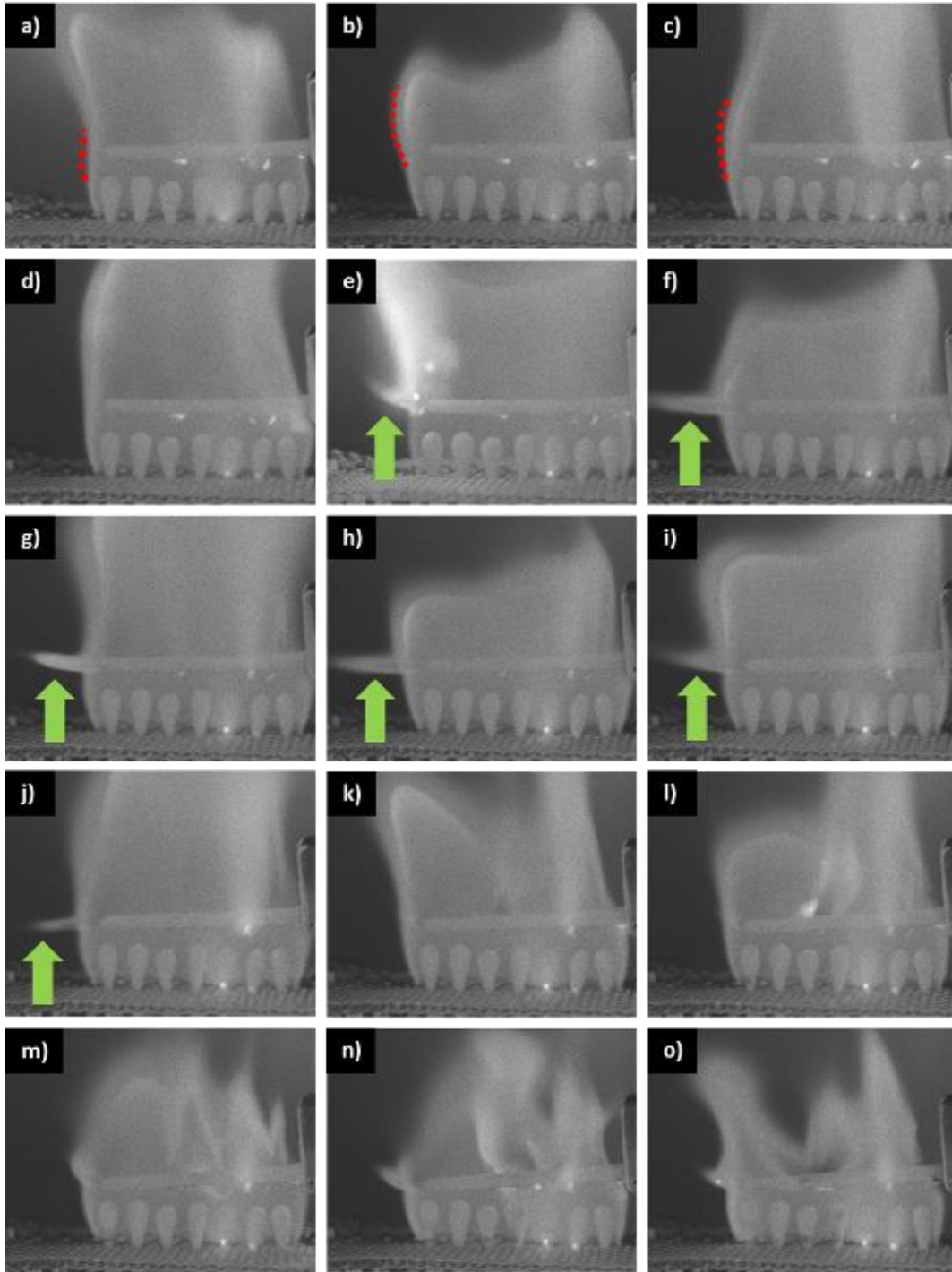


Figure 11. 4 Burning of a freshly-cut plant stem, recorded by high-speed camera. (a) $t=0.7$ s. (b) $t=1.7$ s. (c) $t=2.7$ s. (d) $t=3.7$ s. (e) $t=4.7$ s. (f) $t=5.7$ s. (g) $t=6.7$ s. (h) $t=7.7$ s. (i) $t=8.7$ s. (j) $t=9.7$ s. (k) $t=10.7$ s. (l) $t=11.7$ s. (m) $t=12.7$ s. (n) $t=13.7$ s. (o) $t=14.7$ s. The green arrows point at the jet blown from the stem.

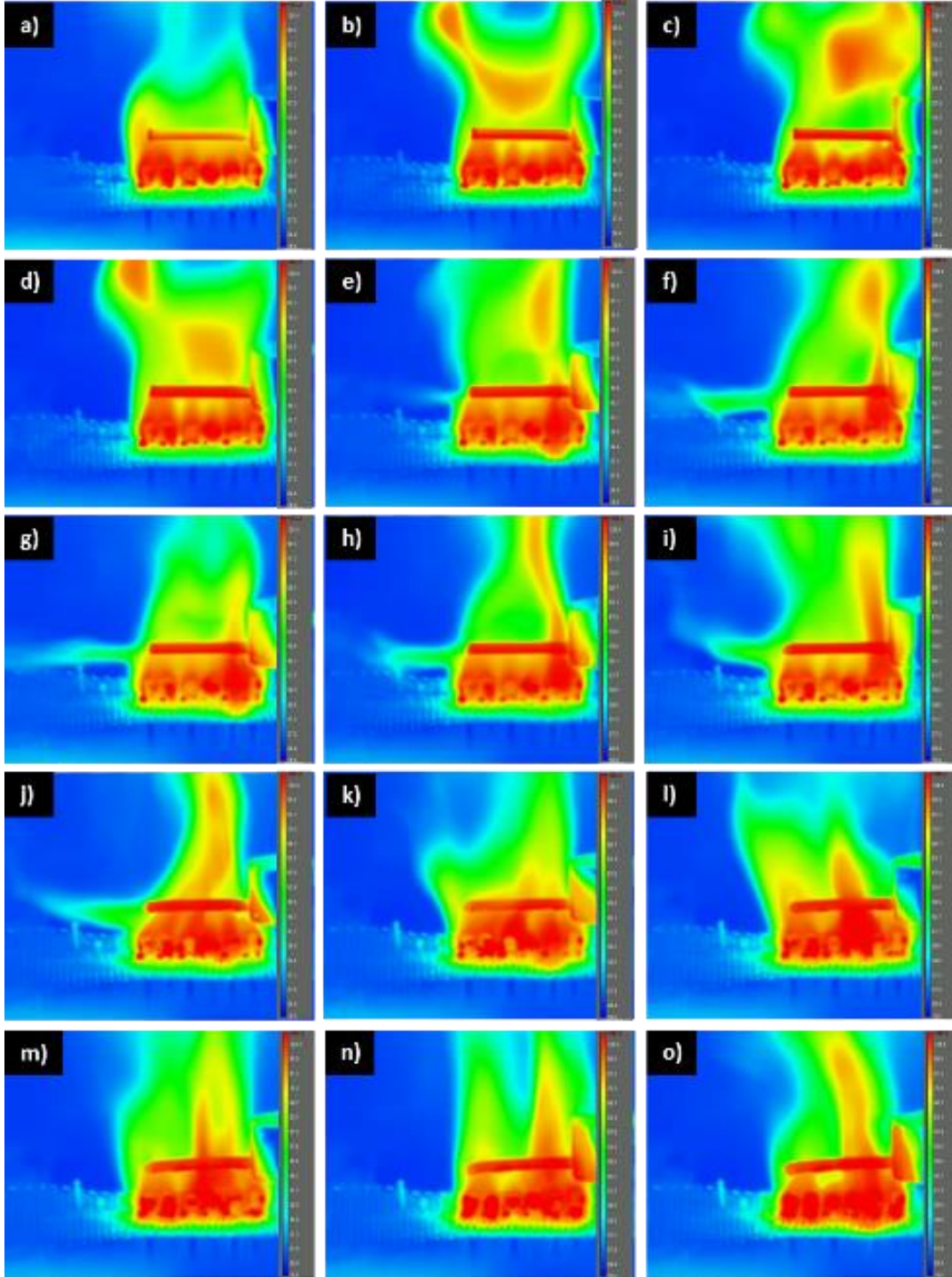


Figure 11. 5 Burning of the freshly-cut plant stem, recorded by the IR camera. (a) $t=0.7$ s. (b) $t=1.7$ s. (c) $t=2.7$ s. (d) $t= 3.7$ s. (e) $t= 4.7$ s. (f) $t= 5.7$ s. (g) $t= 6.7$ s. (h) $t=7.7$ s. (i) $t=8.7$ s. (j) $t= 9.7$ s. (k) $t= 10.7$ s. (l) $t= 11.7$ s. (m) $t= 12.7$ s. (n) $t=13.7$ s. (o) $t=14.7$ s.

11.3.2 Experiments conducted with ethanol-immersed stems

The experiments were also conducted with the stem, which was immersed in ethanol for 20 h (cf. Figure 11.1c). The experiment was recorded by the high-speed camera and the IR camera simultaneously and the corresponding image sequences are shown in Figures 11.6 and 11.7. The recording resolution of the high-speed camera in this experiment was 1024×512 pixels, the sample rate was 200 fps, and the exposure time is $4900 \mu\text{s}$. It took about 0.5 s for the light blue flame from the source to be fully developed. The flame length in the horizontal direction was about 6 cm.

The red dotted lines depicted in Figure 11.6a-11.6d to indicate the evolution of the flame configuration. The ejection on the left develops and it is much wider and brighter and also turns upward due to buoyancy in distinction from the case shown in Figure 11.4. This means that in the present case (Figure 11.6; ethanol-impregnated stem) in distinction from the case of the original stem (Figure 11.4) a combustible vapor mixture (definitely enriched with ethanol vapor) is issued from the stem. It supports an individual horizontal flame which is bent upward by the buoyancy force associated with thermal expansion of the corresponding combustion products. Such jets were formed faster from the ethanol-immersed stem (starting at $t=5.5$ s, cf. Figure 11.6f) compared with the original freshly-cut stem (starting at $t=10.7$ s, cf. Figure 11.4k).

The image sequences obtained by the IR camera shown in Figure 11.7 also reveals a higher temperature of the ejected torch in the present case compared to the vapor jet illustrated in Figure 11.5. This conclusion is supported by the fact that red and yellow color are present in this torch (pointed by the red arrows in Figure 11.7a-11.7e) in distinction to the lower-temperature, green, ejection in Figure 11.5. The issued horizontal torch depicted in Figures 11.6 and 11.7 results from enrichment with ethanol vapor, which is capable of supporting its own combustion.

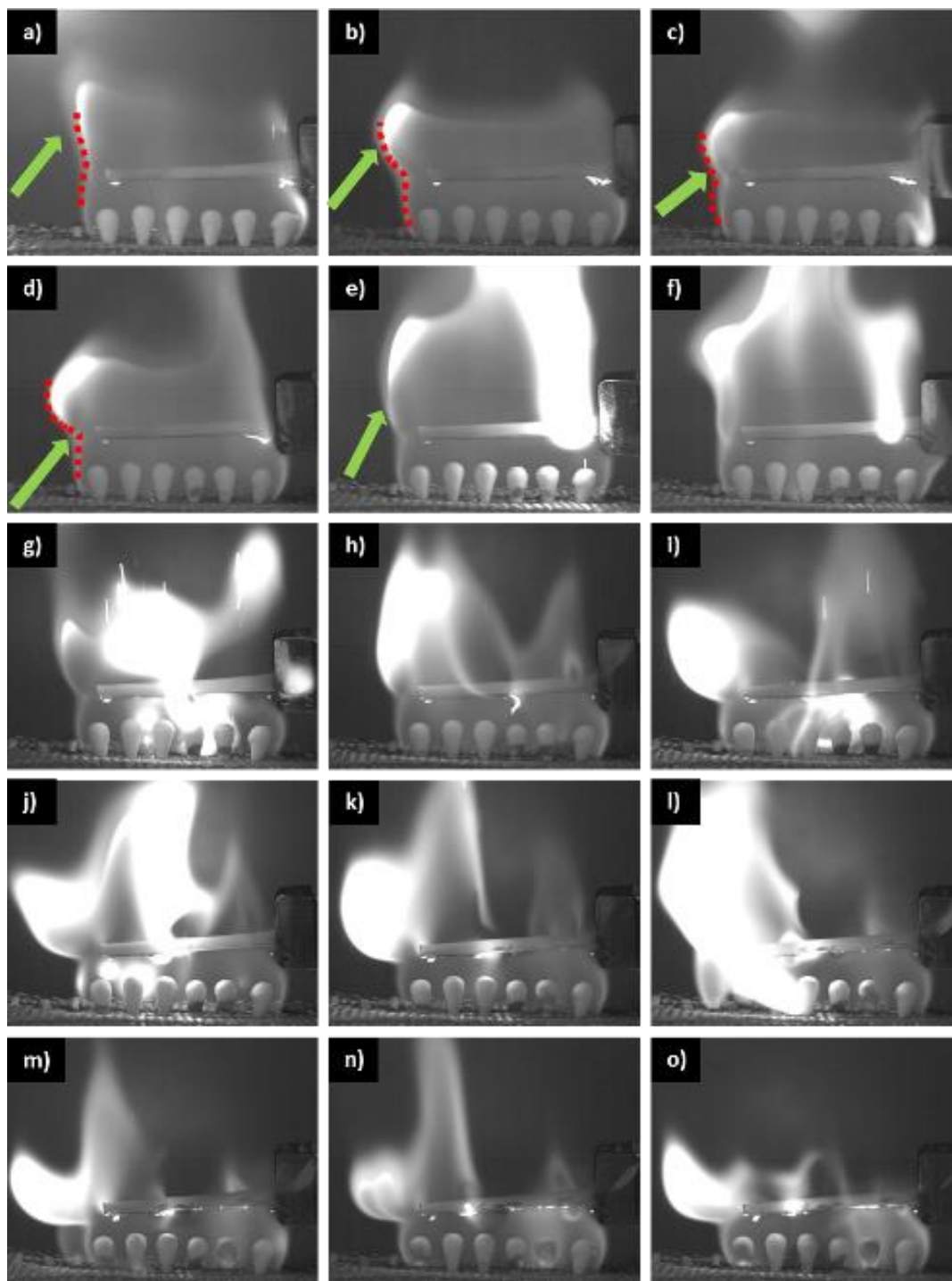


Figure 11. 6 Burning of the ethanol-immersed stem recorded by high-speed camera. (a) $t=0.5$ s. (b) $t=1.5$ s. (c) $t=2.5$ s. (d) $t=3.5$ s. (e) $t=4.5$ s. (f) $t=5.5$ s. (g) $t=6.5$ s. (h) $t=7.5$ s. (i) $t=8.5$ s. (j) $t=9.5$ s. (k) $t=10.5$ s. (l) $t=11.5$ s. (m) $t=12.5$ s. (n) $t=13.5$ s. (o) $t=14.5$ s. The green arrows point at the torch developing from the stem.

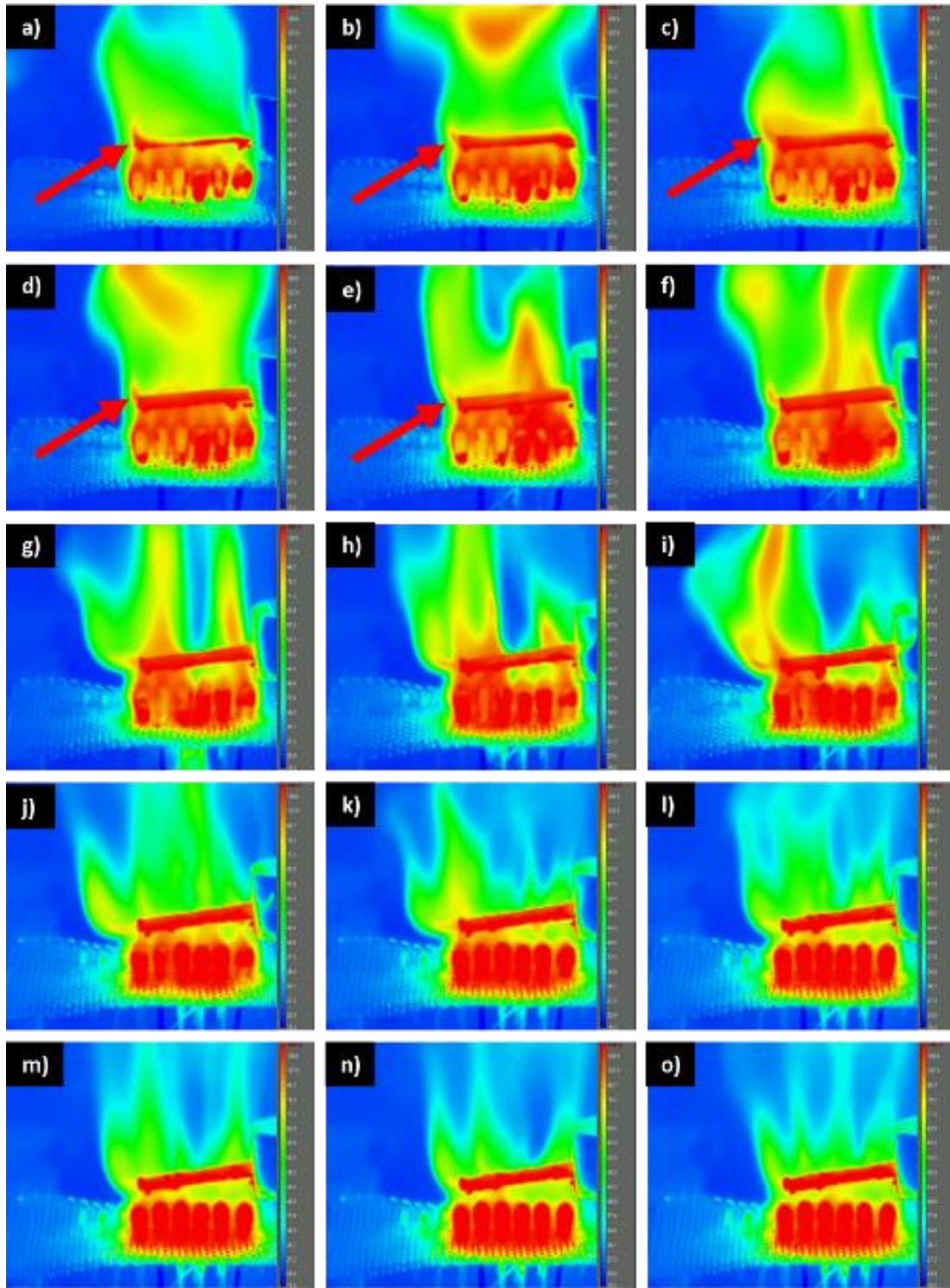


Figure 11. 7 Burning condition of an ethanol-immersed stem recorded by the IR camera. (a) $t=0.5$ s. (b) $t=1.5$ s. (c) $t=2.5$ s. (d) $t= 3.5$ s. (e) $t= 4.5$ s. (f) $t= 5.5$ s. (g) $t= 6.5$ s. (h) $t=7.5$ s. (i) $t=8.5$ s. (j) $t= 9.5$ s. (k) $t= 10.5$ s. (l) $t= 11.5$ s. (m) $t= 12.5$ s. (n) $t=13.5$ s. (o) $t=14.5$ s. The red arrows point

at the torch developing from the stem.

11.4 Model experiments conducted with needles filled up with liquids

11.4.1 Model experiments conducted with the 25G needles filled up with D.I. water

In this subsection, a 25G stainless steel dispensing needle with luer lock connection was used to model stems of sections 11.2 and 11.3. Since needles can be filled by liquids of different origin (e.g. water or ethanol), in the model experiments one can attribute the ejection appearance to a pre-determined liquid. The inner cross-sectional diameter and length of the 25G needle (excluding the plastic part) was 0.47 mm and 50 mm, respectively. The needles were purchased from McMaster-Carr and an example is shown in Figure 11.8.

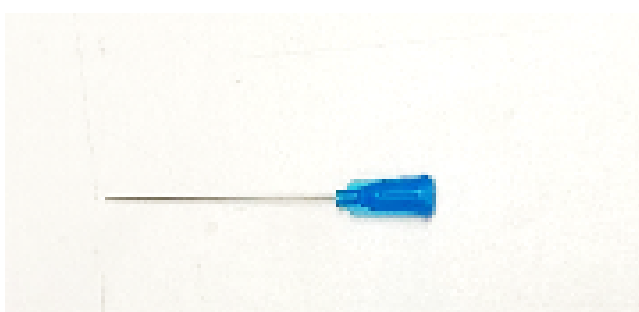


Figure 11. 8 A 25G stainless steel dispensing needle with luer lock connection, purchased from McMaster- Carr.

In the present model experiment, D.I. water was filled in the needle. A 5mL syringe was connected with the needle during the experiment and prevented water outflow from a cold needle. Pure ethanol was used as the flame-supporting fuel and cotton was used as the fuel storage, as before. The syringe was clipped 1cm high above the fuel-containing cotton. The flame size in the horizontal direction was about 3 cm. The model experiments were only recorded by the high-speed

camera. The recording resolution in this experiment was 1024×512 pixels, the sample rate was 3000 fps, and the exposure time was $332.6 \mu\text{s}$. About 0.25 s was taken for the flame to spread the entire length of the fuel row from the ignition moment. At $t=0.0603\text{s}$, the flame just proliferated to the second fuel poll from the utmost left one (cf. Figure 11.9). At that moment water from the needle edge engulfed in the flame became already visible outside as a protruding spherical sector. A further evolution in time is depicted in Figure 11.9.

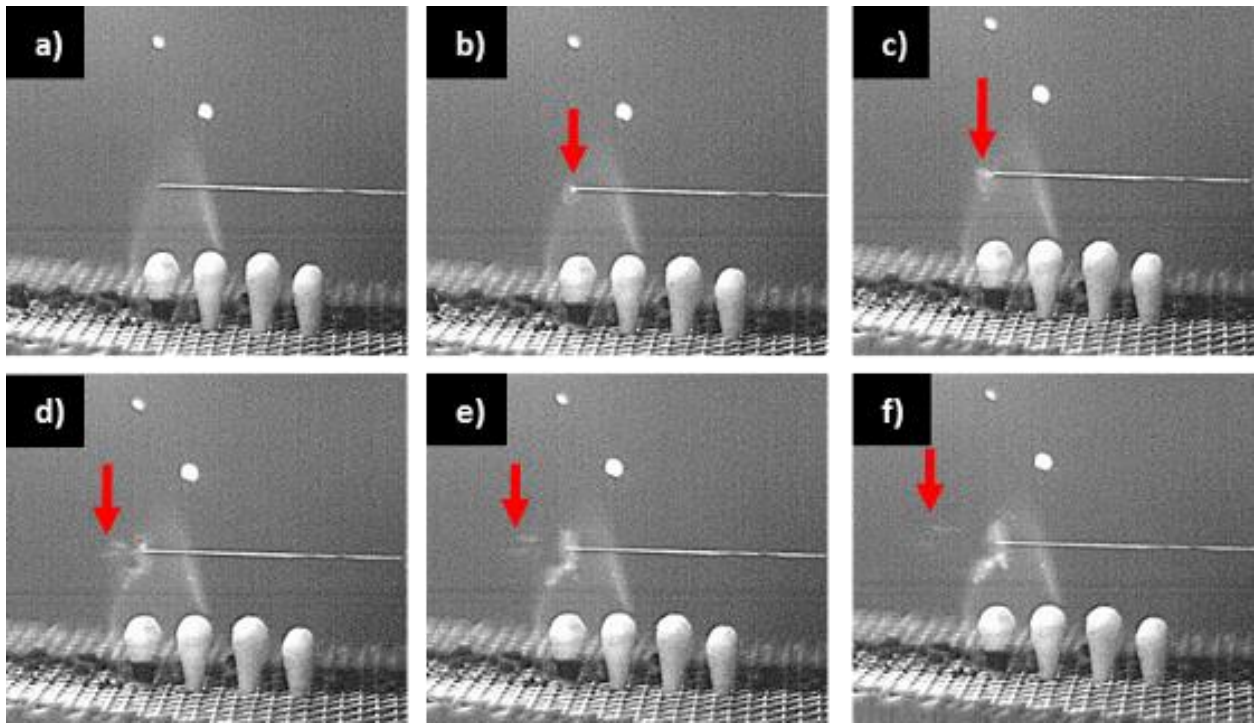


Figure 11. 9 Water droplet shaped as a spherical segment protruding from the edge of the 25G needle engulfed in flame. (a) $t= 0.0603$ s. (b) $t=0.0606$ s. (c) $t=0.0609$ s. (d) $t= 0.0612$ s. (e) $t= 0.0615$ s. (f) $t= 0.0618$ s. The red arrows point at the protruding droplet.

During the process of flame propagation from poll to poll, several water jets were ejected horizontally from the needle with a very high speed. One of such ejections is shown in Figure

11.10. Red arrows in the images in Figure 11.10 indicate the position of the water jet head. The water jet velocity was measured as about 10 m/s. The open software Image J was employed for the image processing to measure the jet velocity.

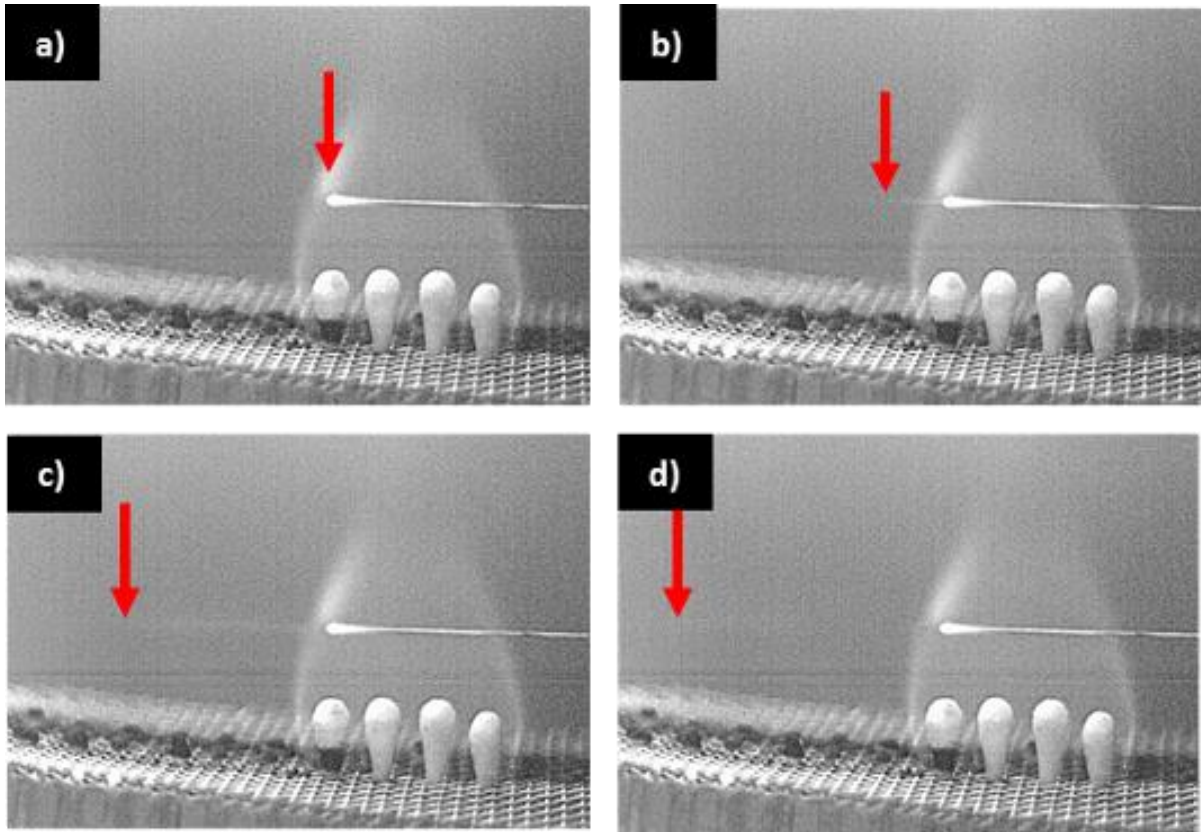


Figure 11. 10 The evolution of a liquid water jet issued from the 25G needle horizontally with the speed of about 10 m/s. (a) $t= 1.3470$ s. (b) $t=1.3473$ s. (c) $t=1.3476$ s. (d) $t= 1.3479$ s. The red arrows in each image indicate the head of the water jet.

The horizontal water jets of this type were capable of entrainment of the surrounding flame in the horizontal direction (cf. Figure 11.11). Similar phenomenon had been also observed in subsection 11.3.1 (cf. Figure 11.4e-11.4j). This implies that the moisture contained in the stem could also entrain leftward the surrounding flame to form the horizontal explosive-like ejections

seen in Figure 11.4.

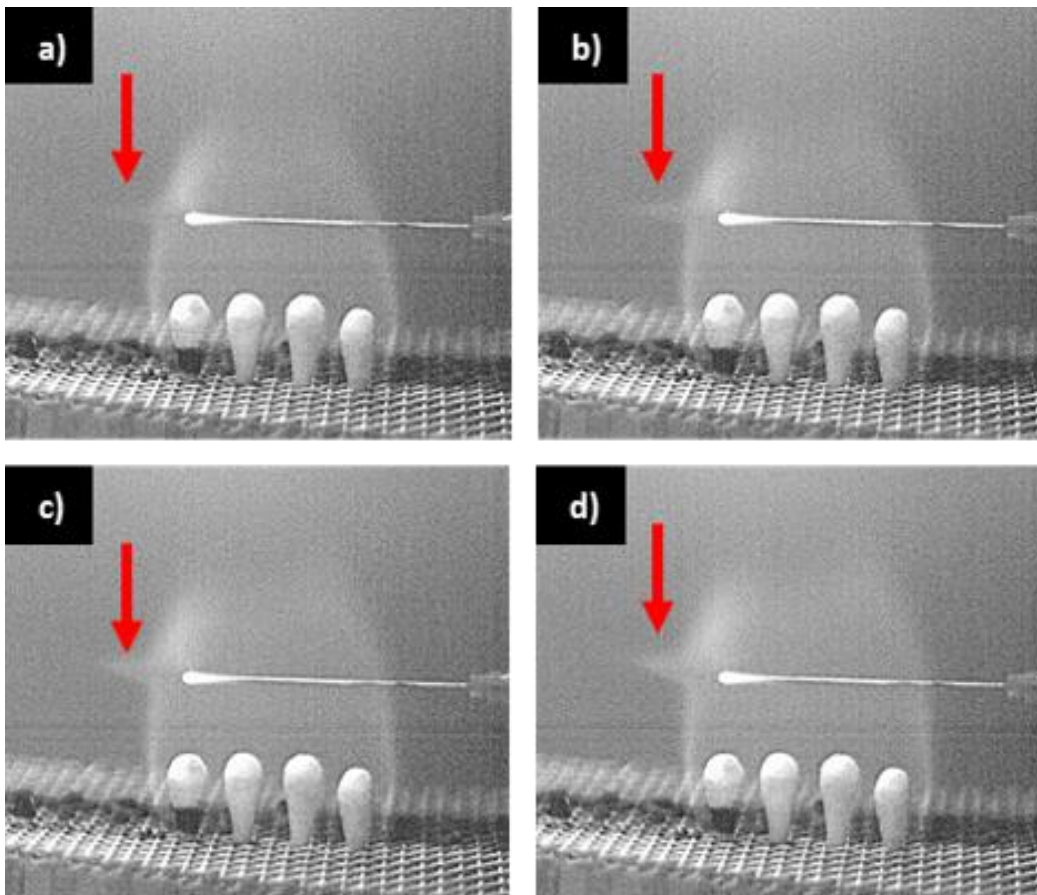


Figure 11. 11 The ejected water vapor issued from the 25G needle entraining the surrounding flame. (a) $t= 1.3630$ s. (b) $t=1.3633$ s. (c) $t=1.3636$ s. (d) $t= 1.3639$ s.

In 0.89 s after the ignition, the 25G needle gradually began to become reddish. This was caused by water absence in the end part of the needle. The time span of 2.50 s with the reddish needle end spreading from left to right is shown in Figure 11.12. This was accompanied by the continuous ejections of both liquid water and water vapor in the form of jet. It can be concluded that water was gradually lost starting from the needle edge engulfed in the flame first.

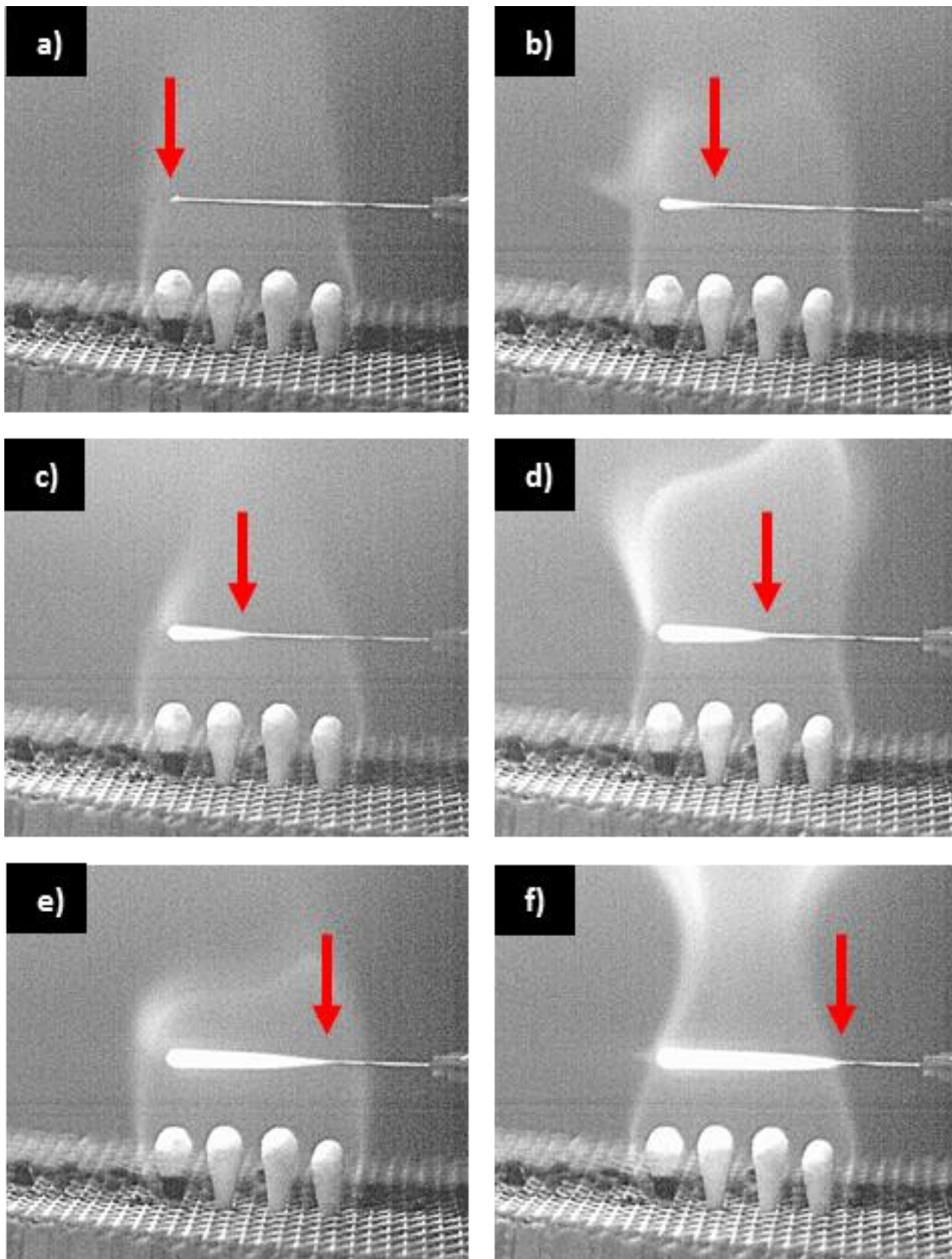


Figure 11. 12 The 2.50 s period of spreading of the reddish section of the 25G stainless steel needle.

(a) $t = 0.89$ s. (b) $t = 1.39$ s. (c) $t = 1.89$ s. (d) $t = 2.39$ s. (e) $t = 2.89$ s. (f) $t = 3.39$ s.

11.4.2 Model experiments conducted with the 18G needles filled up with D.I. water

In this subsection, the 18G stainless steel dispensing needles (rather than the 25G needles of subsection 11.4.1) with luer lock connection were used to mimic the stems of sections 11.2 and 11.3. The inner cross-sectional diameter and length of the 18G needles (excluding the plastic part) is 1.27 mm and 50 mm, respectively. The 18G needles were also purchased from McMaster-Carr and one of them is shown in Figure 11.13.

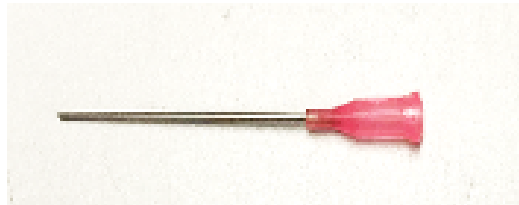


Figure 11. 13 A 18G stainless steel dispensing needle with luer lock connection, purchased from McMaster- Carr.

In this experiment, D.I. water was used filled in needle via a 5mL syringe connected with the needle during the experiment. The experimental setup was exactly the same as the preceding sections. This model experiment was recorded by the high-speed camera. The resolution of the recording process selected in this trial was 1024×512 pixels, the sample rate was 1500 fps, and the exposure time was $660 \mu\text{s}$.

About 0.33 s it took the flame to propagate from left to right over the fuel polls to the length of about 40 mm. During the flame propagation, no water jets were observed to be ejected. Beginning from $t = 0.53$ s, two water droplets were ejected from the opening of the 18G needle (cf. Figure 11.14). Both droplets followed the approximately parabolic trajectories.

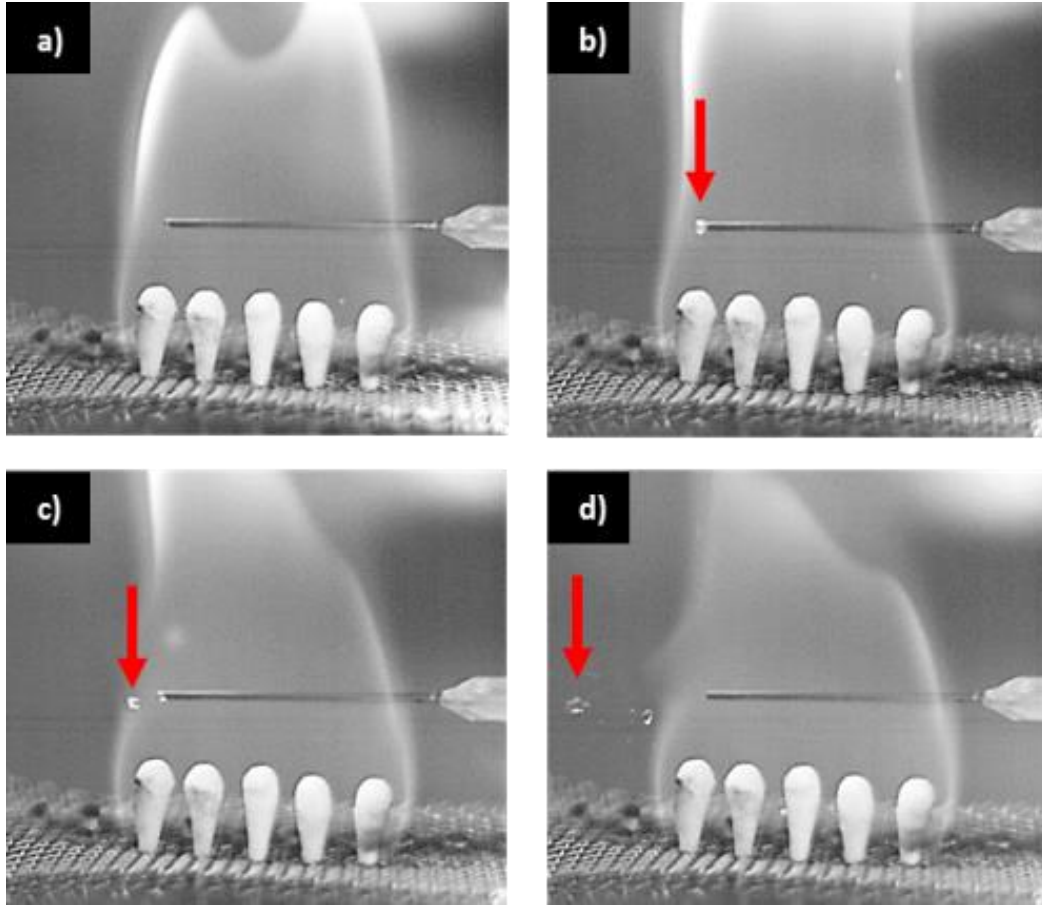


Figure 11. 14 Two initial water droplets issued from the 18G needle. (a) $t=0.530$ s. (b) $t=0.560$ s. (c) $t=0.573$ s. (d) $t= 0.577$ s.

At $t=0.6227$ s, a liquid water jet began to be ejected horizontally from the 18G needle and the period of 0.0007 s of the ejection progress is depicted in Figure 11.15. The image sequences were analyzed by Image J. It was found that the velocity of the horizontal ejection of the water jet was about 5m/s . The red arrows in Figure 11.15a-11.15f indicate the head position of the liquid water jet.

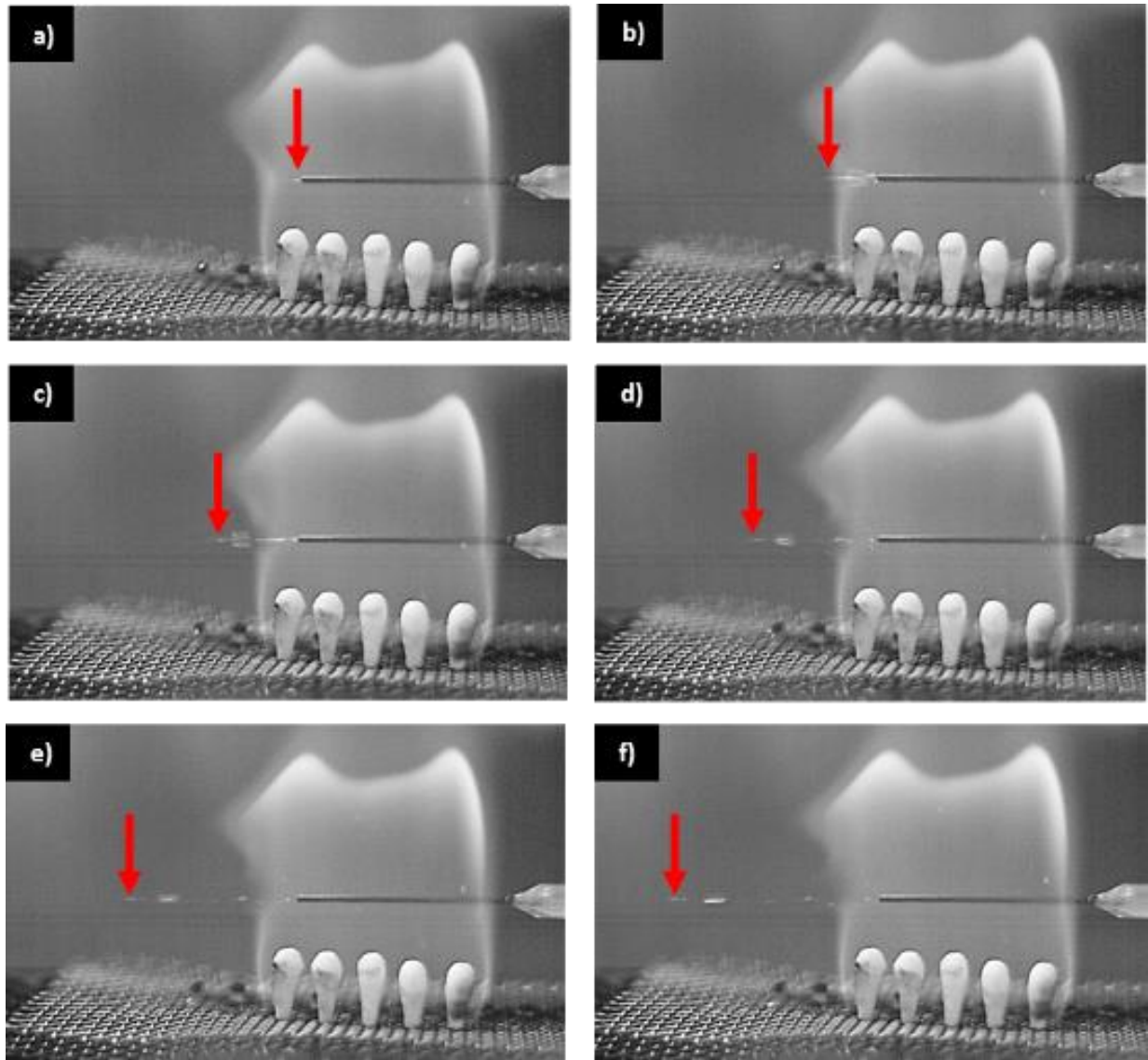


Figure 11. 15 The water jet issued from the 18G needle with the velocity of ~ 5 m/s. (a) $t=0.6227$ s. (b) $t=0.6234$ s. (c) $t=0.6240$ s. (d) $t=0.6247$ s. (f) $t=0.6234$ s. The red arrows point at the head of the ejected water jet.

In this experiment, water vapor jets were also noticed to be formed, but not as obviously as in section 11.3. The example of a water vapor jet issued from the 18G needle is shown in Figure 11.16. The vapor jet is issued intermittently with droplets, as in Figure 11.16. It should be emphasized that with the needle diameter increasing, the size of the ejected water droplets

increases as well.

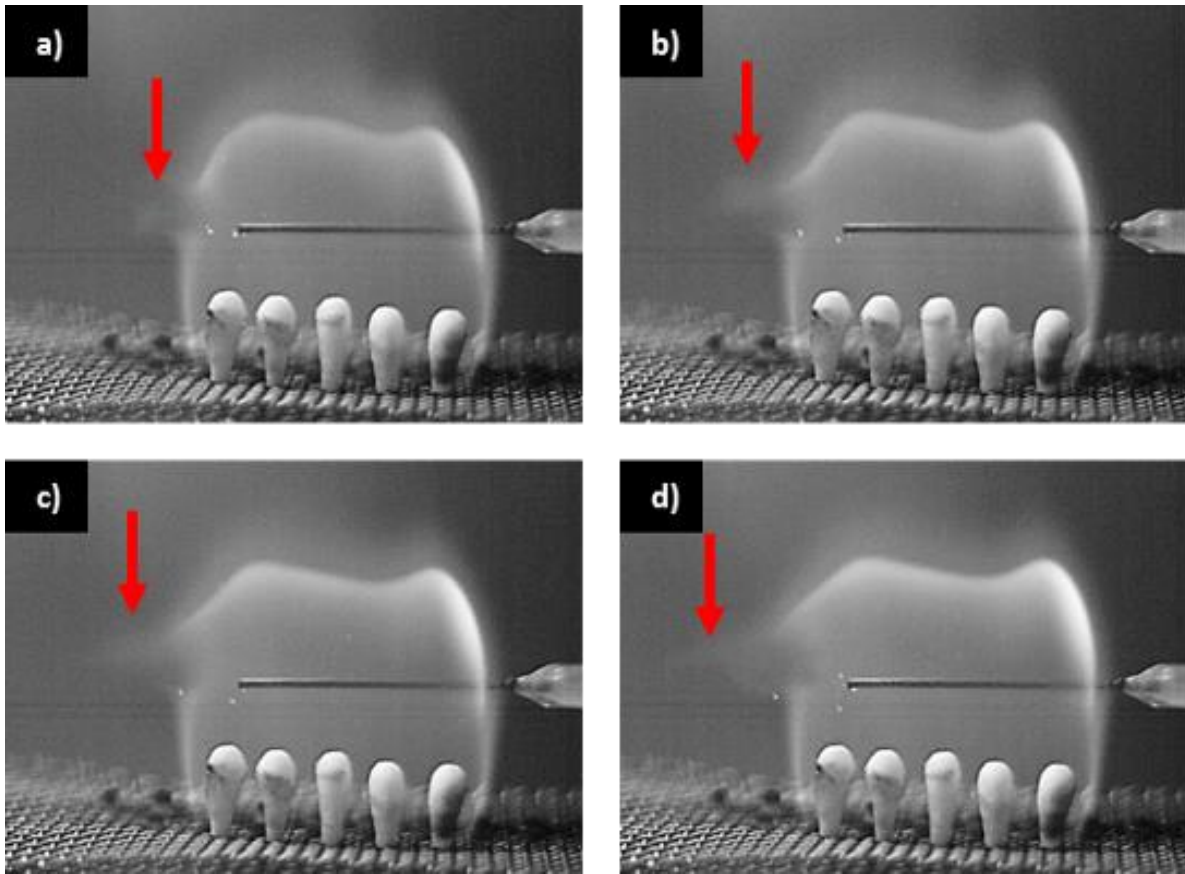


Figure 11. 16 Intermittent water vapor and droplets issued from the 18G needle. (a) $t=0.0.8167$ s. (b) $t=0.8207$ s. (c) $t=0.8247$ s. (d) $t=0.8287$ s. The red arrows point at the intermittent jet.

11.4.3 Model experiments conducted with needles filled up with pure ethanol

In this subsection, the model experiments conducted with the 25G and 18G needle filled up with pure ethanol are described. The experimental setup was same as in the previous sections. The length of the fuel poll line was about 30 mm and the flame propagation time was 0.25s. The experiments were recorded by the high-speed camera. The resolution selected in this experiment was 1024×512 pixels, the sample rate was 300 fps, and the exposure time was $3300 \mu\text{s}$.

The burning ethanol jets were continuously ejected in these experiments and a time period of 0.144 s is shown in Figure 11.17. Due to the limitations of the sample rate and resolution, the mechanism of the formation of the ethanol jets was not clearly resolved in these experiments.

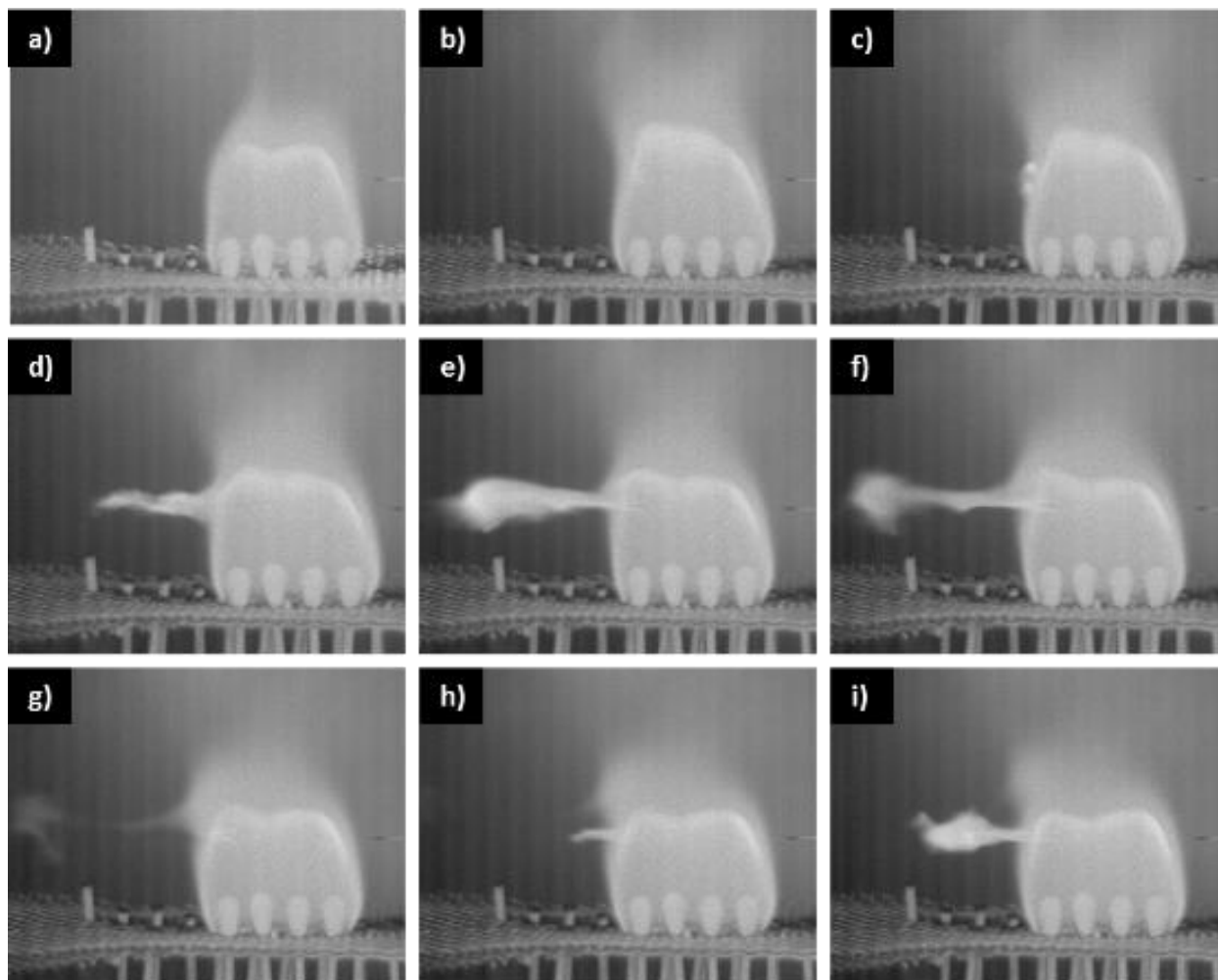


Figure 11. 17 The burning ethanol jets issued from the 25G needle initially filled up with pure ethanol. (a) $t=0.250$ s. (b) $t=0.473$ s. (c) $t=0.476$ s. (d) $t=0.479$ s. (e) $t=0.482$ s. (f) $t=0.485$ s. (g) $t=0.488$ s. (h) $t=0.491$ s. (i) $t=0.494$ s.

In the experiment with the 18G needle initially filled up with pure ethanol, the length of

the line of fuel polls was 40 mm, and it took about 0.33 s for the flame to propagate over the entire line. The resolution selected here was 1024×512 pixels, the sample rate was 1500 fps, and the exposure time was $660 \mu\text{s}$. During the initial flame propagation, ethanol had already started to be ejected in the form of droplets issued from the needle. One could clearly observe the issued flying and burning ethanol droplets (cf. Figure 11.18). The droplet shown here was ignited by the flame which engulfed the needle. The envelop flame could be observed on the droplet surface and its diameter kept decreasing.

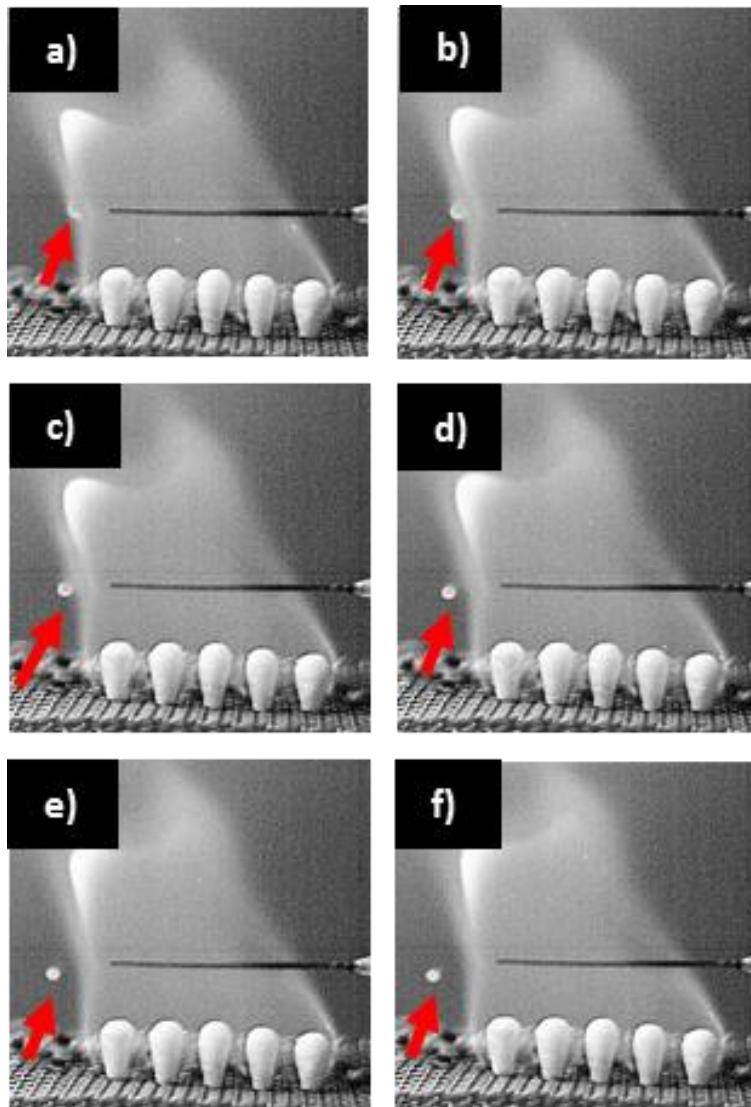


Figure 11. 18 A single burning ethanol droplet ejected from the 18G needle. The droplet was ignited by the flame surrounding the needle and kept diminishing. (a) $t=0.7213$ s. (b) $t=0.7246$ s. (c) $t=0.7249$ s. (d) $t=0.7252$ s. (e) $t=0.7255$ s. (f) $t=0.7258$ s. The red arrows point at the ejected ethanol droplet.

At $t= 0.7433$ s, ethanol began to erupt violently. Under the resolution and recording sample rate used, it was possible to resolve the mechanism of formation of the ethanol jets. Initially, ethanol droplet (of the same size as the diameter of the needle) was ejected. The ejection velocity of such an ethanol droplet was measured as ~ 11 m/s. Then, a liquid ethanol jet would be formed and the flame would propagate over it backward due to the high flammability of ethanol. The corresponding absolute (relative to the ground) flame propagation velocity was about 16 m/s, which was faster than the absolute velocity of liquid ethanol. Accordingly, the flame propagated backward over the jet (cf. Figure 11.19). After the entire liquid ethanol jets had been ejected, a relatively calm flame was observed in the horizontal direction, which was formed by burning ethanol vapor (cf. Figure 11.20). This phenomenon was similar to the one observed in subsection 11.3.2.

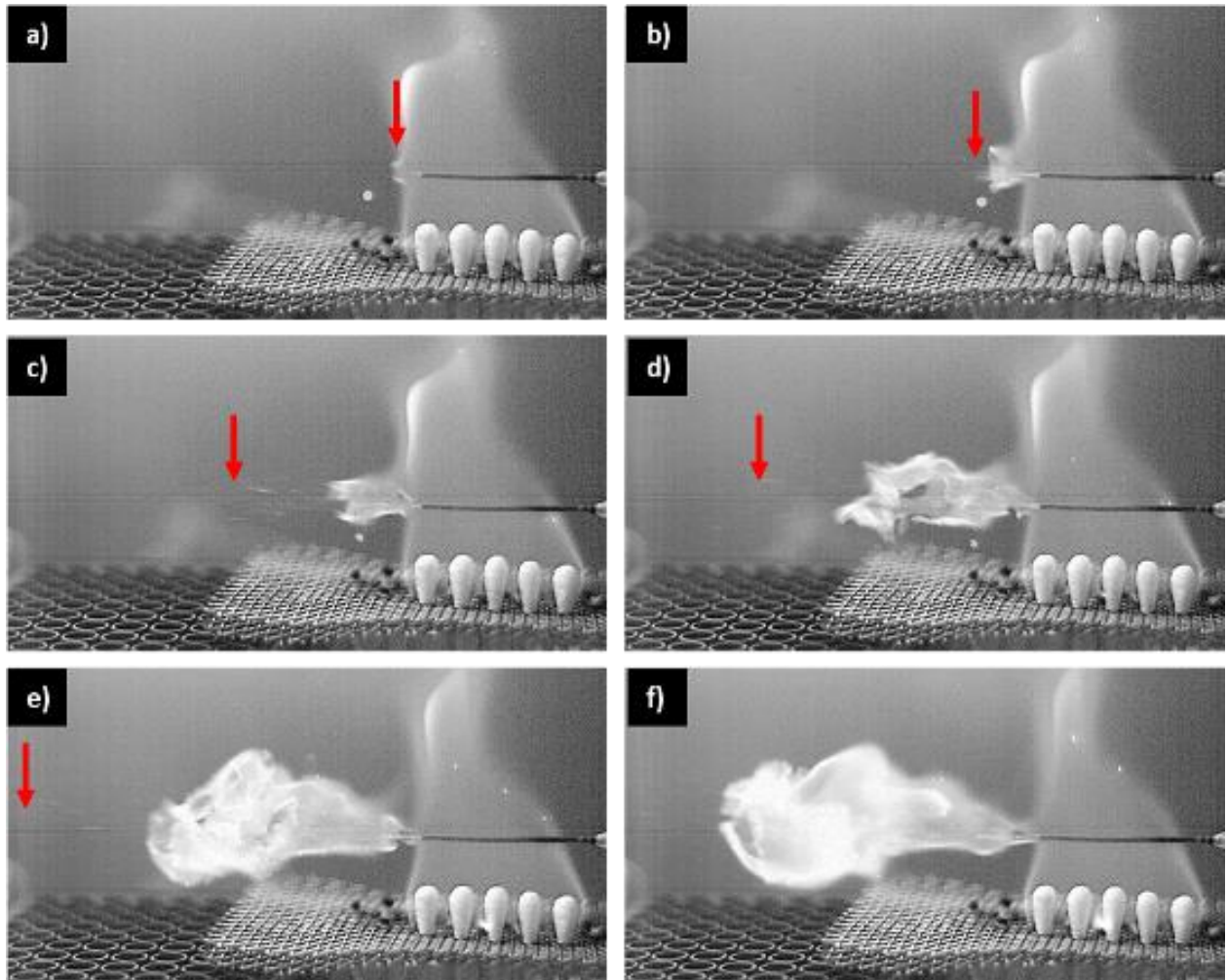


Figure 11. 19 Liquid ethanol jet, and the flame propagating backward over it. (a) $t=0.7433$ s. (b) $t=0.7473$ s. (c) $t=0.7513$ s. (d) $t=0.7553$ s. (e) $t=0.7593$ s. (f) $t=0.7633$ s. The red arrows point at the jet.

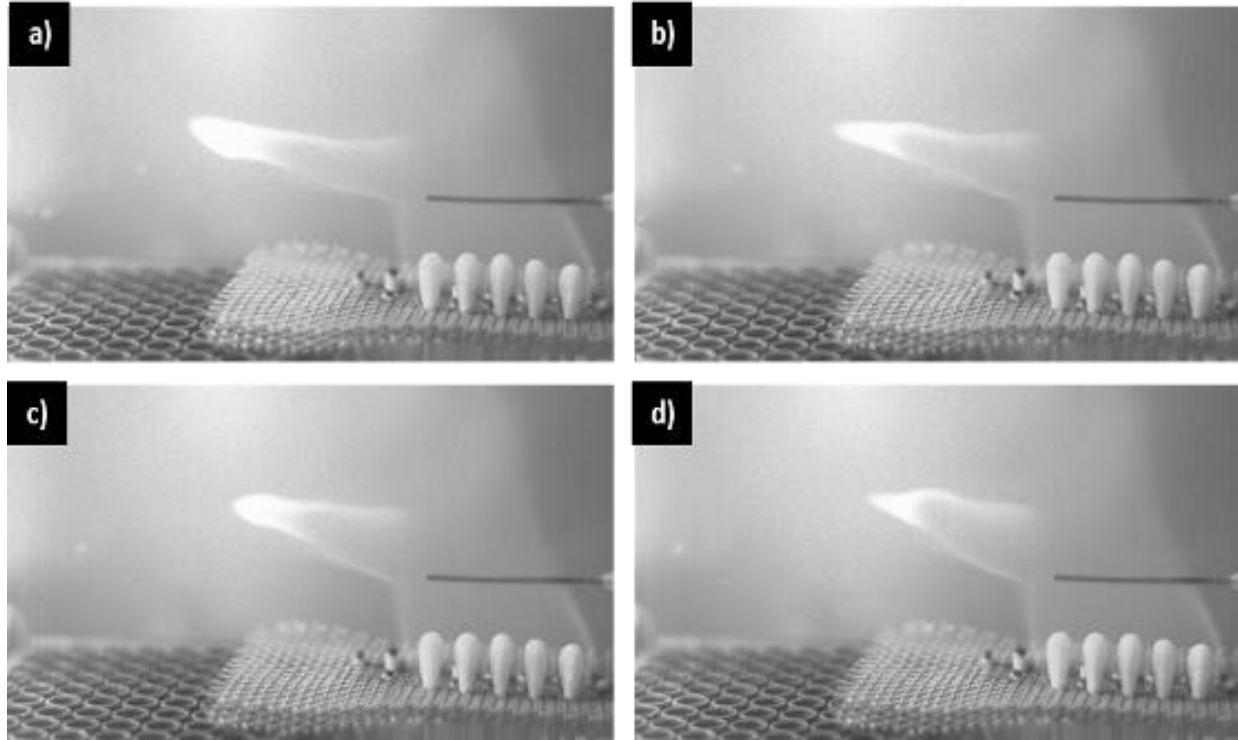


Figure 11. 20 The flame formed by the burning ethanol vapor issued from the 18G needle. (a) $t=0.8246$ s. (b) $t=0.8286$ s. (c) $t=0.8326$ s. (d) $t=0.8376$ s.

11.5 Theoretical of explosive-like ejections from plant stems in fire and discussion

11.5.1 Theoretical

Consider a model cylindrical channel in a straight plant stem. The channel is parallel to the stem and has an opening outside through the stem cut. The stem is supposed to be in flame sustained by surrounding fire (a model forest fire). The channel is originally filled with liquid, which contains water and volatile organic compounds. This liquid can partially or completely evaporate due to the heat supply from the surrounding flame. Accordingly, the channel can be filled with a vapor-liquid mixture.

The thermal balance of the vapor-liquid mixture inside the channel reads

$$\frac{d(m_\ell + m_v)cT}{dt} = 2\pi a L h (T_f - T) + \frac{dm_\ell}{dt} I \quad (11.1)$$

where t is time, m_ℓ and m_v are the liquid and vapor masses inside, c is the specific heat averaged for the liquid-vapor mixture, T is the temperature of the liquid-vapor mixture, T_f is the flame temperature, h is the heat transfer coefficient which accounts for the heat transfer from the surrounding flame through the stem and channel walls to the liquid-vapor mixture inside, I is the latent heat of evaporation, a is the cross-sectional channel radius, and L is its length. Note that due to evaporation, the liquid mass diminishes, and thus, $dm_\ell / dt < 0$, i.e. the last term on the right-hand side in Eq. (11.1) corresponds to the evaporation-driven cooling of the system.

The mass balance of the vapor-liquid mixture inside the channel reads

$$\frac{dm_v}{dt} = -\frac{dm_\ell}{dt} - \frac{\pi a^4}{8\nu_v} \frac{[p_{\text{sat}}(T) - p_{\text{atm}}]}{L} \quad (11.2)$$

The first term on the right-hand side in Eq. (11.2) describes the increase of vapor mass due to the liquid evaporation, whereas the second term corresponds to the vapor loss due to its ejection to the surrounding atmosphere (the flame). Specifically, vapor pressure inside the channel is equal to the saturated vapor pressure corresponding to temperature T , $p_{\text{sat}}(T)$, which is higher than the surrounding atmospheric pressure p_{atm} . Accordingly, vapor is ejected to the surrounding flame with the mass rate given by the Poiseuille law, with ν_v being the kinematic viscosity of vapor.

The saturated vapor pressure is given by the Clausius- Clapeyron, or Antoine, or any other appropriate equation [Reid et al. (1987); Seaver et al. (1989); Yarin et al. (1999)]. For example, for water the following expression can be used [Seaver et al. (1989); Yarin et al. (1999)]

$$p_{\text{sat}}(T) = b_0 + T \left[b_1 + T \left(b_2 + T \left\{ b_3 + T \left[b_4 + T (b_5 + b_6 T) \right] \right\} \right) \right] \quad (11.3)$$

where p_{sat} is given in mbar ($1 \text{ mbar} = 10^2 \text{ Nm}^{-2}$) and T is taken in degrees Celsius. The values of the parameters b_i are given as: $b_0=6.107799961$, $b_1=4.436518521 \times 10^{-1}$, $b_2=1.428945805 \times 10^{-2}$, $b_3=2.650648731 \times 10^{-4}$, $b_4=3.031240396 \times 10^{-6}$, $b_5=2.034080948 \times 10^{-8}$ and $b_6= 6.136820929 \times 10^{-11}$.

In addition, vapor is assumed to obey the ideal gas law

$$p_{\text{sat}}(T) \pi a^2 L = \frac{m_v}{M_v} RT \quad (11.4)$$

where M_v is the molecular weight of vapor, and R is the absolute gas constant.

In the intermediate steady state when the ejections are fully observed in the experiments, all time derivatives vanish, and Eq. (11.2) yields the steady-state evaporation rate as

$$\frac{dm_\ell}{dt} = - \frac{\pi a^4}{8v_v} \frac{[p_{\text{sat}}(T) - p_{\text{atm}}]}{L} \quad (11.5)$$

Substituting the latter expression into Eq. (11.1), one obtains in the steady state that

$$p_{\text{sat}}(T) - p_{\text{atm}} = \frac{16L^2 v_v h (T_f - T)}{a^3 I} \quad (11.6)$$

which determines temperature of the liquid-vapor mixture inside the channel.

The solution of Eq. (11.6) for water is illustrated in Figure 11.21. The following parameter values are used: $v_v \approx 0.1 \text{ cm}^2 / \text{s}$, $T_f = 1000^\circ\text{K}$, $L=10 \text{ cm}$, $a=0.1 \text{ cm}$, $I=2230 \times 10^7 \text{ erg/g}$, $h \approx 10^2 \text{ W} / (\text{m}^2 \text{ K}) = 10^5 \text{ erg} / (\text{s} \text{ }^\circ\text{K cm}^2)$, which correspond to water vapor and the conditions of a forest fire. The solution is illustrated in Figure 11.21 where the two sides of Eq. (11.6) are shown. The intersection of the corresponding two lines yields $T=372.44 \text{ }^\circ\text{K}$, which is very close to the boiling temperature of water under room conditions.

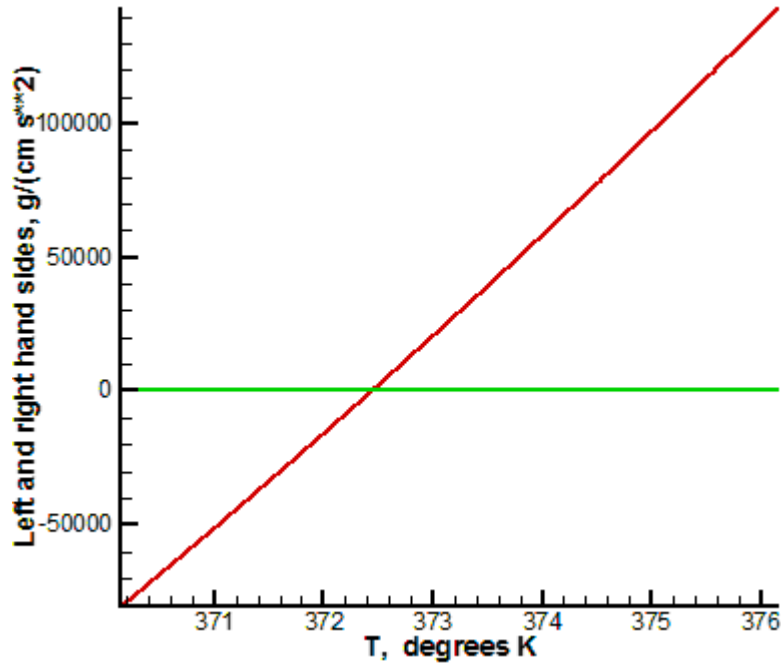


Figure 11. 21 The left- and right-hand sides of Eq. (11.6) are shown by the red and green lines, respectively. Their intersection determines the solution of Eq. (11.6), i.e. the value of the temperature T inside the channel.

It should be emphasized that in the steady state, all supplied heat is spent for liquid evaporation, and the corresponding steady-state vapor mass in the channel, sustained by the balance of liquid evaporation and vapor leakage, is found from Eq. (11.4) as

$$m_v = \frac{p_{\text{sat}}(T)\pi a^2 L M_v}{RT} \quad (11.7)$$

At the found temperature $T=372.44$ °K, the vapor mass in the channel found from Eq. (11.7) is $m_v=0.18$ mg. Note also, that the steady state in a stem in flame is similar to that in a boiling teapot or a kettle.

The magnitude of the vapor eruption velocity V , in conjunction to Eq. (5,) is given by

$$V = \frac{a^2}{8\mu_v} \frac{[p_{\text{sat}}(T) - p_{\text{atm}}]}{L} \quad (11.8)$$

where μ_v is the vapor viscosity.

Taking for the estimate $\mu_v = 10^{-4} \text{ g}/(\text{cm}\times\text{s})$, one obtains from Eq. (11.8) the value of $V=5.52 \text{ m/s}$, in very good agreement with the experimental results. Note that the corresponding Reynolds number $Re \approx 10^2$, which substantiates a posteriori the use of the Poiseuille law in this section.

11.5.2 Discussion

Usually the flaming stage of the vegetation combustion is divided into two sub-stages: the fuel phase and the gas phase [DeBano et al. (1998)]. After a plant is ignited, the first process is known to be the vegetation dehydration, i.e. the distilling process. In this process, water contained in the vegetation is either removed or squeezed into the inner layers, or both processes would happen simultaneously. Indeed, the experimental observations in Figure 11.4e-11.4j revealed water vapor issued during the early stage of the distillation progress. Note also that droplets could also been found at the beginning of this process.

The functionality of the plant stems studied here is to support the plant leaves and deliver to them water and other nutritious, i.e. the channels in such stems are filled with liquid (which was confirmed by the present observations in Figure 11.2). After a stem has been engulfed in the high-temperature flame, it would take some time for the liquid contained by the stem to be heated up to a high enough temperature for massive evaporation to take place (cf. Figure 11.4a-11.4d, where no jets came out from the stem). During this process, a large amount of small bubbles would be generated and some portion of liquid might be squeezed into the inner cells. Then, small jets had

appeared (cf. Figure 11.4e). Water vapor, the main component of the emissions, and other volatile organic volatiles would be emitted [DeBano et al. (1998); Lobert and Warnatz (1993); Greenberg et al. (2006)] and vapor formed near a pre-notched incision would be ejected first. The small jets were followed by violent ejections.

After the distillation process, the oxidation reactions begin in the dried solid skeleton of a plant and its pyrolysis proceeds. Some flammable gases are generated in this process, such as CO and H₂, emitted through the opening of the stem, which can sustain the flame.

11.6 Conclusions

In the present chapter, the *Epipremnum aureum* stems were used as experimental materials to study liquid and vapor emissions at the distillation stage of vegetation burning. The explosive-like ejections resulted from the freshly-cut *Epipremnum aureum* stems subjected to the light blue ethanol flame for 2 s. The temperature of the ejected jets was estimated as 372.70 °K. For the ethanol-immersed stems the ejected material was found to be flammable and engulfed in flame. Model experiments with the 18G and 25G needles filled up with different liquids (water or ethanol) were designed as a model of the stem experiments. A theory explaining and describing eruptive jetting is proposed. It predicts the eruption velocity and temperature in good agreement with the data.

CHAPTER 12

VELOCITY OF FLAME PROPAGATION OF CANOPY FIRE IN A MODEL SYSTEM

12.1 Introduction

In the present chapter, three parameters: the inclination angles (slope), the existence of wind, and the spatial step between flame source are considered simultaneously in the designed model experiments. Experimental setup and materials used to simulate the common forest condition were described in subsection 12.2.1. The fire propagated in upslope/downslope direction with various flame source were described in subsection 12.2.2 and 12.2.3. The wind effect combined the inclination angles (slope) and spatial step between flame sources to the fire transportation progress was shown in subsection 12.2.4. Conclusions were made in section 12.3.

12.2 Experimental

12.2.1 Experimental materials and setup

The experimental setup is depicted in Figure 12.1a. Fisherbrand cotton-tipped applicators (which will be designated as cotton from here on), pure or dipped in ethanol, were applied as the flame source. A metallic mesh was used as a flame source holder. The cotton located regularly and linearly over a surface which could be inclined at the angle θ or be horizontal ($\theta=0^\circ$). Ethanol 200 proof were bought from Decon Laboratories, Inc. Flir T1030sc IR camera and a DSLR camera were employed for the recording of flame transportation. The flame propagation morphologies and velocities were analyzed with NCH video editing software. A small fan was in the 10 cm place

away from the flame source (cf. Figure 12.1b). The wind speed was measured by HOLDPEAK 8668 digital anemometer. The surrounding humidity was 16%.

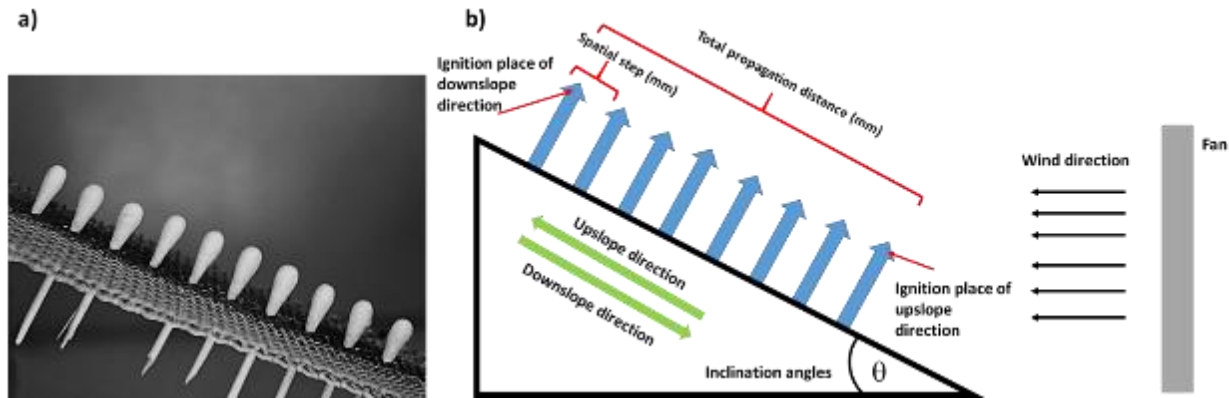


Figure 12. 1 The flame propagation setup. (a) Photograph. (b) Schematic.

12.2.2 The fire propagation in upslope/downslope direction with cotton dipped in ethanol as flame source with no wind effect.

In this subsection, cotton dipped in the ethanol were used as flame sources. The experiments were conducted with the four spatial steps: 9 mm, 11 mm, 13mm, 15 mm, and the flame propagated at six different inclination angles: 0° , 13.5° , 22.3° , 31.0° , 40.4° and 53.9° . The total length of the flame source, i.e. the flame transportation distance, for four spatial distance were 100 mm, 100 mm, 95 mm, 100 mm, respectively. For each angle, three trails of experiments were conducted. Figure 12.2 shows the flame propagation progress in the trial of 9 mm spatial step with 0° inclination angles. Due to the high flammability of ethanol, the length of fully developed flame was same as the total length of flame source (cf. Figure 12.2n). The propagation progress was shown much clearer by employing the IR camera. The appearance of the red zone (relatively higher temperature) in the surface of the flame source indicated the ethanol contained by cotton were

ignited and the flame had propagated to this location (cf. Figure 12.3). The color bars in infrared (IR) image sequences do not show a well-defined temperature due to the unknown emissivity of the burning ethanol contained in cotton. Since the difference of the sampling rate of the DSLR camera and the IR camera, each image shown in Figure 12.2 does not correspond to the same time moment as those in Figure 12.3.

Starting from the ignition moment of the first flame source to the moment of the last flame source had been ignited, the time for fire transporting in flame source were measured. One trial of experimental results was shown here as an example (cf. Figure 12.4). In the trial of 9 mm spatial step with 0° of inclination, the flame transported with nearly a constant value velocity. The red line here was the fitting curve. The corresponding fitting equation was $L = 148.76t - 2.86$, which L was total propagation distance and t is propagation time. The slope of this equation was the overall velocity of the flame transportation. This measurement criterion and calculating methods were applied in all experiment trials. Average values of overall velocities were shown in Figure 12.5.

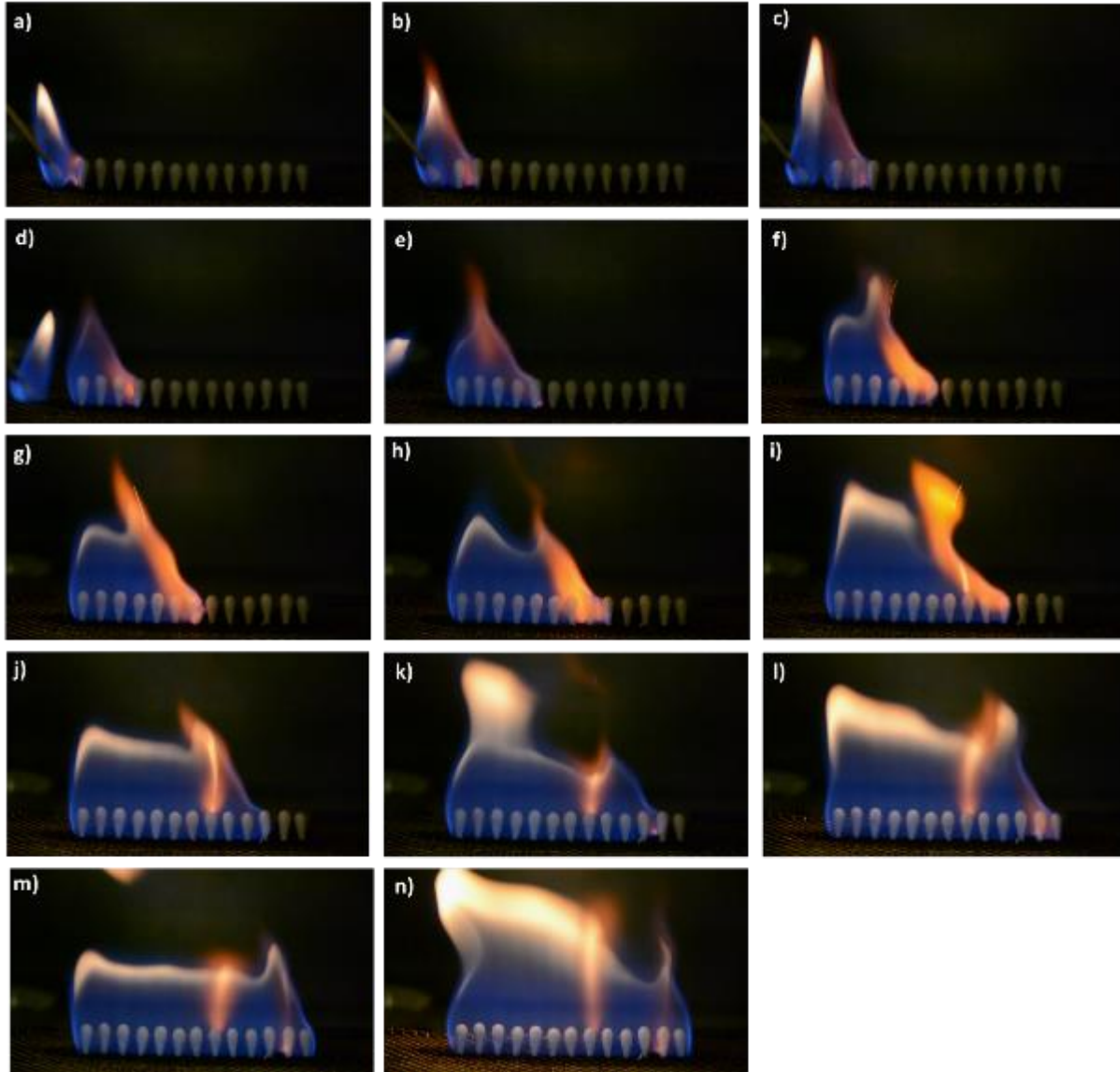


Figure 12. 2 The progress of flame propagating in cotton dipped in ethanol serving as flame source, recorded by DSLR camera. The flame was not affected by wind. The spatial step of this trial was 9 mm and the inclination angle was 0° . (a) $t= 0$ s. (b) $t=0.066$ s. (c) $t=0.132$ s. (d) $t= 0.198$ s. (e) $t= 0.264$ s. (f) $t= 0.330$ s. (g) $t= 0.396$ s. (h) $t=0.462$ s. (i) $t=0.528$ s. (j) $t= 0.594$ s. (k) $t= 0.660$ s. (l) $t= 0.726$ s. (m) $t= 0.792$ s. (n) $t= 0.858$ s.

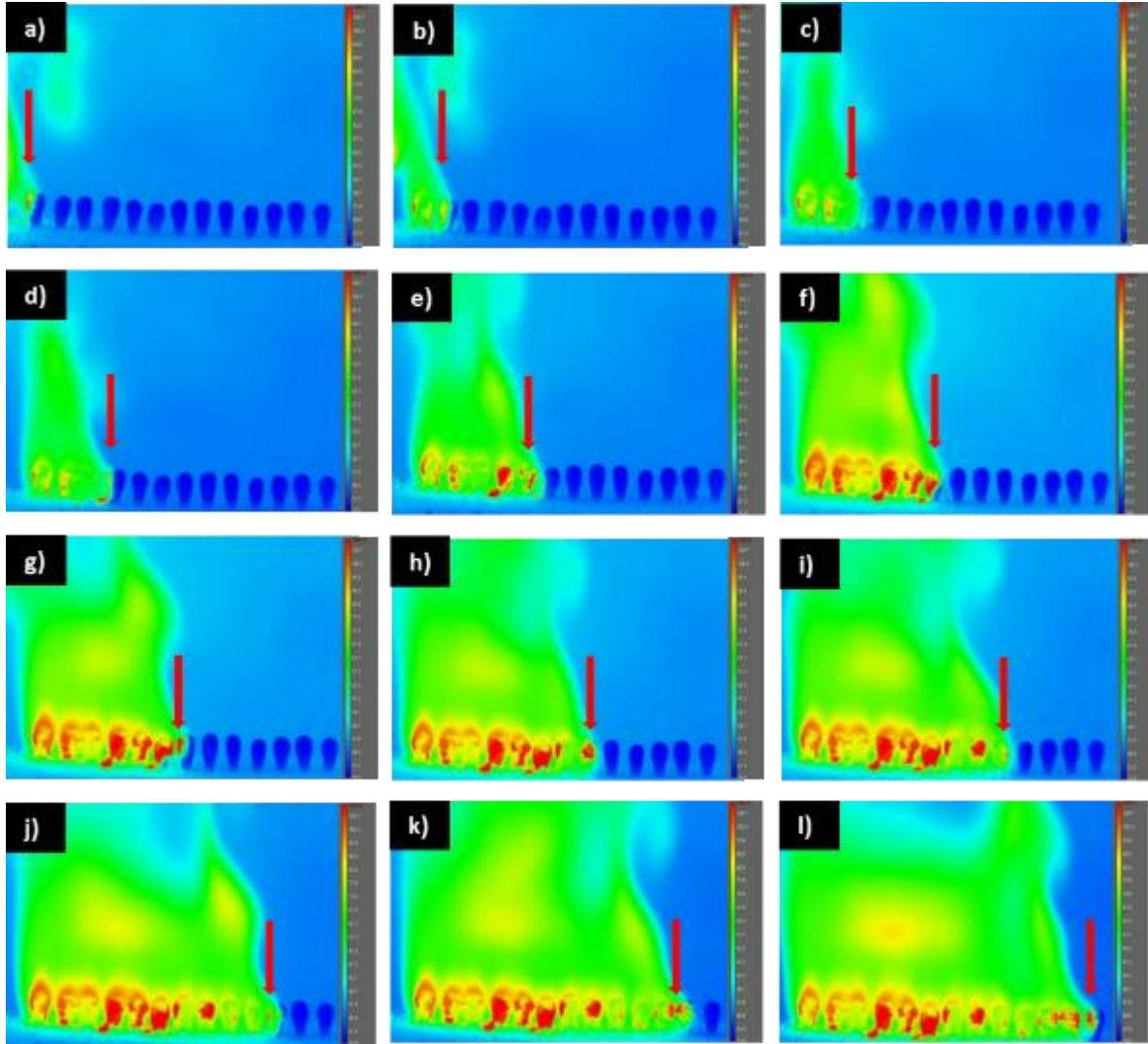


Figure 12. 3 The progress of fire transported in cotton dipped in ethanol serving as flame source, recorded by IR camera. The flame was not affected by wind. The spatial step was 9 mm and the inclination angle was 0° . (a) $t=0$ s. (b) $t=0.066$ s. (c) $t=0.132$ s. (d) $t=0.198$ s. (e) $t=0.264$ s. (f) $t=0.330$ s. (g) $t=0.396$ s. (h) $t=0.462$ s. (i) $t=0.528$ s. (j) $t=0.594$ s. (k) $t=0.660$ s. (l) $t=0.726$ s.

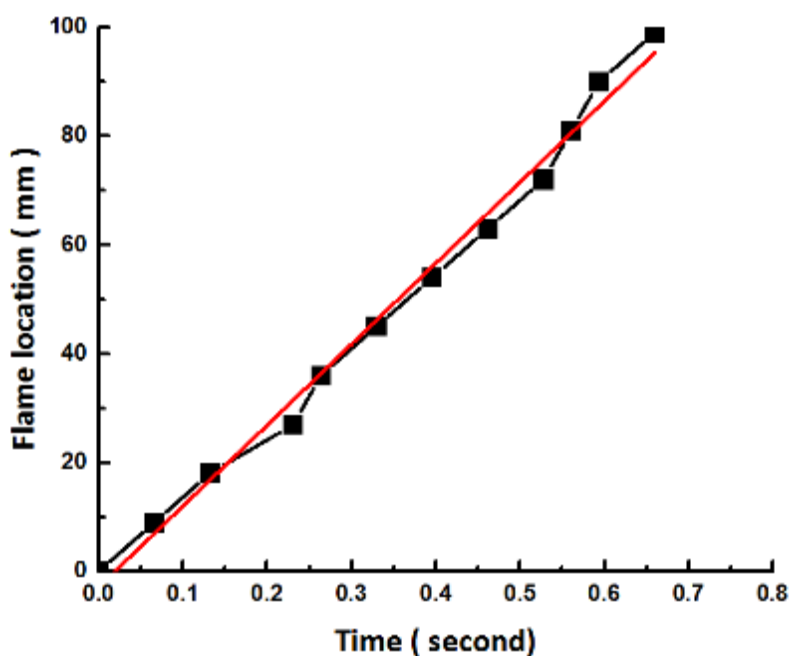


Figure 12. 4 Total propagation time versus propagation distance in the trial of 9 mm spatial step with 0° of inclination. Cotton dipped in ethanol served as flame source. The red line indicated the fitting curve with the fitting equation $L = 148.76t - 2.86$.

The fire could successfully transport in upslope direction through the flame source in 9 mm, 11 mm, and 13 mm spatial steps with all inclination angles, whereas failed to transport in 15 mm spatial steps with the inclination angles 0°, 13.5°, and 22.3°. The flash point of pure ethanol is about 17°C and the maximum value of the overall transporting velocity obtained in these experiments was 230.41 mm/s, which obtained from the trial of 9 mm spatial steps with 53.9° inclination angle. When the inclination angles were smaller than 22.3°, the overall velocity of fire transporting in the flame source with 9 mm and 11 mm spatial step both slightly decreased, and the values obtained from 9 mm spatial step experiments were larger than the ones in 11 mm experiments. When the inclination angle was larger than 22.3°, the overall velocity values obtained

in the trials of 9 mm were nearly the same with the ones obtained from corresponding experiments in 11 mm and 13 mm, i.e. in these three groups of experiments, the effect from the spatial steps to the flame transportation velocity was not significant when the material was highly flammable and the inclination angles were larger than 30°.

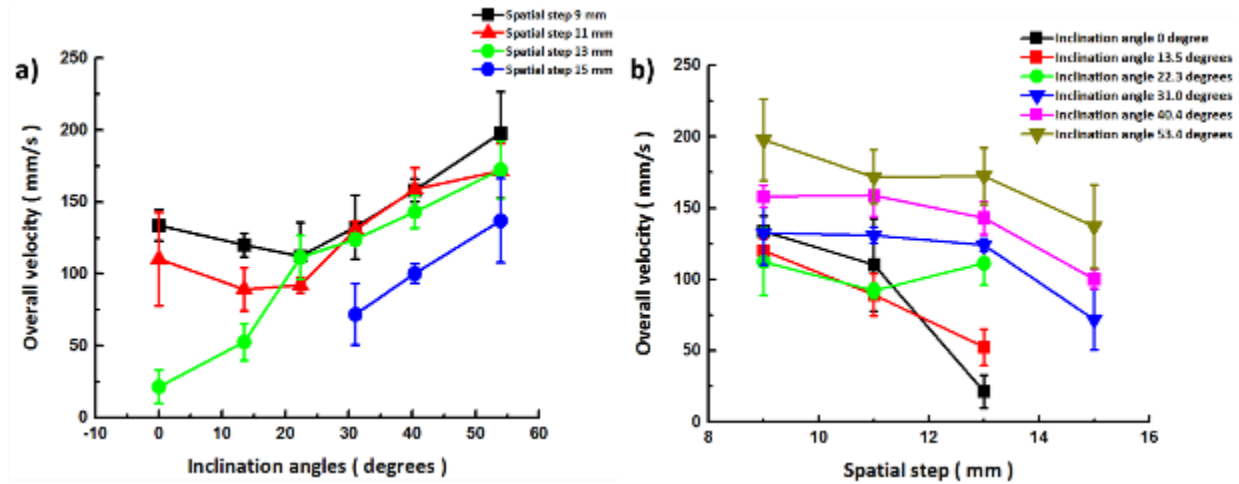


Figure 12. 5 The measured overall velocity with various spatial step and inclination angles. The cotton dipped in ethanol was used as flame source. The fire transported in upslope direction. a) The overall velocity versus the inclination angles. b) The overall velocity versus the spatial step.

The fire successfully transported in downslope direction through the flame source in 9 mm and 11 mm spatial steps with all inclination angles. As the spatial step was 13 mm, the flame could only transport in downslope direction with the inclination angles 0° and 13.5°. The fire was failed to propagate in the trials of 15 mm spatial step experiments. The maximum value of the overall transporting velocity obtained in these trials was 145.78 mm/s, which obtained from the trial of 9 mm spatial steps with 0° inclination angle. With the increasing inclination angles, the velocity of fire transporting through the flame source decreased (cf. Figure 12.6a). The smallest spatial step

experiments processed the largest overall propagation velocity values comparing with the corresponding trials. Hence, the effect from the spatial stem to the fire transporting in downslope direction was significant, as shown in Figure 12.6.

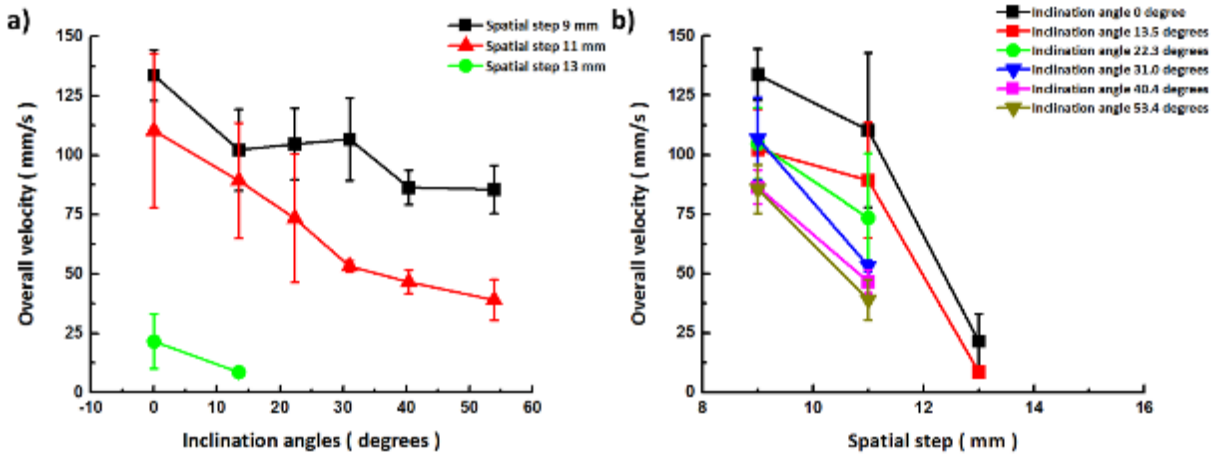


Figure 12. 6 The measured overall velocity with various spatial step and inclination angles. The cotton dipped in ethanol was used as flame source. The fire transported in downslope direction. a) The overall velocity versus the inclination angles. b) The overall velocity versus the spatial step.

12.2.3 The fire propagation in upslope / downslope direction with pure cotton as flame source with no wind effect.

In this subsection, experiments were conducted the pure cotton. The experimental setup, measurement methods and judging criteria used here were the same with previous subsection. In subsection 12.2.2, the fully-developed flame length was equal to the entire length of the flame source due to the high flammability of ethanol and the cotton would not start to burn until the ethanol was burned out. Thus, the flame source after the experiments was remained the same as before. The transporting morphologies of flame in this subsection were observed to be different

from the previous subsection (cf. Figure 12.2n and Figure 12.7e- 12.7f). After igniting the flame source, the cotton was charred and the flame slowly spread in the surface until the whole flame source was surrounded by the fire. The flame source after the experiments became ashes. The fully-developed flame length found here was about 2 cm. The progress of fire transporting was recorded by Flir T1030sc IR camera and DSLR camera. The obtained experimental results were shown in Figure 12.9. Due to the difference in the sampling rate of the DSLR camera and the IR camera, each image shown in Figure 12.7 does not correspond to exactly the same time moment as those in Figure 12.8. The color bars in infrared (IR) image sequences do not show a well-defined temperature due to the unknown emissivity of the burning cotton.

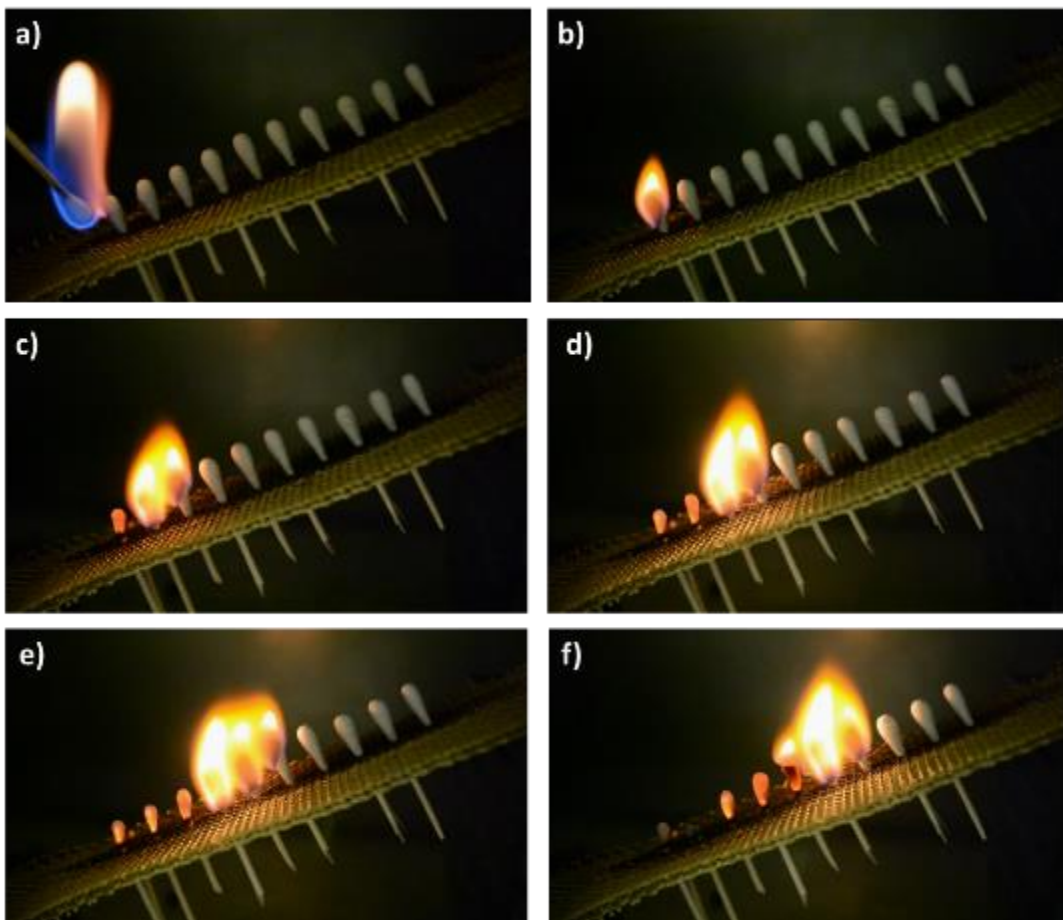


Figure 12. 7 The progress of flame propagating in pure cotton as flame source, recorded by DSLR camera. The flame was not affected by wind. The spatial step of this trial was 11 mm and the inclination angle was 40.0° . (a) $t=0$ s. (b) $t=5$ s. (c) $t=25$ s. (d) $t=35$ s. (e) $t=45$ s. (f) $t=55$ s.

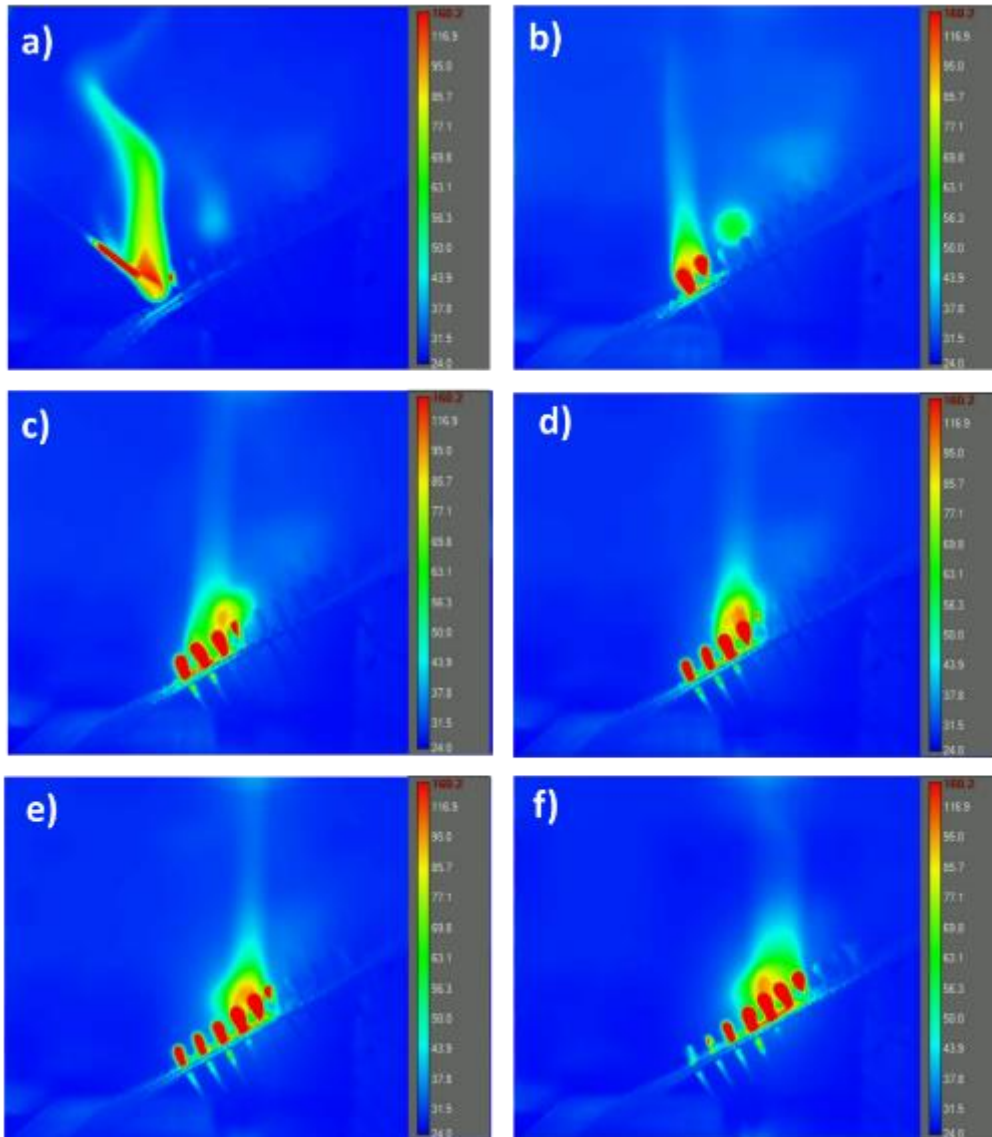


Figure 12. 8 The progress of flame propagating in pure cotton as flame source, recorded by IR camera. The flame was not affected by wind. The spatial step of this trial was 11 mm and the inclination angle was 40.0° (a) $t=0$ s. (b) $t=5$ s. (c) $t=25$ s. (d) $t=35$ s. (e) $t=45$ s. (f) $t=55$ s.

The fire point of the cotton is 210°C and the cotton must be ignited by the open flame for more than 3 seconds. The flame successfully transported in the upslope direction in the experiments of spatial step 9 mm with all inclination angles, whereas failed to transport in 11 mm spatial step with 0° or 13.5° inclination angles and 13 mm spatial step with 0°, 13.5°, 22.3°, and 31.0°. The fire could not transport in any inclination angles of 15 mm spatial step experiments. As shown in Figure 12.9a, the flame transporting velocity would increase as the increasing inclination angles. The maximum overall velocity value obtained here was 4.27 mm/s, which was much smaller than the corresponding value obtained in subsection 12.2.2. When the inclination angles were larger than 40.4°, the changing rate of overall velocity for 9 mm, 11 mm and 13 mm spatial was calculated as 0.026 mm/ s degree, 0.048 mm/ s degree, and 0.110 mm/ s degree, i.e. the increasing values of spatial steps (within the limits that fire could transport) will accelerate the flame transportation velocity if the flame source is not highly flammable.

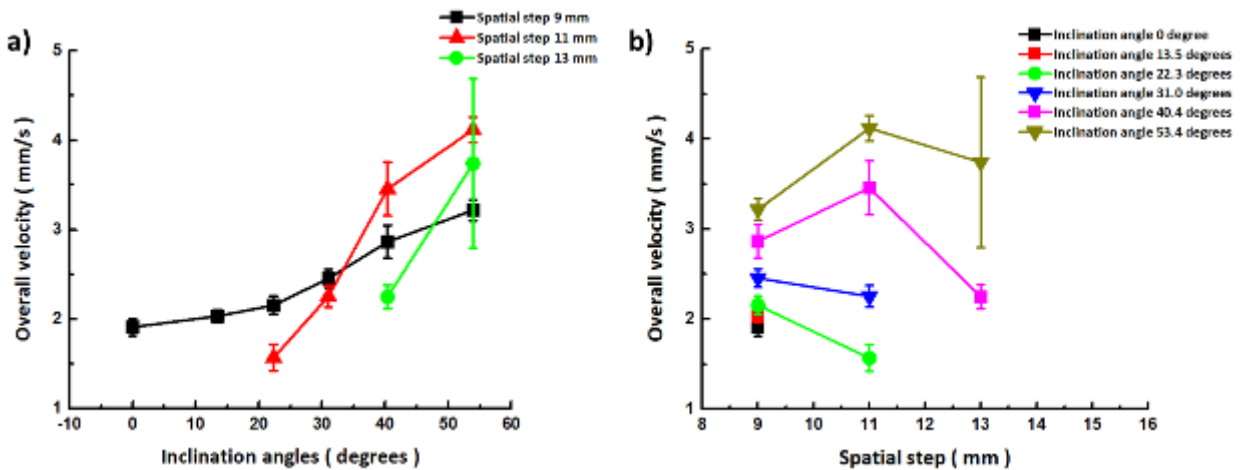


Figure 12. 9 The measured overall velocity with various spatial step and inclination angles. The pure cotton was used as flame source. The fire transported in upslope direction. a) The overall velocity versus the inclination angles. b) The overall velocity versus the spatial step.

The flame only transported in the downslope direction in the experiments of spatial step 9 mm with all inclination angles. The pure cotton was used as flame source. The measured overall velocity with various spatial step and inclination angles were shown in Figure 12.10. The velocity values decreased as the increasing inclination angles and the maximum value of overall velocity obtained here was 2.02 mm/s, which happened in the trial of 9 mm spatial step with 0° inclination angles.

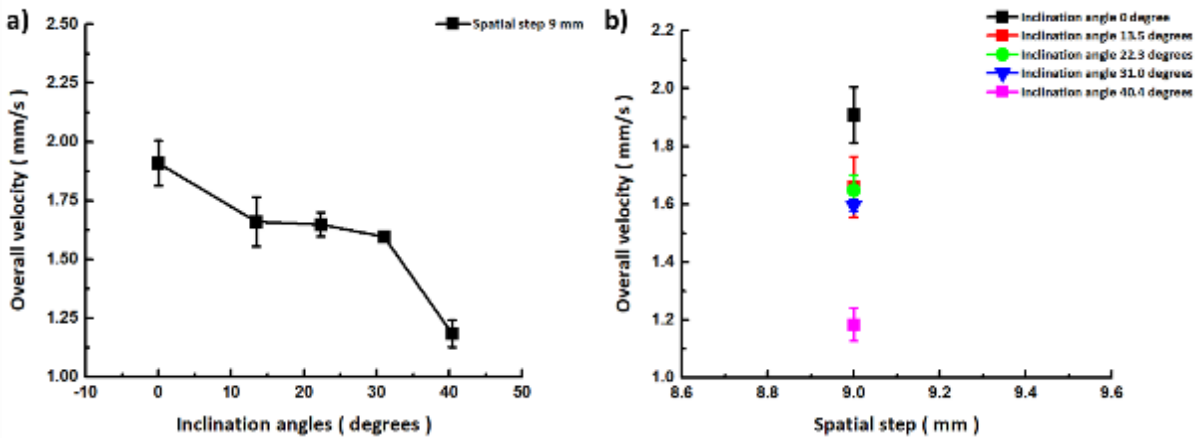


Figure 12. 10 The measured overall velocity with various spatial step and inclination angles. The pure cotton was used as flame source. The fire transported in the downslope direction. a) The overall velocity versus the inclination angles. b) The overall velocity versus the spatial step.

12.2.4 The fire propagation in upslope / downslope direction with pure cotton as flame source with wind effect.

In this subsection, the effect from the wind to the flame transportation velocity, as well as the inclination effect and spatial steps effect, were studied. The experiments were conducted with pure cotton as flame sources. The speed of wind generated from the fan was measured as 2.0 m/s. The

flame propagation progress was recorded by DSLR camera (cf. Figure 12.11) and IR camera (cf. Figure 12.12).

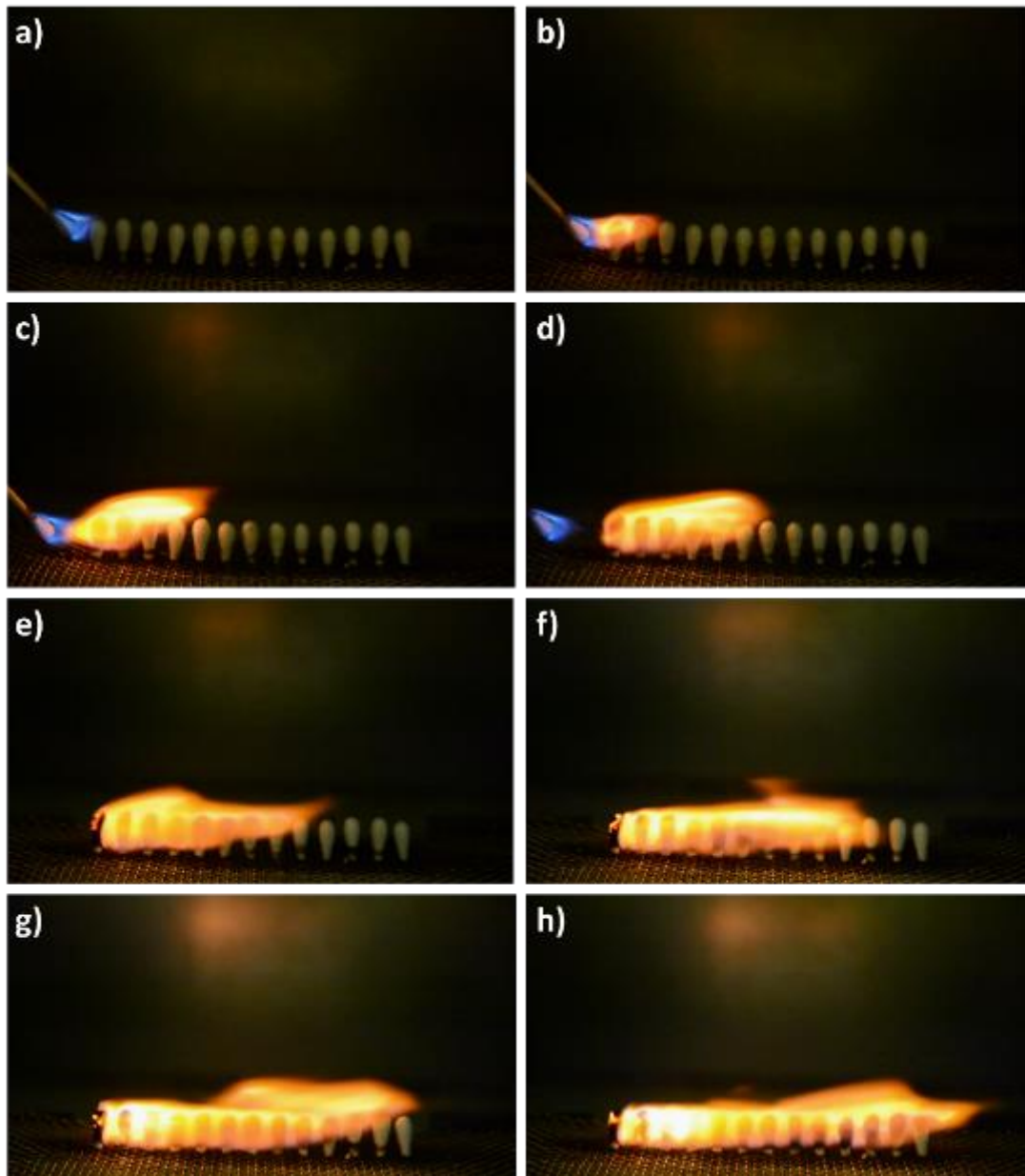


Figure 12. 11 The progress of flame propagating in pure cotton as flame source, recorded by DSLR camera. The flame was affected by 2.0 m/s horizontal blowing wind. The spatial step of this trial was 9 mm and the inclination angle was 0° . (a) $t=0$ s. (b) $t=2$ s. (c) $t=4$ s. (d) $t=6$ s. (e) $t=8$ s. (f)

t= 10 s. (g) t=12 s. (h) t=14 s.

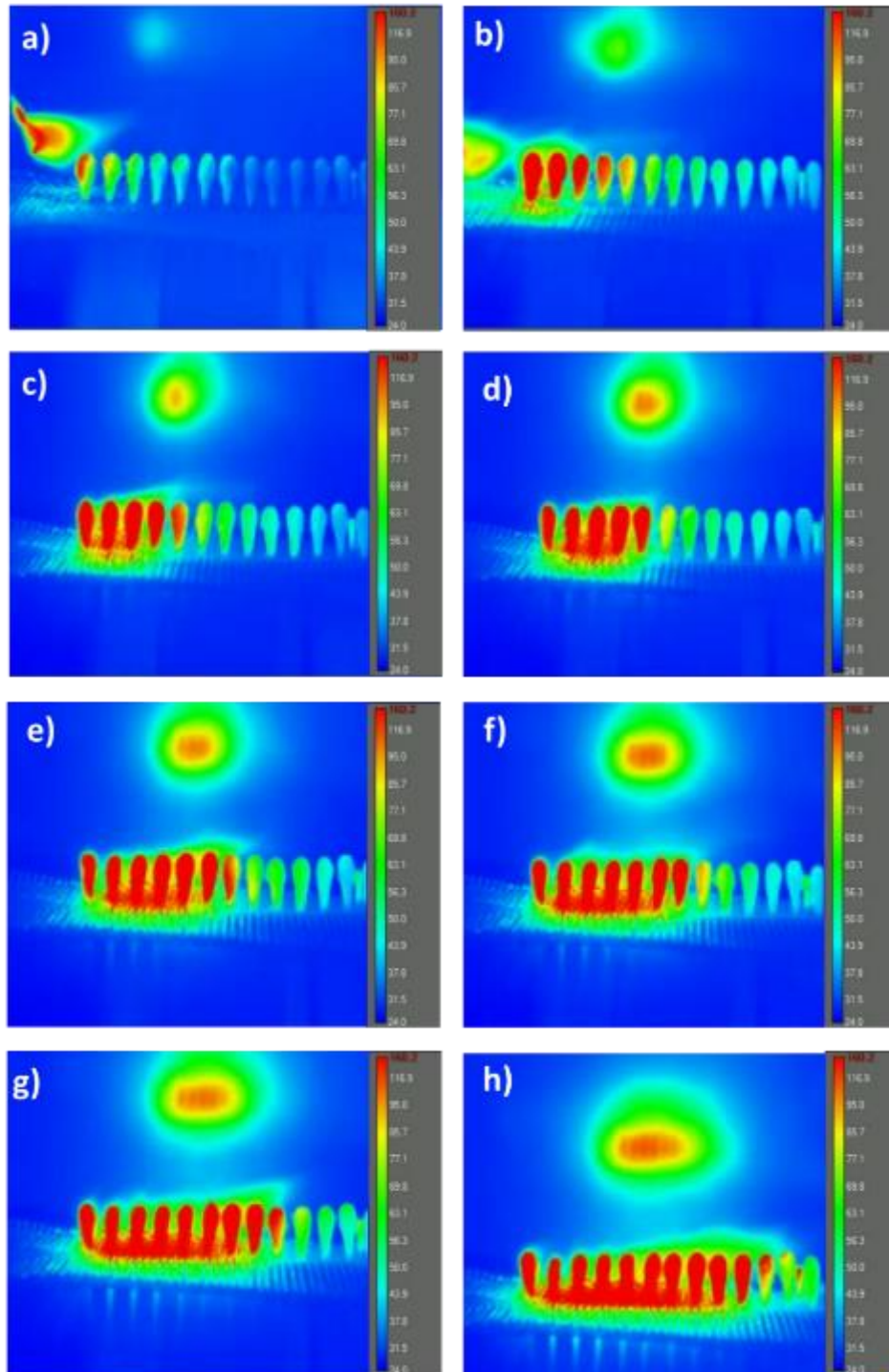


Figure 12. The progress of flame propagating in pure cotton as flame source, recorded by IR camera. The flame was affected by 2.0 m/s horizontal blowing wind. The spatial step of this trial

was 9 mm and the inclination angle was 0° . (a) $t=0$ s. (b) $t=2$ s. (c) $t=4$ s. (d) $t=6$ s. (e) $t=8$ s. (f) $t=10$ s. (g) $t=12$ s. (h) $t=14$ s.

With the horizontal wind effect (cf. Figure 12.1b), the flame only transported in the upslope direction in the experiments of spatial step 9 mm with 0° , 13.5° , 22.3° , 31.0° , 40.4° angles. The measured overall velocity with various spatial step and inclination angles were shown in Figure 10. When the inclination angles changed from 0° to 13.5° , the existence of wind and increased inclination angles contributed to an increased overall transporting velocity. The maximum value of the overall velocity found was 12.49 mm/s, which obtained from the trial with 13.5° inclination angle and was larger than the corresponding values shown in subsection 12.2.3. When the inclination angle was equal to 0° , the average velocity values of the fire propagation were measured as 6.26 mm/s, which was increased 3.3 times by the 2 m/s wind comparing with the corresponding value (1.91 mm/s) obtained from experiments with no wind effect. When the inclination angle was equal to 13.5° the average velocity values of the fire propagation was increased 5.5 times by the 2 m/s wind comparing with the corresponding value (2.03 mm/s) in subsection 12.2.3.

As the inclination angles continued increasing, the fire continuously flowed in the horizontal direction. Thus, the flame could only propagate through the bottom of the cotton in the upslope direction, which significantly decreased the transportation velocity. When the inclination angle was changed into 40.4° , the fire was failed to propagate. The obtained experimental results were shown in Figure 12.13. Also, the fire could not propagate in downslope direction when wind existed (wind direction was the same as before).

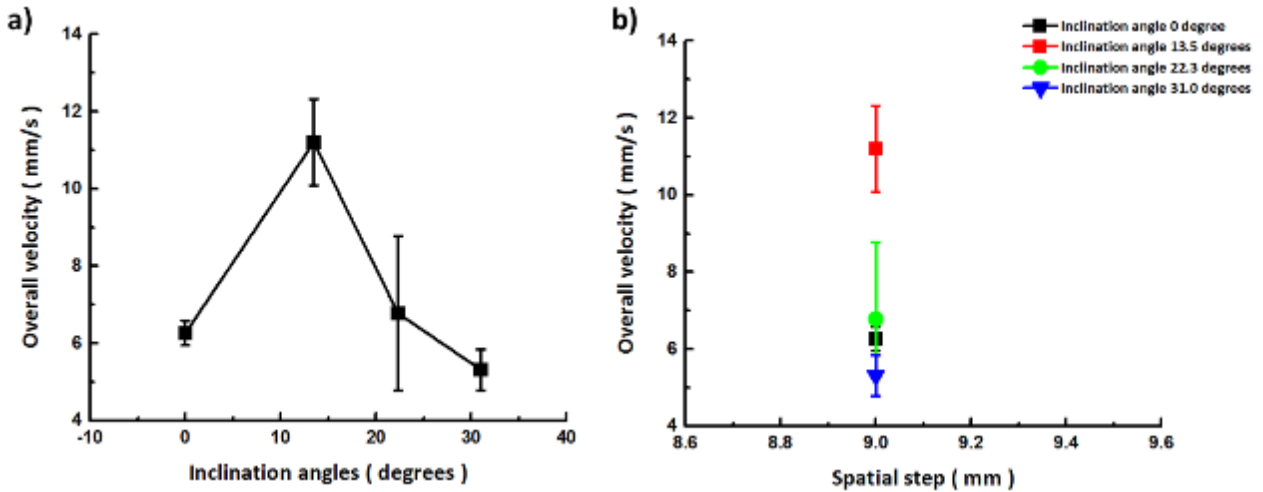


Figure 12.13 The measured overall velocity with various spatial step, inclination angles and 2m/s wind. The pure cotton was used as flame source. The fire transported in upslope direction. a) The overall velocity versus the inclination angles. b) The overall velocity versus the spatial step.

12.3 Conclusions

In the present chapter, the progress of flame propagation was studied experimentally, and the flame propagation velocity effected by spatial step between flame source, the inclination angles and the existence of wind to were calculated. Four spatial step experiments were conducted: 9 mm, 11 mm, 13mm, 15 mm, and the flame propagated at six different inclination angles: 0°, 13.5°, 22.3°, 31.0°, 40.4° and 53.9°. The pure cotton or cotton dipped in ethanol were used as the flame source. The flame propagated in flame source with nearly constant velocity (cf. Figure 12.4). The transportation morphologies were recorded by DSLR camera and IR camera and shown as image sequences in Figure 12.2, 12.3, 12.7, 12.8, 12.11, and 12.12. Obtained velocity values at various conditions were shown in Figure 12.2, 12.3, 12.7, 12.8, 12.11, and 12.13.

CHAPTER 13

CONCLUSIONS

The present work aims at the investigation of the peculiarities of heat and mass transfer process in porous media by the experimental and theoretical approaches. In the experiments various porous media were studied and theories were developed for different applications.

The first part (chapters 4-6) of the present work studies transport of sublimating vapors from different buried sources in such natural porous materials as sand and clay. It encompasses three subjects: (i) adsorption/desorption process; (ii) vapor detection at the free surface of the porous media; (iii) vapor detection at the certain heights from the free surface of the porous media. The main motivation for this part is in forensic applications.

The adsorption/ desorption process (chapter 4) was studied with camphor, naphthalene and 2,4- Dinitrotoluene (DNT) used as adsorbate and sand employed as adsorbent. The experimental results, which aimed at measuring the adsorbed vapor mass at different time moment, were collected from three specially designed setups. The measured adsorbed vapor masses were established as a function of time in these experiments. The theory, which employed the kinetic constants established using the experimental results, was developed. Good agreement of the theoretical predictions with the experimental data was shown. It was demonstrated that the proposed model is a useful tool for the description of multiple forensic situations associated with different volatile substances.

Vapor detection at the free surface of the porous media (chapter 5) was researched with camphor and naphthalene used as the buried sublimating sources and sand (natural and modified)

and kaolinite clay as the model porous substances. This part of the work developed a method, which could measure the naphthalene or camphor mass deposition (from vapor sublimated from a buried source and diffused through a porous medium) by using the image pixel intensity. In comparison with the existing albedo measuring method, the image pixel intensity method developed in chapter 5 was shown to be more sensitive to the physical changes and more accurate. The deposition distribution, the source size, and the location estimation could also be measured by this method. A theory that could predict the deposition mass on a detector located at the free surface of the porous media was proposed. The good agreement between the theoretical estimations and experimental results was revealed. The modified sand explored in chapter 5 was demonstrated to be effective for the accelerations of the vapor release from the buried source to the free surface due to a significant reduction in the surface area of individual sand grains available for the adsorption.

Vapor detection at a certain distance from the free surface for different height ratios of porous layers (chapter 6) also employed naphthalene as a sublimating material and natural sand as a model granular porous medium. By using the detector tubes, the data for the naphthalene concentration collected at different time duration were collected. The theory of sensing of naphthalene vapor diffusing through sand layers of different thickness was proposed and verified by the experimental data. Accordingly, the theory can be used as a predictive tool.

The second part (chapters 7-10) of the present work aims at the heat transfer process in the porous nonwovens. These nonwovens, from a wide range of applications, were used as the experimental materials. The peculiarities of heat transfer in the thermal bonding process, and the parameters that affect the resulting properties of nonwovens were studied in these four chapters.

The work in chapter 7 employed two types of nonwovens, PBT nonwoven and PBT/PE

80/20 nonwovens. Tensile tests using the as-received nonwovens and nonwovens with the additional thermal bonds were conducted. The lab-scale thermal bonding setup was designed to make the additional thermal bonds on the received nonwovens. Two thermal bonding patterns were realized: circular and rhombic. The contact time of the thermal punch was maintained as ~ 1 s. The stress-strain curves, as well as the mechanical properties, such as Young's modulus and the yield stress, were obtained by using the Instron machine. These experiments aimed at the elucidation of the effect of the additional thermal bonds on the overall mechanical performance of nonwovens. The rupture patterns in the experiments with two nonwovens were also observed. A theory which could estimate the applied stress values and distribution in the nonwoven was implemented. This theoretical work also demonstrated that thermal bonds act as stress concentrators, increasing the tensile stress up to 140% at the bond periphery, which can trigger failure at the bond periphery. The experimental observation showed good agreement with theoretical estimates.

Cohesion energies of thermally- bonded nonwovens were measured in chapter 8. Man-made porous media, Polyethylene terephthalate (PET) nonwovens, were used as the experimental materials. The received nonwovens were stacked and thermally bonded at five different temperatures: 160 °C, 170 °C, 180 °C, 190 °C, and 200 °C. The same thermal bonding setup as the one in chapter 7 was employed. Tensile tests were conducted with the as-received PET nonwovens and nonwovens with additional thermal bonds to measure the corresponding mechanical properties. It had been found that under the bonding punch more PET fibers were deformed and sintered as the thermal bonding temperature increased. Blister tests were conducted to measure the cohesion energy of thermally-bonded PET nonwovens at two advance rates: 2 mm/min or 10 mm/min. The values for the cohesion energy of thermally-bonded PET nonwovens measured were on the scale of 10 J/m^2 at the bonding temperatures higher than 160 °C. The theory

developed in this chapter was associated with different scenarios. The first theory could be used to determine the key parameters for an effective calendar bonding process in the nip, which the nonwoven layer passing through the calendar nip. The second theory described the calendar bonding process with the nonwoven layers already passed the calendar nip and still stuck to one of the rollers. This model could be employed to estimate the forces acting on the nonwoven beyond the calendar nip. The cohesion energy of thermally-bonded materials was estimated based on the theory and revealed the value of $W_{\text{cohesion}} \sim 4.2 \text{ J} / \text{m}^2$. Several other models of fiber sintering area in thermal bonding and the effect of cooling on the sintering area in thermal bonding were also developed.

The thermal bonding patterns that affected the mechanical properties of nonwovens were studied in chapter 9. In the first part of experiments, non-bonded Polypropylene (PP) nonwovens were used as porous materials and thermally bonded at 150 °C. The as-received nonwovens and nonwovens with three bonding patterns were studied: (i) 124.59 mm² circular thermal bonding located at the specimen center; (ii) 124.59 mm² circular thermal bonding located at a significantly off-center position of a nonwovens specimen; (iii) 762.0 mm² rectangular thermal bonding located at the center of a nonwoven specimen. The rupture patterns of stretched nonwoven samples were observed and the corresponding mechanical properties were obtained and compared. In the second part of the experiments, the light-weight Spunbond-Meltblown-Spunbond Polypropylene nonwovens, which were pre-bonded before receiving, were used for the elucidation of the effects of the thermal bond area. Additional thermal bonds were made on the samples and two bonding patterns were employed: 124.59 mm² circular bond and 119.54 mm² rhombic bond. The additional single thermal bond was shown to be strongly affecting the mechanical properties of nonwovens, especially the rhombic thermal bond due to the fact that the rhombic shape could overlay 7.1%

more original bonds than the circular shape.

A method which could characterize the Clapeyron effect in polymers during the heating-up process under pressure was proposed in chapter 10. The melting points of three types of nonwovens: polybutylene terephthalate (PBT), polyethylene terephthalate (PET), and heavy-weight RHT pattern Spunbond- Meltblown- Spunbond polypropylene (PP) were measured with four applied pressures: 0.31 atm, 11.65 atm, 26.22 atm, and 104.86 atm. The method developed was demonstrated to be effective and quantified the effect of the applied pressure on increase in the melting point.

The third part of this work (chapters 11-12) aims at the heat and mass transfer during the distillation stage of the forest fire. First, in chapter 11 the explosive-like ejections from the pores of plant stem in fire were discovered and the vapor mass ejected estimated. Natural porous media, namely, stems collected from *Epipremnum aureum* (Golden Pothos, a common indoor plants), were used for the experiments. By employing the Phantom V210 high-speed camera and Flir T1030sc IR camera, explosive-like ejections were observed from plant stems horizontally placed in fire. Similar experiments were also conducted for the ethanol-immersed stems. Model experiments with needles filled up with liquids were also conducted. A theory for estimating the mass loss and the ejection velocity was proposed and successfully compared to the experimental data. Then, in chapter 12 measurements of the velocity of flame propagation of canopy fire in the designed model system were conducted. Experimental setup and materials were used to simulate the common forest condition and several parameters that affect flame propagation were studied: the inclination angle, the wind speed, etc.

CITED LITERATURE

Abdi, S., Nasiri, M., Mesbahi, A., Khani, M. H. (2017). Investigation of uranium (VI) adsorption by polypyrrole. *Journal of Hazardous Materials*, 332, 132-139.

Aggarwal, S. L., Tilley, G. P. (1955). Determination of crystallinity in polyethylene by X-ray diffractometer. *Journal of Polymer Science*, 18, 17-26.

Amoroso, N. J., D'Amore, A., Hong, Y., Wagner, W. R., Sacks, M. S. (2011). Elastomeric electrospun polyurethane scaffolds: the interrelationship between fabrication conditions, fiber topology, and mechanical properties. *Advanced Materials*, 23, 106-111.

Baldan, A. (2012). Adhesion phenomena in bonded joints. *International Journal of Adhesion and Adhesives*, 38, 95-116.

Bhat, G. S., Jangala, P. K., Spruiell, J. E. (2004). Thermal bonding of polypropylene nonwovens: effect of bonding variables on the structure and properties of the fabrics. *Journal of Applied Polymer Science*, 92, 3593-3600.

Bouddour, A., Auriault, J. L., Mhamdi-Alaoui, M., Bloch, J. F. (1998). Heat and mass transfer in wet porous media in presence of evaporation-condensation. *International Journal of Heat and Mass Transfer*, 41, 2263-2277.

Bouزيد, M., Torkia, Y. B., Wjihi, S., Lamine, A. B. (2017). Kinetic adsorption modeling of ethanol molecules onto three types of activated carbons: Microscopic interpretation of adsorption and diffusion parameters. *Journal of Molecular Liquids*, 242, 98-108.

Britton, P. N., Sampson, A. J., Gettys, W. E. (1984). Computer simulation of the mechanical properties of nonwoven fabrics Part III: Fabric failure. *Textile Research Journal*, 54, 425-428.

Brown, H. R. (1994). Adhesion between polymers. *IBM Journal of Research and Development*, 38, 379-389.

- Brunauer, S. *Physical Adsorption of Gases and Vapors*, Oxford University Press, London, 1944.
- Brunauer, S., Emmett, P. H., Teller, E. (1938). Absorption of gases in multimolecular layers. *J Am Chem Soc*, 60, 309-319.
- Carpenter, R., Reddi, B. *Neurophysiology: A Conceptual Approach*. CRC Press, 2012.
- Chandran, P. L., Barocas, V. H. (2007). Deterministic material-based averaging theory model of collagen gel micromechanics. *Journal of Biomechanical Engineering*, 129, 137-147.
- Chaudhry, S. A., Zaidi, Z., Siddiqui, S. I. (2017). Isotherm, kinetic and thermodynamics of arsenic adsorption onto Iron-Zirconium Binary Oxide-Coated Sand (IZBOCS): Modelling and process optimization. *Journal of Molecular Liquids*, 229, 230-240.
- Cheng, X., Kan, A. T., & Tomson, M. B. (2004). Naphthalene adsorption and desorption from aqueous C₆₀ fullerene. *Journal of Chemical & Engineering Data*, 49, 675-683.
- Cherepanov, G.P. *Mechanics of Brittle Fracture*, McGraw Hill, New York, 1979.
- Clarke, C. J. (1996). The kinetics of polymer brush penetration in to a high molecular weight matrix. *Polymer*, 37, 4747-4752.
- Corripio, J. G. (2004). Snow surface albedo estimation using terrestrial photography. *International Journal of Remote Sensing*, 25, 5705-5729.
- D'Amore, A., Stella, J. A., Wagner, W. R., Sacks, M. S. (2010). Characterization of the complete fiber network topology of planar fibrous tissues and scaffolds. *Biomaterials*, 31, 5345-5354.
- Dangseeyun, N., Supaphol, P., Nithitanakul, M. (2004). Thermal, crystallization, and rheological characteristics of poly (trimethylene terephthalate)/poly (butylene terephthalate) blends. *Polymer Testing*, 23, 187-194.
- Dantas, L. B., Orlande, H. R. B., Cotta, R. M. (2003). An inverse problem of parameter estimation for heat and mass transfer in capillary porous media. *International Journal of Heat and Mass Transfer*, 46, 1587-1598.

Dasdemir, M., Maze, B., Anantharamaiah, N., Pourdeyhimi, B. (2012). Influence of polymer type, composition, and interface on the structural and mechanical properties of core/sheath type bicomponent nonwoven fibers. *Journal of Materials Science*, 47, 5955-5969.

Davidson, E. A., Trumbore, S. E. (1995). Gas diffusivity and production of CO₂ in deep soils of the eastern Amazon. *Tellus B: Chemical and Physical Meteorology*, 47, 550-565.

De Boer, R. Theory of porous media: Highlights in historical development and current state. Springer, New York, 2000.

De Gennes, P. G. (1989). Weak adhesive junctions. *Journal de Physique*, 50, 2551-2562.

DeBano, L. F., Neary, D. G., and Ffolliott, P. F. Fire effects on ecosystems. John Wiley & Sons, New York, 1998.

Deryugin, Y. Y., Lasko, G. V. E., Schmauder, S. (2012). Field of stresses in an isotropic plane with circular inclusion under tensile stress. *Engineering*, 4, 583-589.

Ding, W., He, L., Zhao, G., Zhang, H., Shu, Z., Gao, D. (2004). Double porous media model for mass transfer of hemodialyzers. *International Journal of Heat and Mass Transfer*, 47, 4849-4855.

Dobre, T., Pârvulescu, O. C., Stoica-Guzun, A., Stroescu, M., Jipa, I., Al Janabi, A. A. (2016). Heat and mass transfer in fixed bed drying of non-deformable porous particles. *International Journal of Heat and Mass Transfer*, 103, 478-485.

Egitto, F. D., Matienzo, L. J. (1990). Modification of polytetrafluoroethylene and polyethylene surfaces downstream from helium microwave plasmas. *Polymer Degradation and Stability*, 30, 293-308.

Eshelby, J. D. (1957). The determination of the elastic field of an ellipsoidal inclusion, and related problems. Proceedings of the Royal Society of London. Series A. *Mathematical and Physical Sciences*, 241, 376-396.

Eshelby, J. D. (1959). The elastic field outside an ellipsoidal inclusion. Proceedings of the Royal

Society of London. Series A. *Mathematical and Physical Sciences*, 252, 561-569.

Fedorova, N., Verenich, S., Pourdeyhimi, B. (2007). Strength optimization of thermally bonded spunbond nonwovens. *Journal of Engineered Fibers and Fabrics*, 2, 38-48.

Fieldson, G. T., Barbari, T. A. (1993). The use of FTi. r.-atr spectroscopy to characterize penetrant diffusion in polymers. *Polymer*, 34, 1146-1153.

Fowler, A. J., Bejan, A. (1995). Forced convection from a surface covered with flexible fibers. *International journal of heat and mass transfer*, 38, 767-777.

Freundlich, H. M. F. (1906). Over the adsorption in solution. *J. Phys. Chem*, 57, 1100-1107.

Geguzin, Y. E. *Migration of Macroscopic Inclusions in Solids*. Springer, Heidelberg, 2014.

Gehrke, C.W., Wixom, R.L., Bayer, E. *Chromatography- A century of discovery 1900–2000, The Bridge to the Sciences/Technology*. Elsevier, Amsterdam, 2001.

Geoghegan, M., Clarke, C. J., Boue, F., Menelle, A., Russ, T., Bucknall, D. G. (1999). The kinetics of penetration of grafted polymers into a network. *Macromolecules*, 32, 5106-5114.

Goldstein, R. J., Cho, H. H. (1995). A review of mass transfer measurements using naphthalene sublimation. *Experimental Thermal and Fluid Science*, 10, 416-434.

Grate, J. W., Wise, B. M., Abraham, M. H. (1999). Method for unknown vapor characterization and classification using a multivariate sorption detector. Initial derivation and modeling based on polymer-coated acoustic wave sensor arrays and linear solvation energy relationships. *Analytical Chemistry*, 71, 4544-4553.

Green, A. E. (1956). Hypo-elasticity and plasticity. Proceedings of the Royal Society of London. Series A. *Mathematical and Physical Sciences*, 234, 46-59.

Greenberg, J. P., Friedli, H., Guenther, A. B., Hanson, D., Harley, P., Karl, T. (2006). Volatile organic emissions from the distillation and pyrolysis of vegetation. *Atmospheric Chemistry and Physics*. 6, 81-91.

Gregg, S.J., Sing, K.S.W. *Adsorption, surface area, and porosity*, Academic Press, London, 1982.

Griffy, T. A. *A model of explosive vapor concentration II. In Advances in Analysis and Detection of Explosives*. Springer, Dordrecht, 1993.

Hegde, R. R., Bhat, G. S., Campbell, R. A. (2008). Thermal bonding of polypropylene films and fibers. *Journal of Applied Polymer Science*, 110, 3047-3058.

Ho, Y. S., McKay, G. (1999). Pseudo-second order model for sorption processes. *Process Biochemistry*, 34, 451-465.

Hughes, C. D., Sethi, N. K., Baltisberger, J. H., Grant, D. M. (1989). Polyethylene crystallinity from static, solid-state NMR spectra. *Macromolecules*, 22, 2551-2554.

Ignatowicz, K. (2011). A mass transfer model for the adsorption of pesticide on coconut shell based activated carbon. *International Journal of Heat and Mass Transfer*, 54, 4931-4938.

Islam, A., Hansen, H. N., Bondo, M. (2010). Experimental investigation of the factors influencing the polymer-polymer bond strength during two-component injection moulding. *The International Journal of Advanced Manufacturing Technology*, 50, 101-111.

Israelachvili, J. N. *Intermolecular and Surface Forces*. Elsevier, New York, 2011.

Jenkins, M. L., Dauskardt, R. H., Bravman, J. C. (2004). Important factors for silane adhesion promoter efficacy: surface coverage, functionality and chain length. *Journal of Adhesion Science and Technology*, 18, 1497-1516.

Ji, H., De Gennes, P. G. (1993). Adhesion via connector molecules: The many-stitch problem. *Macromolecules*, 26, 520-525.

Jones, W. M. (1951). Mobility in a sorbed layer. Part I— The flow of gases and vapours through porous media. *Transactions of the Faraday Society*, 47, 381-392.

Jones, W. M. (1952). Mobility in a sorbed layer. Part II— Surface flow through pores of molecular dimensions. *Transactions of the Faraday Society*, 48, 562-567.

Keller, A., Lester, G. R., Morgan, L. B. (1954). Crystallization phenomena in polymers- Preliminary investigation of the crystallization characteristics of polyethylene terephthalate. *Philosophical Transactions of the Royal Society of London. Series A, Mathematical and Physical Sciences*, 247, 1-12.

Keumnam, C., Irvine Jr, T. F., Karni, J. (1992). Measurement of the diffusion coefficient of naphthalene into air. *International Journal of Heat and Mass Transfer*, 35, 957-966.

Kim, H. S., Pourdeyhimi, B., Abhiraman, A. S., Desai, P. (2002). Effect of bonding temperature on load-deformation structural changes in point-bonded nonwoven fabrics. *Textile Research Journal*, 72, 645-653.

King, M. D., Strange, M. G., Leone, P., Blaine, L. R. (1986). Multiwavelength scanning radiometer for airborne measurements of scattered radiation within clouds. *Journal of Atmospheric and Oceanic Technology*, 3, 513-522.

Kirsch, G. (1898). Die Theorie der Elastizitat und die Bedürfnisse der Festigkeitslehre. *Zentralblatt Verlin Deutscher Ingenieure*, 42, 797-807.

Kolbasov, A., Sinha-Ray, S., Yarin, A. L., Pourdeyhimi, B. (2017). Heavy metal adsorption on solution-blown biopolymer nanofiber membranes. *Journal of Membrane Science*, 530, 250-263.

Lagergren, S. (1898). About the theory of so-called adsorption of soluble substances. *Kungliga Svenska Vetenskapsakademiens Handlingar*, 24, 1-39.

Landau, L. D., Lifshitz, E. M. *Theory of Elasticity*. Pergamon Press, Oxford, 1970.

Langmuir, I. (1918). The adsorption of gases on plane surfaces of glass, mica and platinum. *Journal of the American Chemical Society*, 40, 1361-1403.

Langmuir, I. (1916). The constitution and fundamental properties of solids and liquids. Part I. Solids. *Journal of the American Chemical Society*, 38, 2221-2295.

Lee, M. W., An, S., Jo, H. S., Yoon, S. S., Yarin, A. L. (2015). Self-healing nanofiber-reinforced

polymer composites. 2. Delamination/debonding and adhesive and cohesive properties. *ACS Applied Materials & Interfaces*, 7, 19555-19561.

Lennard-Jones, J. E. (1932). Processes of adsorption and diffusion on solid surfaces. *Transactions of the Faraday Society*, 28, 333-359.

Li, J., Lu, Y., Ye, Q., Cinke, M., Han, J., Meyyappan, M. (2003). Carbon nanotube sensors for gas and organic vapor detection. *Nano Letters*, 3, 929-933.

Liao, T., Adanur, S. (1999). Computerized failure analysis of nonwoven fabrics based on fiber failure criterion. *Textile Research Journal*, 69, 489-496.

Librovich, V. B., Yarin, A. L. (1988). Problems of the mechanical strength in the combustion theory. *Archivum Combustionis*. 8, 79-99.

Liechti, K. M., Shirani, A. (1994). Large scale yielding in blister specimens. *International Journal of Fracture*, 67, 21-36.

Lin, W., Cossar, M., Dang, V., Teh, J. (2007). The application of Raman spectroscopy to three-phase characterization of polyethylene crystallinity. *Polymer Testing*, 26, 814-821.

Liscinsky, D. S., Yu, Z., True, B., Peck, J., Jennings, A. C., Wong, H. W., Miake-Lye, R. C. (2013). Measurement of naphthalene uptake by combustion soot particles. *Environmental Science & Technology*, 47, 4875-4881.

Lobert, J. M., Warnatz, J. (1993). Emissions from the combustion process in vegetation. *Fire in the Environment*. 13, 15-37.

Ma, Q., Chen, Z. (2014). Numerical study on gas diffusion in isotropic and anisotropic fractal porous media (gas diffusion in fractal porous media). *International Journal of Heat and Mass Transfer*, 79, 925-929.

Maier, C., Calafut, T. *Polypropylene: The definitive user's guide and databook*. William Andrew, Norwich, 1998.

- Mandal, B. K. *Polymer Synthesis-Strategies and Tactics*, Covalent Press, Inc, 2009.
- Masel, R. *Principles of Adsorption and Reaction on Solid Surfaces*, Wiley Interscience, New York, 1996.
- Michielsen, S., Jain, S. (2010). Thermal bonding of nonwovens as simulated by polypropylene films: Effect of time, temperature, and molecular weight. *Journal of Applied Polymer Science*, 117, 3322-3330.
- Michielsen, S., Pourdeyhimi, B., Desai, P. (2006). Review of thermally point-bonded nonwovens: Materials, processes, and properties. *Journal of Applied Polymer Science*, 99, 2489-2496.
- Mishra, S. R., Chandra, R. (2017). Kinetics and isotherm studies for the adsorption of metal ions onto two soil types. *Environmental Technology & Innovation*, 7, 87-101.
- Muskhelishvili, N. I. *Some Basic Problems of the Mathematical Theory of Elasticity*, Noordhoff International Publishing, Leyden, 1975.
- Nield, D. A., Bejan, A. *Convection in porous media*. Springer, New York, 2017.
- O'Connor, K. P., McLeish, T. C. B. (1993). "Molecular Velcro": Dynamics of a constrained chain into an elastomer network. *Macromolecules*, 26, 7322-7325.
- O'Connor, K., McLeish, T. (1994). Entangled dynamics of healing end-grafted chains at a solid/polymer interface. *Faraday Discussions*, 98, 67-78.
- Osagie, E., Owabor, C. N. (2015). Adsorption of benzene in batch system in natural clay and sandy soil. *Advances in Chemical Engineering and Science*, 5, 352.
- Oura, K., Lifshits, V. G., Saranin, A. A., Zotov, A. V., Katayama, M. *Surface Science: An Introduction*, Springer, Berlin, 2003.
- Payne, R. E. (1972). Albedo of the sea surface. *Journal of the Atmospheric Sciences*, 29, 959-970.
- Raphael, E., De Gennes, P. G. (1992). Rubber-rubber adhesion with connector molecules. *The*

Journal of Physical Chemistry, 96, 4002-4007.

Reid, R. C., Prausnitz, J. M., Poling, B. E. *The Properties of Gases and Liquids*. McGraw-Hill, New York, 1987.

Rhead, M. M., & Pemberton, R. D. (1996). Sources of naphthalene in diesel exhaust emissions. *Energy & Fuels*, 10, 837-843.

Russel, S. J. *Handbook of Nonwovens*. Woodhead Publishing, Cambridge, England, 2006.

Sajjadi, M., Azaiez, J. (2015). Heat and mass transfer in melting porous media: Stable miscible displacements. *International Journal of Heat and Mass Transfer*, 88, 926-944.

Seaver, M., Galloway, A., Manuccia, T. J. (1989). Acoustic levitation in a free-jet wind tunnel. *Rev. Sci. Instrum.* 60, 3452-3459.

Smith, K., Ogale, A. A., Maugans, R., Walsh, L. K., Patel, R. M. (2003). Effects of bond roll pattern and temperature on the microstructure and properties of polyethylene nonwovens. *Textile Research Journal*, 73, 845-853.

Snow, E. S., Perkins, F. K., Robinson, J. A. (2006). Chemical vapor detection using single-walled carbon nanotubes. *Chemical Society Reviews*, 35, 790-798.

Staszal, C., Sett, S., Yarin, A. L., Pourdeyhimi, B. (2016). Sintering of compound nonwovens by forced convection of hot air. *International Journal of Heat and Mass Transfer*, 101, 327-335.

Staszal, C., Sinha-Ray, S., Yarin, A. L., Pourdeyhimi, B. (2017). Adhesion of blended polymer films. *Polymer*, 112, 92-101

Staszal, C., Yarin, A. L., Pourdeyhimi, B. (2018). Polymer adhesion in heat-treated nonwovens. *Journal of Applied Polymer Science*, 135, 46165.

Stein, R. S., Misra, A. (1980). Morphological studies on polybutylene terephthalate. *Journal of Polymer Science: Polymer Physics Edition*, 18, 327-342.

Swinnerton, J. W., Linnenbom, V. J., Cheek, C. H. (1962). Determination of Dissolved Gases in Aqueous Solutions by Gas Chromatography. *Analytical Chemistry*, 34, 483-485.

Temkin, M., Pyzhev, V. (1940). Kinetics of ammonia synthesis on promoted iron catalysts. *Acta Physicochimica, URSS*, 12, 217-222.

Theiler, J., Wohlberg, B. (2013). Detection of unknown gas-phase chemical plumes in hyperspectral imagery. *Proc. SPIE*. 8743, 874315.

Thomas, S., Visakh, P. M. Handbook of engineering and specialty thermoplastics, Volume 3: Polyethers and polyesters. *John Wiley & Sons*, New Jersey, 2011.

Thundat, T., Chen, G. Y., Warmack, R. J., Allison, D. P., Wachter, E. A. (1995). Vapor detection using resonating microcantilevers. *Analytical Chemistry*, 67, 519-521.

Tikhonov, A. N., Samarskii, A. A. *Equations for Mathematical Physics*. Dover Publ., New York, 1990.

Toal, S. J., Trogler, W. C. (2006). Polymer sensors for nitroaromatic explosives detection. *Journal of Materials Chemistry*, 16, 2871-2883.

Troccoli, A., Allen, P. K. (2006). Recovering illumination and texture using ratio images. 3D data processing, visualization, and transmission. *Third International Symposium on IEEE*, 655-662.

Vogt, C. Kimberly- Clark Corporation. Nonwoven fabric or similar article. United States patent US239,566. 1976 April 13.

Wang, C. W., Sastry, A. M. (2000). Structure, mechanics and failure of stochastic fibrous networks: Part II—Network simulations and application. *Journal of Engineering Materials and Technology*, 122, 460-468.

Wang, S., Zhang, Y., Abidi, N., Cabrales, L. (2009). Wettability and surface free energy of graphene films. *Langmuir*, 25, 11078-11081.

Wang, X., Michielsen, S. (2001). Morphology gradients in thermally point-bonded polypropylene

nonwovens. *Textile Research Journal*, 71, 475-480.

Wang, X., Michielsen, S. (2002). Morphology gradients in thermally point-bonded poly(ethylene terephthalate) nonwovens. *Textile Research Journal*, 72, 394-398.

Wang, Y. H., Lin, S. H., Juang, R. S. (2003). Removal of heavy metal ions from aqueous solutions using various low-cost adsorbents. *Journal of Hazardous Materials*, 102, 291-302.

Warner, S. B. (1989). Thermal bonding of polypropylene fibers. *Textile Research Journal*, 59, 151-159.

Weast, R. C., Melvin, J. A., Beyer, W. H. *CRC Handbook of Chemistry and Physics*. CRC Press, Boca Raton, 1988.

Yang, X., Li, Y., Lira, C. T. (2017). Kinetics modeling of adsorption and desorption of benzaldehyde and benzyl alcohol on polymeric resin in supercritical CO₂. *Journal of CO₂ Utilization*, 21, 253-260.

Yarin, A. L., Lee, M. W., An, S., Yoon, S. S. *Self-Healing Nanotextured Vascular Engineering Materials*. Springer Nature, Switzerland AG, 2019.

Yarin, A. L., Pourdeyhimi, B., Ramakrishna, S. *Fundamentals and Applications of Micro- and Nanofibers*. Cambridge University Press, Cambridge, 2014.

Yarin, A.L., Brenn, G., Kastner, O., Rensink, D., Tropea, C. (1999). Evaporation of acoustically levitated droplets. *J. Fluid Mech.* 399, 151-204.

Yaws, C. L. *The Yaws Handbook of Vapor Pressure: Antoine Coefficients*. Gulf Professional Publishing, Houston, 2015.

Zambra, C. E., Moraga, N. O., Escudey, M. (2011). Heat and mass transfer in unsaturated porous media: Moisture effects in compost piles self-heating. *International Journal of Heat and Mass Transfer*, 54, 2801-2810.

Zeldovich, I. A., Barenblatt, G. I., Librovich, V. B., Makhviladze, G. M. *The Mathematical Theory*

of Combustion and Explosion. Plenum Press, New York, 1985.

Zhang, H., Gu, W., Li, M. J., Li, Z. Y., Hu, Z. J., Tao, W. Q. (2014). Experimental study on the kinetics of water vapor sorption on the inner surface of silica nano-porous materials. *International Journal of Heat and Mass Transfer*, 78, 947-959.

Zhang, J., Chen, Q., You, C. (2015). Numerical simulation of mass and heat transfer between biochar and sandy soil. *International Journal of Heat and Mass Transfer*, 91, 119-126.

Zhang, W., Staszal, C., Yarin, A. L., Shim, E., Pourdeyhimi, B. (2018). Point-bonded polymer nonwovens and their rupture in stretching. *Polymer*, 146, 209-221.

Zhang, W., Vilensky, R., Zussman, E., Yarin, A. L. (2018). Adsorption and mass transfer in granular porous membranes/media due to inserted volatile materials. *International Journal of Heat and Mass Transfer*, 116, 248-258.

Zhang, W., Yarin, A. L., Pourdeyhimi, B. (2019). Cohesion energy of thermally-bonded polyethylene terephthalate nonwovens: Experiments and theory. *Polymer Testing*, 78, 105984.

Zhang, W., Zussman, E., Yarin, A. L. (2018). Detection of vapor released from sublimating materials encased in porous medium. *International Journal of Heat and Mass Transfer*, 118, 1357-1372.

Zhu, J., Jacobson, L., Schmidt, D., Nicolai, R. (2000). Daily variations in odor and gas emissions from animal facilities. *Applied Engineering in Agriculture*, 16, 153-158.

Zhu, Q. Y., Xie, M. H., Yang, J., Li, Y. (2011). A fractal model for the coupled heat and mass transfer in porous fibrous media. *International Journal of Heat and Mass Transfer*, 54, 1400-1409.

Zhu, X., Shi, Y., Cai, N. (2017). High-pressure carbon dioxide adsorption kinetics of potassium-modified hydrotalcite at elevated temperature. *Fuel*, 207, 579-590.

Zimon, A. D. *Adhesion of Dust and Powder*. Springer, Heidelberg, 2012.

APPENDICES

Appendix A: Characterization of sand particles

(This section has been previously published in Zhang, W., Vilensky, R., Zussman, E., Yarin, A. L. (2018). Adsorption and mass transfer in granular porous membranes/media due to inserted volatile materials. *International Journal of Heat and Mass Transfer*, 116, 248-258)

To determine the sand size distribution and sphericity of sand particles, 100 sand particles were randomly chosen, and the optical microscope Olympus BX-51 was used to observe each of them separately, as is shown in Figure A1a and A1b.

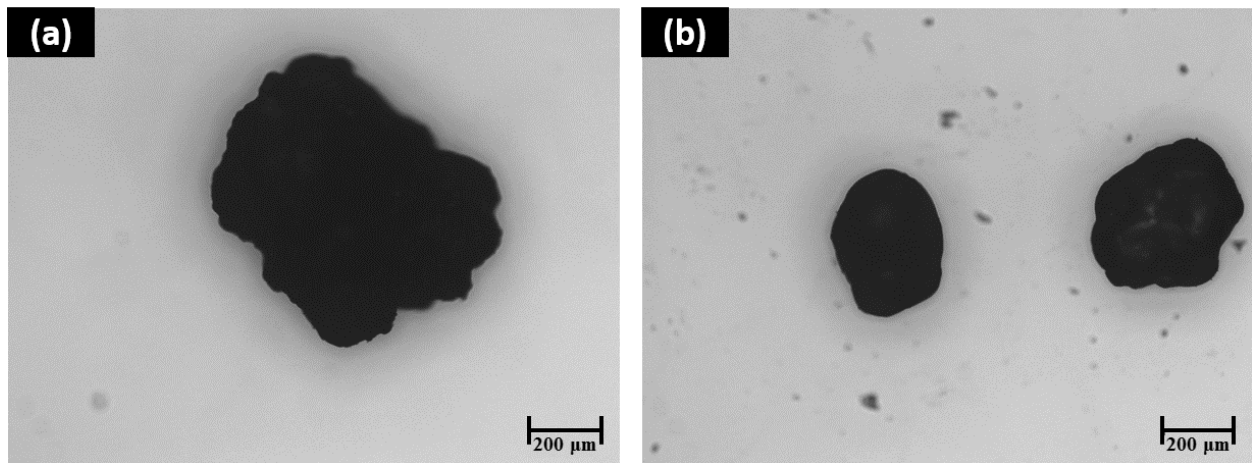


Figure A1. Sand particles observed with $\times 4$ magnification.

The images of sand particles were processed with Image-Pro Plus 7 software to measure the projected area, and the original and processed images are shown in Figures A2a and A2b, respectively. The projected areas were then measured, and the equivalent diameters were

APPENDIX A (Continued)

calculated. The equivalent diameter distribution is shown in Figure A3. The maximum equivalent diameter of sand particle is $1067.64\ \mu\text{m}$. The sand particle diameter is rendered dimensionless by its maximum value as

$$\bar{d} = d_s / d_{\text{max}} \quad (\text{A1})$$

where \bar{d} is dimensionless equivalent diameter and d_{max} is the maximum value of the equivalent diameter.

The normalized particle-size distribution $f(\bar{d})$ in Figure A3 is plotted in terms of \bar{d} . The average equivalent diameter of 100 sand particles is found as $\int \bar{d} f(\bar{d}) d\bar{d}$. Its dimensional value is $498.46\ \mu\text{m}$.

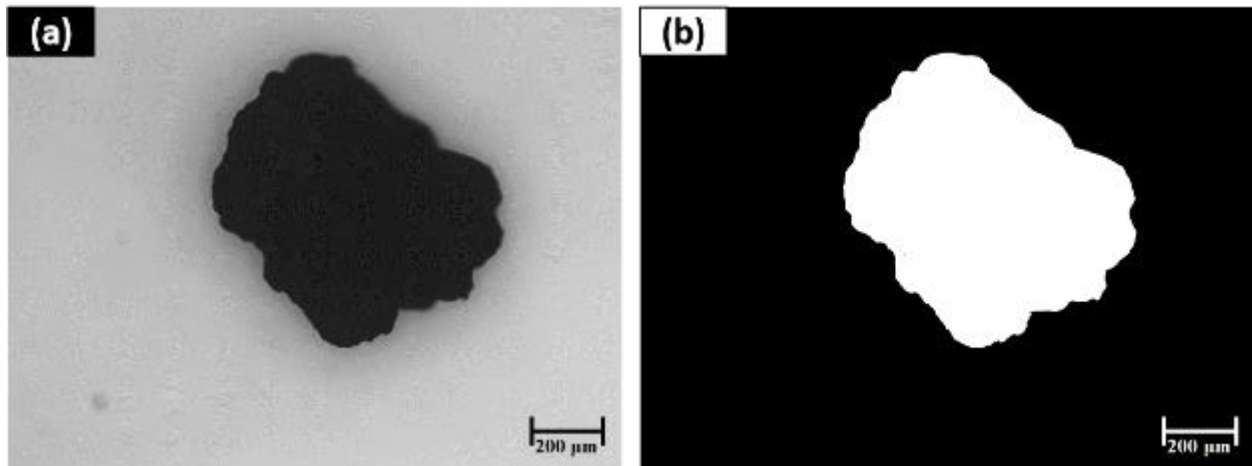


Figure A2. The image processed of a sand particle processed by Image-Pro Plus 6.0 software. (a) The original image. (b) The corresponding processed image.

APPENDIX A (Continued)

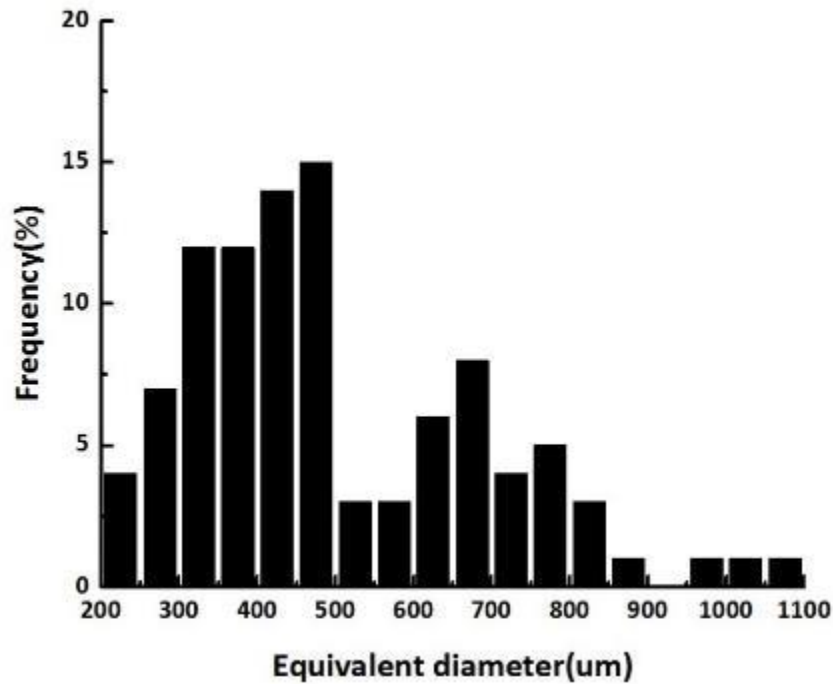


Figure A3. Sand-size distribution.

Sand particle sphericity Ψ is defined as [Jones (1951)]

$$\Psi = \frac{d_s}{D_c} \quad (A2)$$

where d_s is the diameter of a circle whose area is equal to that of the grain projection, D_c is the diameter of the smallest circle circumscribing the sand grain. The sphericity measurements and the corresponding sphericity distribution $\Psi(\bar{d})$ are shown in Figure A4 and Figure A5, respectively. The maximum value of the sphericity is 0.9353 and the average value of sphericity $\bar{\Psi}$ found using Eqs. (A1) and (A3) is 0.8281.

APPENDIX A (Continued)

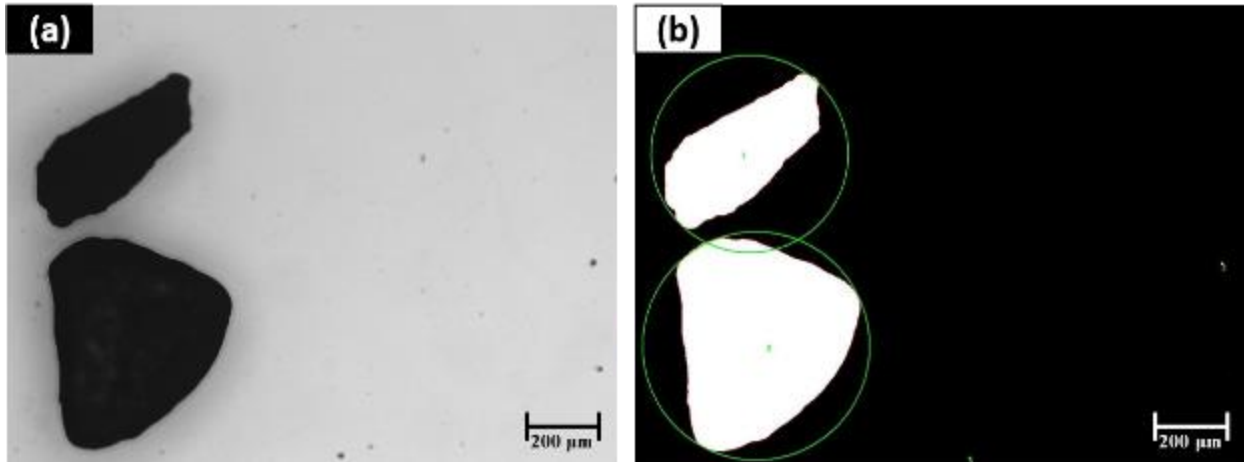


Figure A4. Measurement of sphericity. (a) The original images of two sand particles. (b) The corresponding processed images of these particles, with the green circles being the smallest circles circumscribing them.

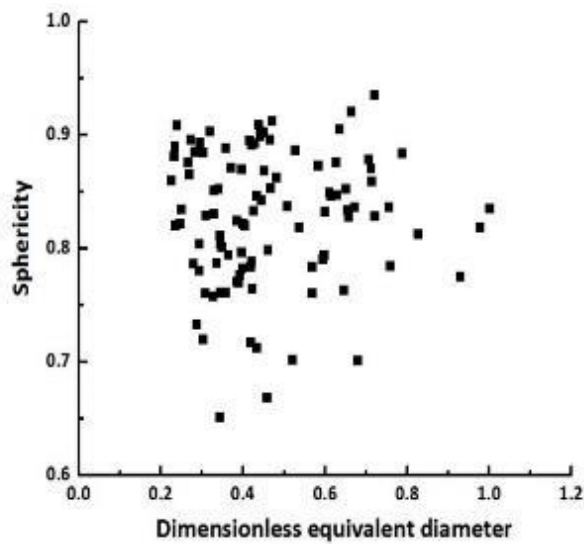


Figure A5. Sphericity distribution of 100 sand particles.

The average sphericity is found as

$$\bar{\Psi} = \int \Psi(\bar{d})f(\bar{d})d\bar{d} \tag{A3}$$

Appendix B. Permeability measurements

(This section has been previously published in Zhang, W., Vilensky, R., Zussman, E., Yarin, A. L. (2018). Adsorption and mass transfer in granular porous membranes/media due to inserted volatile materials. *International Journal of Heat and Mass Transfer*, 116, 248-258)

Two methods were used to measure permeability of sand layers. The first method used an Air-Tite disposable 60 ml syringe and Advantec® GD-120 glass fiber filter with the thickness $\Delta L_f = 0.52$ mm. The inner diameter of the syringe was 28.09 mm. A piece of glass-fiber filter was cut out in order to fit the syringe diameter. The J-B Weld quick-setting epoxy was used for attaching the filter to the syringe bottom to prevent sand spillage from the sand-filled syringe through its opening normally used to attach a needle. The D.I. water flow rate was chosen such that it could sustain a constant water level in the syringe, i.e. to compensate exactly the gravity-driven water flux from the syringe (cf. Figure B1). First, there was no sand in the syringe to find the filter permeability in the preliminary experiment (Figure B1a). Second, 60 mm height of sand was located in the syringe above the filter and permeability of the sand-filter system was measured (Figure B1b).

APPENDIX B (Continued)

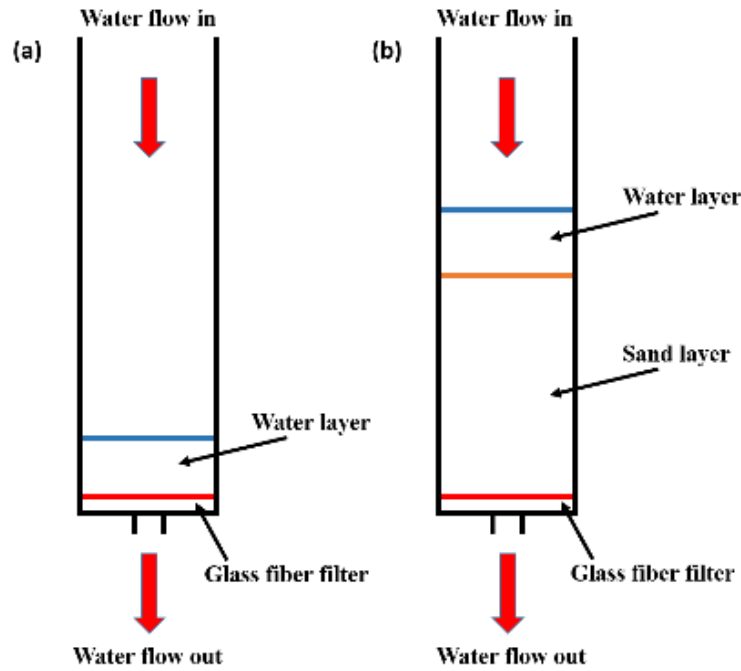


Figure B1. Experiment setup used for permeability measurements. (a) Measurement of the glass-fiber filter permeability. (b) Measurement of sand layer permeability.

The water layer height in the case of only glass-fiber filter in Figure B1a was $\Delta L_{w1} = 7.5 \text{ mm}$ and the water flow rate was $Q_1 = 770 \text{ ml/h}$. The sand layer in Figure B1b had $\Delta L_s = 60 \text{ mm}$, the water layer above it had $\Delta L_{w2} = 24 \text{ mm}$, and the water flow rate was $Q_2 = 460 \text{ ml/h}$. The viscosity of water at 25°C is $0.001 \text{ Pa}\cdot\text{s}$.

Permeability k could be evaluated using the most general form of Darcy's law for incompressible fluids which accounts for the effect of the hydrostatic pressure variation across porous medium [Jones (1952)]

APPENDIX B (Continued)

$$Q = \frac{kA}{\mu} \left(\frac{\Delta P}{\Delta L} + \rho g \right) \quad (B1)$$

where Q is the volumetric flow rate, A is the cross-sectional area, μ is the viscosity, ΔP is the pressure differential applied to porous layer, ρ is the liquid density, g is gravity acceleration, and ΔL is the layer thickness. The pressure drop could be evaluated as [Gregg and Sing (1982)]

$$\Delta P = \rho g h \quad (B2)$$

where h is height of liquid column above the layer.

In the experiment of Figure B1a, the height of water column $h = \Delta L_f + \Delta L_{w1} = 8.02$ mm and $Q_1 = 770$ ml/h, and thus, according to Eqs. (B1) and (B2) the permeability of the glass fiber filter is evaluated as $k_f = 2.24 \times 10^{-12} \text{ m}^2$ (2.26 Darcy). In the experiment of Figure B1b, $h = \Delta L_f + \Delta L_{w2} + \Delta L_s = 84.52$ mm, then total pressure is evaluated as $\Delta P_{\text{total}} = 845.20$ Pa and pressure differential acting on the glass fiber filter and the sand layer together could be evaluated as

$$\Delta P_{\text{total}} = \Delta P_s + \Delta P_f \quad (B3)$$

Hence the pressure differentials acting on the glass fiber filter and the sand layer in tandem are calculated as $\Delta P_f = 42.64$ Pa and $\Delta P_s = 802.56$ Pa. Accordingly, the permeability of the sand layer could be obtained as

$$k_s = k_f \left(\frac{\Delta P_f}{\Delta L_f} + \rho g \right) / \left(\frac{\Delta P_s}{\Delta L_s} + \rho g \right) \quad (B4)$$

This yields the permeability of the sand layer as $k_s = 8.81 \times 10^{-12} \text{ m}^2$ (8.93 Darcy).

The second method used to measure the permeability of the sand layer was the constant head

APPENDIX B (Continued)

testing method, which employed a permeameter. This method is also based on Darcy's law which disregards the hydrostatic component in Eq. (B1) and is used to measure the hydraulic conductivity k and permeability k_s of sand following [Gehrke et al. (2001)]

$$k = \frac{\Delta Q L_s}{A \Delta t \Delta h} \quad (\text{B5})$$

where k is hydraulic conductivity, A is the cross-sectional area of the permeameter, Δh is hydraulic head across the sand sample, Δt is time interval to measure the filtrated volume ΔQ and L_s is the height of compacted sand samples. Accordingly,

$$k_s = k \frac{\mu}{\rho g} \quad (\text{B6})$$

where k_s is permeability.

In this case, the diameter of the permeameter cell was 0.075 m and the height of compacted sand samples was $L_s = 0.132$ m. Three different hydraulic heads across the sand sample, 0.685 m, 0.840 m and 1.020 m, were applied separately. The time interval Δt was 120 s. The measured values of ΔQ and the corresponding permeability values are listed in Table B1. Hence, the average permeability value measured by the second method (using the permeameter cell) was $k_s = 1.14 \times 10^{-11} \text{ m}^2$ (11.55 Darcy).

APPENDIX B (Continued)

Table B1. Three values of the hydraulic head, the measured filtrate volumes and the corresponding values of sand permeability.

Hydraulic head Δh (m)	Filtrated volume $\Delta Q \times 10^{-6}$ (m ³)	Permeability $\times 10^{-12}$ (m ²)
0.685	348	12.49
	330	11.84
0.840	397	11.61
	380	11.11
1.020	455	10.96
	428	10.31

The Kozeny-Carman equation reads [Oura et al. (2003)]

$$\frac{1}{k_s} = \frac{180}{\Psi^2 D_p^2} \frac{(1-\varepsilon)^2}{\varepsilon^3} \quad (B7)$$

where D_p is the diameter of an average equivalent spherical sand particle, and ε is the porosity of the sand layer. In the present case, $D_p = 498.46 \mu\text{m}$, the sphericity is $\Psi = 0.8281$, permeability value is taken as the average value of permeability obtained by the above-mentioned two methods, which is $k_s = 1.01 \times 10^{-11} \text{m}^2$ (10.23 Darcy), and thus, the porosity of sand layers used in the experiments is $\varepsilon = 0.191$.

Appendix C: The origin of the rupture pattern surrounding bonds

(This section has been previously published as Zhang, W., Staszal, C., Yarin, A. L., Shim, E., Pourdeyhimi, B. (2018). Point-bonded polymer nonwovens and their rupture in stretching. *Polymer*, 146, 209-221.)

The origin of the failure patterns surrounding the additional thermal bonds can be traced to the classical Kirsch problem and its extension discussed in the present section. The Kirsch problem describing stretching of an elastic medium with a circular hole of radius R along the y -axis by stress $\sigma_{yy}=\sigma$ at infinity is sketched in Figure C1.

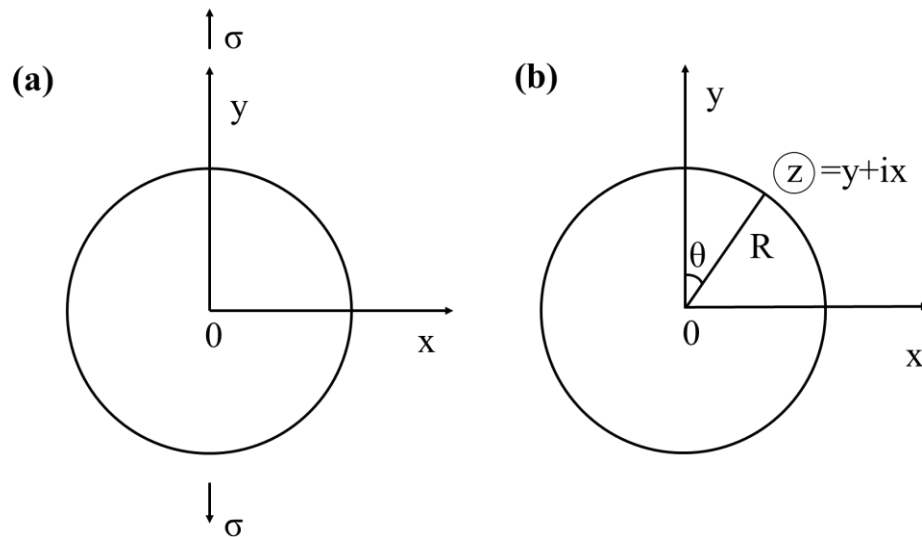


Figure C1. (a) Sketch of the Kirsch problem. (b) The polar coordinates and the complex z -plane.

The corresponding stress field reads

APPENDIX C (Continued)

$$\sigma_{rr} = \frac{\sigma}{2} \left(1 - \frac{R^2}{r^2} \right) + \frac{\sigma}{2} \left(1 + \frac{3R^4}{r^4} - \frac{4R^2}{r^2} \right) \cos 2\theta \quad (C1)$$

$$\sigma_{\theta\theta} = \frac{\sigma}{2} \left(1 + \frac{R^2}{r^2} \right) - \frac{\sigma}{2} \left(1 + \frac{3R^4}{r^4} \right) \cos 2\theta \quad (C2)$$

$$\sigma_{r\theta} = -\frac{\sigma}{2} \left(1 - \frac{3R^4}{r^4} + \frac{2R^2}{r^2} \right) \sin 2\theta \quad (C3)$$

where the Cartesian xy , and polar $r\theta$ coordinate systems are introduced in Figure C1b. It should be emphasized that the planar Kirsch problem describes the plane-stress case, i.e.

$$\sigma_{zz} = 0 \quad (C4)$$

where z is the third Cartesian coordinate normal to x and y and should not cause any confusion with the complex variable $z=y+ix$ (with i being the imaginary unity introduced in Figure C1b). It should be emphasized that the non-standard introduction of the complex variable z is related to the fact that in Figure C1b the angle θ is reckoned from the axis of stretching y , rather than from the x -axis. Still, $z=re^{i\theta}$.

The corresponding Airy function U , which is the solution of the biharmonic equation $\nabla^4 U = 0$ of the planar theory of elasticity, can be found from Eqs. (C1)- (C3) using the following relations [Landau and Ligshitz (1970)]

$$\sigma_{rr} = \frac{1}{r} \frac{\partial U}{\partial r} + \frac{1}{r^2} \frac{\partial^2 U}{\partial \theta^2}, \quad \sigma_{\theta\theta} = \frac{\partial^2 U}{\partial r^2}, \quad \sigma_{r\theta} = -\frac{\partial}{\partial r} \left(\frac{1}{r} \frac{\partial U}{\partial \theta} \right) \quad (C5)$$

It reads

$$U = \frac{\sigma}{2} \left(\frac{r^2}{2} - R^2 \ln r \right) - \frac{\sigma}{4} \left(r^2 + \frac{R^4}{r^2} - 2R^2 \right) \cos 2\theta \quad (C6)$$

APPENDIX C (Continued)

The Airy function U is determined by the two Goursat functions (or the complex elastic potentials)

$\varphi(z)$ and $\chi(z)$ as [Muskhelishvili (1975)]

$$U = \operatorname{Re} \left\{ \bar{z}\varphi + \chi \right\} \quad (\text{C7})$$

Comparing Eqs. (C6) and (C7), it is easy to see that

$$\varphi(z) = \frac{\sigma z}{4} + \frac{\sigma R^2}{2z}, \quad \chi(z) = -\frac{\sigma R^2}{2} \ln z - \frac{\sigma}{4} \left(z^2 + \frac{R^4}{z^2} \right) \quad (\text{C8})$$

It is convenient to introduce a new function $\psi(z) = \chi'(z)$, i.e.

$$\psi(z) = -\frac{\sigma R^2}{2z} - \frac{\sigma}{2} \left(z - \frac{R^4}{z^3} \right) \quad (\text{C9})$$

which will be used below.

It should be emphasized that the same functions $\varphi(z)$ and $\psi(z)$ can be found using Eqs.

(C1)- (C3) and the stresses

$$\sigma_{xx} = \sigma_{rr} \sin^2 \theta + \sigma_{r\theta} \sin 2\theta + \sigma_{\theta\theta} \cos^2 \theta \quad (\text{C10})$$

$$\sigma_{xy} = (\sigma_{rr} - \sigma_{\theta\theta}) \frac{1}{2} \sin 2\theta + \sigma_{r\theta} \cos 2\theta \quad (\text{C11})$$

$$\sigma_{yy} = \sigma_{rr} \cos^2 \theta - \sigma_{r\theta} \sin 2\theta + \sigma_{\theta\theta} \sin^2 \theta \quad (\text{C12})$$

having in mind that

$$\sigma_{xx} + \sigma_{yy} = 4 \operatorname{Re} \{ \varphi' \} \quad (\text{C13})$$

$$\sigma_{xx} - \sigma_{yy} + 2i\sigma_{xy} = (\bar{z}\varphi'' + \psi') \quad (\text{C14})$$

Accordingly, the displacements along the y and x axes, v and u , respectively, are found as

[Muskhelishvili (1975)]

APPENDIX C (Continued)

$$v + iu = \frac{1}{2G} \left[\kappa\phi - z\overline{\phi'(z)} - \overline{\psi(z)} \right] \quad (C15)$$

where the shear modulus G is given by

$$G = \frac{E}{2(1+\nu)} \quad (C16)$$

with E being Young's modulus and ν is Poisson's ratio. Also,

$$\kappa = \frac{3-\nu}{1+\nu} \quad (C17)$$

for the plane stress problem (C4) [Cherepanov (1979)].

Solution of the problem with a circular elastic inclusion can be constructed as a linear superposition of three problems (Figure C2). Problem (I) is a uniform biaxial stretching with the dimensionless factors k_x and k_y to be found, and problems (II) and (III) being the Kirsch problems. Such a linear superposition is possible due to linearity of the theory of elasticity and the fact that the boundary conditions for stretching at infinity for the uniaxial stretching are satisfied by it. Moreover, it will be shown below that the boundary condition at the interface of the inner material 2 and the outer material 1, which is the requirement that the displacements are identical on both banks of the interface (since the materials are bonded), can also be satisfied by the choice of the factors k_x and k_y .

APPENDIX C (Continued)

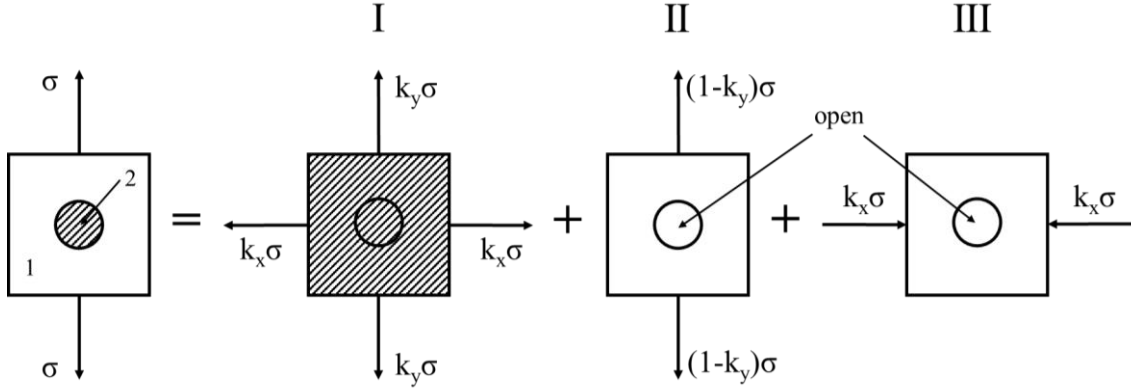


Figure C2. Split of the problem on stretching of elastic material (1) with a circular elastic inclusion (2) into a linear superposition of three problems (I), (II) and (III).

The uniform biaxial stretching in the inner material 2, as well as in the outer material for problem I is given by the following elastic potentials

$$\varphi(z) = \frac{(k_x + k_y)\sigma}{4} z, \quad \psi(z) = \frac{(k_x - k_y)\sigma}{4} z \quad (\text{C18})$$

Using Eqs. (C8), (C9), (C15) and (C18), and superimposing the solutions for problems I, II, and III, one can find the displacement field in the outer material in the case of uniaxial stretching along the y-axis of an elastic material 1 with a circular elastic inclusion in the following form

$$v = \frac{\sigma}{E_1} (k_y - \nu_1 k_x) y + \frac{(1-k_y)\sigma}{2G_1} \operatorname{Re} \left\{ \kappa_1 \left(\frac{z}{4} + \frac{R^2}{2z} \right) - z \left(\frac{1}{4} - \frac{R^2}{2z^2} \right) + \frac{R^2}{2z} + \frac{1}{2} \left(\frac{-R^4}{z} - \frac{R^4}{z^3} \right) \right\} - \frac{k_x\sigma}{2G_1} \operatorname{Im} \left\{ \kappa_1 \left(\frac{z_1}{4} + \frac{R^2}{2z_1} \right) - z_1 \left(\frac{1}{4} - \frac{R^2}{2z_1^2} \right) + \frac{R^2}{2z_1} + \frac{1}{2} \left(\frac{-R^4}{z_1} - \frac{R^4}{z_1^3} \right) \right\} \quad (\text{C19})$$

$$u = \frac{\sigma}{E_1} (k_x - \nu_1 k_y) x + \frac{(1-k_y)\sigma}{2G_1} \operatorname{Im} \left\{ \kappa_1 \left(\frac{z}{4} + \frac{R^2}{2z} \right) - z \left(\frac{1}{4} - \frac{R^2}{2z^2} \right) + \frac{R^2}{2z} + \frac{1}{2} \left(\frac{-R^4}{z} - \frac{R^4}{z^3} \right) \right\} - \frac{k_x\sigma}{2G_1} \operatorname{Re} \left\{ \kappa_1 \left(\frac{z_1}{4} + \frac{R^2}{2z_1} \right) - z_1 \left(\frac{1}{4} - \frac{R^2}{2z_1^2} \right) + \frac{R^2}{2z_1} + \frac{1}{2} \left(\frac{-R^4}{z_1} - \frac{R^4}{z_1^3} \right) \right\} \quad (\text{C20})$$

APPENDIX C (Continued)

where subscript 1 corresponds to material 1 and

$$z = y + ix, \quad z_1 = x - iy \quad (C21)$$

In the inner material 2, accordingly,

$$v = \frac{\sigma}{E_2} (k_y - v_2 k_x) y \quad (C22)$$

$$u = \frac{\sigma}{E_2} (k_x - v_2 k_y) x \quad (C23)$$

With $y=R\cos\theta$ and $x=R\sin\theta$, i.e. at the interface, Eqs. (C19)- (C21) yield

$$v = \frac{\sigma}{E_1} (k_y - v_1 k_x) y + \frac{3(1-k_y)\sigma}{E_1} y + \frac{k_x \sigma}{E_1} y \quad (C24)$$

$$u = \frac{\sigma}{E_1} (k_x - v_1 k_y) x - \frac{(1-k_y)\sigma}{E_1} x - \frac{3k_x \sigma}{E_1} x \quad (C25)$$

Equating Eqs. (C22) and (C23) with Eqs. (C24) and (C25), respectively, to satisfy the condition of the identical displacements of both materials at the interface (the bonding condition), one obtains a system of two equations for two unknowns, k_x and k_y , which yields

$$k_x = \frac{E_2 [E_1 (-1 + 3v_2) + E_2 (1 - 3v_1)]}{(E_1 + 2E_2)^2 - [v_2 E_1 + E_2 (1 - v_1)]^2} \quad (C26)$$

$$k_y = \frac{E_2 [(3 - v_2)E_1 + E_2 (5 + v_1)]}{(E_1 + 2E_2)^2 - [v_2 E_1 + E_2 (1 - v_1)]^2} \quad (C27)$$

In the case of very stiff inclusions when the ratio $E_2 / E_1 \rightarrow \infty$, Eqs. (C26) and (C27) are reduced to the following ones

$$k_x = \frac{1 - 3v_1}{3 + 2v_1 - v_1^2}, \quad k_y = \frac{5 + v_1}{3 + 2v_1 - v_1^2} \quad (C28)$$

APPENDIX C (Continued)

Then, the displacements in material 1 along the stretching axis y , i.e. at $x=0$, are found from Eqs.

(C19)- (C21) as

$$v|_{x=0} = \frac{\sigma}{E_1} (k_y - \nu_1 k_x) y + \frac{(1-k_y)\sigma}{2G_1} \left[\kappa_1 \left(\frac{y}{4} + \frac{1}{2y} \right) - y \left(\frac{1}{4} - \frac{1}{2y^2} \right) + \frac{1}{2y} + \frac{1}{2} \left(y - \frac{1}{y^3} \right) \right] - \frac{k_x \sigma}{2G_1} \left[\kappa_1 \left(-\frac{y}{4} + \frac{1}{2y} \right) + y \left(\frac{1}{4} + \frac{1}{2y^2} \right) - \frac{1}{2y} + \frac{1}{2} \left(y - \frac{1}{y^3} \right) \right] \quad (C29)$$

$$u|_{x=0} = 0 \quad (C30)$$

The stress fields in the outer material 1 can be found as a superposition of the corresponding stress fields for problems I, II and II. Namely, for the combination of problems I and II, we obtain from Eqs. (C8), (C9), (C13) and (C14)

$$\sigma_{xx} = \text{Re} \left\{ \bar{z} \varphi'' + \psi' + 2\varphi' \right\} \quad (C31)$$

$$\sigma_{yy} = -\text{Re} \left\{ \bar{z} \varphi'' + \psi' - 2\varphi' \right\} \quad (C32)$$

$$\sigma_{xy} = \text{Im} \left\{ \bar{z} \varphi'' + \psi' \right\} \quad (C33)$$

where primes denote derivatives by z , and

$$\varphi' = \frac{(k_x + k_y)\sigma}{4} + \frac{(1-k_y)\sigma}{4} - \frac{(1-k_y)\sigma}{2} \frac{R^2}{z^2}, \quad \varphi'' = (1-k_y)\sigma \frac{R^2}{z^3} \quad (C34)$$

$$\psi' = \frac{(k_x - k_y)\sigma}{2} + \frac{(1-k_y)\sigma R^2}{2z^2} - \frac{(1-k_y)\sigma}{2} \left(1 + \frac{3R^4}{z^4} \right) \quad (C35)$$

Accordingly, the stress field corresponding to problem III reads

$$\sigma_{xx} = -\text{Re} \left\{ \bar{z}_1 \varphi'' + \psi' - 2\varphi' \right\} \quad (C36)$$

$$\sigma_{yy} = \text{Re} \left\{ \bar{z}_1 \varphi'' + \psi' + 2\varphi' \right\} \quad (C37)$$

APPENDIX C (Continued)

$$\sigma_{xy} = \text{Im} \left\{ \bar{z}_1 \varphi'' + \psi' \right\} \quad (\text{C38})$$

where primes denote derivatives by z_1 , and

$$\varphi' = \frac{k_x \sigma}{4} + \frac{k_x \sigma R^2}{2 z_1^2}, \quad \varphi'' = -k_x \sigma \frac{R^2}{z_1^3} \quad (\text{C39})$$

$$\psi' = -\frac{k_x \sigma R^2}{2 z_1^2} + \frac{k_x \sigma}{2} \left(1 + \frac{3R^4}{z_1^4} \right) \quad (\text{C40})$$

Adding Eq. (C31) to (C36), Eq. (C32) to (C37) and Eq. (C33) to (C38), one obtains all the fields of the stress components in the outer material 1.

In inner material 2, Eq. (C18) yield

$$\varphi' = \frac{(k_x + k_y) \sigma}{4}, \quad \varphi'' = 0, \quad \psi' = \frac{(k_x - k_y) \sigma}{2} \quad (\text{C41})$$

which with Eqs. (C30)- (C32) yield the stress fields in these materials.

Appendix D: Publisher permissions

The permissions for the published papers used in the present thesis obtained from the publisher are listed on the following pages. The permissions granted by Elsevier are for the work on adsorption and mass transfer in granular porous membranes/media due to the inserted volatile materials contained in subsection 2.1.1, section 3.1, and chapter 4; for the work on detection of vapor released from sublimating materials encased in porous medium contained in subsection 2.1.2, section 3.2, and chapter 5; for the work on point-bonded polymer nonwovens and their rupture in stretching contained in subsection 2.2.1, section 3.3, and chapter 7; for the work on cohesion energy of thermally- bonded polyethylene terephthalate nonwovens in subsection 2.2.2, section 3.4, and chapter 8. Links to these published works are shown as follows:

- Adsorption and mass transfer in granular porous membranes/media due to inserted volatile materials: <https://doi.org/10.1016/j.ijheatmasstransfer.2017.09.012>
- Detection of vapor released from sublimating materials encased in porous medium: <https://doi.org/10.1016/j.ijheatmasstransfer.2017.11.069>
- Point-bonded polymer nonwovens and their rupture in stretching: <https://doi.org/10.1016/j.polymer.2018.05.024>
- Cohesion energy of thermally-bonded polyethylene terephthalate nonwovens: Experiments and theory: <https://doi.org/10.1016/j.polymertesting.2019.105984>

APPENDIX D (Continued)



RightsLink®

[Home](#)[Account Info](#)[Help](#)

Title: Adsorption and mass transfer in granular porous membranes/media due to inserted volatile materials

Author: W. Zhang, R. Vilensky, E. Zussman, A.L. Yarin

Publication: International Journal of Heat and Mass Transfer

Publisher: Elsevier

Date: January 2018

© 2017 Elsevier Ltd. All rights reserved.

Logged in as:
WENSHUO ZHANG
Account #:
3001446953

[LOGOUT](#)

Please note that, as the author of this Elsevier article, you retain the right to include it in a thesis or dissertation, provided it is not published commercially. Permission is not required, but please ensure that you reference the journal as the original source. For more information on this and on your other retained rights, please visit: <https://www.elsevier.com/about/our-business/policies/copyright#Author-rights>

[BACK](#)[CLOSE WINDOW](#)

Copyright © 2019 Copyright Clearance Center, Inc. All Rights Reserved. [Privacy statement](#). [Terms and Conditions](#).

Comments? We would like to hear from you. E-mail us at customer@copyright.com

APPENDIX D (Continued)



RightsLink®

Home

Account
Info

Help



Title: Detection of vapor released from sublimating materials encased in porous medium
Author: Wenshuo Zhang, Eyal Zussman, Alexander L. Yarin
Publication: International Journal of Heat and Mass Transfer
Publisher: Elsevier
Date: March 2018

Logged in as:
WENSHUO ZHANG
Account #:
3001446953

LOGOUT

© 2017 Elsevier Ltd. All rights reserved.

Please note that, as the author of this Elsevier article, you retain the right to include it in a thesis or dissertation, provided it is not published commercially. Permission is not required, but please ensure that you reference the journal as the original source. For more information on this and on your other retained rights, please visit: <https://www.elsevier.com/about/our-business/policies/copyright#Author-rights>

BACK

CLOSE WINDOW

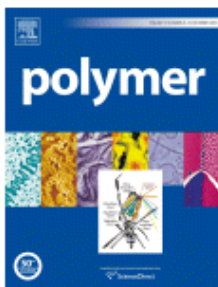
Copyright © 2019 [Copyright Clearance Center, Inc.](#) All Rights Reserved. [Privacy statement](#). [Terms and Conditions](#).

Comments? We would like to hear from you. E-mail us at customer@copyright.com

APPENDIX D (Continued)



RightsLink[®]

[Home](#)[Account Info](#)[Help](#)

Title: Point-bonded polymer nonwovens and their rupture in stretching

Author: Wenshuo Zhang, Christopher Staszal, Alexander L. Yarin, Eunkyong Shim, Behnam Pourdeyhimi

Publication: Polymer

Publisher: Elsevier

Date: 20 June 2018

© 2018 Elsevier Ltd. All rights reserved.

Logged in as:
WENSHUO ZHANG
Account #:
3001446953

[LOGOUT](#)

Please note that, as the author of this Elsevier article, you retain the right to include it in a thesis or dissertation, provided it is not published commercially. Permission is not required, but please ensure that you reference the journal as the original source. For more information on this and on your other retained rights, please visit: <https://www.elsevier.com/about/our-business/policies/copyright#Author-rights>

[BACK](#)[CLOSE WINDOW](#)

Copyright © 2019 [Copyright Clearance Center, Inc.](#) All Rights Reserved. [Privacy statement](#). [Terms and Conditions](#).

Comments? We would like to hear from you. E-mail us at customercare@copyright.com

APPENDIX D (Continued)



RightsLink



Home



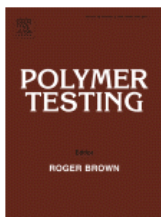
Help



Email Support



WENSHUO ZHANG ▾



Cohesion energy of thermally-bonded polyethylene terephthalate nonwovens: Experiments and theory

Author: Wenshuo Zhang, Alexander L. Yarin, Behnam Pourdeyhimi

Publication: Polymer Testing

Publisher: Elsevier

Date: September 2019

© 2019 Elsevier Ltd. All rights reserved.

Please note that, as the author of this Elsevier article, you retain the right to include it in a thesis or dissertation, provided it is not published commercially. Permission is not required, but please ensure that you reference the journal as the original source. For more information on this and on your other retained rights, please visit: <https://www.elsevier.com/about/our-business/policies/copyright#Author-rights>

BACK

CLOSE WINDOW

CURRICULUM VITAE

WENSHUO ZHANG

Department of Mechanical and Industrial Engineering, University of Illinois at Chicago (UIC)
842 W. Taylor Street, Chicago, IL 60607-7022

EDUCATION

University of Illinois at Chicago, Chicago, IL, USA *May 2015-Dec. 2019*

- Ph.D. Candidate, Mechanical Engineering

Illinois Institute of Technology, Chicago, IL, USA *Aug. 2013- May 2015*

- M.S., Chemical Engineering

Southwest Petroleum University, Chengdu, China *Sep. 2009- June 2013*

- B.S., Chemical Engineering

PUBLICATIONS

1. S. Sinha-Ray, **W. Zhang**, B. Stoltz, R.P. Sahu, S. Sinha-Ray, A. L. Yarin. “Swing-like pool boiling on nano-textured surfaces for microgravity applications related to cooling of high-power microelectronics”. *npj Microgravity*, 3(2017), 1-9.

2. S. Sinha-Ray, **W. Zhang**, R.P. Sahu, S. Sinha-Ray, A. L. Yarin. “Pool boiling of Novec 7300 and DI water on nano-textured heater covered with supersonically-blown or electrospun polymer nanofibers”. *International Journal of Heat and Mass Transfer*, 106(2017), 482-490.

3. **W. Zhang**, R. Vilensky, E. Zussman, A. L. Yarin. “Adsorption and mass transfer in granular porous membranes/media due to inserted volatile materials”. *International Journal of Heat and Mass Transfer*, 116 (2018), 248-258.

4. **W. Zhang**, E. Zussman, A. L. Yarin. “Detection of vapor released from sublimating materials encased in porous medium”. *International Journal of Heat and Mass Transfer*, 118 (2018), 1357-1372.

5. **W. Zhang**, C. Staszal, A. L. Yarin, E. Shim, B. Pourdeyhimi. "Point-bonded polymer nonwovens and their rupture in stretching". *Polymer*. 146 (2018), 209-221.
6. A. Sankaran, **W. Zhang**, A. L. Yarin. "Pool boiling in deep and shallow vessels and the effect of surface nano-texture and self-rewetting". *International Journal of Heat and Mass Transfer*. 127 (2018), 857-866.
7. **W. Zhang**, A. L. Yarin, B. Pourdeyhimi. "Cohesion energy of thermally-bonded polyethylene terephthalate nonwovens: experiments and theory". *Polymer Testing*. 78 (2019), 105984.
8. **W. Zhang**, E. Zussman, A. L. Yarin. "Heat and Mass Transfer Resulting in Eruptive Jetting from Stems and Leaves during Distillation Stage of Forest Fire". Submitted.
9. **W. Zhang**, A. L. Yarin, B. Pourdeyhimi. "A New Method of Characterization of the Clapeyron Effect for Polymers". Submitted

MEETING ABSTRACTS AND PRESENTATIONS

1. **W. Zhang**, E. Zussman, A. L. Yarin, "Sensing underground gas release", Korea University and University of Illinois at Chicago International Workshop. Chicago, Illinois (April 2016; April 2017; July 2018).
2. **W. Zhang**, A. L. Yarin, B. Pourdeyhimi, "Bonding area/pattern that affect the properties of nonwovens: experiments and modeling. Bi-annual industrial board research review meetings at The Nonwoven Institute. Rayleigh, North Carolina (November 2017; May 2018; November 2018; May 2019; November 2019).

TEACHING EXPERIENCE

University of Illinois at Chicago - Graduate Teaching assistant

- ♦ Introduction to Computer-Aided Design, ME447: **Fall 2015**
Instructed computer-aided design utilizing the SolidWorks platform.
- ♦ Fluid Mechanics, ME211: **Spring 2017**
Instructed the fluids laboratory section of the class.

- ♦ Introduction to Thermodynamics, ME205: **Fall 2017**
Grading assistant and tutor.
- ♦ Numerical Method of Mechanical Engineering, ME428: **Fall 2019**
Grading assistant and tutor.